Mechanical Characterisation of Mammalian Cells during Monolayer Formation using Atomic Force Microscopy

Jessica Lee Barkhuisen

Submitted for the degree of Doctor of Philosophy

Heriot-Watt University

School of Engineering and Physical Sciences

ABSTRACT

Exploring the elasticity of mammalian cells - through interpretation of the Young's elastic modulus [E] - has become one of the most useful benchmark biomarkers for investigating the relationship between the physiological and mechanical properties of cells. Such investigations have, until now, primarily focussed on interpreting how cells physically respond at the single cell and monolayer developmental stages. Less consideration into how single cell mechanics translates at intermediary and/or higher cell density developmental stages has been fully addressed. Therefore, attempting to investigate and interpret the mechanical properties of a cell at various stages of development e.g. increasing cell numbers and degree of monolayer confluency, will provide further insight into how tissue structures develop, as well as how cell-associated diseases such as cancer progress. Various techniques are utilised when attempting to determine the Young's modulus of biological samples. One such method, atomic force microscopy (AFM), has emerged as a useful tool for determining the Young's modulus of soft biological samples. When utilising AFM for the mechanical characterisation of cells, cell samples are often prepared as adherent cultures with a variety of AFM cantilever geometries and experimental parameters utilised. Variation in the selection of AFM parameters between studies can result in variation between tested batches of cell samples. Markedly, when attempting to measure the Young's modulus of mammalian cell lines by AFM, little consideration has been given regarding how the specific stage of cell development and degree of monolayer confluency can affect derived elasticity outputs. Recent studies have highlighted the apparent differences in the elasticity of cells present at alternate stages of development; single isolated cells present with a higher Young's modulus compared to cells within a structured cell monolayer. Further to this, AFM indentation and resulting [E] has been reported to be sensitive to the indentation depth analysed. Variation in the selection of an appropriate AFM loading force, and how this can affect the outcome of cell mechanical outputs, such as resulting final cell deformation and derived cell [E] has been not fully considered. Therefore, the primary aim of this thesis was to carry out a defined and bridged approach for investigating cell mechanics at precisely defined stages of monolayer formation. Using an incremental loading force range, together with cell [E] map and morphological fluorescence cell imaging, this thesis demonstrates the variation in derived mammalian cell [E] outputs through different stages of cell monolayer development. With variation in mechanical outputs described and associated to the most relevant intercellular and intracellular cytoskeletal and cell organelle components.

ACKNOWLEDGEMENTS

Throughout the duration of my PhD studies at Heriot-Watt University, a number of people have been highly supportive in guiding and supporting me through the task. Firstly, I would like to express the utmost gratitude for my supervisor's Dr Yuhang Chen and Professor Nik Willoughby for giving me the opportunity to pursue a PhD at Heriot-Watt University, as well as their endless support, patience and guidance during my time as a research PhD student. I would like to thank my fellow PhD peers and students at Heriot- Watt, who made this journey all the more memorable; Thank you Maryam, Javi, Behnam, Frank, Solenn, Michael and Antonio.

I would also like to thank the laboratory staff at the Edinburgh Super-Resolution Imaging Consortium (ESRIC) at Heriot-Watt. Thank you Dr Alison Dun and Dr Rebecca Saleeb for your repeated patience and assistance in all practical laboratory work carried out within ESRIC.

This doctoral thesis could not have been carried out without the EPSRC scholarship grant awarded to me. I am absolutely grateful for the opportunity that was given to me.

Lastly, I would like to thank my family and friends for their endless and unconditional support during my academic and research studies.

DEDICATION

For my parents, thank you for supporting me in all of my academic endeavours.

To my husband and daughter, thank you for giving me the courage and strength to persevere with my research and passions.

ACADEMIC REGISTRY
Research Thesis Submission

Name*:*	Jessica Lee Barkhuisen		
School:	Engineering and Physical sciences		
Version: *(i.e. First, Resubmission, Final)*	Final	Degree Sought:	Ph.D. Mechanical Engineering

Declaration

In accordance with the appropriate regulations I hereby submit my thesis and I declare that:

1) The thesis embodies the results of my own work and has been composed by myself
2) Where appropriate, I have made acknowledgement of the work of others and have made reference to work carried out in collaboration with other persons
3) The thesis is the correct version of the thesis for submission and is the same version as any electronic versions submitted*.
4) my thesis for the award referred to, deposited in the Heriot-Watt University Library, should be made available for loan or photocopying and be available via the Institutional Repository, subject to such conditions as the Librarian may require
5) I understand that as a student of the University I am required to abide by the Regulations of the University and to conform to its discipline.
6) I confirm that the thesis has been verified against plagiarism via an approved plagiarism detection application e.g. Turnitin.

* *Please note that it is the responsibility of the candidate to ensure that the correct version of the thesis is submitted.*

Signature of Candidate*:*		Date:	

Submission

Submitted By *(name in capitals):*	
Signature of Individual Submitting:	
Date Submitted:	

For Completion in the Student Service Centre (SSC)

Received in the SSC by *(name in capitals):*			
Method of Submission *(Handed in to SSC; posted through internal/external mail):*			
E-thesis Submitted (***mandatory for final theses)***			
Signature:		Date:	

“Dream big.

Start small.

But most of all, start”

-

Simon Sinek

CONFERENCES AND AWARDS

The following conference presentations have been made during my PhD candidature:

- **Conference presentations and awards**

(2015) Annual (EPS) Poster and research presentation, Heriot-watt University.

(2015) 1ST Year postgraduate research prize, school of engineering and physical sciences (EPS), Heriot-watt University.

- **Conference proceedings**

Examining mechanical properties of three-dimensional hollow tissue structures: micro-ultrasound, atomic force microscopy and computational modelling. Valerie Bentivegna(1), **Jessica Barkhuisen(2**), Javier Palacio Torralba(2) , Iwan Schaap(2) , Yuhang Chen(2), Sandy Cochran(3) and Inke Näthke(1). 7th Annual PiCLS Symposium, Dundee, Scotland, October 2016.

AFFLIATIONS AQUIRED DURING STUDENTSHIP

Associate fellow of the higher education academy (HEA) and completion of the learning and enhancement and development skills courses (LEADS1 and LEADS2).

TABLE OF CONTENTS

LIST OF FIGURES

LIST OF TABLES

ABBREVIATIONS

2D - Two-dimensional

3D – Three-dimensional

ABP – Actin binding protein

AFM – Atomic force microscopy

DMT – Derajaguin, Muller and Toporov

DP – Data processing

E – Elasticity

ECM – Extra cellular matrix

ICM – Intracellular matrix

MDCK – Madin – Darby canine kidney

MSC – Mesenchymal stem cell

PBS – phosphate buffered saline

RBC – red blood cells

CHAPTER 1

Introduction

1.1 Motivation

The human body comprises a multitude of different types of heterogeneous tissue structures, each of which are formed by millions of cells. Over the past few decades, much research has elucidated how cells within tissue and organ compartments function, and communicate through biological signalling pathways [1]. Many advances have thus followed, in the fields of regenerative science and stem cell engineering, and have led to the point where we are now able to culture and direct various types of progenitor cells into specialised fates, for the purposes of treating degenerative disorders, injury or disease [2], [3]. However, although noteworthy, these advances are limited in most scenarios to cell-only transfusion therapies. Unfortunately, despite continued efforts in tissue engineering, it still remains challenging to treat and regenerate vital tissue compartments following injury, where transfused progenitor cells neither fully integrate or acquire optimal cell perfusion into host tissues [4], [5]. Therefore, while it may be possible to chemically direct (through defined cell biochemical signalling pathways), different progenitor stem cells into alternate specialised fates, the failure of transfused and transplanted donor cells to integrate and regenerate damage tissues, suggests that further consideration regarding additional cell properties such as the mechanical characteristics of mammalian cells during tissue development needs to addressed.

The mechanical properties of tissue constructs have been observed at the organ level, with ample evidence presented for tissue elasticity, rigidity, viscoelasticity, osmotic pressure and sheer stress mechanical properties [6]. However, less evidence exists, whereby scientists have attempted to bridge the derived mechanical properties at the organ scale with the derived mechanical properties at the cellular scale. How mammalian cells act and vary their mechanical properties at each hierarchical level of an organ scale tissue construct is not fully defined. Moreover, how do pathological changes in a cell(s) function, for example tumour growth, produce highly variable mechanical outputs when investigated at alternate stages of proliferation and development. For instance, a single cancerous cell in cell culture, is far more malleable to deformation, compared to healthy mammalian cells [7].

For both healthy and diseased tissue cells, one mechanical property, the Young's elastic modulus [E], has become a hallmark indicator for defining how a mammalian cells mechanical property can vary for different development states. The Young's elastic modulus of mammalian cells has been shown to vary among different cell types [8], as well as during different developmental conditions, such as cell apoptosis [9] , senescence [10]–[12], differentiation [13]–[16], as well as in response to induced chemical imbalance [17].

Among the numerous methods available for investigating mammalian cell Young's elastic moduli outputs, Atomic Force Microscopy (AFM) has gained popularity for its ability to produce high resolution three-dimensional images for sample surface topography, which, if combined with force spectroscopy, is able to define and assign surface properties, such as cell Young's elastic modulus to specific mammalian cellular regions. Most notably, this can be achieved in an *in vitro* cell culture environment [16]. However, much of the existing AFM studies reported on live mammalian cells,

primarily only investigate the mechanical properties (the Young's elastic modulus) of cell samples at either the single, grouped or monolayer stages of development. Little evidence has shown what the resulting Young's elastic modulus outputs are for AFM studies focussing on precise stages of cell monolayer development. Investigating cell Young's elastic moduli outputs through mammalian cell monolayer development is paramount to defining how mammalian cells begin to form larger three-dimensional tissue layers and structures.

As a result, the primary aim of this PhD thesis is to investigate how live mammalian cell Young's elastic moduli outputs, acquired using AFM, are affected under specific stages of monolayer development during the formation and maturation of cell monolayers. By investigating cell Young's elastic moduli outputs using a multiscale cell developmental approach, it would be possible to establish an experimental and analytical framework for interpreting how changes in cell Young's elastic moduli properties may arise with increase in cell number and proliferation. This could then be translated into how cells respond to their respective tissue microenvironments. The overarching objective of the thesis, is determining how such processes being how these pathways can be replicated (or inhibited) for clinical purposes. For example, being able to direct the progression of cell fate using culture scaffolds or chemical perturbation, which could allow for the protentional development of ex-vivo regenerated tissue constructs for the treatment of injury or disease. Furthermore, applying similar investigative methods to determine how a cell adapts its mechanical properties (such Young's elastic modulus) and transforms in cell degeneration or disease, could allow for the investigation into how to inhibit such processes.

1.2 Thesis scope and structure

This thesis has two major goals. The first is to establish and test a robust and reliable protocol for investigating the Young's elastic modulus outputs of mammalian cells across specified cell developmental scales using AFM. Experimental themes in the selection of cell type(s), culture protocols, AFM measurement conditions and data analysis techniques are all to be addressed. Defining a reproducible framework for investigating cell Young's elastic modulus outputs across cell monolayer development stages, is paramount for addressing how cell mechanical properties can be affected during mammalian tissue formation. The second goal is to apply some context to the established protocol in the form of investigating and relating AFM measurements to specified intracellular cytoskeletal components.

In order to achieve the aforementioned goal of multiscale mammalian cell analysis using AFM, this thesis is structured to allow for the progressive investigation of topics, theories and protocols associated with mammalian cell analysis by AFM. This thesis is structured to first give a concise literature review of topics associated with the analysis of the mechanical properties of mammalian cells and tissues, followed by the materials and methodology used for the experimental assays presented in this thesis. These chapters are then followed by the data acquired for investigations pertaining to (1) adapting the proposed AFM method and protocol for mammalian cell analysis, (2) investigating how cell state affects derived AFM Young's elastic moduli measurements, (3) correlating cell state, and derived AFM Young's elastic moduli outputs to associated cell morphology (4) correlating cell state at incremental length scales to further optimized AFM protocols and biological frameworks (cytoskeletal components, and cell junctional complexes).

Further detail about the content presented in each chapter of this thesis is presented as follows;

Chapter 2: Length scales in biology; An overview of evidence and concepts for investigating the mechanical properties of cells and tissues

This chapter reviews the main topics and concepts of hierarchical biological and cell developmental length scales associated with investigating the mechanical properties of mammalian cells. An overview of the current understanding of hierarchy in tissue microstructure and the two most often utilised approaches for biomechanical analysis, i.e. bottom-up and top-down approaches is discussed. Current evidence for tissue mechanical analysis and associated outputs are addressed, at both the macroscopic (tissue) and microscopic (cell) length scale. This chapter also reviews some of the various methods currently utilised to measure and interpret cell mechanics, with one of the hallmark indicators of variations in tissue and cell mechanical properties (Young's elastic modulus) discussed. Specific focus on AFM as a tool for investigating cell Young's elastic modulus is addressed.

Chapter 3: Materials and Methods

In this chapter, the general materials and methods utilised for all forms of experimentation in this thesis are presented and discussed, including the selected mammalian cell line, its preparation, maintenance and manipulation for AFM experimentation. Furthermore, the protocol, set-up and operating modes of AFM used to carry out all AFM cell indentation to derive cell Young's elastic moduli outputs is detailed. Live and fixed cell fluorescence microscopy protocols are described. Lastly, the methods and contact models, software and statistical tests used for interpreting and analysing all acquired AFM and cell imaging data are detailed.

Chapter 4: Application of current AFM protocols for mammalian cell Young's elastic moduli analysis: Adapting the experimental approach

Prior to investigating the potential variations in live cell AFM Young's elastic moduli measurements, proper consideration and testing of different AFM experimental parameters and data analysis was carried out. In doing so, it was possible to confidently compare derived AFM cell Young's elastic moduli outputs across a number of samples under different experimental conditions. This allowed for greater reproducibility and confidence of the results presented in each chapter. This chapter addresses the troubleshooting assays that were carried out to produce an appropriate protocol for AFM Young's elastic moduli analysis on live mammalian cells across a multiscale cellular platform, an appropriate protocol for AFM data acquisition and data analysis was tested and established. Test assays included; selection of an appropriate cell line, selection and testing of appropriate cantilever probes on the selected cell line, experimental parameters such as loading forces, cell regional selection for AFM cantilever indentation, and fixed cell AFM topography imaging was investigated. Further to this, the method of AFM force curve analysis and application of the contact model(s) used to derive the Young's elastic moduli analysis is presented and discussed in this chapter.

Chapter 5: Effect of stage of cell developmental on Atomic force spectroscopy Young's elastic moduli measurements

Following the assessment and application of AFM protocol parameters for live mammalian cell AFM indentation (Chapter 4), the next phase of AFM experiments focussed on evaluating how the cell sample (in terms of variation in stage of cell proliferation) can affect the accuracy and reproducibility of derived AFM Young's elastic moduli outputs. Variation in mammalian cell height, cortical thickness, nuclear organelle morphology and activity of cytoskeletal elements have all been implicated as

key morphological variations that occur as mammalian cells proliferate to produce confluent cell monolayers. It is often the case however, that little consideration is given with regards to the stage of cell development in terms on stage of monolayer growth during AFM experiments investigated mammalian cell Young's elastic moduli trends. Therefore, this chapter aimed to determine how the stage of cell monolayer development can affect the indentation/deformation depth achieved for mammalian cells by and thus the derived cell Young's elastic moduli trends. This was achieved by carrying out mammalian cell indentations across an incremental cantilever loading force range (0.5nN-3.0nN). Three specific cell monolayer developmental stages (single, semi-confluent and maximal density confluence monolayer cells) were assessed and compared.

Chapter 6: Stage of MDCK cell development and associated AFM Young's elastic moduli trends: A review of potential underlying mechanisms for observed outcomes

Based on the result presented in Chapter 5, the purpose of this chapter is to outline and hypothesize which cellular mechanism components may give rise the derived AFM Young's elastic moduli results presented. The internal and surface components of mammalian cells which are most associated with cell mechanical Young's elastic moduli outputs such as the actin cell cortex, cell junctional complexes and cell nucleus is discussed. This is followed by two hypotheses as to what might give rise the results obtained, namely (1) variation in cell morphology with progressive cell development, or (2) development of increased stress along the cell-cell junction regions and cell cortical region with progressive development. These hypotheses are discussed, and then validated in the results chapters that follow.

Chapter 7: Hypothesis 1: Morphological variation of MDCK cells across three stages of cell monolayer development

Having tested and derived an appropriate AFM protocol for analysing the Young's elastic modulus on the selected mammalian cell line (Chapter 4), as well as investigated the requirement for considering the stage of cell monolayer development (at three specified length scales) and its applicably to AFM Young's elastic moduli analysis (Chapter 5), MDCK cell fluorescent morphology analysis images were acquired and assessed for variation in morphological variations for the three stages of cell monolayer development presented in Chapters 4 and 5. This was carried out to investigate the first hypothesis described in Chapter 6. The morphological transitions that mammalian cells progress through, as well as the differences in the selection of an appropriate AFM protocol i.e. cantilever loading force, and resulting cell indentation/deformation depths with respect to cell monolayer development, can have a great effect on derived AFM Young's elastic moduli output trends. Therefore, the purpose of this chapter was to investigate variations in cell morphology through monolayer development. This comparison was carried out for single cells in comparison to semi-confluent and maximal density monolayer cells. Fluorescent microscopy methods (FLoid EVOS imaging and 3D confocal imaging) were used to analyse and measure morphological variations in cell (1) height, (2) cortical layer thickness and (3) nuclear organelle morphology at each specified stage of cell development.

Chapter 8: Hypothesis 2: Progressive cell development of MDCK cells results in the alteration of MDCK Young's elastic moduli properties along the cortex and cell junction regions

Based on the results derived and presented for the cell morphological analysis at specified stages of cell monolayer development (Chapter 7), the aim of this chapter was to analyse the theory of actin cortex Young's elastic moduli gradient transitions and

downregulation at cell-cell interface junctions. This was carried out to investigate the second hypothesis proposed in Chapter 6. This involved analysing AFM Young's elastic moduli outputs pertaining to the inner cell cortical layer of single, monolayer and intermediate (cell doublet pair and cell cluster, internal and periphery) cell monolayer developmental stages. As discussed in the motivation of this thesis, much of the research carried out aimed at investigating how mammalian cells adapt their mechanical properties in terms of their Young's elastic moduli outputs, have predominantly focused on the single cell, cell group and higher cell density monolayer developmental stages. Therefore, this chapter analysed force map Young's elastic modulus profiles for the nuclear cortical region of MDCK cells, as well as the cell-cell junction region across incremental stages of cell monolayer development. A single selected loading force of 0.8nN was used to gather and analyse MDCK cell Young's elastic moduli trends pertaining to the inner actin filament cortex. Using a single selected indentation force of 0.8nN and applying the Hertz-Sneddon contact model function (for appropriate MDCK cell deformation limits of the Hertz-Sneddon contact model), this chapter presents the variation in AFM derived MDCK cell Young's elastic outputs for (1) single, (2) cell doublet pair, (3) internal cell cluster cell, (4) periphery cell cluster cell and (5) semi-confluent and (6) maximal density monolayer confluence cells. MDCK cell Young's elastic moduli trends for the cell cortical region and cell-cell junction region are presented, and the results interpreted and discussed.

Chapter 9: Looking back and working forward

In this final chapter, the main conclusions obtained from the results and work carried in this thesis is summarized and highlighted. Future work and experiments relating to the topic(s) are proposed, with the hope of continuing the establishment of a novel framework for multiscale cell mechanical analysis at higher cell developmental length scales.

CHAPTER 2

Length scales in biology: An overview of evidence and concepts for investigating the mechanical properties of cells and tissues

2.1 Length scales in biology: From cells to tissue structures

When attempting to *measure* nature, scientists have defined a spatial, temporal and expansive scale by which all naturally existing entities can be conveniently observed and quantified [18]. This scale has allowed for the establishment of various hierarchical denotations for different types of tissue structures within the human body – which exist across several length scales i.e. molecular structure to macroscopic tissue anatomy [19]. Markedly, both tissue formation - which begins at the molecular level - as well as the physiological performance of a fully developed organ structure are both equally attributed to the same hierarchical scale. A useful model often used to illustrate the varying organizational levels found within biological structures, is the fibrous connective tissue band (tendon) that connects muscle to bone (Figure 2-1).

Notably, while many studies have used the distinctive hierarchical anatomy of a tendon to illustrate differences in biological length scales, smaller biological structures, such as single mammalian cells, also exhibit a hierarchical structure; A single mammalian cell comprises organelle structures such as the nuclear organelle, which has a diameter in the micrometre scale, but is supported by intracellular protein networks whose diameters are in the nanometre scale. In the context of applying the defined hierarchical length scales to specific physiological or disease processes, researchers often adopt one of two

main approaches; a (1) top-down or (2) bottom-up approach [18], [20]. In the top-down approach - most often utilised - the biological system is analysed from a macroscopic perspective. For example, when investigating the pathological effects of hypertension, physicians usually correlate arterial wall thickening to an increase arterial blood pressure [21].

[A]

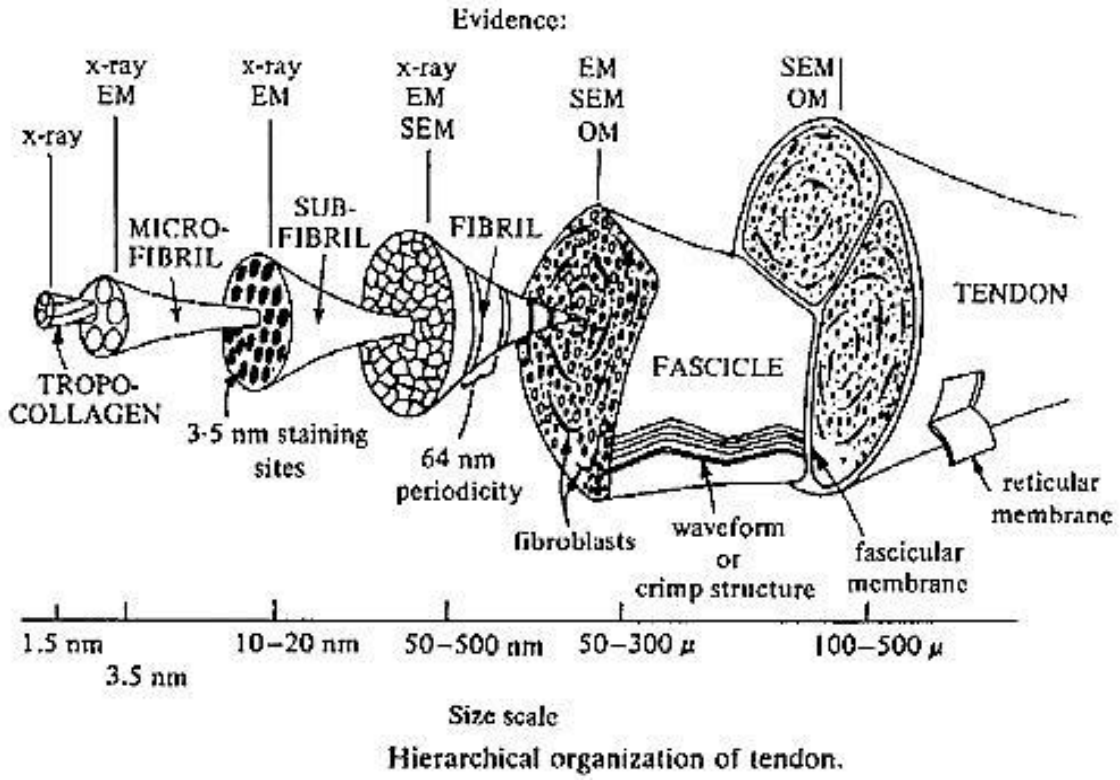

Hierarchical organization of tendon.

[B]

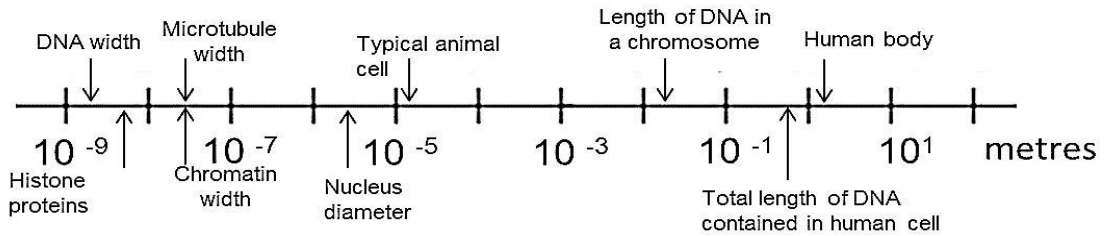

Figure 2-1. Length scales in Biology. **[A]** Anatomical structure and correlating lengths of the mammalian tendon (Figure, Cowen and Doty, 2007, p20) [19], **[B]** Length scales found within smaller mammalian structures such as single cells (Figure adapted and self-illustrated, taken from Akhtar, et al, 2011 [22].

However, although the top-down approach seems relatively simple, as one would expect, variables or measurements obtained by this method often do not accurately represent the true underlying physiological or pathophysiological process. In the given example this would be how the individual arterial endothelial cells collectively respond to increasing amounts of circumferential tension by producing molecular growth factors, which stimulates their proliferation, thereby increasing the relative thickness of the artery [21].The process described, is an example of how cellular level events can lead to tissue level disruptions and pathologies. As a result, when a more detailed analysis of the individual elements comprising a biological structure is required, scientists adopt the bottom-up approach [23]. The advantage of the bottom-up approach is that it allows for a 'reversed-reductionist' study of a biological structure or system as a consequence of the behaviours stemming from its most basic elements i.e. interactions at the single cell level, which give rise to tissue-level structure and physiological function [18].

Therefore, in summary, when attempting to investigate and define a novel biological parameter through which a single cell may function to give rise to a fully functional tissue structure, a bottom-up analysis of the interactions that occur at a single cell and cell-by-cell length scale is most suitable. This will produce a more complete interpretation of how a tissue structure may form across a multiscale platform.

2.2 Mechano-transduction

The first indication that a physical stress can influence the physiological function and architecture of a tissue was over 100 years ago, when German scientist Julius Wolf demonstrated the increased remodelling - strength and density - of bone tissue subjected to increasing loads of force [24]. To date, the tissue-level observation of bone

remodelling has become a standard example of how a physical mechanical cue, can prompt a cellular-level biochemical signalling cascade. For example, when subjected to increasing macro-scale loads, osteocyte cells collectively respond to the increasing perturbations within their local environment, by up-regulating the expression and activity of various protein kinases and calcium signalling channels. This in turn induces a wave of transcriptional responses that activate the secretion of additional molecules and chemokines that bind to and recruit bone-remodelling osteoblast and osteoclast cells – thus increasing the overall density of mineralised bone [25].

Referring to the example described in bone remodelling, the interplay and looped-feedback in cellular response arising from external mechanical cues is commonly referred to as ‘mechano-transduction’. Events that occur during tissue formation processes such as cellular assortment, adhesion, deformation, and migration are all processes subject to the concept of mechano-transduction. The interplay and concept of cellular physical and biochemical mechanisms involved in mechano-transduction is illustrated (Figure 2-2).

It is important to note that in order for scientists to advance our interpretation of how tissue structures naturally form, more time and investigations needs to be made in determining how the mechanical properties of cells relates to internal cell biochemical signalling pathways. Current mechanobiology studies have demonstrated a number of noteworthy mechanisms (in the realm of mechano-transduction as discussed) that demonstrate how a cells fate can be directed using external mechanical cues. As well as differentiation directed mechano-transduction, mammalian cells have been shown to adapt their shape, apical membrane stiffness and actin microfibre alignment based on the underlying culture substrate; softer substrate rigidities have resulted in rounded, non-spread cell morphologies with few stress fibres, while stiffer substrates resulted in

flatter, spread cells with large amounts of stress fibres [26]. Therefore, as well as directing cells through differentiation and development by means of instruction via external scaffolds or substrates, consideration in terms of what substrate platform for culture that different cells require to appropriately mimic that of an *in vivo* tissue system is also required.

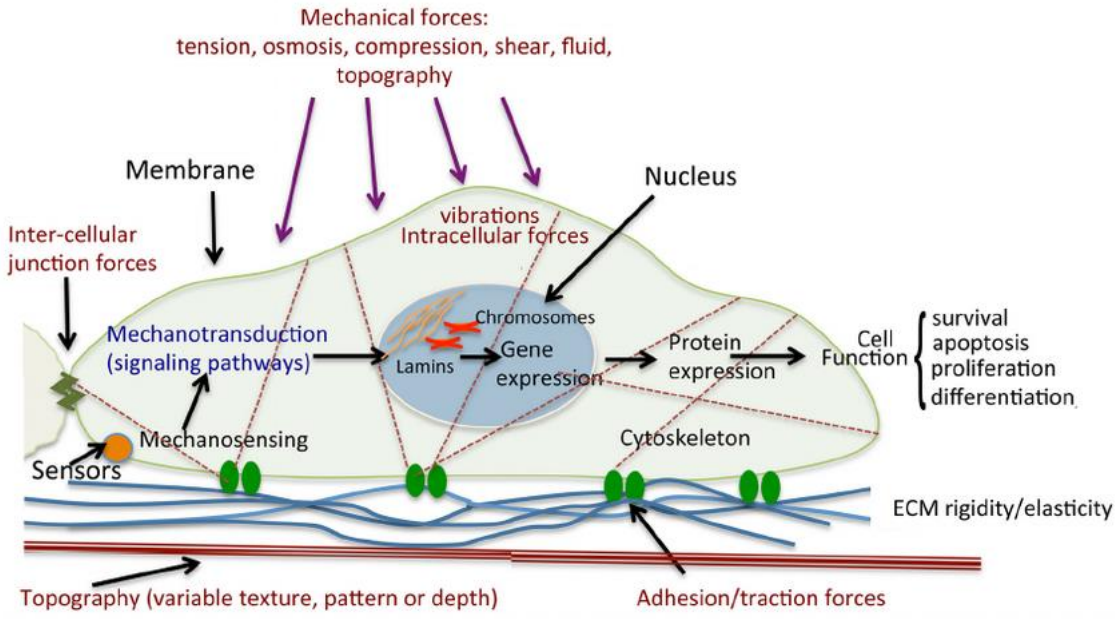

Figure 2-2. Mechano-transduction schematic. External mechanical cues or forces acting on mammalian cells stimulate the cells internal biochemical signalling pathways via surface mechano-sensors. The conference of cell fate and function in response to external physical perturbations, is achieved through an array of external membranous proteins connected to the external membranous environment – the extracellular matrix (ECM). ECM forces applied directly to the cell surface travel through integrin anchored focal adhesions which connect directly to the internal cell cytoskeletal microfilaments, and indirectly to microtubules and intermediate filaments. This results in the modulation of protein and gene expression and therefore cell fate and function (differentiation, proliferation and survival) (Figure taken from Tsimbouri, et al ,2015)[27].

2.3 Tissue Mechanics – An overview

To date, scientists have identified six levels of organisation within the human body; (1) biomolecular, (2) cellular, (3) tissue, (4) organ, (5) organ system and (6) organism [28]. In the context of studying tissue mechanics, a tissue structure can be further defined as "the aggregation of morphologically similar cells and associated intercellular elements, all acting together to perform various specific functions within the human body" [29]. In theory, each tissue structure within the human body often comprises a heterogeneous mix of two or more of the four major types of tissue present within the human body; (1) muscular, (2) nervous, (3) epithelial and (4) connective tissue (Table 2-1). In principle, when investigating the mechanical properties of different tissues, experimental outputs represent the macroscopic length scale, and are a summation of the mechanical responses of numerous cells functioning in unison - a top-down analysis. Such investigations often revolve around investigating specific types of mechanical properties namely; (1) Porelasticity, which is the interaction and behaviour of a porous medium and pore fluid with respect to applied stresses, (2) viscoelasticity, which is a material with both viscous and elastic properties, and (3) electro-mechanical properties such neuromuscular pathways [30]. For all methods of tissue mechanical analysis, experimental output values are often inhomogeneous, and greatly depend on the position and state at which a tissue exists at the point of experimentation i.e. type of bone, condition of the bone, active or inactive muscles, healthy or cancerous tissue.

2.4 Methods for investigating tissue mechanics: Summary of methods

Experimental techniques used to investigate the mechanical properties of macroscale tissue constructs fall into three broad categories; (1) *ex-vivo* mechanical tests, (2) *in-vivo* mechanical tests, (3) and/or computational modelling. For clinical and physiological relevance, it is often more desirable to determine the mechanical properties of a given

tissue in its natural state. However, due to patient discomfort and ethical restrictions, most mechanical tests are acquired using tissue biopsy samples taken from live or cadaveric donors. In summary, some of the current investigative and experimental techniques utilised to measure the macroscopic mechanical properties of different tissues include; Stress/relaxation tensile and/or tissue compression tests (typical for soft tissues with both solid and fluid like behaviour i.e. viscoelastic) [31]; Cyclic loading and unloading of tensile and/or compressive tissue loads (typical for viscoelastic and tissue energy dissipation assays) [22]; Electrical impedance assays (useful for measuring *in vivo* muscular mechanical outputs for specific disease states) [32]; Pulse wave velocity (commonly used for estimating large artery stiffness/distortion in response to pulse pressures) [33]; Acoustic pulse methods (high frequency acoustic pulse waves primarily used for elastically stiff tissue types such as tumour masses) [34]; and lastly, computational simulation experiments configured to approximate tissue scale mechanical properties through inputting various mechanical values and constraints e.g. fluid flow, RBC movement, cancer cell growth [35], [36].

Notably, as previously discussed, the mechanical properties acquired from tissue-level mechanical analysis are subject to the summated effects of the various cell and cell matrix components within the chosen tissue. As a result, experimental values are often used to define and correlate changes in tissue structure at a macroscopic length scale. Such observations are useful for identifying clinical markers associated with tissue level deformations associated with disease progression i.e. presence of a tumour or arterial wall thickening. However, tissue level investigations are less useful for underpinning how the mechanical properties of a tissue exist at the cell and molecular length scale.

Table 2-1. Mechanical properties of the four major tissue types found in the human body [28], [30].

Tissue type	Tissue function	Tissue mechanics
Muscle	Generate forces required to move body's skeleton. Transportation of blood (and contents) throughout body. Energy and heat generation.	Physical functions. Uniform contraction and distortion of muscle cells to move skeleton and pump blood. Electromechanical functions. Uniform mechanical contraction in response to nervous tissue inputs.
Cardiac		
Skeletal		
Smooth		
Epithelial	Cover and lining of body surfaces, hollow organs, cavities and ducts. Forms glands.	Physical functions. Covers, supports, lines and protects body structures. Some poroelastic properties (glandular structures/ oedematous tissues (skin).
Covering and lining		
Glandular		
Connective	Protects and supports body organs. Binds organs and tissues together. Provides immunity to pathogens. Gaseous transport.	Poroelastic properties (bone and bone marrow). Viscoelastic properties (bone and cartilage). Physical functions. Support and connects cells forming organ structures. Chemical and immune responses.
Blood		
Bone		
Cartilage		
Dense connective (Elastin, collagen)		
Loose connective (adipose tissue)		
Nervous	Responds to external stimuli by generating electrical and chemical impulses to activate muscular and glandular responses.	Poroelastic properties. No true mechanical function. Research investigations have outputs pertaining to the resulting electro physical and chemical responses evoked via stimulation.
Central		
Peripheral		

2.5 Tissue mechanics - The ECM and intercellular mechanics

The extracellular matrix (ECM), is the non-cellular component that resides within all tissues and organs of the body. The ECM is a composite mixture of extracellular protein molecules that provide structural support to the specific, and surrounding tissue cells from which they are secreted from (Figure 2-3A). The ECM is a form of physical scaffold, providing support to tissue cellular components, as well as physical platform through which key biochemical and biomechanical cues are signalled for cell and tissue morphogenesis, differentiation and homeostasis [37]. In both humans and other

mammals, the strength and behaviour of most aging tissues is controlled mainly by, but not limited to, the relative composition and organisation of the ECM protein network in its fibrillary form. Across the heterogenic mixture of cells and tissue constructs present within the human body, cellular processes such as cell-adhesion, cell-cell communication and cell differentiation, are all dependent on the presence and optimal function of the tissue microstructure and ECM. The ECM is, in essence, a subcellular scaffold that characterises the strength and function of different tissue structures [38]. The mechanical properties of the ECM and its individual microstructure components has been studied in a variety of experimental assays. For example, nanoindentation by atomic force microscopy of porcine aorta demonstrated the significant contribution of ECM collagen and elastin fibres. Chemical perturbation of the these fibres resulted in significant reduction (50 times) in the Young's elastic modulus values obtained from force mapping of the porcine aorta [39]. Atomic force microscope indentation of bovine carotid artery and underlying subendothelial basement membrane demonstrated similar Young's elastic moduli trends (2.5 ± 1.9 kPa for carotid artery and 2.7 ± 1.1 kPa for subendothelial membrane) [40]. This suggest that the role and support (fibrillary composition) of the ECM can vary in different tissues and between mammalian species. The ECM comprises a multitude of fibrillary proteins (Figure 2-3A). The ECM is composed of proteins such as collagen, fibrin, laminin, and elastin.

Attempts have also been made to investigate and derive the mechanical properties of individual fibril components of the ECM. Nanoindentation of tail type 1 collagen fibrils using atomic force microscopy produced elastic modulus values in the range of 5 GPa to 11.5 GPa [41], and a range of 100 MPa and 360 MPa for rat tail collagen type 1 fibres analysed using optical tweezers [42]. Additional studies using optical tweezers found the Young's modulus of un-crosslinked and crosslinked fibronectin fibres of 1.7

MPa and 14.5 MPa respectively [43]. Furthermore, elastin fibres have been shown to have a Young's modulus of around 1 MPa [44].

2.6 Tissue mechanics – Intercellular junctions

During tissue and organ formation, mammalian cells are linked together and the ECM to form tissue by specific types of specialised intercellular adhesion junction complexes (Figure 2-3B). There are three main categories of cell-cell adhesion complexes. Firstly, tight junctions. These junctions are primarily found at the apical ends of cells, and are composed of occluding and claudin transmembrane proteins that bind to intracellular membrane proteins such as zonula occludens (ZO). The second type of cell junction are adherens junctions, which are composed of E-cadherin transmembrane proteins linked to intracellular adapter proteins (such as B-catenin) which the bind to the actin cytoskeletal network. The third type of cell junction complex is the desmosomal junction, which are formed by desmoglein and desmocolin proteins that bind internal adaptor proteins such as desmoplankin [45]. Interestingly, genetic and chemical perturbation studies have emphasised the apparent direct correlation with the formation of adherens, but not desmosomal junctions and tissue scale tension [46].

[A]

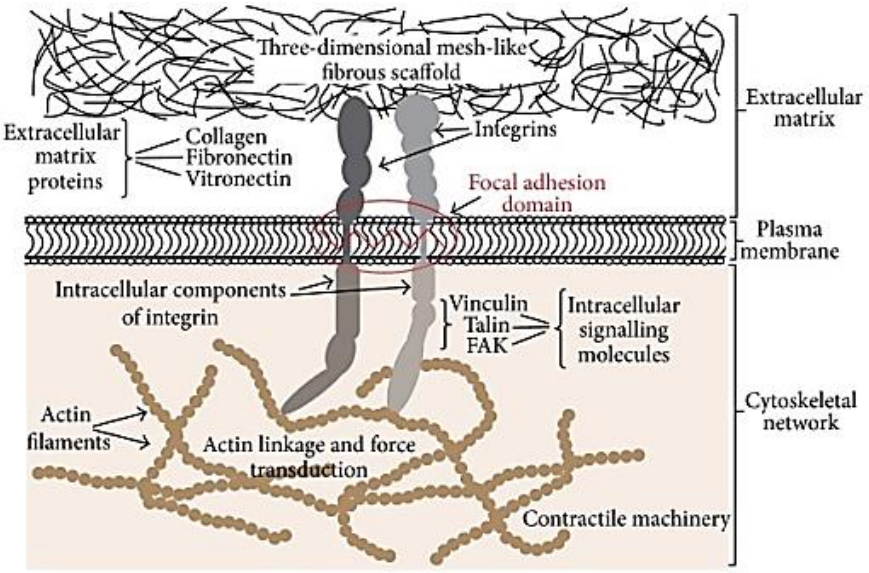

[B]

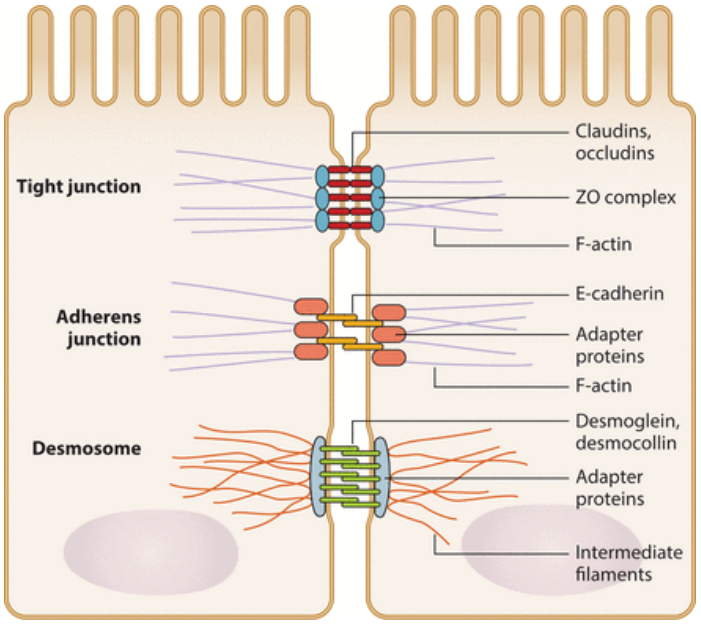

Figure 2-3. **The ECM and cell-cell adhesion**. **[A]** The ECM is composed of several distinct types of molecules. These include; insoluble collagens, which make up the basement membrane and provide strength and resilience to cells. Soluble glycosaminoglycans (fibronectin, laminin and vitronectin), which anchor cells by binding collagens, proteoglycans and cell surface receptors resulting in bidirectional tissue assemblies. Cell adhesion molecules such as integrins, which control cell-cell and cell-ECM adhesion to help modulate mechano-transduction signalling pathways (Figure, Lodish, 2008) [47], [48]. **[B]** Cell-cell adhesion within tissues is controlled via the interaction of various ECM proteins with transmembrane and intracellular cell protein complexes. These proteins function to anchor and bind to transmembrane cell surface receptors, thus binding and linking multiple cells and cellular arrangements to one another. The number and type of cell-cell adhesion complexes present on a cell is dependent on the cell type (tissue specific) as well as function of the cell (Figure, Wei & Huang, 2013) [45].

2.7 Cellular mechanics

Interestingly, given that most mammalian cells have a relatively conserved internal structure; numerous biochemical assays have demonstrated the differential propensity of similar mechanical cues affecting cell function(s) in very diverse ways i.e. a specified load on one cell type, may evoke a wholly unrelated response compared to a different cell type under the same force load. For example, referring to the mechanical properties of white blood cells; during an immune response towards an invading pathogen, both macrophages and monocyte cells migrate through blood vessel constrictions far smaller than their total cellular diameter. Both cell types have a similarly conserved internal microstructure (ICM), and are of a similar size (~10μm). However, monocyte cells appear to migrate much faster through narrow constrictions, compared to macrophages [49]. This example has elucidated how the structure of a mammalian cell can be conserved, but their physical properties can diverge quite considerably. The divergence in cell mechanical function(s) for mammalian cells from similar tissue origin, can act a useful and significant biomarker for sorting and distinguishing heterogeneous cell types within similar tissues, as well as interpreting how pathological processes (tumour growth) progress within different tissues. However, before one can begin to interpret and define novel mechanisms by which cells adapt their physical properties during physiological processes, we have to discuss which parameters are most useful often utilised to study the mechanical properties of biological samples. Next, the terminology and mechanical parameters used to investigate the mechanical properties of biological samples is discussed.

2.7.1 Cell mechanics – defining terminology and units of mechanical parameters investigated

The stiffness of a material is a measure of the structural characteristics of said material, and is subjective as to the geometry and composition of the material. It is the extent to which a material resists deformation to an externally applied force [50]. The stiffness of a material can be defined as;

$$k = \frac{F}{\delta} \tag{2-1}$$

Here, [K] is the stiffness of the material, [F] the applied force/stress of the material, and [δ] the displacement produced by the applied stress on the material. The resulting units of material stiffness are N/m^{-1}. The relationship of the stiffness of a material to the elastic properties of a material can be described by the Young's elastic modulus. The Young's elastic modulus of a material, relates to the mechanical properties of the material (intrinsic to the material properties), and is a measure of the relationship between a stress (force per unit area) and strain (resulting material deformation) of the material within the linear elasticity regime;

$$E = \frac{\delta}{\epsilon} \tag{2-2}$$

Here, E is the Young's elastic modulus, δ the force in Newtons (stress) applied to the material (force per unit area) and ϵ the strain (resulting deformation of the material). The resulting derived Young's elastic modulus is expressed in units of Pascals (N/m^2). Notably, when a material undergoes elastic deformation as a result of an external stress, where the linear elastic regime is considered, the elastic deformation is reversible i.e. the material properties return to its original shape or structure following deformation by

an applied stress or load [51]. The reversible deformation of the material in linear elastic regime can be described by a materials stress-strain curve (Figure 2-4). The relationship between the stress versus strain (the slope of the curve) represents the elastic modulus of the material [52].

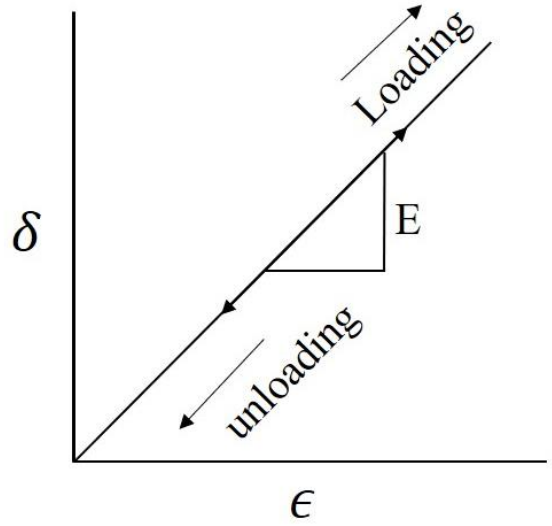

Figure 2-4. Schematic representation of linear elastic stress versus strain curve for the loading and unloading of an elastic material. The slope of the curve represents the elastic material properties of the material (Young's elastic modulus). In a linearly elastic material, the loading and unloading portions follow the same path.

Referring to investigating the mechanical properties of mammalian cells, the Young's elastic modulus is one particular parameter (among others) that is used as a quantitative measure of the elastic mechanical properties of mammalian cells. By applying an external load (stress) onto the surface of a cell, the resulting strain (deformation) in the region of applied load, can then be used to derive the Young's elastic material properties of the cell for the region under stress.

Markedly, although the Young's elastic modulus has been utilised for investigating cell mechanical properties, mammalian cells can exhibit a variety of interesting mechanical properties out with the linear elastic contact regime. For example, although a

mammalian cell can act like a solid material, and maintain its shape following an applied external stress, it can also preform reversible deformations, which is characteristic of a liquid material, which has been demonstrated previously [53]. In the case of such cellular deformations, the cell deformation is referred to as viscoelastic, whereby the cells exhibit both elastic and viscous (liquid) mechanical properties. In more detail the physical property of viscoelasticity refers to a material property where the relationship between the aforementioned stress and strain is time dependent. The stress-strain curve that arises as result of the unloading and loading of viscoelastic material (Figure 2-5) demonstrates a non-linear elastic deformation, and energy dissipation between the loading and unloading curves – described as hysteresis.

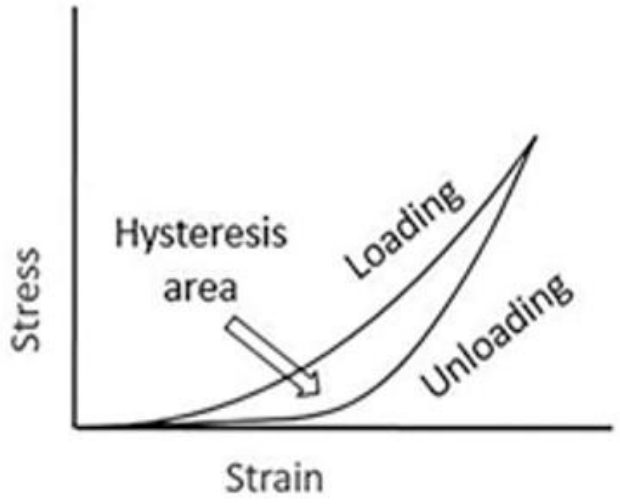

Figure 2-5. Schematic representation of non-linear elastic stress versus strain curve for the loading and unloading of a viscoelastic material. Viscoelastic materials exhibit energy dissipation up deformation, which can be observed through hysteresis in the stress-strain curve [52].

It should also be noted that the material property of viscoelasticity is time dependent. When measuring material viscoelasticity, the strain rate, frequency or time-dependent deformation of the material must be measured [52]. Additionally, the viscoelastic

properties of a material can also be derived using stress relaxation or creep experiments. During creep mechanical testing techniques, the material is subjected to constant load of stress, following which the time-dependent resulting strain is recorded. In the case of stress relaxation assays, a constant strain is applied to the material, and the resulting time-dependent reduction is stress is recorded [54]. Additional mechanical property parameters utilised to investigate biological material properties is the shear modulus and bulk modulus of a material. The shear modulus of a material is sometimes referred to as the *modulus of rigidity*. This mechanical parameter, denoted G, described the response of material towards a shear stress, and as result the ratio between shear stress and strain defined by the following equation;

$$G = \frac{F/A}{\triangle x/\ell} = \frac{F\ell}{A\triangle x} \tag{2-3}$$

Here, [G] denotes the shear modulus, [F/A] denotes the shear strain, where [F] is the force (stress) acting on the material, [A] the area on which the force is acting. [$\triangle x/\ell$] is the shear strain, where [$\triangle x$] is the transverse displacement of the material, and [ℓ] the initial length of the material [55]. The bulk modulus of a material, denoted *K* or *B*, is a measure of how a material resists compression. Specifically, it defines the response of a material to hydrostatic pressure, and is the ratio of pressure increase to response of change of volume of the material. The bulk modulus can be defined as follows;

$$K = -V\frac{dP}{dV} \tag{2-4}$$

Here, [P] is pressure exerted on the material, [V] is volume of the material in response to a pressure and [dP/dV] denotes the derived pressure in respect to derivative volume [56].

2.8 Cell mechanics – Plasma membrane, ICM, and actin cortex

Having described and discussed some of the mechanical parameters by which mammalian cells and biology constructs can be measured, next a discussion into some of the important biological components and mechanical properties of mammalian cells such as the plasma cell membrane, the intracellular matrix (ICM), internal and actin cell cortex is carried out. The mechanical properties discussed surround the mechanical parameter – the Young's elastic modulus. There is a range of Young's elastic moduli values obtained when investigating the mechanical properties of biological tissues Figure 2-6 demonstrated the mechanical diversity of biological tissues. As illustrated by Figure 2-6, there exists a large range of elastic moduli (Pa to MPa) values for different biological constructs. When attempting to investigate the variation in the Young's elastic moduli of adherent monolayer cells, an appreciation for the cellular components that may contribute to the mechanical response of the cell following mechanical perturbation is required.

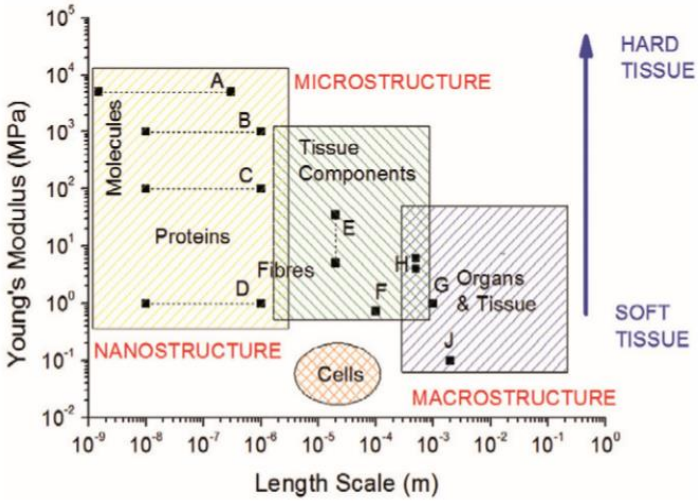

Figure 2-6. Diversity of mechanical properties in biology. Superimposed [A-J] are measurements of the elastic moduli of various biological constructs; [A]single collagen fibrils [B] fibrillar collagen [C] fibrillin microfibrils [D] elastin [E] ferret aorta [F] porcine aorta [G] human radial artery [H] rat aorta and [J] human aorta. (Figure taken from Akhtar, et al, 2011 [22]**).**

2.8.1 The plasma membrane

The cell membrane, also referred to as the plasma membrane of a cell is described as the semi-permeable membrane layer that encloses and surrounds the cytoplasmic body of a cell [57]. The most fundamental function of the cell plasma membrane is to form a barrier between the internal cell environment and extracellular space. The plasma membrane is often described as a fluid mosaic model. According to this model, there is a two-molecule thick lipid bilayer (to be described). Cholesterol lines the internal region of this lipid later (Figure 2-7), and various important types of transmembrane proteins are embedded in membrane [58]. The cell membrane is able to control and regulate what enters and exits a cell, it is selectively permeable and facilitates the transport of molecules and material between the intra and extracellular environments for cell homeostasis, activity and survival. Material is transported into and across the plasma membrane, towards or out of the internal cell environment through a variety of cell membrane processes; Passive diffusion or osmosis of small molecules and ions driven by concentration gradients across the cell membrane [57]. The presence of transmembrane protein channels that extend across the plasma membrane, allow for the active transport of larger molecules such as amino acids, carbohydrates and cell signalling molecules [58], lastly, the fusion of intracellular vesicles with the plasma membrane, a process known as exocytosis, facilitates the excretion of internal cellular materials into the surrounding external cell medium [58]. Opposingly, the plasma membrane can form "blebs" that surround extracellular material, pinch off, and internalise as membrane vesicles (membrane invagination) into the cytosolic region of the cell, a process known as endocytosis [58]. As well as being a layered barrier for the internal cell environments, and facilitating the delivery of biochemical materials across the cellular compartments, the cell plasma membrane also has additional highly important cell functions. It also acts an anchor for the attachment of particular cell

cytoskeletal proteins thus aiding the support of a cells internal structure and shape. The plasma cell membrane is primarily composed of a mixture of lipids and proteins (Figure 2-6). Around 50% of the volume of the plasma membrane is composed of specific transmembrane proteins [58]. The most fundamental component of the cell membrane is the phospholipid bilayer. The phospholipids that form the lipid bilayer are composed of a hydrophilic head that faces the internal cytosol and external extracellular fluid, and hydrophobic tail that lines then internal region of the lipid bilayer.

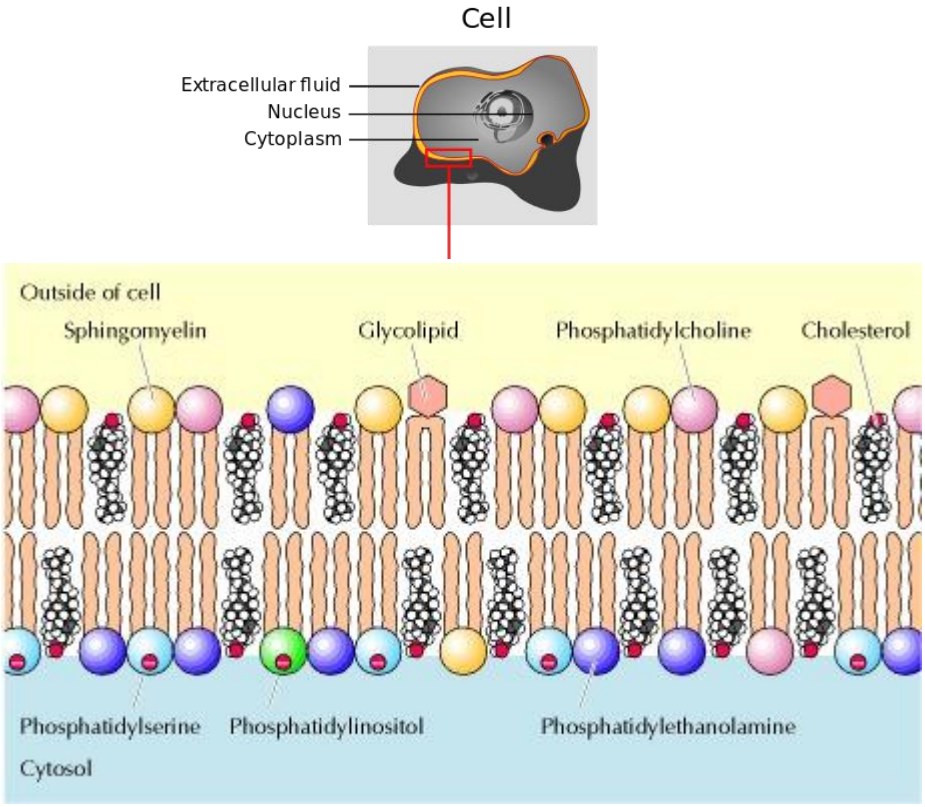

Figure 2-7. The plasma membrane. The plasma membrane comprises a double layer of phospholipids molecules. The types of phospholipids present are phosphatidylcholine, sphingomyelin, glycolipids, phosphatidylethanolamine, phosphatidylserine, and phosphatidylinositol. Cholesterol is distributed between the phospholipid molecules (Figure adapted from M.Ruiz, 2019 [59] and Harvey and Lawrence, 2000 [58]**).**

When exploring the mechanical properties of the cell membrane, aside from the current disused functions of the lipid bilayer, the cell membrane also comprises a variety of processes such as external signal detection, cell cytokinesis and cell motility. All of these processes involve the dynamic activity and interaction of the cell plasma membrane with the internal cell cytoskeleton. This involves an exchange of force between the plasma membrane and the internal environment of the cell [60]. Conventionally, the plasma membrane lipid bilayer was assumed to act as a Newtonian fluid – a fluid whose viscosity does not change with rate of flow [61]. However, it has been shown that the plasma membrane reacts to an external force in a time-varying non-linear manner of strain, and are therefore is a non-Newtonian fluid, and can be regarded as a viscoelastic fluid material [62]. The deformation of the plasma membrane as a result of an external force is often described by the compression, area expansion and bending moduli of the plasma membrane [63]. The bending modulus and surface tension of the plasma membrane has been shown to vary between specified neuronal mammalian cell lines as well as macrophage cells [64]. Computational simulations and theoretical frameworks have also attempted to model and produce values for the Young's elastic modulus of lipid membranes in different phases (liquid, gel and interdigitated), values were determined as 0.28 and 0.67 in units of E (elasticity) = ϵ / σ^3 for the fluid and interdigitated states respectively [65]. The shear modulus properties of the plasma membrane has also been investigated and demonstrated [66]. Given that the lipid membrane is considered a fluid model, comprising embedded transmembrane proteins that are able to diffuse laterally within the fluid mosaic, the shear modulus of the plasma membrane is applicable to its function.

The cholesterol content within the lipid bilayer contributes to the fluidity and permeability of the bilayer. The effect of cholesterol, which is found between the hydrophobic tails of the phospholipid molecules has been investigated by amplitude

modulation-frequency modulation atomic force microscopy (AM-FM AFM) [67]. Using a model bilayer system, namely 1, 2-dipalmitoyl-sn-glycero-3-phosphocholine (DPPC), the effect of differing molar fractions of cholesterol (0–60%) on the viscoelastic properties of the lipid bilayer. This study showed that at low cholesterol concentrations, the lipid bilayer displays a distinct phase separation and is predominantly elastic. However, higher cholesterol content results in a homogenous lipid bilayer with both elastic and viscous properties [67].

2.8.2 The intracellular matrix (ICM)

The intracellular matrix (ICM) comprises the internal structural elements within a mammalian cell. Similar to the ECM, the cell ICM comprises a structural scaffold - commonly referred to as the cytoskeleton – which is composed of a fibrillary network of three types of protein filaments; (1) microfilaments, (2) intermediate filaments and (3) microtubules (Figure 2-8). When investigating cell mechanical properties, the majority of evidence implicates actin microfilaments as the principle transmitter of external static/dynamic cellular loads/tension, with intermediate filaments and microtubules conferring cellular processes such as cell shape, rigidity and organelle transport [22]. Under load force, external solid forces are conferred throughout the cell via the internal cytoskeleton [68]. Together, all three protein networks transmit information about the mechanical function of the cell to adjacent cells, and then onto the underlying ECM structures at the ventral and lateral surfaces of the cells [69].

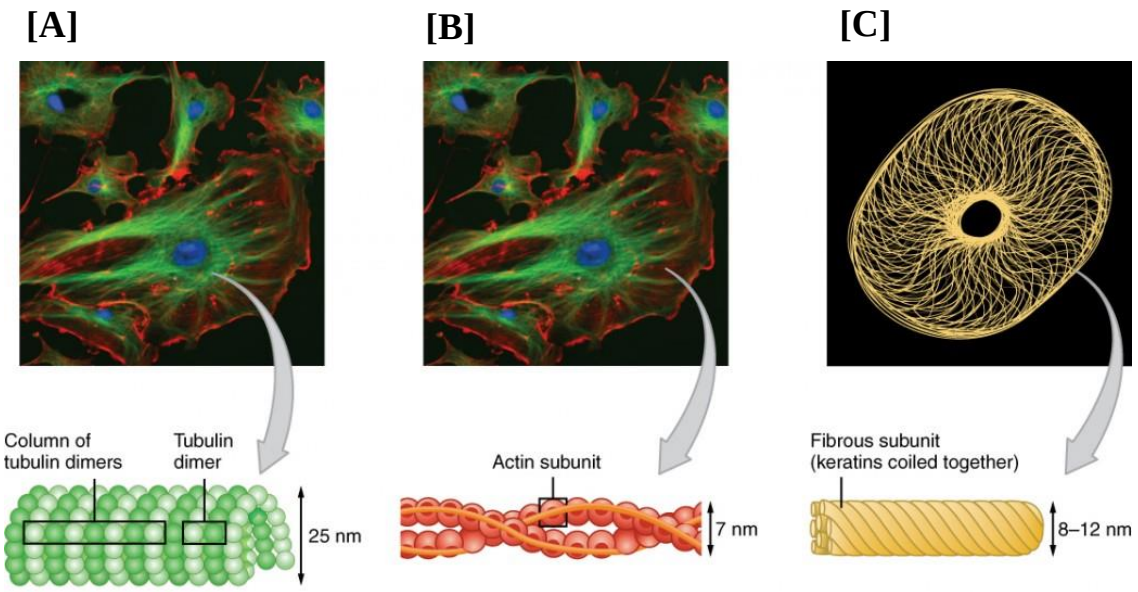

Figure 2-8. **The cell cytoskeleton.** The intracellular cell cytoskeleton has three protein filament components. **[A]** microtubules composed of tubulin protein subunits, **[B]** actin filaments composed of chains of actin protein subunits and **[C]** intermediate filaments composed of long fibrous subunits of proteins (such as types I and II keratins) (Figure, R.U. OpenStax College, available online, accessed December 2018) [70].

The mechanical properties of each intracellular cytoskeletal component have been investigated. Microtubules, which provide the internal framework and support for the transport and function of internal cell organelles, have been shown to exhibit a Young's elastic modulus of around 1000-1500 MPa (as determined by bending suspended microtubules using an AFM cantilever) [71]. The microfilament protein – actin, which contributes to cell motility, maintenance of cell shape, and binds to cell-cell junctional complexes (adheres junctions specifically) has been shown to exhibit a Young's elastic modulus of between 1800 and 2500 MPa [72]–[74]. Lastly, intermediate filaments such as keratin, vimentin and desmin, which function as the main tension-bearing element of the cytoskeleton to maintain cell shape and rigidity have demonstrated a bending modulus of around 300 MPa (as determined by bending single vimentin filaments using an AFM cantilever) [75].

2.8.3 The actin cortex

As previously noted, the majority of cellular mechanobiology studies implicate actin microfilaments as the most significant principle modulator of external cellular stress and tension [22], [76]. Reducing the internal filament length scale to the inner cell cortical region; numerous developmental and physical cellular events have been shown to be subject to the involvement and dynamic activity of the dense inner cortical actin meshwork that lies beneath the plasma membrane (Figure 2-9). The actin cortex is described as a thin network of crosslinked actin protein filaments bound to the inner surface of the plasma membrane, and is present in almost all mammalian cells [77]. It has been evidenced that cortical actin has two primary discernible structural arrangements; large parallel bundles and tightly compacted meshes [78]. Gradients in tension and stress within the cortical actin layer have been associated with multiple cell developmental events such as cell migration, cytokinesis and cell mitosis [13], [79], [80]. For example, a progressive increase in cortical tension has been observed during mitotic cell rounding [79], with mitosis associated cell shape transformations subject to the modulation and contraction of the actin cortex meshwork [81].

Interestingly, towards the end of cell division in mitosis, the gradient of cortical cell tension becomes localised towards the cell centre, which is thought to drive cell furrow ingression and cleavage of the cell [82]. A similar process has been evidenced during the formation of cell-cell adhesion contacts; a gradient decrease in cortical tension is observed towards the cell-cell interface zones in developing zebrafish progenitor cells [83]. The downregulation of cortical actin density along the cell-cell junction interface has been evidenced in multiple mammalian cell lines; MDCK [84], cancerous cells [85], zebrafish [83], and xenopus gastrula cells [86]. It is suggested that the downregulation of cortical cell tension along the cell-cell boundary region is in part due

to the effects of cadherin signalling. Cell adhesion is "within limits, proportional to cadherin expression levels"[87]. Cadherins are described as the transmembrane cell-cell adhesion proteins that regulate cell contact(s) stability and tension. [88]. During cell-cell adhesion, the binding of cadherin transmembrane protein to one another triggers local adhesion signalling at the cell contact region. This signalling cascade is mediated via the activation of Rac1 (a signalling G protein) by p120-catenin, which results in the inhibition of expression of RhoA (a GTPase protein associated with cell cytoskeletal regulation). This results in adaptor proteins such as α-catenin interfering with the actin polymerising protein Arp2/3. Therefore, cell-cell bond formation and signalling affect the reduces actin polymerization, and therefore, alters cell cortical tension.

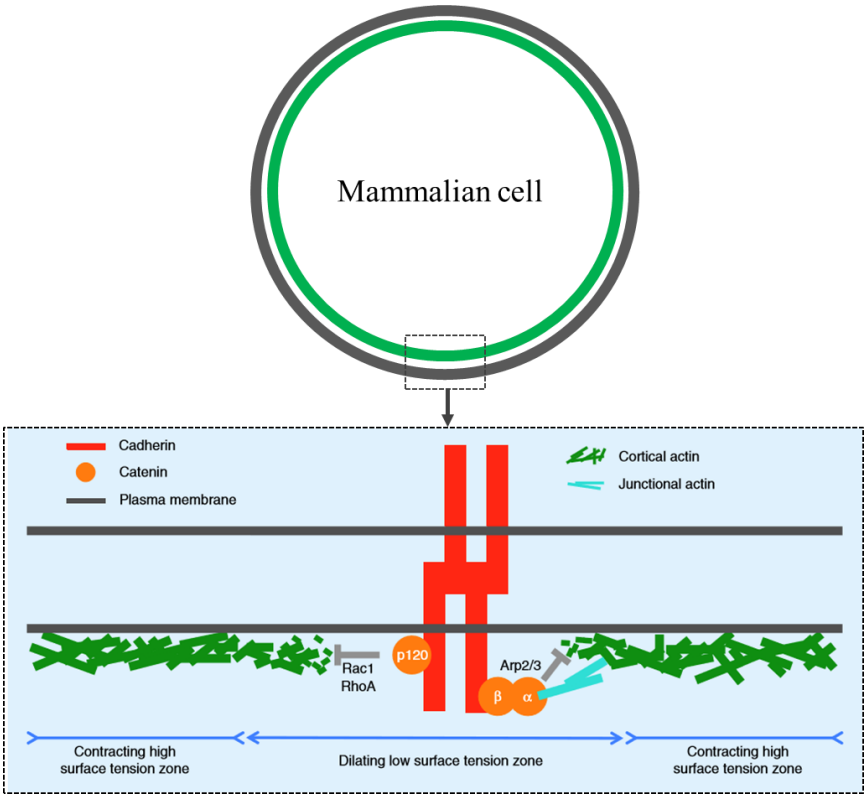

Figure 2-9. **The Actin cortex.** Cadherin mediated local signalling pathways at the cell contact interface involving cell signalling molecular such as p120-catenin, Rac1, RhoA, a-catenin and Arp2/3, are all involved in mediating the disruption of cortical cell tension along cell-cell contact zones, thus lowering cell–cell interfacial tension and expanding the contact zone (Figure taken and adapted from Maitre & Heisenberg, 2013) [88].

The architecture and mechanics of the actin cortex has also been evidenced to be subject to state of cell pluripotency; naïve embryonic stem cells present with a greater density of irregular organised actin fibres, which, upon transitioning through development, transform into cortically organised stress fibres [89]. The thickness and density of the actin cell cortex is also a major controlling factor towards overall cell cortical mechanical function. The thickness of the actin cortex has been estimated to range from 130nm to 1μm [90]–[93], with cortical actin mesh densities estimated at ~ 100nm [77]. Furthermore, the control of actin cortical tension and dynamic deformation of the cell cortex during certain cellular events has been linked to particular actin binding proteins. One such protein, namely myosin-2, has been described as the most significant actin binding protein linked to the generation of contractile tension in the actin cortex [77]. Myosin proteins are described colloquially as motor proteins, which, more precisely are ATPase enzymes that move along actin microfilaments through the coupling hydrolysis of ATP [58]. Sometimes described as mechanochemical enzymes, myosin motor proteins function to drive actin filament contraction and movement during cellular processes such as cell migration, and mitosis. Evidence has shown that the activity one particular myosin motor protein (myosin-2) is the predominant factor affecting overall cell cortical tension [92], with the induced inhibition of myosin-2 activity resulting in a near 80% decrease in cortical tension [77]. However, alternate studies have shown that both actin and myosin fibre density contribute equally to the stiffness of adherent mammalian cells [76].

2.9 Methods for investigating cell mechanics – Summary of methods

A defined method for investigating the mechanical properties of mammalian cells between the single cell and cell monolayer developmental length scales in terms of derived Young's elastic modulus cell outputs – and an appreciation for how said

Young's elastic moduli trends relate to internal cell function - is paramount when attempting to define a novel process by which a mammalian cell adapts it mechanical properties during tissue development or disease development. Notably, as well as deriving the Young's elastic modulus, it should be noted that there are numerous cell mechanical exploratory techniques for investigating mammalian cell mechanical properties. Experimental techniques used to determine the mechanical properties of micro and nano scale cellular properties fall into three broad categories; (1) methods for adherent cells, (2) methods for non-adhered/suspension cells, and lastly (3) computational cell modelling software analysis [94]. As a standard, when utilising each type of method, a high spatial resolution is a paramount in order to relate the mechanical outputs of mammalian cells at the subcellular scale to cellular function. Therefore, scientists often adopt methods based on a specific set of objectives required for their analysis. The types of techniques utilised to measure the mechanical properties of adhered cells include; (1) cell poking, (2) atomic force microscopy; (3) micropillars/plates; (4) optical tweezers, (5) magnetic twist cytometry, (6) acoustic microscopy, (7) hydrodynamic deformation and (8) fluorescent oil droplet deformation [94], [95]. Methods for working on non-adhered suspended cells include (1) micropipette aspiration, (2) optical tweezers, (3) optical stretcher and most recently (4) real-time deformability [96]–[98]. It is often the case when attempting to investigate cell mechanical outputs, that more than one method of measurement is utilised. However, synergy between the data outputs must always be accounted for, as not all methods are designed to measure the same mechanical parameter, for example the cell Youngs's elastic modulus. With the current established, as well newly developed methods available for cell mechanical analysis (Figure 2-10), one such method, Atomic force microscopy (AFM), remains one of the more popular methods utilised for deriving the Young's elastic modulus of different types of mammalian tissue cells [99]. It has

been demonstrated that when utilising specified protocol parameters, an AFM can produce outputs for the Young's modulus [E] of soft biological samples with a reproducibility limit of 4% difference between two samples [100].

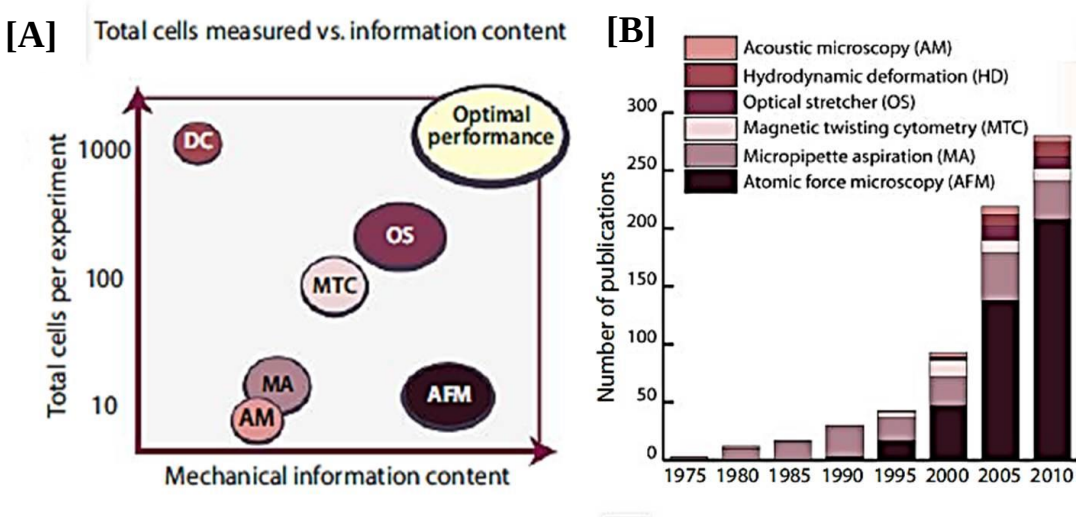

Figure 2-10. **Methods for cell mechanical analysis. [A]** Among the various cell mechanical analysis methods, AFM produces the highest amount of mechanical data in terms of output content about the mechanical attributes of different cell types. However, AFM can have a low throughput of cells per experiment (~10 cells per hour), compared to other more robust methods. **[B]** Given its limitations, AFM has still been one of the methods most utilised for investigating cellular mechanics in publications over the last decade (Figure adapted from Guck & Chilvers, 2013) [99].

As previously noted, one of the most popular methods for gathering mammalian cell Young's elastic moduli outputs are AFM. Investigating mammalian cell mechanical properties (through interpretation of the Young's elastic modulus) has become one the most applicable mechanical outputs for investigating the relationship between cell physiological state and cell mechanical properties. The primary method utilised to measure the Young's elastic modulus in thesis was AFM.

2.10 Investigating the Young's Elastic Modulus of Mammalian cells

Much research has been carried out in an attempt to define how the mechanical properties of a mammalian cell correlates to the physiological status of a cell i.e. cell type, healthy or cancerous cells. The Young's elastic modulus is increasingly becoming a hallmark indicator for defining how the mechanical properties of a cell affect cell state and function. Mammalian cells, as well as many soft tissues, often present with a much lower Young's elastic modulus compared to most other natural solid materials [30]. In this thesis, the Young's elastic modulus was used as the primary mechanical parameter to investigate mammalian cell mechanical properties. Variation in the Young's elastic modulus for mammalian cells during different cell biological states is discussed next. It should be noted, that mammalian cells are not in reality, elastic solids, and do in fact present with viscoelastic behaviour as a result of their solid and fluid (cytoplasm) components. However, if the applied external stress is kept relatively low such that all stress-strain outputs are kept in the linear elastic regime, and deformations are small, this can allow the mammalian cell to return to its original shape in the region of applied stress. Therefore, the Young's elastic modulus can be utilised to investigate the mechanical properties of the cell for a given deformation. As a result of the research objective of this thesis, the Young's elastic modulus of mammalian cells was investigated. Next, the variation in the derived Young's elastic modulus for mammalian cells under different development states is discussed.

2.10.1 Young's elastic modulus – Cell differentiation, Senescence, and Apoptosis

The Young's elastic modulus of mammalian cells has been shown to be subject to numerous cell developmental and physiological events. During embryonic morphogenesis, progenitor and differentiated tissue cells undergo a multitude of

biochemical and structural transformations. Cellular processes such as cell division (cytokinesis), differentiation (fate selection), cell ageing and cell death (apoptosis) all encompass a multitude of internal structural changes that occur within a cell as it progresses through different physiological states. Therefore, utilising differences in the measured Young's elastic moduli of cells at different stages of development has emerged as a useful method for distinguishing stages of cell development. For example, it has been shown that the derived Young's elastic moduli of a given mammalian cell can vary quite considerably, depending on the stage of cell development; a near 3-fold difference in single cell Young's elastic moduli was observed for early differentiating mouse embryonic stem cells (16.06 kPa), compared to latent undifferentiated stem cells (1.49 kPa) [13], [14]. Similar cell [E] output trends have been demonstrated in human embryonic stem cell lines [15], [16]. Natural cell aging has also been investigated (in vitro); serially passaged chondrocytes were shown to exhibit a statistically significant ($p < 0.0001$) reduction in measured Young's elastic moduli outputs in relation in increasing number for cell passages [10]. As with heterogeneous connective tissue blood cells (section 2.6), an opposing outcome was observed for human dermal fibroblasts [11] and human foreskin epithelial cells [12], whereby progressive cell passaging resulted in an increase in derived cell Young's moduli outputs. Cell age , with respect to the age of the patient donor , has also been shown to affect measured cell Young's elastic moduli [E] outputs; Fibroblasts taken from younger donors exhibited lower derived [E] outputs (~0.5kPa) in comparison to cells obtained from older donors (30 kPa) [101]. Natural cell death or – apoptosis - has also been shown to have a great effect on measured cell [E] outputs (0.09 kPa $\leftrightarrow$ 48.98 kPa) of serially passaged MSCs [9]. In summary, based on some of the aforementioned mechanical assays investigating mammalian cell Young's elastic moduli it is evident that measuring the Young's elastic modulus of different mammalian cells at various stages of development, is a useful

parameter by which differences in cell state and development can be examined and correlated to cell Young's elastic moduli outputs for their respective cellular functions.

2.10.2 Young's elastic modulus – Cancer

One of the more notable areas of mammalian cell mechanical assays currently being investigated is the apparent variation observed in the derived mechanical properties and characteristics obtained from malignant and metastatic cancerous cells. In the past, very little was understood about the mechanical properties of cancerous cells, other than the stark contrast between the physical properties of cancerous nodules and the surrounding healthy tissue cells. Advances in cell culture and mechanical analysis has since demonstrated that, at the single cell length scale, a cancerous cell can be up to one order of magnitude softer than healthy non-cancerous cells [102]. Notably, it is reported that there is up to70% decrease in the measured Young's elastic moduli for multiple primary cancerous cell types compared to their healthy corresponding tissue cells [7]. Multiple studies have demonstrated that cancerous cells (at the single cell developmental stage) regardless of tissue type are generically softer than healthy cells [103], which suggests a common highly conserved feature among cancer cell types. Furthermore, the stage of cancer cell development has been shown to be subject to additional variation in cell Young's elastic moduli with evidence demonstrating a statistically significant difference between the Young's elastic modulus of healthy, transforming and malignant cancerous cell types [104]. Given the numerous biological mutations and physiological abnormalities present in oncogenic cells compared to healthy tissue cells, utilising the measured Young's elastic moduli for cancerous cells in comparison to non-cancerous cells is fast becoming a key biomarker for distinguishing physical differences between cancer cell lines during cancer cell development i.e. how internal biological mutations affect the mechanical properties of the cells and disease

progression. For example, it has been shown that highly metastatic aggressive cancer cell types exhibit the greatest decrease in their measured Young's elastic moduli, with the degree of tissue invasiveness directly correlated to the elastic compliance and deformability of the cancerous cells [105], [106]. It is possible therefore to assume that a reduction in cancer cell Young's elastic moduli may be a pre-requisite for cancer cells that predisposes their metastatic ability to invade neighbouring tissues. However some researchers believe cancer cell metastatic potential is directly influenced by mechanical property differences within the tissue of origin, for example, pancreatic tumours exhibit a greater measured [E] than brain tumour cancer cells [107].

2.10.3 Young's elastic modulus – Multiscale cell length scales

As previously discussed, much research has been carried out investigating the mechanical properties of different types of tissue cells under different physiological conditions. At the intracellular length scale, the internal ICM environment has been shown to exhibit inhomogeneous mechanical properties; studies have shown the great variance in the derived Young's elastic moduli of the nuclear, cytoplasmic and cell periphery regions of a cells undergoing mechanical analysis by atomic force microscopy Young's elastic moduli analysis [12], [108]. Further to this, analysis of human endothelial cells demonstrated the heterogeneity of cell [E] trends between the central cell body region (higher derived Young's modulus) and periphery (lower derived Young's moduli) cell regions [109].

Moving up through the cell development and proliferation length scale, to the multi-cell length scale; numerous studies have addressed interpreting how mammalian cells - both healthy and cancerous – adapt their mechanical properties at predominantly at the single and monolayer length scales. Less evidence for cell mechanical analysis (Young's elastic modulus) at more specified stages of development have been obtained. Current

studies investigating multiscale trends in mammalian cell Young's elastic moduli have evidenced differences in single, groups of cells and monolayer cell AFM Young's moduli [E] outputs [109]–[113].

Focussing on selected cell lines undergoing mechanical analysis (for the Young's elastic modulus [E]), Vero epithelial cells (African green monkey) presented with greater derived [E] trends at the single cell length cell compared to monolayer cells [111]. MDCK epithelial cells (canine) presented with lower derived [E] trends at low isolated cell densities (5-10 cells/mm^2), compared to higher cell densities (500 cells/mm^2) [110], while NIH3T3 murine embryo fibroblast cells exhibited no significant difference in cell [E] trends with variation in cell density/development [110]. Human umbilical vein endothelial cells (HUVEC) cells exhibited greater [E] outputs for grouped (3-5 cell clusters), followed by single cells, with HUVEC cells having the lowest derived [E] outputs [109]. An opposing trend was presented for HUMEC cells whereby the derived [E] of cells was found to gradually decrease towards the periphery of a monolayer compared to single isolated cells [114].

Addressing cancerous cell Young's elastic moduli trends at multiscale and individual stages of development has also demonstrated a variation in derived Young's elastic moduli for cancerous cells at alternate stages of development. Tumorigenic, immortal and metastatic HUMEC cancer cells exhibit no significant difference in derived Young's moduli between single and monolayer stages of cell length scale development [114]. Therefore, compared to immortal cultured cell types, this suggests that cancerous cells may function differently in terms of their derived Young's elastic moduli outputs at increasing stages of cell monolayer development. However, this assumption would require much additional investigation at the multiscale cellular level for multiple selected cancerous tissue cell types. Furthermore, given that most tissue structures

(including cancerous tumours) exist in the three-dimensional length scale and comprise a heterogeneous mixture of tissue cells, further analysis would need to be carried out to determine how the derived Young's elastic modulus of healthy and cancerous cells is affected by cell-cell heterogeneity.

2.11 Atomic Force Microscopy (AFM)

When attempting to measure the material properties and mechanical characteristics of biological samples, a challenge exists in the interpretation of the derived output as to what these values mean in terms of how a biological system functions with relation to its response to mechanical perturbations using different analysis techniques. As discussed in section 2.9, a range of investigate methods exist for investigating different physical properties of biological samples, specifically mammalian cells. As demonstrated (Figure 2-10), one such method, AFM, has over the past three decades, become one of the most useful platforms for simultaneously investing the mechanical and morphological priorities of living mammalian cells.

First developed in 1986, the atomic force microscope operates as a form of scanning tunnelling microscope (STM), in combination with a stylus profilometer, and is able to derive informative data about the topography and mechanical attributes of biological samples at an atomic scale [115]. During experimentation, an AFM is capable of producing high resolution three-dimensional images, which combined with force spectroscopy, is able to define and assign surface properties, such as surface topography and the mechanical properties such the Young's elastic modulus of a sample. As result, AFM can be used for a range of applications in research and development. For example, it can be used to study the mechanical, electrical and magnetic properties of selected materials quantitively [116]. The AFM is capable of applying and measuring forces from the piconewton (pN) to micronewton (mN) range for sample areas ranging from

the sub-nanometre length scale to the tens of micrometre length scale, in both air or liquid environments, thus allowing for the investigation of sample properties such as surface topography, roughness, elasticity, surface adhesion, surface friction, viscoelasticity and energy dissipation [117]. As a result of the AFM capabilities, in the field of biomechanical research, AFM has allowed scientists to investigate the nanomechanical properties of biological samples such as DNA, RNA, molecular proteins, cell membrane phospholipids and cellular as well as subcellular components (cell organelles) in an *in vitro* culture environment [8], [53]. The AFM has a multitude of available techniques and modes that can allow for the investigation of specified mechanobiological research questions (Figure 2-11).

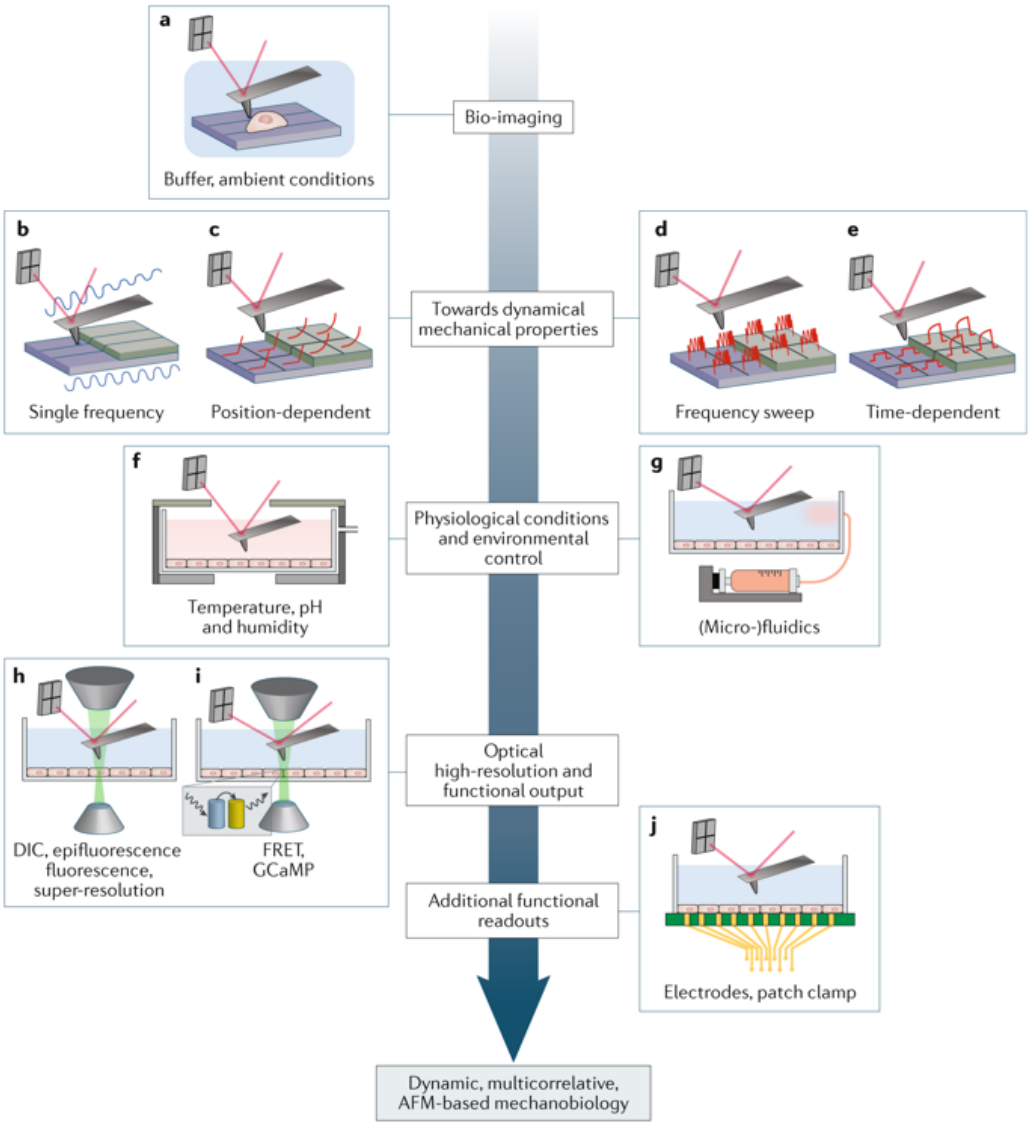

Figure 2-11. Summary of AFM operational techniques. [a] Bioimaging, detection of cantilever deflection to measure surface properties of biological system **[b]** Force modulation, scanning the cantilever across a surface, applying a driving signal to the cantilever oscillate and **[c]** Force mapping, sample mechanical properties are mapped pixel-by-pixel using spectroscopy based on force–distance or force–time curves **[d]** Force mapping by modulating cantilever at varying frequencies **[e]** Time-dependent mechanical response of a sample to an indenting cantilever **[f]** AFM can be customised to include chambers allow the mechanical characterization and simultaneous observation under controlled conditions, pH, CO_2 concentration, humidity, temperature **[g]** Biological or biochemical compounds can be exchanged between mechanobiological investigative systems to investigate additional parameters **[h-i]** Optical microscopy and atomic force microscopy (AFM) can be combined for the morphological and mechanical characterization of complex biological systems [j] The Simultaneous characterization of both physiological and mechanobiological sample properties can be obtained by introducing complementary tools, including the patch clamp technique or multielectrode arrays. (DIC, differential interference contrast; FRET, Förster resonance energy transfer; GCaMP, genetically encoded calcium indicator consisting of green fluorescent protein, calmodulin and M13 protein) (Figure and legend descriptions taken from Krieg et al, 2019) [117].

2.11.1 AFM Operational principle

In principle, an AFM operates through the detection of repulsive or attractive forces present between the AFM indenting cantilever and the chosen underlying sample surface. An AFM set-up comprises a probe, that is positioned on the underside of reflective cantilever beam. The cantilever beam and geometry of the probe form the key elements of the AFM operational principle. The net repulsive or attractive forces acting between the cantilever and sample will depend on the relative distance between the sample and cantilever. The cantilever is controlled to move towards the surface of a selected sample (the mode and manner of which to be discussed further), which results in the interaction between the cantilever underlying probe and sample surface. This results in bending or deflection of the cantilever beam. The resulting bending of the cantilever is detected by a piezoelectric actuator, which converts the movement of the cantilever following sample interaction directly into linear motion (Figure 2-12). This data can then be analysed to derive selected mechanical and physical properties of the underlying sample material.

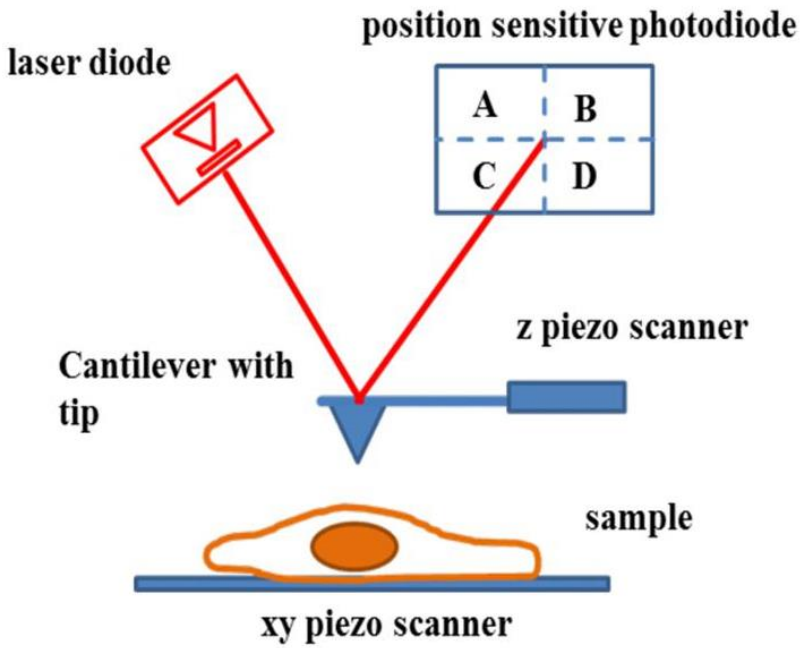

Figure 2-12. **AFM Operating Principle Schematic.** During an AFM experiment, a programmable load (force applied by the AFM cantilever beam) is applied to a chosen underlying sample. This results in the deflection of the cantilever upon interaction with sample (based on the material properties of the sample and cantilever). Deflection of the cantilever beam displaces the laser bean signal reflected from the topside of the cantilever beam onto the photodiode detector. The deflection of the laser beam signal is converted into an applied force versus sample deformation. The degree of force-displacement for the sample indentation allows for the quantification of the physical properties of the sample (Figure, taken from Babu & Radmacher, 2019) [118].

Referring to Figure 2-12, the extent at which the cantilever beam is deflected or bent based on the interaction with an underlying sample surface, depends on the surface properties of the sample undergoing AFM analysis, as well the material properties of the cantilever beam and indenting underlying probe [119]. The receiving photodiode detector that receives the laser beam signal, is split into four quadrants to allow for the detection of cantilever deflection in the z dimension, but also the lateral directions of cantilever movement. The characterisation and representation of the forces acting between the cantilever underlying probe and the sample surface can be described by a Lennard – Jones potential curve (Figure 2-13). A Lennard – Jones potential curve that

describes the interaction of forces between two atoms, as a function of the distance between the atoms [120].

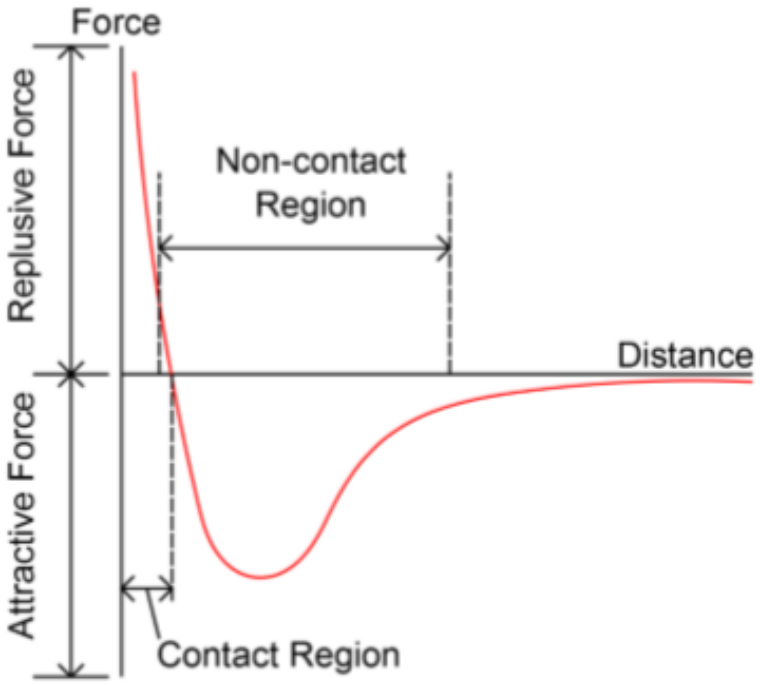

Figure 2-13. A Lennard – Jones potential curve to describe the interaction of forces between a cantilever and underlying sample surface (Figure taken from Gilman, 2009) [121]**.**

The initial contact between the cantilever and underlying sample surface is defined by repulsive forces, which results in the probe being repelled away from the underlying sample surface [120], [121]. In fact, contact between the cantilever and underlying sample is defined as a repulsive force that results in the cantilever being deflected or pushed away from the sample surface. However, on approach to the sample surface. as the cantilever moves further towards the underlying sample, the distance between the two bodies decreases, and the forces between the two bodies is in fact attractive, until a stable minimum is reached [120]. The artractive forces actig between the sample and cantilever are caused by long range force interncations, often described as van der

Waals forces acting between the two bodies[122]. As illustrated (Figure 2-12), the AFM cantilever beam is the component that has as receiving laser beam transmitted/reflected onto a photodetector diode [123]. When investigating the mechanical properties of any biological system by AFM, correct selection of an appropriate cantilever, which have spring constants similar to that of the biological sample is critical. The spring constant (k) of a cantilever refers to the stiffness of the cantilever. It infers information about the material properties of the cantilever and the degree to which it may bend (depending on its stiffness) in relation to being pressed against or into an underlying sample. Specifically, the spring constant of a cantilever refers to how much resistance it exhibits to a displacement when a force is applied on it. The units of the cantilever spring constant are (Nm^{-1}). AFM cantilevers are available as silicon or silicon nitride 100-500µm beams ranging in thickness between 0.5-5µm. The cantilever chosen for a given experiment, is chosen based on the application of the experiment. The cantilever chosen should always be durable such that under selected loading forces, it will not fracture or bend beyond the limits required for sample investigations. If the cantilever has a higher spring constant (is stiffer) than the material properties of the sample, the bending (deflection) of the cantilever can become minimal, and the derived measurement somewhat insensitive to the true mechanical properties of the sample. Counter wise, if the cantilever has a softer spring constant that the underlying sample, there may be insufficient deformation of the sample, which could result in breakage of the cantilever, or inaccurately obtained mechanical properties of the sample [117].

As stated, on the underside of the cantilever beam is the indenting cantilever probe. Cantilever probes are available in a range of geometries, and are selected based on the application of the sample deformation and contact model applied to derived sample mechanical properties. The primary cantilever probe geometries available are spherical, parabolic, pyramidal, and conical. It should be noted that cantilever beams can also be

used as flat ended indenting beams (without an underside probe component). The probe is the component that primarily interacts with the surface of the underlying sample. The probe of the cantilever beam is often composed of the same material as the cantilever. Cantilever probes are available in a selection of shapes depending on the nature of the underlying sample being investigated. For live biological samples, such as cultured mammalian cells, it is often suggested that large spherical and or pyramidal shaped probes are used to indent the samples as to produce less damage to the sample surface.

2.11.2 AFM Operational modes

AFM has a number of operational modes. The mode and application selected is dependent of the experimental approach and material properties of the sample being investigated, deformed or imaged by AFM. Experiential approaches considered can also be surrounding the sample environment for AFM investigation. The primary operational modes available are (1) contact mode, and (2) non-contact or tapping intermittent mode (Figure 2-14). For this research thesis, the AFM operational mode selected was contact mode. This mode was selected as it allows for the derivation of the Young's elastic moduli of an underlying sample, as well as control of contact of the cantilever with the sample at specified loading forces (nN). Within the contact mode, force mapping and imaging was utilised. Each tool within the contact mode of the AFM was used to investigate the mechanical properties (specifically the Young's elastic modulus) of living mammalian cells, as well image the selected mammalian cell line.

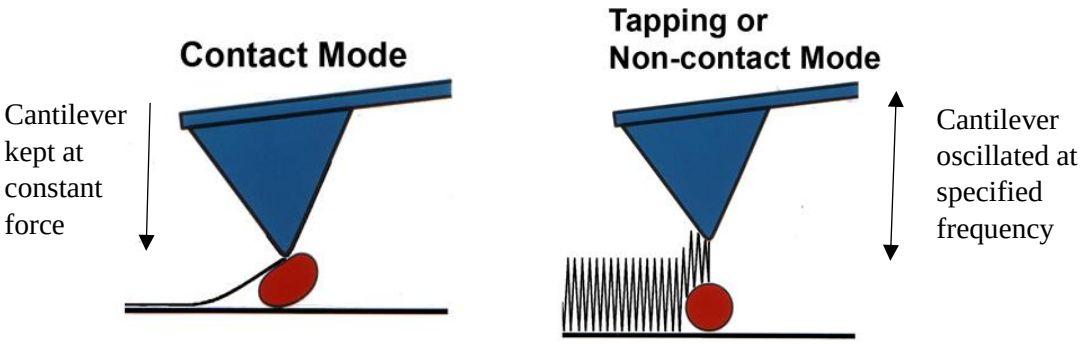

Figure 2-14. AFM opertional modes. In AFM contact mode, the AFM cantilever is kept at a constant force when move over the surface of a selected sample. The height of the cantilever is adjusted as its moves, in constact contact with an underlying sample. In tapping or non-contact mode, the cantilever is osciallted near its natural resonance frequency, making only brief intermittmenr contact with the sample. Topographical images and material properites of the sample can be derived through monitouring the difference between the cnatilever probe and sample surface (as a result of changes in the oncsicalltion amplitude of the cantilever) (Figure, taken from Hansma 2019) [124], [125].

2.11.3 AFM operational modes - Non-contact tapping mode

In non-contact mode on an AFM, the cantilever is oscillated over the underlying sample by a piezoelectric generator. The cantilever is oscillated at the resonance frequency of the cantilever beam, which provides a stable amplitude of oscillation [121]. When the cantilever is oscillated over the sample, the attractive forces experienced by the cantilever through the short-range van der Waals interactions will reduce the amplitude of oscillation of the cantilever [122]. As the distance between the cantilever and sample reduces further, the amplitude of oscillation will further decrease [121]. The set-point force of the cantilever in the case of non-contact tapping mode, is the specified as the magnitude of the cantilever oscillation.

2.11.4 AFM Operational modes – Contact mode

AFM contact mode is the most direct force spectroscopy mode and imaging mode on an AFM. In this mode, samples can be investigated in liquid as well as air environments. In AFM contact mode, the selected force acting on the cantilever beam is kept at a constant as the cantilever and underlying probe are brought into contact with the underlying sample. In contact mode, the force set-point working on the cantilever is predefined, and the resulting degree of deflection of the cantilever corresponds to the set-point force applied to the underlaying sample surface. As a cantilever is moved across a sample surface in contact mode, changes in the surface topography of the sample will resulting a variable increase and decreases in the cantilever deflections. The degree of cantilever deflection is dependent on the surface and material properties and topography of the sample. When using contact mode to investigate live biological samples, it should be noted that the applied force is always kept at a scale that does not damage the underlying cells. The force selected however should be within degree to detect and investigate the properties of the cell surface, for example, the plasma membrane and/or cell cortex. In contact mode, when deforming live mammalian cells, since the cantilever is kept in constant contact at a selected force with the underlying sample, the selected cantilever used must have specific material properties i.e. very flexible. As such, silicon and/or silicon nitride cantilevers are most often used.

2.11.4.1 AFM Contact mode – Force Spectroscopy

In AFM contact mode, force spectroscopy is the method designed to perform single force-indentation measurements on samples that exist at micro and nano length scales. When using this function, a selected point of interest is selected for a given underlying sample. The cantilever beam and underlying probe are then brought into contact with the sample, and with a defined loading force, indent the sample in the selected region. In

this mode, the z position of the cantilever is scanned while the lateral position (x and y) is set at a fixed point. The resulting indentation can then be used to derive the material properties of the sample such as Young's elastic modulus for the indentation of the selected region. When using this approach, there is no limit as to how many individually manually selected indentation points can be designated for a given sample. The AFM cantilever probe is directed to indent each selected point in the sequence set-up, or it can be paused between each sample indentation event. The cantilever probe moves towards and deforms the underlying sample in the vertical plane, resulting a complete force-displacement curve with both an extend and retract curve. The x/y scan range for AFM indentation is set at a limit of 100µm ^{x} 100µm. The z-axis is set at a limit of 15µm. Vertical movements of the cantilever and underlying probe and the surface of the selected sample results in indentation of the sample surface. This produces an extend-retract cycle of the cantilever and produces a force-displacement curve (Figure 2-15) [126].

2.11.4.2 AFM Contact mode – Force mapping

Force mapping is an extension of the conventional force spectroscopy mode on an AFM. During force mapping, the cantilever and underlying probe moves across an underlying sample and performs several indentations. In this force spectroscopy method, a defined force map region for a selected sample is used to acquire multiple force indentation measurements automatically. Each force map is constructed from an array of pixels, known as the force map index. Each pixel within a force map represents a single point of sample indentation by the AFM cantilever. Force map indexes can range from 8 ^{x} 8 pixels to 128 ^{x} 128 pixels. The mechanical properties of the sample at each indentation pixel can then be analyzed to create a "force-map" for mechanical characteristic of the selected sample. For example, the mechanical properties across the

surface of a mammalian cell**.** By obtaining the resulting force map for a selected region on a mammalian cell, it is possible to present and account for differences in cellular Young's elastic moduli and potential inhomogeneity of mechanical properties within different cellular regions.

2.11.5 AFM force-displacement curve

During cantilever sample indentation, the resulting bending of the cantilever is detected by a piezoelectric actuator, which converts the movement of the cantilever following sample interaction directly into linear motion. This data can then be analysed to derive selected mechanical and physical properties of the underlying sample material. Deflection of the cantilever beam in response to sample interaction and sample deformation is converted into a force-displacement curve (Figure 2-15). A force-displacement curves measures the mechanical deformation response of a material under force load [117]. The force of cantilever indentation can be plotted as displacement as well as against time. Force-time curves are often derived for samples where the indentation of the sample is required to be held at a constant, for example, investigating the change in the material response of a property over time or a material that has viscoelastic properties[127]. A typical force-displacement curve has four primary sections; (1) The approach or baseline portion. This is the portion where the cantilever approaches the sample surface. The target height of the sample (µm) and extend speed (µm/s) of the cantilever are all manually controlled through the AFM interface protocol software. (2) The second portion of the curve is the extend portion of the curve. This portion of the curve represents the point where the cantilever makes contact with the underlying sample. This results in the cantilever being deflected in response to the material properties of the sample. The loading force (nN) of the cantilever is also manually controlled via the AFM software interface. (3) The third and next portion of

the curve is the retracting portion of the curve. In this portion, the cantilever pulls away or retracts from the underlying sample surface. Once the maximal selected loading force is reached, the cantilever then retracts from the sample surface. (4) Lastly, the adhesion portion of the curve is the section of the force curve most susceptible to attractive adhesive forces between the cantilever probe and underlying sample [123]. A delay in retraction due to an adhesive force is dependent on the strength of adhesion and density, or concentration of adhesive surface materials on an underlying samples surface. An example force-displacement curve acquired during AFM indentation on a live mammalian cell in liquid media is presented (Figure 2-16). In the case of the example presented, there is no prominent section demonstrating work of adhesion. However, the force curve for a live mammalian cell does demonstrate a concept defined as curve *hysteresis.* This is not uncommon in biological samples. The term hysteresis is used to describe the scenario in a stress-strain curve where a material is loaded with a stress, and the resulting unloading curve follows a different pathway to the loading curve. The resulting difference in the loading and unloading curve is termed hysteresis and is the energy lost or dissipated by the material (Figure 2-17) [128]. It is more common for viscoelastic materials to exhibit this form of stress-strain behaviour as described and demonstrated in section 2.7.1**.** As previously noted, viscoelasticity is a term given for properties of a material that exhibits both liquid (viscous) and elastic characteristics when undergoing a deformation stress, whereby the material exhibits time dependent behaviours of creep and stress [19]. Since mammalian tissues and indeed, single mammalian cells, comprise a liquid internal element such as the internal cytoplasm, mammalian cells can have viscoelastic behaviour when undergoing AFM cantilever deformation. This is evident based on the shape of the loading and unloading region of the force-displacement curve example illustrated. However, by keeping cantilever loading rate (speed of deformation) low, it should be possible to avoid viscous effects of

the cells as a result of deformation, and measure only the cells elastic properties i.e. strain with stretch of a material with an external load to allow for the original shape of the cell region to return once the stress is removed.

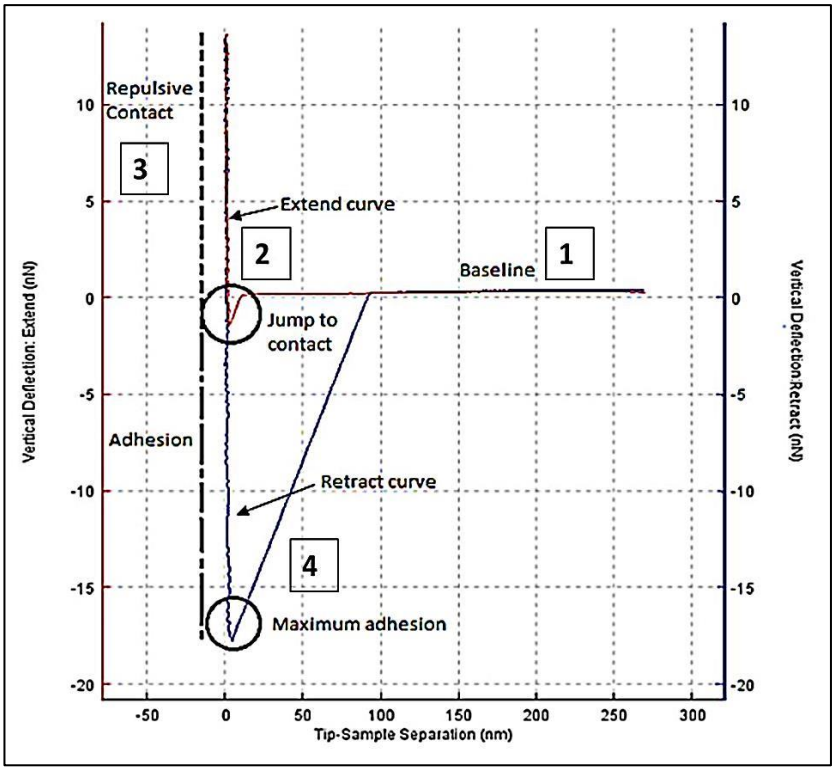

Figure 2-15. AFM force-displacement curve. Curve shown is an example curve for an AFM indentation obtained using a cantilever with an underlying conical tip geometry probe, carried out on a glass substrate sample in air. (1) The approach or baseline part of the curve is the point of cantilever approach to the underlying sample surface. During the approach, the loading force (nN) is equal to zero and the curve is linear along the x-axis. The vertical deflection (y-axis) is not equal to zero due the presence of natural weak forces (Van der Waals forces for example) in the approaching cantilever environment. Debris, or a highly viscous media can have an additional physical effect on the cantilever prior to sample interaction and deformation. When the selected sample target height is met (manually controlled) the cantilever moves down and contacts the sample surface and deforms the sample resulting in the (2) extend/deflection portion of the curve. The cantilever continues to deform the sample until the selected force is reached. (3) The cantilever then retracts from the sample surface. (4) The degree of adhesion between the cantilever and sample controls the maximal adhesion output for the force-displacement curve. Notably, x-axis (or cantilever deflection) is converted during AFM indentation to tip-sample separation. This is due to height signal of the cantilever being corrected for cantilever bending i.e. the deflection of the cantilever is removed for the acquired cantilever height signal, such that only the height of the cantilever (and not piezo) during sample deformation is taken into account (Figure taken from JPK instruments DP manual, 2012) [126].

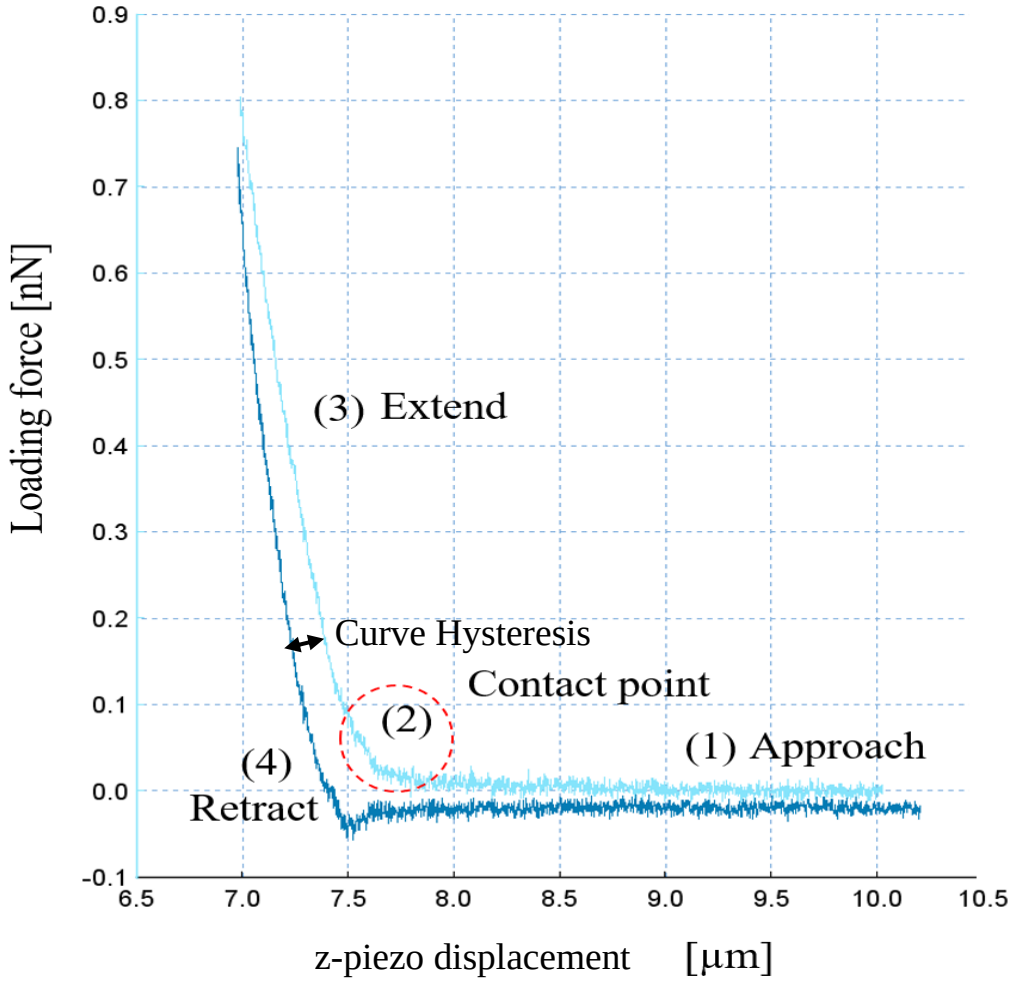

Figure 2-16. **AFM force versus z-piezo displacement curve acquired on live mammalian cell.** Curve obtained from the indentation of a live MDCK cell in liquid media at 37˚C. Regions of an AFM force indentation curve are labelled (1) approach or baseline where force = 0nN and no contact with sample (2) contact and indentation of sample resulting in cantilever bending or deflection, (3) extend/indentation into the underlying sample, (4) retraction of cantilever from the sample surface. In the example of this curve, there is a difference in the loading and unloading pathway of the curve (as denoted). This is referred to as curve hysteresis, and is indicative of energy loss/dissipation during the MDCK cell deformation.

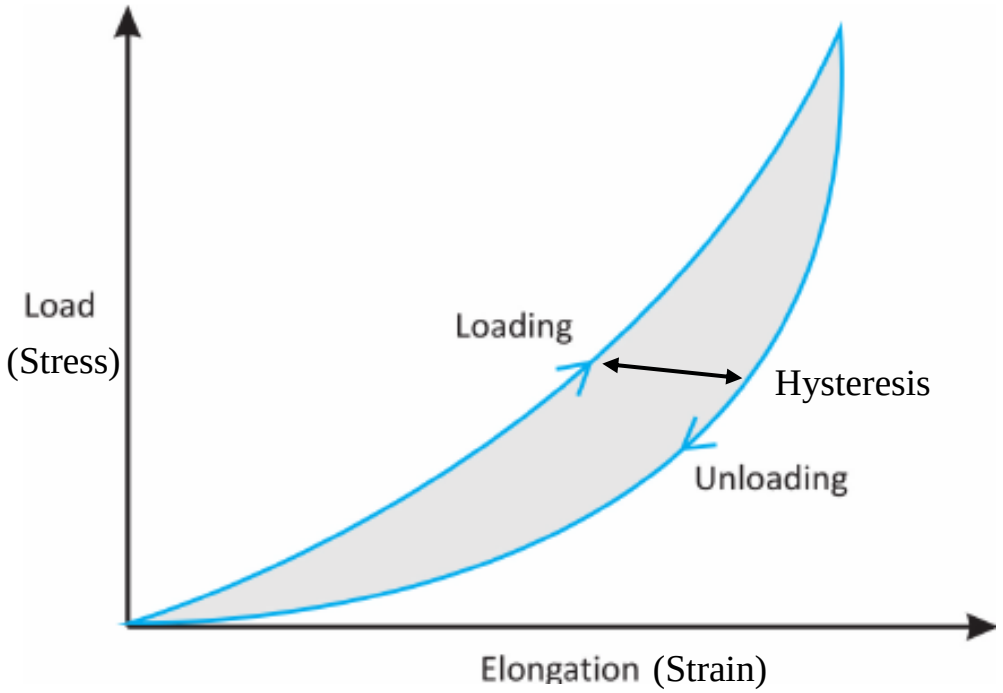

Figure 2-17. **Stress-Strain curve hysteresis.** When a material is loaded with a specified stress, the material presents with resulting strain (elongation or deformation). When the loading is removed, the unloading curve follows a different pathway to the loading curve. This difference is illustrated by the grey area). This results due to energy dissipation and is dependent on the loading rate and material properties (elastic or viscoelastic) of the material (Figure, taken and adapted, Robi, et al 2013) [128].

2.12 Deriving the Young's elastic modulus from AFM force curves – Application of the Contact models

When attempting to derive the Young's elastic modulus and elastic properties of a mammalian cell from an AFM force-displacement curve, a range of mechanical contact models have been defined and are available. The contact model selected is often chosen based on the experimental objectives defined for a particular AFM cell indentation assay. Differences in the contact models surround applications based on type of cantilever geometry chosen, mammalian cell characteristics (shape or presence of sample surface features) as well as applications where the weak electrostatic forces between the cantilever and underlying sample prior to deformation are considered in the

contact model. In order to make confident assumptions about the derived Young's elastic modulus of mammalian cell and AFM force curve outputs generated in biological AFM studies, appropriate AFM testing parameters as well as analysis models have to be carefully selected.

For the AFM experiments carried out in this thesis, a Nano Wizard 3 JPK AFM was used alongside the JPK data processing software. In this software, specific contact models were available to interpret and analyse acquired force-displacement curves. These are the Hertz-Sneddon contact model, and the Deriaguin-Muller-Toporov (DMT) contact model. It should be noted that there are multiple additional contact models available for interpreting and deriving the elastic and material properties of mammalian cells. However, for the purpose of this thesis, the Hertz-Sneddon contact model was used within the JPK data processing software. The most commonly utilised contact model from deriving the approximate mechanical properties from samples undergoing AFM indentation are the Hertz-Sneddon, the DMT model and the Johnson-Kendall-Roberts (JKR) model [117]. Additional contact models (such as the DMT and JKR) are to be presented in the sections to follow for review of selected contact models available.

2.12.1 Contact models – Hertz, Hertz-Sneddon, DMT, and JKR

One of the first contact models defined for investigating the mechanical and deformation properties of objects was the 'Hertz theory of elastic deformation'. First published in the 1800s, the Hertz theory was defined through investigating the contact area between two spheres. The resulting deformation of the two spheres was dependent on the material properties of the spheres and the load of force generated when bringing the two spheres into contact with one another [129]. Following on from the Hertz theory, continual developments in the field of mechanical modelling has resulted in numerous additional contact models being defined for investigating the material and

deformation properties of objects. Notable additional contact models include the Hertz-Sneddon model and DMT theory and JKR theory [122], [130]. The Hertz-Sneddon contact model was derived to modify the Hertz contact theorem by way of accounting for variation in the geometry of the indenting body brought into contact with the opposing material object. The Hertz-Sneddon contact theorem includes contact models for conical, flat-ended cylindrical, pyramidal and parabolic shaped indenting probes [123], [130]. Further to the traditional Hertz and Hertz-Sneddon contact models, an additional regularly utilised contact model is the DMT theorem. In the DMT model, additional mechanical affects such as the small Van der Waals forces outside the contact regime between the two objects in contact are considered when deriving the elastic and material properties of the objects [122]. Further to this, an additional contact model developed from the Hertz model – the JKR theory – which considers the variation in forces of adhesion between the two contacted bodies is also utilised [131].

2.12.1.1 The Hertz theory

Originally derived to investigate the contact mechanics between two bodies, the Hertz contact model (Figure 2-18), was first investigated by modelling the elastic deformation of two glass lenses brought into contact with one another, with the initial hypothesis being that the contact area between the two lens bodies is elliptical. Simplification of the deformation between the two bodies resulted in the assumption that each of the lens bodies can exist as an elastic half-space, loaded over a small region of its planar surface. This results in a region of highly concentrated stress between the two bodies, separate from all other stresses acting on them. This highly concentrated region of contact stress is directly related to the shape of the bodies in contact and the manner in which they are supported [129].

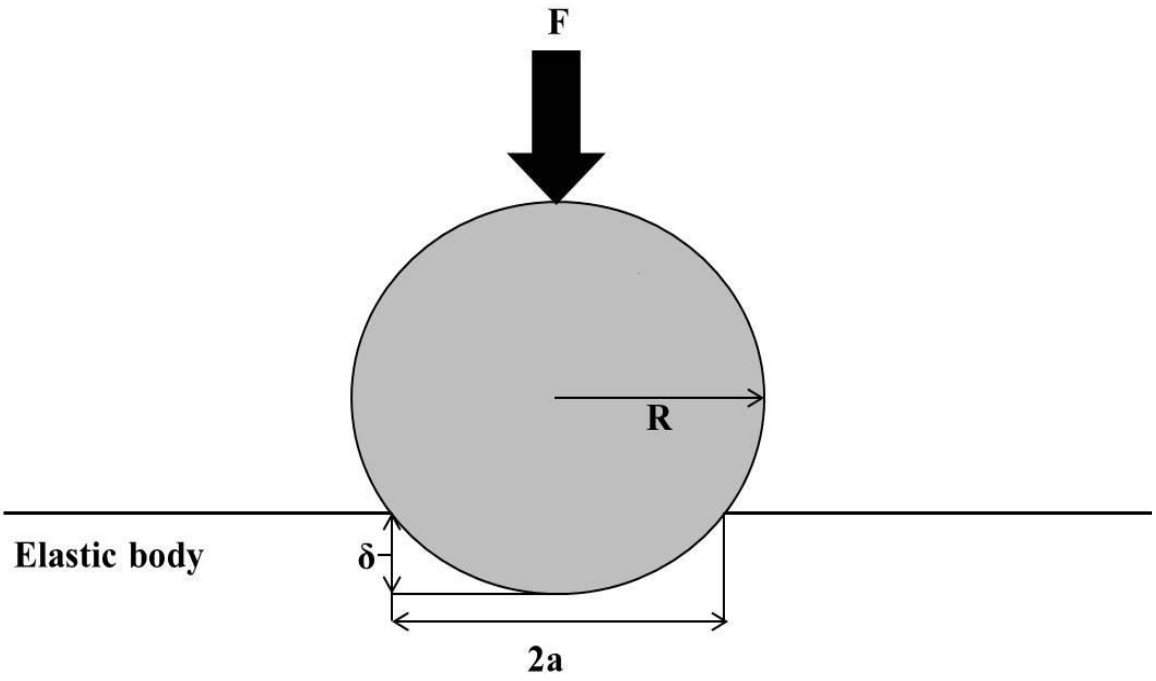

Figure 2-18. **Hertz contact model schematic.** The Hertz contact model is applied to analyse the contact mechanics between two elastic bodies. The parameters applied in the Hertz contact model are the radius of the contact region/area between the two bodies [a], the radius of the spherical indenter [R], the indentation depth of the spherical indenter [$\boldsymbol{\delta}$] and the force applied by the spherical indenter [F]. The radius of the contact region between the two bodies and resulting indentation depth are both dependent on the force applied to the surface of the sample (Figure adapted from Chadwick, et al 2002) [129], [131], [132]

In order to appropriately derive the elastic properties of elastic bodies, the Hertz model makes certain assumptions about the objects undergoing mechanical investigation. Referring the parameters detailed in Figure 2-18; the radius of the contact region/area between the two bodies [a], the radius of the spherical indenter [R], the indentation deformation depth of the spherical indenter [δ], and lastly, the force applied by the spherical indenter [F], the following assumptions are made by the Hertz contact model when calculating the elastic deformation between two bodies;

- Each body is considered as an elastic half-space,
- The surfaces of the bodies are considered continuous and non-conforming such that the region of contact between the two bodies is smaller than the dimensions of the contacting bodies (a < R),
- The strains are small (a < R),
- There is no friction between the two bodies, and only a normal applied force is transmitted between them.

To demonstrate how the Hertz contact theorem derives the elastic modulus (material property) - the following equations have been defined; For an elastic half-space that is deformed by a spherical elastic solid, the Hertz model demonstrates that the area of contact and radius [a] can be derived by:

$$a = \left(\frac{3FR}{4E^*}\right)^{\frac{1}{3}} \tag{2-5}$$

And the indentation depth (deformation of the elastic material) can be derived by:

$$\delta = \frac{a^2}{R} = \left(\frac{9F^2}{16RE^{*2}}\right)^{\frac{1}{3}} \tag{2-6}$$

Here as previous, [a] is the radius of the contact region/area between the two bodies, [R] the radius of the spherical indenter, [δ] the indentation deformation depth of the spherical indenter, [F] the force applied by the spherical indenter, and lastly [E] the Young's elastic modulus of the material under deformation.

To derive the total indenting load of force applied by the spherical indenter to deform/compress the underlying body, Eq. (2-2) can be modified as follows;

$$F = \frac{4ER^{\frac{1}{2}}}{3(1-\nu^2)}\delta^{\frac{3}{2}} \qquad (2\text{-}7)$$

To derive the final Young's elastic modulus of the underlying body following a force of deformation, the following equation is utilised;

$$\frac{1}{E^*} = (1 - \frac{\nu_1^2}{E_1}) + (1 - \frac{\nu_2^2}{E_2}) \qquad (2\text{-}8)$$

The variables denoted [E*] and [ν] in equations (2-5, 2-6, 2-7) and (2-8) are the Young's elastic modulus and the Poisson's ratio respectively [133]. To clarify the use of the variables shown in the above equations, the Poisson's ratio needs to be described and defined. The Poisson's ratio, is a ratio between the contraction strain (transverse, lateral or radial) normal to the applied load stress - to the extension strain in the direction of the applied load. A rudimentary description would be to imagine a material sample, which when stretched in one particular direction, results in a thinner geometry in the lateral direction, but if compressed in a particular direction will get thicker in the lateral direction [134]. Essentially, the Poisson's ratio is a term derived to describe the process of a material compression in which the material tends to expand in directions perpendicular to applied direction of compressive load.

The Poisson's ratio can be expressed as follows;

$$\mu = \frac{\varepsilon t}{\varepsilon l} \tag{2-9}$$

Here, [μ] is the Poisson's ratio, [εt] the transverse strain [m/m] and [ε_l] the longitudinal or axial strain [m/m]. To better define and derive the transverse and/or longitudinal or axial strain, the following is defined;

For longitudinal or axial strain;

$$\varepsilon t = \frac{dl}{L} \tag{2-10}$$

Here, [εt] is the transverse strain, dl the change in material length [m] and [L] the initial material length [m].

For contraction (transverse, lateral or radial strain);

$$\varepsilon t = \frac{dr}{r} \tag{2-11}$$

Here, [εt] is the transverse (lateral or radial strain), [dr] the change in material radius [m] and r the initial material radius [m].

The value obtained for the Poisson's ratio provides information about the material property of a sample – how compressible or incompressible a material is. A perfectly incompressible material would a Poisson's ratio of exactly 0.5, which is derived if the material is elastically deformed at small strains. In the case of AFM analysis of mammalian cells and the derivation of the Young's elastic modulus, it is often the case the Poisson's ratio is assigned as 0.5 in the Hertz contact model (and certain model derivatives). This is just one of the assumptions made by the contact model for

mammalian cell Young's elastic moduli analysis (additional assumptions and limitations to be discussed in sections to follow). Assigning a Poisson's ratio of 0.5 to mammalian cells assumes the cells as incompressible, and is an approximation of the material properties of a mammalian cell which implies the cell is isotropic and homogenous [135]. Although it is often the case that this value (0.5) is assigned in certain AFM studies on mammalian cells, some published studies have reported Poisson's ratio's for single mammalian cells at reduced values; Using combining AFM and acoustic probes, Shin and colleagues reported a better fit for derived AFM force-displacement data gathered on compressing osteoblast-like cells using a Poisson's ratio of 0.37 ± 0.03 [136].

When deriving the elastic properties of mammalian cells from AFM force-displacement curves, the Hertz contact model is often applied to the extend portion of the force displacement curves as it is less affected by the attractive adhesive forces when retracting from the samples surface. Simply put, the resulting bending force between the cantilever as it contacts the sample surface can be described using Hooke's law;

$$F = k \times x \tag{2-12}$$

Where [F] is the force applied to the sample, [k] is the spring constant of the cantilever, and [x] is the resulting deflection (bending) of the cantilever upon sample deformation. Hooke's law describes the elastic properties of a material as a function of the relationship between stress and strain. Hooke's law states that a stress on a material is proportional to strain, and the stress-strain curve is linear. The relationship between stress and strain or coefficient of proportionality (slope of the curve) defines the elastic properties of the material (Young's elastic modulus) [137], [138]. The resulting deformation depth [δ] of the sample in a given stress-strain event, at the given stress

(force) can then be derived from the cantilever deflection and the z-piezo [Z] displacement as follows;

$$\delta - \delta_0 = (z - z_0) - (x - x_0) \quad (2\text{-}13)$$

Here, [δ_0] refers the contact point of the cantilever with the underlying sample. This is a simplification of the indentation carried out between two elastic bodies (in terms of the stress-strain relationship during sample deformation by a cantilever.

It should be noted that many of the alterative contact models that are also used to investigate the elastic material properties of samples were developed based on the Hertz model contact theorem. These models were developed and are utilised where some of the assumptions made by the Hertz-contact theorem are not met, or, additional surface or material properties are being investigated. For example, where experimental objectives such as investigating the surface adhesion of a material, the geometry of the cantilever, and or thickness of the material are considered in the contact model. Furthermore, when applying the Hertz contact model to derive Young's elastic moduli (for mammalian cell investigations), the thickness of the cell must be considered. The Hertz model is most suitable for application where sample deformation is shallow (< 10% of total sample thickness) [139].

2.12.1.2 The Hertz-Sneddon theory

As previously outlined, the Hertz contact model theorem, in the field of contact mechanics, provided the foundation for further experimental and theoretical models to be developed. Some of the additional models further defined were investigated to account for variation on the geometry of the indenting cantilever underlying probe. This is the Hertz-Sneddon modification, and was derived by Ian Sneddon in 1965. This

contact model demonstrated the correlation between the force load of the cantilever, and resulting material displacement in relation to the contact of the indenting cantilevers underlying probe [130]. The models investigated and defined by Sneddon, lead to an equation which can be applied for the calculation of the applied load and resulting Young's elastic modulus of a sample when using cantilever indenturing probes of different geometrical shapes. The Hertz-Sneddon modification allowed for the development of contact models used to derive the elastic properties of a material for the following cantilever probe geometries [123], [140];

In the case of a spherical indenter, the equation is modified as:

$$F = \frac{E}{1-\nu^2}\left[\frac{a^2+R^2}{2}\ln\frac{R+a}{R-a} - aR\right] \qquad (2\text{-}14)$$

Where [a] is the radius of contact sphere, and [R] is the radius of the sphere and [V] the Poisson's ratio of the sample.

The Hertz-Sneddon modification for a four-sided pyramidal indenter;

$$F = 0.7453\frac{E}{1-\nu^2}\,\delta^2\tan\alpha \qquad (2\text{-}15)$$

Here [α] denotes the face angle of the pyramidal indenter.

For flat-ended cylindrical indenters, the relation between load and displacement is given as:

$$F = \frac{2ERn}{(1-\nu^2)}\delta \qquad (2\text{-}16)$$

Here [E] is the elastic Young's modulus, [Rn] is the radius of the flat-end indenter, [ν] is Poisson's ratio and lastly [δ] is the indentation/deformation depth of the sample.

For the conical indenters, the Hertz-Sneddon equation given as:

$$F = \frac{2E\tan\alpha}{\pi(1-\nu^2)}\delta^2 \qquad (2\text{-}17)$$

Here, all parameters are the same as above, with [α] as the half angle of the cone.

Having discussed the adaption of the Hertz-contact model that considers the geometry of the cantilever indenting probe, next the second contact model mentioned in the introduction of this section (section 2.12.1) – the DMT theory, is next described. As previously mentioned, the Hertz model has been modified by many scientists based on the application of the contact model for different experimental conditions i.e. Cantilever geometry (Hertz-Sneddon modification). However, in this model, as with the Hertz model the attractive adhesive forces between the two contacting bodies in negated. In the case of the DMT model, this is not the case.

2.12.1.3 The DMT theory

The Deriaguin-Muller-Toporov (DMT) model of elastic contact is another contact model developed from the principles of Hertzian contact mechanics. Developed in 1975, the DMT theory considers the elastic interaction between two bodies, but also

considers additional attractive forces such as adhesive interactions outside the contact regime [122]. Specifically, the Van der Waals interactions are taken into consideration in the DMT model. These low level attractive forces are capable of affecting the elastic interaction between a spherical indenter and underlying sample [122], [141]. In greater detail, the DMT theory allows for the derivation of the work of adhesion/forces resulting from the Van der Waals interactions outside the contact regime;

$$F_{adh(DMT)} = 2\pi\Delta\gamma R \tag{2-18}$$

Here, [R] is the radius of the spherical body, and [$\Delta\gamma$] is the work of adhesion.

The contact radius between the indenting sphere and underlying body is derived by;

$$a_{DMT} = \frac{3R}{4E^*}(F + 2\pi\Delta\gamma R)^{\frac{1}{3}} \tag{2-19}$$

Here, as previous, [R] is the radius of the spherical body, [F] is the loading external force, and [$\Delta\gamma$] is the work of adhesion.

The final resulting Young's elastic modulus [E*] of the underlying body is derived by;

$$\frac{1}{E^*} = (1 - \frac{\nu_1^2}{E_1}) + (1 - \frac{\nu_2^2}{E_2}) \tag{2-20}$$

Here, [E_1] and [E_2] denote the Young's elastic modulus, and variables [ν_1] and [ν_2] denote the Poisson ratios of the two bodies in contact with one another.

2.12.1.4 The JKR theory

Having discussed the Hertz contact model and derivates (Hertz-Sneddon and DMT), another contact model theory that describes the elastic deformation of two bodies in

contact is the Johnson-Kendal-Roberts (JKR) theory. In the Hertz, and Hertz-Sneddon contact theorems, the adhesive and attractive forces between the two bodies in contact are negated. In the case of the JKR theory, and similar to the DMT theory, the adhesive and attractive forces are considered. In the case of the JKR theory, the effect of surface energy and work of adhesion at the contact area between the two elastic solids was investigated. The JKR theory demonstrated that the adhesion between the two bodies is not significant at high deformation forces, however, at low force (as it tends to zero), the adhesion forces does become significant and cannot be negated as with the conventional Hertz contact theorem [131]. Further development of the JKR theory also demonstrated that at low deformation forces, contact area between the two elastic solids is significantly larger than shown by the Hertz contact theorem [142]. The JKR theory investigates the adhesive forces between a rigid sphere and a rigid surface, whereby rigid sphere with a radius [R] that comes into contact with a rigid surface, the adhesion force [F_A] between the sphere and the surface can be derived as follows:

$$F_A = 2\pi\Delta\gamma R \tag{2-21}$$

Additional to the model and equation defined, in order to separate the two surfaces in contact, mechanical work is required to overcome the work of adhesive forces between the sphere and planar surface. This work of adhesion - which creates a 'new' surface, can be defined as follows;

$$\Delta\gamma = \gamma_1 + \gamma_2 - \gamma_{12} \tag{2-22}$$

Here, work of adhesion is [$\Delta\gamma$], [γ_1] and [γ_2] are the surface energies of two spheres for creating a unit area of a 'new' surface, and [γ_{12}] is the interface energy.

2.13 Limitations of application of Hertz contact model in Young's moduli Mammalian cell AFM measurements

As stated, in this thesis, the Hertz-Sneddon contact model was utilised for the analysis of all derived AFM force-displacement curves to obtain the Young's elastic modulus of the chosen mammalian cell line under investigation. The Hertz-Sneddon contact model was utilised for two reasons; (1) The requirement and scope of the research required investigation of the Young's elastic modulus (specifically) for mammalian cells at alternate stages of monolayer development, (2) To derive the Young's modulus, the AFM system used had two different contact models available for mammalian cell elastic moduli analysis, namely Hertz-Sneddon and DMT. In this thesis two different cantilever geometries were used (spherical and pyramidal). Therefore, based on the type of data required and difference in cantilever geometry, the hertz-Sneddon contact model was used. It should be noted that there are limitations when utilising the Hertz-Sneddon contact model for live cell mammalian cell measurements. As previously discussed, when applying the Hertz-Sneddon contact model to derive the mechanical properties of two elastic bodies, certain assumptions about the two bodies in contact have to be made. The Hertz-Sneddon contact model assumptions for live mammalian cell AFM force-displacement calculations are;

- Mammalian cells are considered as linear elastic infinitely deep homogenous isotropic solids.
- Inherent viscoelastic properties within the cell are negated.
- The cells are not considered as active.
- Secondary effects resulting from the external mechanical load (such as cytoskeleton re-orientation) are not considered.
- Cells are considered incompressible (Poisson's ratio 0.5) as noted previously

Notably, referring to the above assumptions made by the Hertz-Sneddon contact model (as a derivative of the Hertz contact model), it is evident that many of the assumptions are not met in biological complex samples. This leads to limitations in the application of the model and the results derived for live biological samples. For example, mammalian cells are not in reality linearly elastic bodies. They exhibit viscoelastic behaviour. This is evident based on the hysteresis curve derived for mammalian cell AFM cantilever indentation (Figure 2-16). Therefore, the stress-strain relationship during mammalian cell deformation would need to consider sample viscosity [117]. When a cantilever deforms a mammalian cell at a given region, the energy distributed by the indenting cantilever is not given back by the cell (as is not the case of absolute elastic materials). The dissipation of the energy (hysteresis) is evident in live cell AFM force-displacement curves (Figure 2-16). However, the viscous contributions of the material can be reduced by maintaining appropriate and reduced cantilever loading rates. In this case there is still a limitation however, as too lower loading rate could result in the remodelling of the sample under indentation. At too higher indentation velocities, higher resistance of the sample can be observed and thus more viscous effects of the cell sample measured. However, at too low indentation velocity, the indentation stress could result in irreversible deformation of the cell. Furthermore, the material properties of the outer cell environment such as the ECM can begin to govern the derived elastic property behaviour of the sample indentation as low indentation speeds (timescales) [143].

Additional limitations to be considered when deriving the Young's elastic modulus of mammalian cells by AFM encompass matters surrounding the thickness of the cell sample, and fitting of the Hertz-Sneddon contact model. In traditional Hertzian contact mechanics, the model assumes that sample (cell) indentation depth is negligible in comparison to the thickness of the sample. However fitting of the contact model to

derive the Young's elastic modulus of the elastic body under indentation is subject to the indentation depth analysed [119], [123]. Indentation of biological samples by more than 10% of sample thickness will result in the material properties of the underlying substrate contributing to the derived elasticity measurements [132]. Therefore, the deformation depth of the sample has to be carefully considered. The Hertz model is only valid for relatively small indentations of around 5-10% of total sample thickness [123], which reduces the occurrence of artificial and inaccurate contact model fitting due to the influence of the underlying substrate. For live mammalian cells, this value can range from 100-500nm. However, even if careful consideration is taken when applying an appropriate loading force and loading rate, there is still a limitation; the accurate derivation of the Young's elastic modulus from a force-displacing curve requires the accurate determination of the point of contact of the cantilever and the underlying sample. For biological samples whose surface topographies can be somewhat uneven and complex such as mammalian cells, a precise signature of the contact region in a force-displacing curve for a sample where deflection of the cantilever starts to take effect can sometimes not be clear or precisely determined. This can make values obtained for indentation/deformation depths of the sample inaccurate by tens of nanometres [117]. Markedly, as with the limits of sample thickness of the Hertz-contact model, it is typically recommended that a sample deformation depth at least > 400nm be required to avoid contact point detection errors [144],[145].

There have been corrections made to account for samples with finite thickness, and additional contact model theorems have been defined for measuring thinner regions of elastic materials (such as mammalian cells) [146], [132], [147]. An example of one such correction can be demonstrated by discussing the work presented by Gavara and Chadwick (2012); In their study on AFM indentation of polyacrylamide gels of graded thicknesses and adherent fibroblast cells they tested the application of their Bottom

Effect Cone Correction (BECC) model in comparison to the Hertz-Sneddon contact model for deriving the elastic properties of each sample type. Specifically, their BECC model defines a correction for the height of the samples for commonly used Hertz-Sneddon mode for conical cantilever tips;

$$F = \frac{8E \tan\theta \delta^2}{3\pi} \left\{ \left\{ 1 + 1.7795 \frac{2\tan\theta}{\pi^2} \frac{\delta}{h} + 16(1.7795)^2 \tan^2\theta \frac{\delta^2}{h^2} + 0\left(\frac{\delta^3}{h^3}\right) \right\} \right. \quad (2\text{-}23)$$

Here [F] is the applied force, [δ] is indentation of the material, [θ] is the half-opening angle of the cantilever cone, [*h]* is the height of the sample at the location of indentation [146].

In their study, Gavara and Chadwick found the Hertz-Sneddon model can grossly overestimate the derived elasticity of polyacrylamide gels and does not allow for the discrimination of specific regions of fibroblast surface properties compared to their BECC model. Using their BECC model they were able to effectively derive elastic values of polyacrylamide gels for larger (>85% thickness) before non-linear mechanical properties were met. The BECC model was also able to discern distinct regions of fibroblast mechanical properties relating to cytoskeletal stress fibres [146].

Further to the limitations in sample thickness and cantilever loading rates, some biological samples present with non-linear mechanical outputs and can stiffen under certain strains [148], which could render the application of the contact model inaccurate. Additionally, The Hertz model contact theorem assumes the cells as infinitely thick (as stated above), however this is not the case and mammalian cells are typically only around a few micrometres thick across their cell body regions. The Hertz contact theorem and derivatives also assume that there are no other forces of interaction between the two surfaces in contact (such as adhesion or friction). This is a limitation

since mammalian cells can present with adhesive properties following cantilever indentation [149]. In this case, contact models such as the JKR or DMT theory would be more appropriate to investigate the mechanical properties of the mammalian cells. Therefore, when using the Hertz-Sneddon contact model, careful consideration of experimental protocol application on the AFM has to be carried out. Lastly, although the Hertz-Sneddon contact model does allow for the derivation of the Young's elastic moduli of mammalian cells for different cantilever geometries, it has been demonstrated that the Hertz model assumption for small deformations (10% of sample thickness) becomes invalid using sharp and/or pyramidal cantilever indenters [132]. Therefore, this renders many of the commercially available cantilever geometries as inappropriate for investigating certain elastic material properties of biological samples. However, it is suggested that if large spherical cantilevers are used, with large enough curvature radii, it then becomes possible to apply deformation forces to biological samples that can allow for the derivation of reliable material properties of the sample. Specifically, it is suggested that radii of 5μm can result in strains that are kept in the linear elastic region for quite large deformation forces [132].

2.14 AFM - Mammalian cell Young's moduli measurements

As previously discussed, AFM is one of the most highly useful cell mechanical analysis tools for investigating and characterising the mechanical properties and surface topographies of mammalian cells in an *in-vitro* environment. With continued advances in the field of AFM measurements, mammalian cells can now undergo mechanical analysis under conditions that mimic those of an *in-vitro* culture environment. Biological samples can be analysed and imaged at appropriate temperatures with optimal CO_2 concentrations and perfusion.

Automatic force mapping tools with controlled approach, indentation and retract speeds can allow for high resolution surface topography analysis without negatively affecting the surface of the mammalian cells or needing to fix, stain or label the cells surface which would produce artificial cell surface Young's elastic moduli values. To date, numerous cell types from multiple body tissues have undergone AFM mechanical analysis in an attempt to derive the Young's elastic modulus values for a different mammalian cell type (Table 2-2).

Table 2- 2. Young's elastic moduli of various mammalian cell types derived using AFM force indentation analysis.

Cell Type	**Length scale analysed**	**[E] kPa**	**Reference**
Cardiomyocytes	Single cell	90-110	[150]
Fibroblasts	Single cell	0.5-7	[16]
Embryonic (human) **Embryonic** (mouse)	Monolayer Monolayer	0.05-10 1.49-16	[16] [14]
Endothelial cells Human umbilical vein	Single cell Cluster group Monolayer	0.84-0.89 0.75-0.73 0.88-0.95	[109]
Epithelial cells (human foreskin) (canine kidney MDCK)	 Single cell Monolayer	 14-33 5.7-5.8	 [12] [151]
Mesenchymal	Single cells	0.81-1.13	[9]

2.15 AFM – Cancer cell Young's elastic moduli measurements

As previously discussed, much research has been carried out investigating how the physical and mechanical characteristics of cancer cell lines relate to cancer cell development and disease prognosis. Correlating derived AFM mammalian cell Young's elastic moduli measurements from various cancer cell lines to their respective healthy tissue counterparts has revealed a trend in cancer cell mechanical outputs. A common highly conserved feature of cancer tissue remains the clinical presentation of stiffer tissue mass surrounded by softer healthy tissue [152]. Studies investigating AFM cancer cell Young's elastic moduli outputs for different cancer cell lines and their respective healthy tissue counterparts, demonstrated a reduced Young's elastic modulus across all cancer cell types (Table 2-3).

Table 2- 3. Young's elastic moduli of various cancer cell types derived using AFM force indentation analysis.

Cancer Cell Type	**Length scale analysed**	**[E] kPa (healthy cells)**	**[E] kPa (tumour cells)**	**Reference**
Carcinoma of the lung	single	2.10 -2.89	0.56-0.65	[7]
Breast ductal carcinoma	single	1.93-2.43	0.50-0.58	[7]
Pancreatic adenocarcinoma	single	0.54-0.66	0.54-0.58	[7]
human mammary tumorigenic cells	Single monolayer	2.34-3.87 2.49-4.37	1.62-5.55 3.72-5.07	[112]
Ovarian cancer cells	Single	2.47-4.47	0.88-1.38	[106]
Prostate cancer cells	Single	2.8-3.2	0.3-0.35	[153]
Bladder cancer cells	Cell clusters	16.0-16.9	3.0-3.1	[154]

2.16 Investigating the Young's elastic modulus of mammalian cells at alternate stages of cell confluence and monolayer development

Notably, although AFM provides the ability to measure and analyse mammalian cell Young's elastic moduli, there is a great deal of disparity among AFM studies as a result of differences in experimental approaches and protocols. The variation in derived AFM Young's moduli outputs for different mammalian cell lines at alternate stages of cell monolayer development, ascends the question if such variations are due to differences in cell line (species and/or tissue type), or if the derived AFM output trends may result from variation in AFM methodology approaches. Differences in the geometry of the AFM cantilever probe selected i.e. spherical [110]–[112] versus pyramidal [113] and/or loading force i.e. 0.4nN [113], 0.2 -1.0nN [111] or 2.5nN [112], could result in the variation in AFM [E] trends derived. This may not be due to biological variation, but arise as a result of the alternate indentation and deformation depths associated with selection of different loading forces and more localised penetrative cantilever geometries. The location of cantilever probe indentation; cell body and central cell regions can vary in height and location of the large internal nuclear organelle can also produce differences between AFM studies investigating cell elastic properties at different stages on monolayer development. If similar cell regions are selected for AFM cantilever deformation, a slight variation in cell deformation may result in a variation of calculated AFM cell elastic properties, which is likely due to the presence of large internal organelle structures. Furthermore, a great deal of intracellular variation due to the presence and activity of the intracellular cytoskeleton, increase in the number of cell-cell bonds, internal organelle movement and activity, could also greatly affect the synergy among AFM studies investigating mammalian cell elastic properties with increase in monolayer development. Secondly, the stage of mammalian cell development in terms of cell cycle and/or number of repeated in-vitro passage cycles

could also result in a great deal of variation for studies carrying out AFM indentation on similar mammalian cell lines. If AFM experimental parameters are kept absolute and uniform for each individual AFM cell mechanical assay, it could be possible for individual groups to draw reliable conclusions for how similar cell lines (tissue type/origin) vary in their elastic properties through increasing stages of monolayer development. Current variances among AFM studies on similar cell lines make it difficult to define a novel process through which a tissue monolayer develops.

2.17 Inhomogeneity across tissue constructs – A mechanical challenge

While it may be useful to measure the mechanical output properties of tissue biopsies for clinical research purposes, a great problem posed with the interpretation of such outputs, is the relationship between macroscopic tissue function and the underlying cellular make-up of the tissue. Interpreting the mechanical outputs of tissue length scale constructs for the replication of cellular processes *ex-vivo*, is a primary objective in the field of tissue engineering. More eloquently put by Marquez and colleagues in their remodelling of the Zahalak continuum law… "Continuum constitutive laws are needed to ensure that bio-artificial tissue constructs replicate the mechanical response of the tissues they are designed to replace…" [155]. Moreover, Marquez and colleagues highlighted that both tissue and cellular mechanical properties are gathered during tissue mechanical measurement assays, and that the actual distribution of mechanical strain within a tissue greatly depends on the relative mechanical properties and orientation of the underlying tissue cells. Out-of-plane orientation of cellular distribution greatly affects both cellular stiffness and as well as global tissue stiffness, with uniform planar orientations of cells producing far stiffer tissue mechanical outputs, compared to an otherwise identical tissue construct with randomly orientated tissue cells [155]. Preferential cellular alignment and cell traction or *contact guidance* was found to

produce a similar effect on measurement outputs in ECM tissue undergoing mechanical analysis [156]. Furthermore, cellular alignment and contact guidance are both physical cell functions which inherently affect intracellular components such as the position of cell nuclear organelle and cell cytoskeleton. Given the scale of heterogeneity that exists in the derived Young's elastic moduli across different internal single cell regions [12], mechanical analysis across various tissue and higher cell length scales remains somewhat incomplete. Approaches in mammalian cell Young's moduli analysis aimed at merging how the mechanical outputs of cells (and their respective internal environments) relates to cell-cell mechanical functions and ultimately tissue function, will provide a more concise overview of how tissue structures physically develop and function across a multiscale inhomogeneous platform.

As discussed, and highlighted in this chapter, there is an inconsistent and lack of synergy among mammalian cell mechanical Young's elastic moduli analysis using AFM. Alternate protocol approaches – such as loading forces and cantilever selection – make it difficult to compare and correlate studies attempting to address cell mechanics. Many of the aforementioned AFM cell mechanical assays primarily focus on isolated or intermediate cell group or cluster stages of monolayer development, which cannot be translated into a complete cell-by-cell narrative of how mammalian cell monolayer layer formation ensues from the single to monolayer developmental stages. Given that most of the tissues that make up the organs and organ compartments within the mammalian body are composed of multiple layers of cells, accounting for how the mechanics of a cell transitions from the single to monolayer developmental length scale, will provide an insight into how single cells (and their internal components) vary and adapt their mechanical properties *in-vitro* to produce monolayer and tissue scale structures.

In summary, to highlight the current gaps in defining and interpreting mammalian cell mechanics between different mammalian cell AFM assays, the current challenges are;

- Inconsistent and diverse AFM measurement approaches for cell mechanical analysis – in terms of selected cantilever types and loading force ranges
- Missed and lack of appreciation for how varied AFM protocol parameters can affect cell mechanical analysis for similar cell lines
- Inconsistent and diverse AFM protocol approaches in selected mammalian cell length scales used for analysis
- Missed/lack of correlation between mechanical outputs of intermediate (doublet and cluster) cell developmental length scales and mammalian cell monolayer development

Therefore, using a structured and defined approach for live mammalian cell AFM indentation analysis, this thesis investigates variations in cell mechanical properties (Young's elastic modulus) with increase in cell monolayer developmental length scale. Themes surrounding cell developmental length scale across precise increases in cell number(s), cantilever indentation and cell deformation depths, cantilever loading forces and intracellular environment are all investigated and presented. The primary objective of this thesis is to attempt to analyse and bridge the gap in cell mechanical analysis, using mammalian cell AFM mechanical analysis and imaging techniques, to improve and build upon the current narrative of biological and mechanical control of mammalian cell monolayer development.

CHAPTER 3

Materials and Methods

3.1 Introduction

In this chapter, the general materials and methods used to carry out all experiments are described. Atomic force microscopy (AFM) was the primary method for cell mechanical analysis of cells, in investigating the elastic properties of the selected cell line, as well as for the imaging and analysis of cell surface topography. For all AFM data obtained on the selected cell line, the elastic moduli outputs were obtained and calculated using the JPK AFM and JPK SPM analysis software by way of application of the Hertz-Sneddon contact model.

3.2 General cell* culture protocol

All cell culture protocols including reagent preparation were carried out in an aseptic manner i.e. using sterile consumables handled in a manner to minimise the risk of microbial contamination, with all procedures performed within a class II microbiology safety cabinet.

Note: Prior to all cell culture activities (passaging/thawing/ AFM sample preparation) all media aliquots and liquid reagents (TrypLE, PBS) were pre-warmed at 37 °C.

*Selected cell line to be denoted for each experiment in each chapter.

All reagents and equipment used for cell culture and culture media preparation are listed as follows:

Equipment	**Reagents:**
T(25)cm^2 vented volumetric flasks	(Selected mammalian cell line*)
Sterile 15ml and 50ml universal tubes	Cell culture media
Gilson pipette aid	TrypLE select (10X)
5ml, 10ml and 25ml volumetric pipettes	PBS (10X)
Bench top centrifuge	Trypan blue
Haemocytometer Fuchs-Rosenthal	
Pipette gun	

3.3 Preparation of cell culture media

The selected cell line for each experiment was cultured in standard culture media, prepared by adding the following individual constituents; Phenol red-free RMPI 1640 (500ml) (Fisher Scientific), 1% Penicillin/Streptomycin (Fisher Scientific), 10% Fetal bovine serum (FBS) (heat inactivated) (Fisher Scientific) and GlutaMAX^{TM} supplement (Fisher Scientific). Once prepared, the cell culture media was stored at 2-8°C until used for cell culture/passaging.

3.4 Cell culture passaging

Following thawing from frozen stores, the selected cell line was cultured in standard cell culture media at 37°C and 5% CO2 until ~80% confluent. Confluent cells were detached from culture flasks using the TrypLE select (10X) cell dissociation enzyme. Dissociated cells were then pelleted at 1000rpm for 3 minutes and re-suspended in standard culture media for subsequent passage in a new culture flask (at recommend

spilt ratios). For methods where specific cell densities were required for experimentation, re-suspended cells were counted using a C-Chip haemocytometer (DHC-FO1 Grid pattern – Fuchs-Rosenthal). Cells were counted by mixing a sample of cell suspension with trypan blue at a 9:1 ratio. Cells were then counted and numbers adjusted for the dilution factor of the haemocytometer; the cell yields following each passage were calculated and appropriate cell densities seeded onto culture dishes for each experiment.

3.5 Cell cycle synchronisation

Due to the previously discussed physical variations that occur within cells during the cell cycle (Ch2, section 2.7.1), cell cultures were synchronised into the same cycle phase (G1 phase) prior to all AFM analysis. This was carried out with the aim of attempting to reduce any mechanical variances between cell samples which may arise due to cell cycle events. In doing so, it also allows for greater reproducibility and improved data comparisons between each cell sample. Cell cultures were synchronised using a nutrient (FBS serum) starvation protocol as previously described [157]**,** using restriction of the serum reagents and materials as detailed in sections 3.2 and 3.3.

3.6 AFM sample preparation

All AFM sample preparations were carried out in an aseptic manner to minimise the risk of microbial contamination of the AFM samples, with all procedures performed within a class II microbiology safety cabinet.

All reagents and equipment used for AFM sample preparation are listed;

Equipment and reagents used for AFM sample preparation:

Equipment	Reagents
60mm AFM culture dishes (Figure 3-1)	Cell culture media (Section 3.3)
Standing portable UV lamp	Selected cell line
Parafilm	

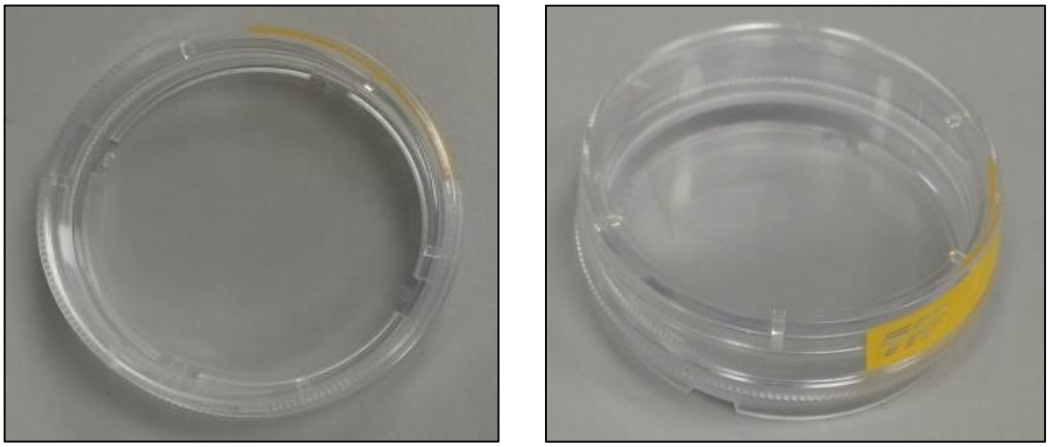

Figure 3-1. AFM sample dish. 60mm non-coated AFM sample cell culture dishes (TPP).

3.6.1 Preparation of cell sample for AFM experimentation

Following each cell passage, remaining re-suspended cells were used to prepare cell samples for experimentation by AFM. Cells were seeded onto plastic UV sterilised (non-coated) 60mm culture dishes (Figure 3-1), at ~1 x10^4 cells/ml to produce well developed cell seeding densities for AFM measurements. Samples were always prepared and incubated at 37°C, 5% CO2, 12-24 hours prior to analysis to allow for adequate cellular attachment and reduce over-confluence or death of cells for AFM analysis. Due to previously reported studies demonstrating the affected compliance of

loosely attached cells with artifical elastic outputs [158], only properly attached cells were selected for AFM indentation. Attached cells were identified through observation for adquate cell surface area deformation (lamellipoda formation) and spreading onto the AFM culture dishes. Prepared sample dishes were monitored carefully for required cell length scale phenotypes for each live cell analysis. When required, cells were suspended and plated at lower densities ($> 2 \times 10^3$) to ensure the presence of single attached cell phenotypes.

3.7 AFM set up and experimental protocol

3.7.1 AFM microscope

All AFM experiments were carried out using a Nanowizard®III Bio AFM (JPK Systems, Berlin), mounted on top of a Zeiss Observer D1 inverted optical microscope, situated within a JPK isolation box to reduce any ambient noise interference during AFM measurement (Figure 3-2). All AFM elasticity measurements were obtained in contact modes; force spectroscopy and force mapping. For each chapter, force indentation modes and experimental parameters are denoted and discussed. In all cases, unless otherwise stated for specific experiment aims, an attempt was made to keep all force indentation parameters uniform across all experiments in order to draw reliable and reproducible conclusions and outcomes based on data outputs from each experiment. Indentation loading force (nN), indentation speed (extend speed) (μm/s), Z-length (μm) and target sample height (μm) are denoted in each section (experiment). Force indentation measurements were collected for each sample over a period of no more than 1 hour per AFM sample.

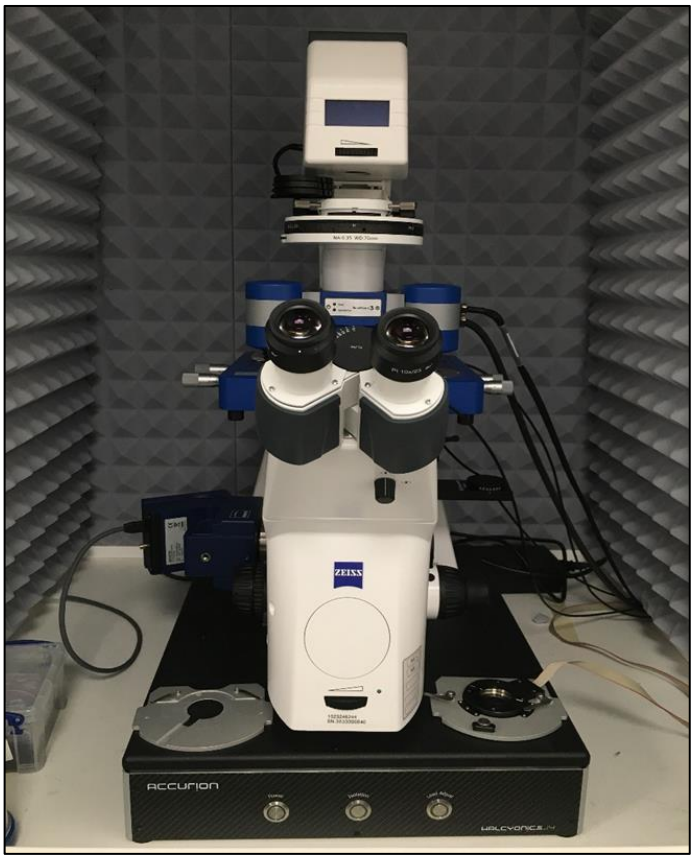

Figure 3-2. AFM NanoWizard III Bio within acoustic isolation chamber. The AFM is situated on top of a vibration isolation table.

3.7.2 Preparing and loading cell sample onto AFM stage

Following 12-24 hours incubation, prepared AFM sample dishes were assessed for cellular attachment and confluence by brightfield microscopy. AFM samples that contained appropriate densities and required phenotypes of cells (subject to the aims of each experiment) were then mounted into the pre-heated BioCell stage (Figure 3-3) which maintains the cells and culture media at 37°C for the period of AFM experimentation. In order to maintain the viability of live cell samples for AFM experimentation, it is essential to control the *in vitro* environment of the live cells during AFM experimentation. To minimise the effect of cellular debris and viscosity of FBS, all cell culture media was removed from the AFM sample dishes, and replaced

with pre-warmed serum free sterile RMPI-160 culture media prior to commencing AFM experimentation.

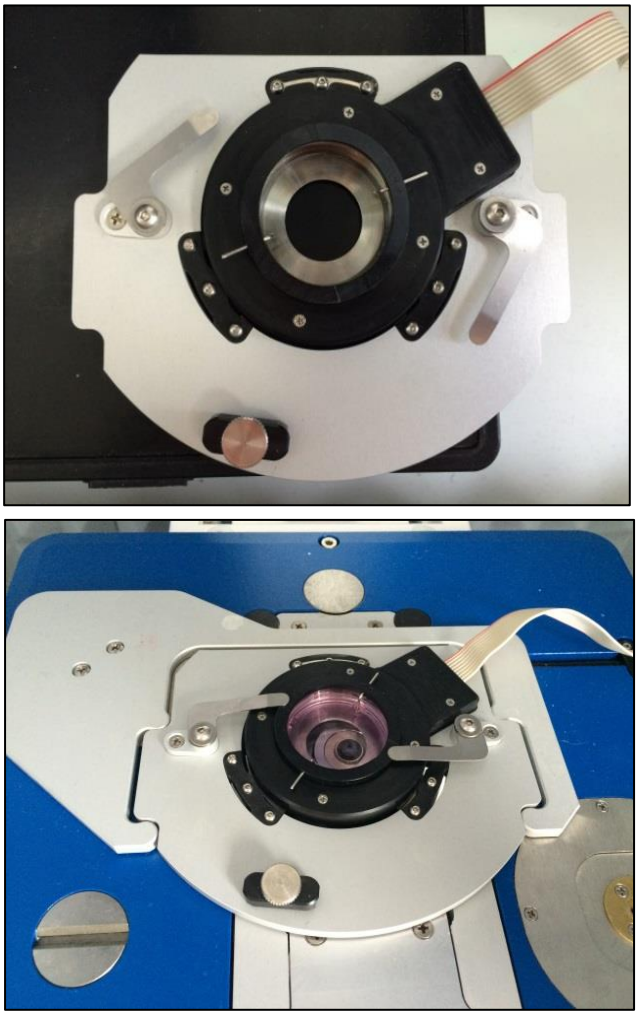

Figure 3-3. **AFM BioCell stage and chamber.** Unoccupied BioCell stage and chamber (top panel), and loaded with a prepared AFM cell culture sample (bottom panel).

3.7.3 AFM cantilever probes

When carrying out AFM indentation on live mammalian cells, selection of a suitable AFM cantilever probe geometry and material properties is essential. Cantilever properties such as; tip geometry, coating material and spring constant are all factors to consider when selecting the most appropriate probe for indenting soft, active mammalian cells. Cantilevers with soft spring constants are often selected for working

with live cells (typically around ~0.02 N/m), and are usually fabricated from silicon nitride (Si_3N_4) due it its material flexibility with a range of depth indentations. Selection of cantilevers with a reflective coating, such as gold, increases the sensitivity of the data acquisition for cantilever indentation by providing optimal reflection of the laser beam from the surface of the cantilever to the receiving photodiode. For AFM elasticity measurements, two different types of cantilevers were used in this thesis; **(1)** ORC8-10 silicon nitride Au/Bot pyramidal cantilevers with nominal spring constants 0.38 N m^{-1} and 0.05 N m^{-1} (Bruker, Germany), (Figure 3-4A) and **(2)** PNP-TR silicon nitride Cr/Au coated borosilicate glass 5µm diameter colloidal tipped cantilevers, with nominal spring constants 0.32 N m^{-1} and 0.08 N m^{-1} (sQUBE, USA) (Figure 3-4B). As previously noted, cantilever probe geometry is selected based on the selected sample undergoing AFM indentation. Cantilever geometries include conical shaped, spherical (colloidal), and/or pyramidal shaped. Spherical cantilever geometry was chosen due to previously published evidence of cell membrane tethering with the use of sharp conical/pyramidal shaped probes, with spherical shaped probes (2-10µm diameters) producing less penetrative, evenly distributed force indentation displacements [114], [123], [159]–[164].

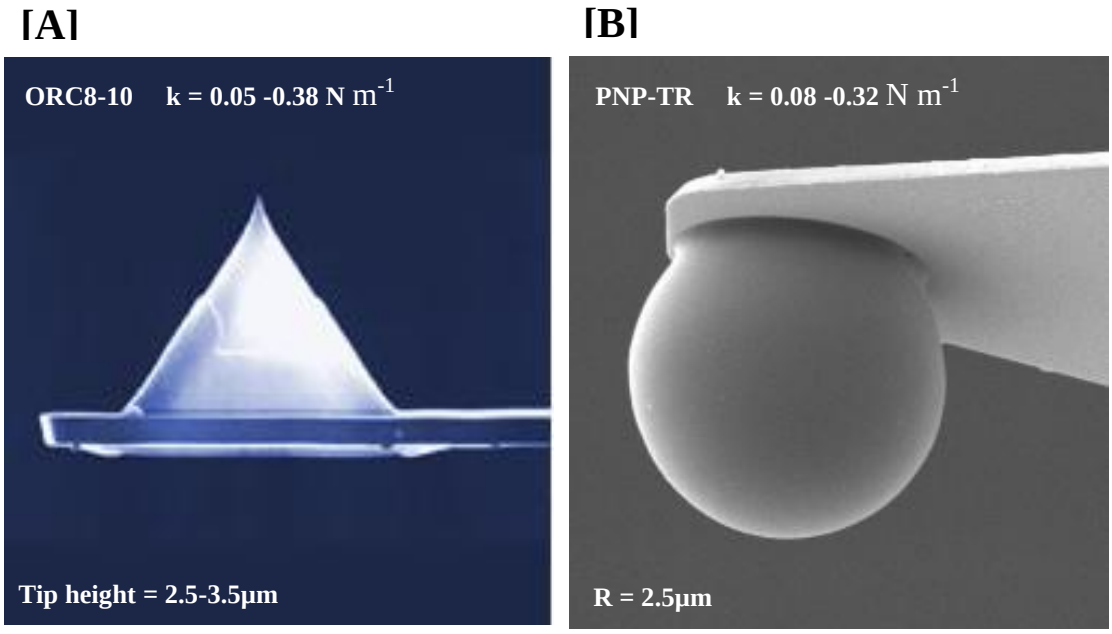

Figure 3-4. AFM cantilever geometry. [A] Micrograph image of pyramidal shaped cantilever (Bruker, Germany). Pyramidal cantilever porbe tip height has a length of 2.5-3.5µm**. [B]** Micrograph image of colloidal/spherical shaped cantilever probe (Sqube, USA). Colloidal cantilever probes have a sphere radius of (R = 2.5 µm).

3.7.4 Cantilever sensitivity and spring constant calibration

Once the appropriate cantilever was selected and mounted, cantilever probes were always pre-calibrated using the surface of a clean AFM culture dish. Cantilever calibration can be carried out with and without liquid media (in air). For the purposes of working with live cell samples for AFM indentation, cantilever probes were calibrated in a liquid environment. For AFM experiments, colloidal cantilevers were pre-calibrated in pre-warmed serum free RMPI-1640 cell culture media. Once the cantilever was mounted, prior to calibration, cantilevers were always left to pre-warm for ~1hour in the serum free culture media placed within the BioCell AFM heating stage. This was done to avoid any thermal fluctuations that may arise as the metal coating on the cantilever warms within the culture media. Such fluctuations can result in poor calibration and inaccurate AFM indentation outputs.

Once pre-warmed, the cantilever and AFM indentation software are then calibrated for force indentation. To begin calibration the laser beam is aligned along the back section of the cantilever probe (Figure 3-5A), the position of the laser bean is aligned according to cantilever geometry and manufacture instructions. The corresponding laser signal on the receiving laser photodiode is aligned to the centre of the cross hairs and the cantilever is manually positioned over a subjective selected region of interest on an empty AFM culture dish (Figure 3-5B). The default vertical deflection of the laser beam on the receiving photodiode is measured in units of Volts. During cantilever calibration, the sensitivity and spring constant of the vertical deflection of the cantilever is converted from units of Volts to nano-Newton (nN). This allowed for the application of an appropriate indentation loading force (nN) for all AFM force indentation and force mapping experiments. To calibrate the cantilever, a single force indentation is first acquired at ~1V on the clean AFM culture dish surface. This calibration curve is then used to calibrate cantilever sensitivity (Figure 3-6A). The cantilever spring constant is calibrated using the thermal noise determination method (Figure 3-6B). The thermal noise determination method determines the cantilever sensitivity by computing the free fluctuations at the end of the cantilever as a result of thermal vibrations [165]. The balance between the resulting free fluctuations and deflection of the cantilever upon indentation of the sample surface provides an accurate spring constant for the cantilever.

[A] **[B]**

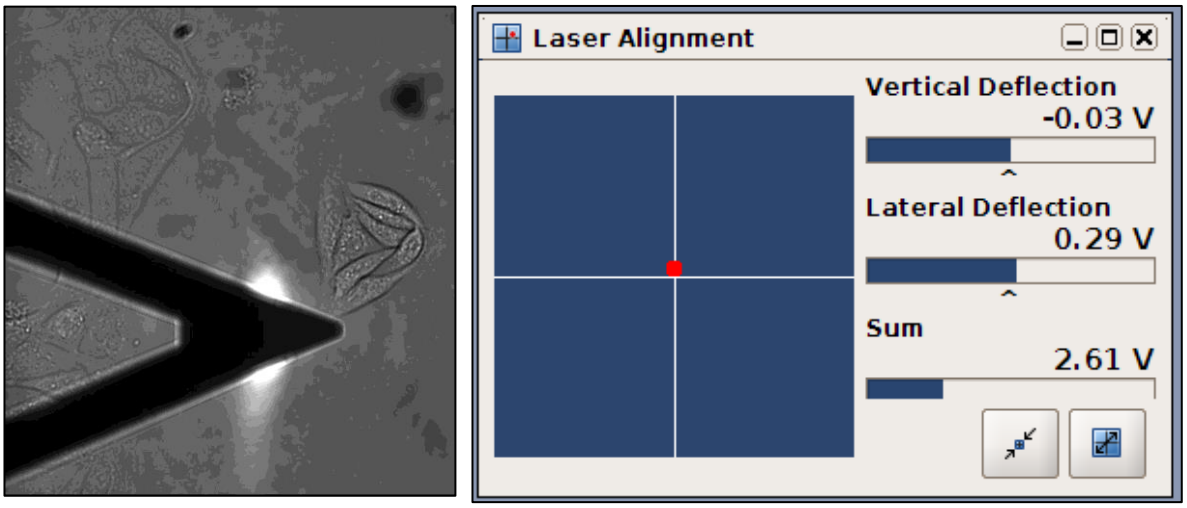

Figure 3-5. AFM laser alignment. [A] The AFM laser is aligned along the reflective back surface of the cantilever beam. **[B]** The laser signal is reflected back towards a receiving laser photodiode within the AFM. This is manually aligned prior to cantilever calibration to ensure a sum value above 1.0V to allow for an accurate calibration indentation.

[A]

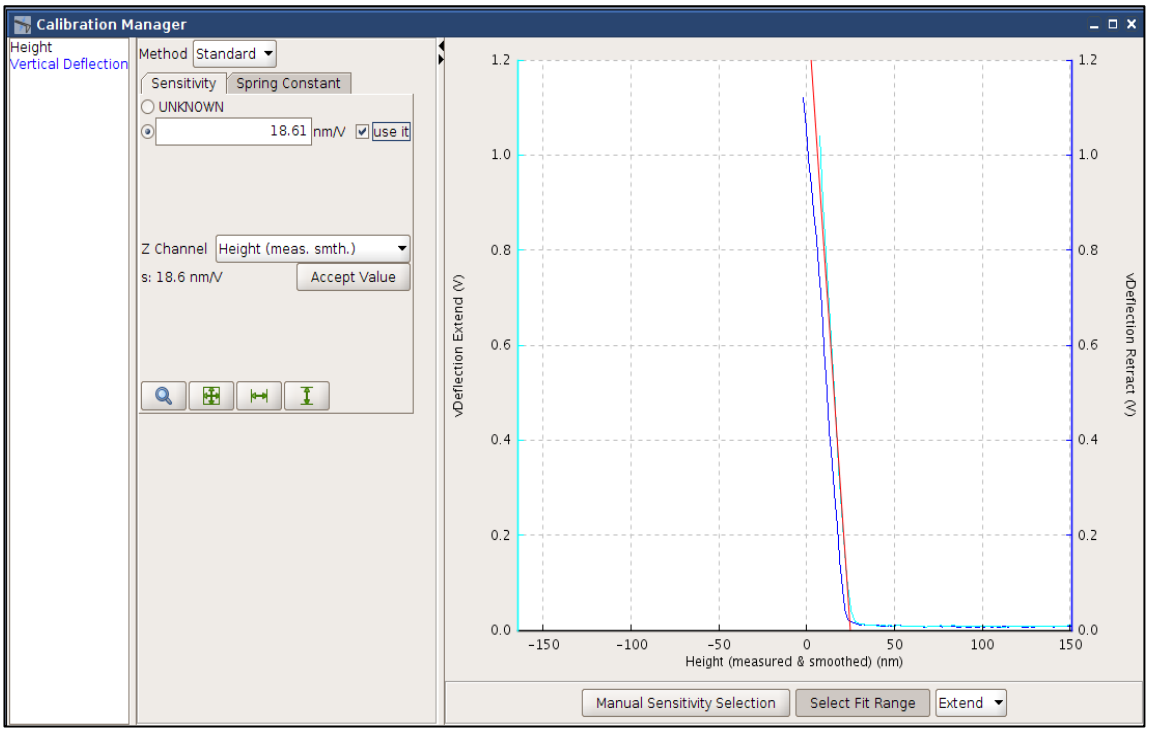

[B]

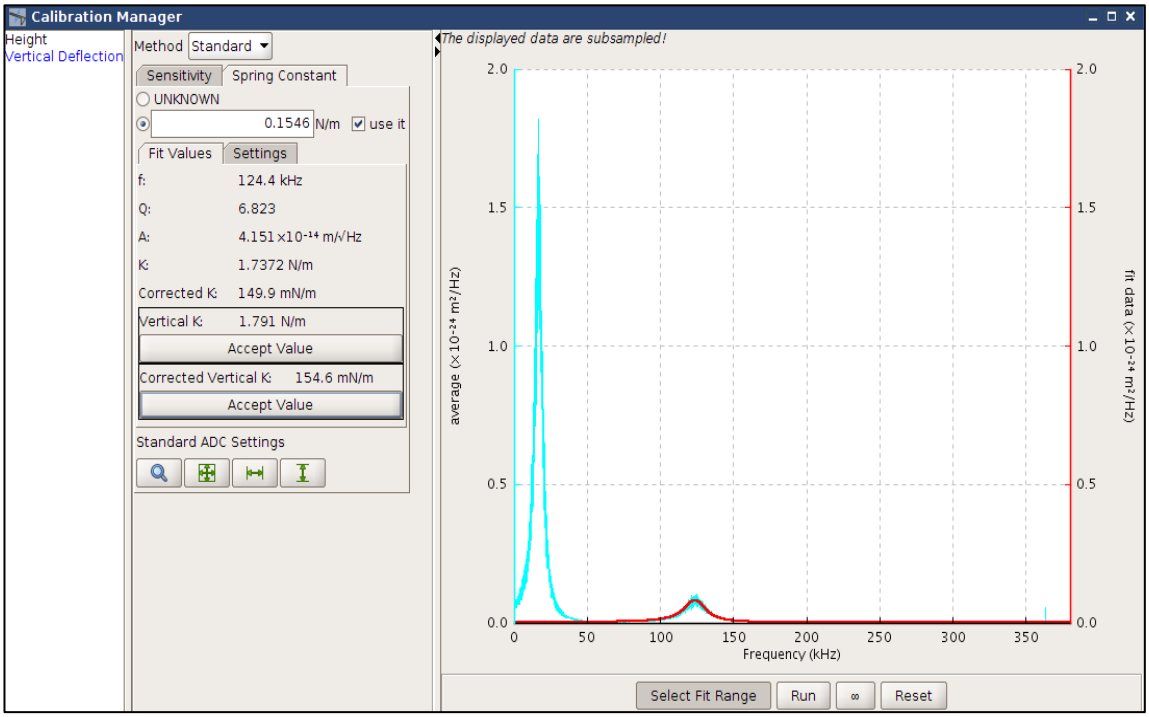

Figure 3-6. Cantilever calibration. [A] Cantilever sensitivity measurement to convert the unit of vertical deflection from Volts to nN. The approach curve (light blue line) is fitted (red line) to create a tangent and convert the sensitivity measurement**. [B]** The thermal noise detection method is used to determine the cantilever spring constant. During this method, one or more frequency spectrum peaks are obtained. The largest peak of the curves is most often fitted with the Lorentz curve. If the larger curve does not have a baseline on either side (as illustrated), the second largest curve is fitted. Following an accurate Lorentz curve fit, the cantilever spring constant can then be determined and the vertical deflection unit converted from V to nN.

3.7.5 AFM optical direct overlay

When carrying out both force spectroscopy and force mapping live cell indentation(s), positioning the cantilever accurately over a precise selected region is paramount when attempting to draw conclusions about the mechanical characteristics of biological samples. When manual cantilever positioning is carried out, using only the coarse movement knobs, the position of the cantilever over the sample is subjective and often inaccurate for the selected region of interest. Therefore, to accurately select and indent a specified sample region, optical overlay of the cell sample with the cantilever is carried out, thus resulting in more precise automated cantilever movement.

The first step in optical overlay calibration is to first create high contrast between the cantilever and surrounding AFM sample dish. To calibrate the optical overlay, an empty, clean AFM sample dish is always used. High contrast between the cantilever and surround, allows the AFM software to recognize the position of the cantilever, following which an image of the central region of cantilever position is acquired (Figure 3-7A). The image and data acquired during AFM optical calibration is independent from the AFM force spectroscopy calibrations. Once the cantilever position is calibrated, the AFM sample dish is replaced with a sample dish containing the live mammalian cells. A mammalian cell of interest is sourced and captured with the CCD camera. This image is imported into the operating force spectroscopy/force mapping scan region (Figure 3-7B). A desired region within the selected mammalian cell can then be selected by placing a scanning map over the region of interest (Figure 3-7C). The selected region of interest is then used to acquire single or force map indentations for the selected mammalian cell. Optical overlay accuracy was found to be accurate with all calibrations.

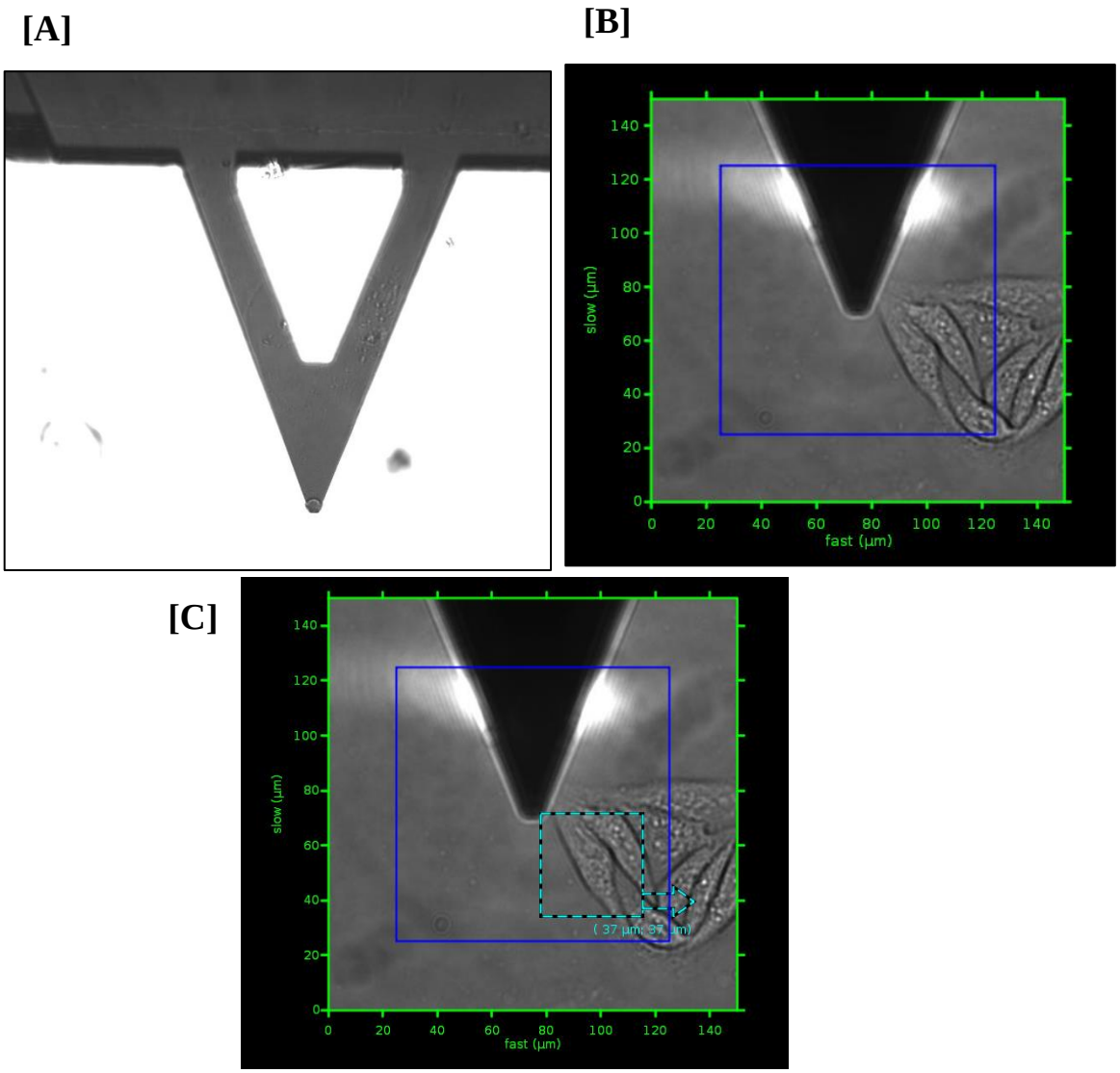

Figure 3-7. AFM direct optical overlay cantilever calibration. **[A]** High image contrast is created between the cantilever probe and underlying AFM sample dish. This allows the AFM software to locate and calibrate the central position of the cantilever probe over the maximal field of view. **[B]** The calibrated cantilever probe is then retracted and following the placement of a live cell sample, positioned over a selected live cell sample whereby the sample is within the AFM software scanning region. **[C]** A specified sample region within the scanning region can be selected, following which the cantilever probe is directed to scan/image and/or indent the selected region. Example images acquired for live MDCK cell cluster.

3.7.6 AFM Force spectroscopy mode – Single point indentation

As previously described, force spectroscopy (contact mode) on and AFM allows for the indentation of various selected single force indentation measurements on a specific sample. All selected indentation points are manually selected and there is no limit as to how many individual manually selected points can be designated for a given sample. The cantilever moves towards and deforms the underlying sample in the vertical plane, resulting a complete force-displacement curve with both extend and retract portions of the curve. The selected indentation points are listed and manual instruction allows the user to control which point to indent in what order (Figure 3-8).

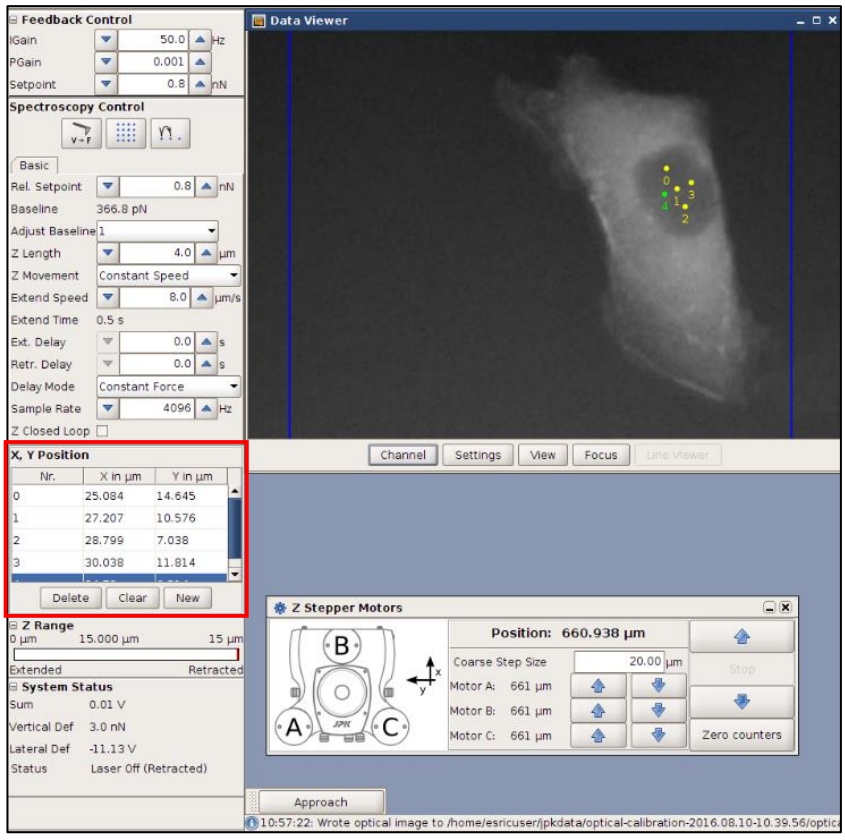

Figure 3-8. Single point force spectroscopy. Multiple points of interest are selected for a chosen cell region and listed (red box) by the AFM indentation feedback control panel (left). The current selected point for indentation is highlighted in green. The user manually selects which points and in what order to indent the selected region. Example image shown - live single MDCK cell with 4 selected indentation points for nuclear region (MDCK transfected to express GFP for Actin cytoskeletal protein).

3.7.7 AFM Force mapping mode

As previously described, AFM force mapping is an extension mode of the conventional force spectroscopy mode on an AFM. During force mapping, the cantilever performs several force-displacement indentations across selected points of an underlying sample. A defined force map region for a selected sample is used to acquire multiple force indentation measurements for a selected sample automatically. Force map sizes can be defined with a minimum of 8 × 8-pixel index and a maximum and 128 × 128-pixel indexes. For all force maps detailed in the following chapters, 8 × 8 force map indexes were used (Figure 3-9), thus producing a total of 64 force-displacement curves for each force map indentation of the selected cell line.

Force map indentation parameters were kept at a constant for each experiment, with indentation speeds and loading forces denoted in each chapter.

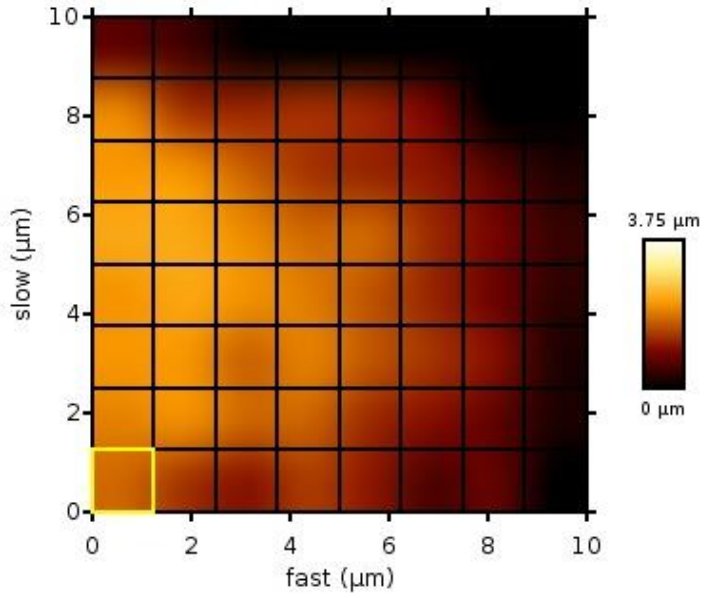

Figure 3-9. Example 8 × 8 force map index. Force map acquired over the central nuclear region of an MDCK cell sample. For all force map indexes, the cantilever probe performs a single force-displacement indentation at each pixel (yellow highlighted square) of the selected force map index. The force map also gathers information about the surface of the sample, such as the height following indentation and deformation of the selected region (as shown by the height channel - right channel). In this example, the representative height of the MDCK following force deformation across the MDCK cell has a maximal height estimate of 3.75µm.

3.8 Live cell imaging

As well as obtaining force curves to determine the Young's elastic modulus of live mammalian cell samples, additional cell samples were prepared for AFM and/or live cell fluorescent imaging. When probing the cellular length scale of tissues for mechanical properties, experimental output values are often directly attributed (but not limited) to the molecular activity and conformational changes of the inhomogeneous intracellular matrix, as well as the presence of intracellular organelles, such as the cell nucleus. Gathered cell images were used to investigative and correlate the surface topographies and/or presence of internal cellular structures to the force map images/elastic values for cells existing at alternate cell length scales. Cell surface topography, height offsets, location of internal cell nucleus, and expression of particular cellular structure components such as the ICM protein – actin - was assessed by cell imaging methods. Both live cell as well as fixed cell images were gathered. Cell imaging methods included AFM topographical imaging, AFM fluorescence imaging and 3D confocal fluorescence microscopy imaging.

3.8.1 Live cell fluorescent imaging – AFM

To precisely discriminate the nuclear and cytoplasmic intracellular regions of the selected cell line, the cells were transduced to express an actin protein bound conjugated green fluorescent protein (GFP) marker, using the BacMam 2.0 CellLight reagent system (Life Technologies) [166]. CellLight live cell fluorescent probes allowed for the concurrent measurement of live cell elastic moduli, with minimal toxicity or cell fixation for intercellular environment imagining and nuclear organelle localisation. Prepared live cell AFM samples were labelled with CellLight reagents at ~ 50 particles per cell (PPC). Prior to AFM indentation, mammalian cell samples were analysed using and EVOS Floid imaging station to assess GFP fluorescence (Figure 3-10). Following

confirmation of GFP fluorescence, cell samples were then mounted into the AFM. The Presence of GFP fluorescence was assessed under the AFM fluorescent filter (Figure 3-11). As previously stated, to improve intracellular regional localisation direct optical overlay for tip-to-optical calibration for the colloidal probe was carried out for each force indentation and cell imaging experiment. Previous evidence has demonstrated that live cell transfection with actin associated GFP tags do not have any significant effect on intracellular fibre assembly, cell mechanical function or outputs [76].

[A]

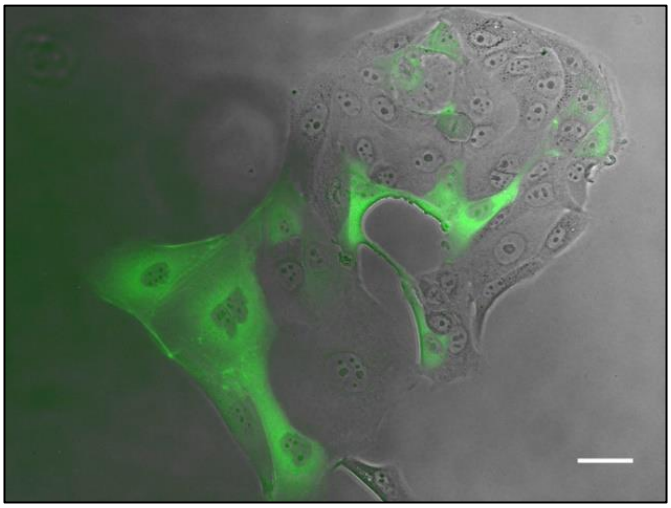

[B]

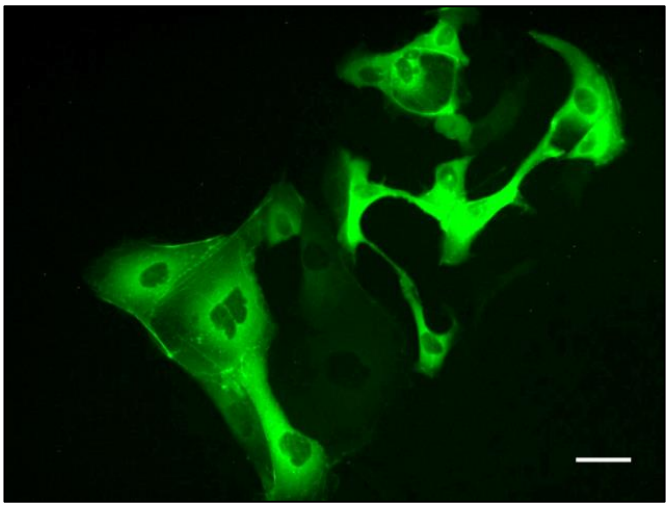

Figure 3- 10. EVOS FLoid fluorescent cell imaging. [A] Live MDCK cell (bright filed) EVOS Floid micrograph for GFP CellLight reagent at ~ 50 particles per cell (PPC). **[B]** GFP fluorescent (green light) EVOS FLoid micrograph image. Example MDCK cell micrographs demonstrating confirmation of transfected actin-conjugated GFP cell-permeant fluorescent labels (ThermoFisher)[Scale bars 20μm].

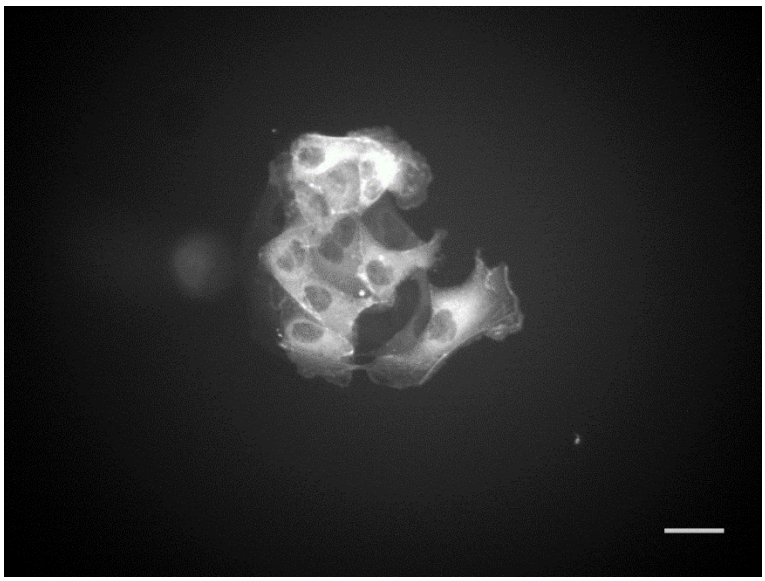

Figure 3-11. Example AFM optical overlay micrographs for actin GFP. CellLight reagent labelled live MDCK cell sample. MDCK nuclear regions were identified and selected as regions lacking any prominent actin GFP fluorescence marker signal. GFP actin labels allowed for the identification and localisation of MDCK cell edge, periphery, cell boundary and nuclear regions under the AFM microscope. Optical overlay images were acquired prior to all AFM indentation experiments for each cell sample [Scale bar 20μm].

3.8.2 Live cell fluorescent imaging – EVOS FLoid cell imaging

In Chapter 7 of this thesis, mammalian cell morpholgy variation with increase in cell developmental length was evaluated by 2D and 3D fluorescence microscopy. 2D MDCK morphology analyses was carried and compared with AFM and 3D morphology outputs. MDCK EVOS Floid micrograph images were analysed for 2D morphology variations at each length scale using ImageJ. For nuclear organelle and cell boundary morphology analysis, mammlain cells were bathed in Hoechst 33342 nucleic acid cell-permeant nulcear counterstain (ThermoFisher), followed by fixation in 4% paraformaldeyde, and incubation with an ActinGreen ^{TM} ReadyProbe Reagent (ThermoFisher). As previous (section 3.8.1), uptake of cell fluorescence for each cell length scale was confirmed via a sample image test using an EVOS FLoid microscope

imaging station. 2D cell morphology measurements included; Nuclear organelle area (μm^2), sphericity, and cell body/cytoplasmic area (μm^2). Actin/GFP channel intensity/expression was also analysed for variations across each cell developmental length scale using the integrated density (IntDen) measurement function within the ImageJ measurements toolbox. (IntDen) by definition is the sum of pixel intensity over a defined selected area in the image ROI manager toolbox. To correctly quantify GFP fluorescence for each MDCK cell analysed, (IntDen) outputs were corrected using the corrected total cell fluorescence (CTCF) calculation;

(IntDen) = sum of the intensity of pixels for one MDCK cell

(Background) = average signal per pixel for a selected region beside the MDCK cell

(CTCF) = corrected true intensity of signal for MDCK cell;

CTCF = (IntDen) – (Area of cell x Mean fluorescent background) (3-1)

The method of quantifying CTCF for biological samples has been previously cited [167]–[169]. Precise outcomes and chapter specific protocols to be detailed further in Chapter(s) 5, 7 and 8.

3.9 Fixed cell imaging

Fixed cell imaging was carried out for the selected cell lines for two purposes; (1) to acquire clear high-resolution AFM topographical images of selected cell samples and (2) assess the selected cell line for 3D morphological variations across a cell developmental length scale using 3D confocal microscopy.

3.9.1 Fixing of cell samples for fixed cell imaging

For experiments where the cell samples were required to be fixed for AFM and/or 3D confocal fluorescent imaging, cell samples were fixed prior to imaging and image analysis.

Equipment and reagents used to fix cell culture samples:

Equipment
Sterile 50ml universal tubes 5ml volumetric pipettes
Pipette gun
60mm AFM culture dishes
25mm glass cover slips (3D confocal microscopy)
75mm glass slides (3D confocal microscopy)
Reagents
4% Formaldehyde solution in PBS (fixative solution) (Fisher Scientific)
ProLong® Gold antifade reagent (mountant) (Life Technologies)

To fix the cell samples, all media was removed from the sample culture dishes. The samples were then washed in PBS, following which a 4% formaldehyde solution was added to the AFM culture dish and left to incubate at room temperate for ~15 minutes. Where AFM surface topography imaging was being carried out; following incubation, the fixative solution was removed from the culture dishes, and the fixed cell samples stored in PBS solution until used for AFM imaging. For 3D confocal imaging, the samples were labelled and fixed on 25mm glass coverslips. Following fixation, sample coverslips were then mounted onto 75mm glass slides using a ProLong® Gold antifade reagent.

3.9.2 Fixed cell imaging – AFM

Following the cell fixation process, prepared AFM cell samples dishes were mounted into the AFM Biocell stage. In all cases, cells were imaged in liquid (serum free RMPI), using PNP-TR silicon nitride Cr/Au coated borosilicate glass 5µm diameter colloidal tipped cantilevers, with a nominal spring constant of 0.32 N m^{-1} (sQUBE, USA) (section 3.7.3). In all cases, imaging parameters were adjusted to obtain accurate, non-tethering and clear surface images of the cells. Image parameters were taken with forces of up to 2nN and scan rates of up to 2Hz. AFM images for fixed cell samples were used to analyse cell surface topographical properties such as cell height and surface texture following AFM surface imaging.

3.9.3 Fixed cell imaging - 3D confocal microscopy

In Chapter 7 of this thesis, 3D mammlian cell morphology from single cell through monolayer development was evaluated by 3D confocal fluoresence microscopy. For 3D nuclear organelle and cell boundary/cytoplasm morphology analysis, mammlian cells were bathed in Hoechst 33342 nucleic acid cell-permeant nuclear counterstain (ThermoFisher), followed by fixation in 4% paraformaldeyde, and incubation with an ActinGreen ^{TM} ReadyProbe Reagent (ThermoFisher). 3D mammalian cell morphology measurements were aquired using a Leica SP8 scanning confocal 3D multicolour gated STED microscope. MDCK cell confocal images were aquired as XYZ stacks with step stack distances of 0.150µm between Z-stacks for two channels simultaneously. Aquired MDCK image stacks for each cell developmental length scale were automatically and simultanesouly deconvoluted using the Leica Hyvolution imaging tool utilised during MDCK stack acquisition. MDCK cell morphology was analysed and measurements aquired using the Imaris imaging analysis software. Following the generation of isosurface bodies for the nuclear organelle (Hoescht 33342) channel

using the Imaris Surpass toolbox, nuclear organelle surface area and sphercity values were obtained for nuclei across each mammalian developmental length scale.

To analyse and assess 3D morphological variations for the selected cell line, cell height, nuclear organelle z-diameter and cortical membrane thickness was analysed from the aquired 3D confocal stacks using the Imaris software XYZ stack section viewer toolbox. z-projections for each cell developmental length scale were analysed for morphology variations across each developmental length scale.

3.10 Data processing

Unless otherwise stated, all resulting force curve elasticity (elastic Young's modulus) values detailed were obtained by application of the Hertz-Sneddon contact model for the selected cantilever geometries (spherical and pyramidal). As previously stated, all force indentation parameters were kept uniform for each consecutive experiment as to allow for the correct application of the contact model. For all force indentation curves obtained, the JPK SPM data processing tool was used to analyse all acquired AFM data acquired in this thesis.

3.10.1 Force curve analysis

Following force indentation and acquisition of a single or multiple (force mapping) force-displacement curves, force-displacement curves were first analysed by manually interpreting and manipulating entire force curves using the JPK Data processing software. This involved removing sections of the force curves that go beyond the limit of a reliable Hertz-Sneddon contact model fit. To achieve this, the entire region of a force-displacement curve is selected, which results in the point of first contact/indentation between the probe tip and the sample being determined by the JPK

software. This then allows the user to select specific functions within the JPK software required to apply the Hertz-Sneddon contact model (function) to the force curve (Figure 3-12).

Prior to application of the specific functions, the approach (extend) portion of a force displacement curve is selected along the region where there is no force of deflection between the cantilever and the underlying sample – this is the approach baseline. The first function is then selected and applied. This is (1) the subtraction of the baseline, which automatically calculates the average value of the baseline and subtracts this from the whole force curve. This results in a zero-force approach baseline. Next is (2) removal of any offset or tilt at the baseline of indentation and subtraction of the cantilever bending from the approach piezo movement. (3) The third function used is determination of the contact point between the sample and cantilever. The contact point is calculated as the zero-force point of the x-axis vertical deflection curve. These functions yield a force-displacement curve that displays the channel 'tip-sample separation' or force versus displacement. The tip-sample separation function corrects the height for the cantilever bending signal during sample indentation. The correction for cantilever bending is calculated whereby the initial height signal is derived from the piezo movement during sample indentation. Following sample indentation/deformation, the cantilever deflects/bends in the opposite direction to the piezo z movement. Applying the correct functions to yield the tip-sample separation channel allows the user to analyse and plot the appropriate contact model to the correct indentation channel i.e. cantilever indentation/deflection rather than piezo height movement. Once all functions have been applied, the Hertz-Sneddon contact model function can then be applied to the processed force displacement curve. The JPK SPM data processing software allows for the application of the Hertz-Sneddon and DMT contact models

depending on the chosen geometry of the cantilever (Hertz-Sneddon) or application of AFM experiment (DMT for investigating cell adhesion).

For all cases where the JPK SPM processing software was used, the Hertz-Sneddon contact model for a spherical/colloidal and pyramidal cantilever probe was used is detailed below;

1) The Hertz-Sneddon contact model (JPK SPM software) for a spherical cantilever probe;

$$F = \frac{E}{1-\nu^2}\left[\frac{a^2+R^2}{2}\ln\frac{R+a}{R-a} - aR\right] \quad (3\text{-}2)$$

2) The Hertz-Sneddon contact model (JPK SPM software) for a pyramidal cantilever probe;

$$F = 0.7453\,\frac{E}{1-\nu^2}\,\delta^2\tan\alpha \quad (3\text{-}3)$$

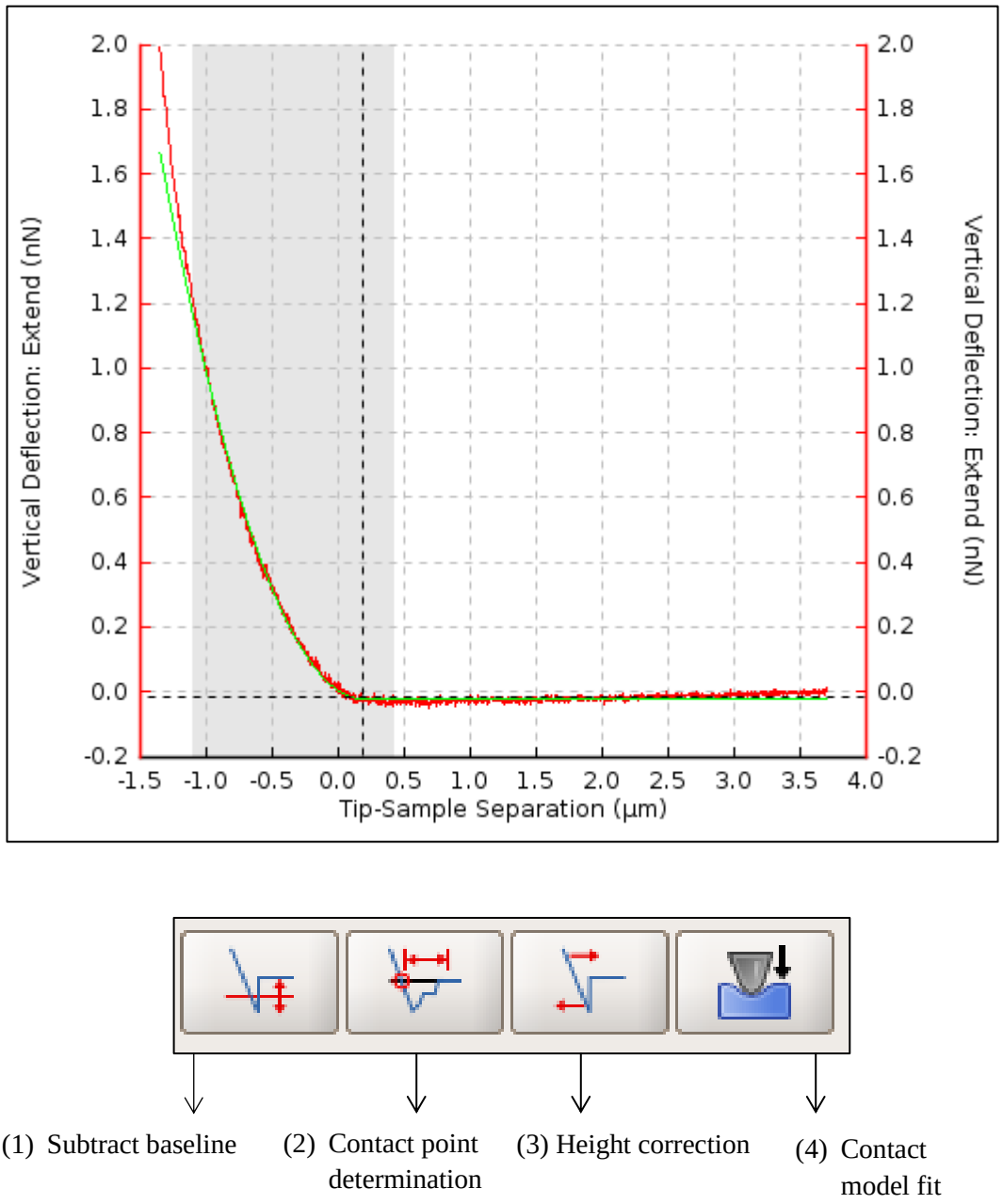

Figure 3-12. **AFM force-displacement curve analysis.** The SPM data processing toolbox for an acquired force-displacement curve (as displayed). The data processing functions are applied to the extend portion of the force-displacement curve (top panel, red curve). The functions applied to the curve (bottom panel) are, in order; (1) subtraction of the baseline, (2) contact point determination for the force curve, (3) correction of the height for the cantilever bending to calculate tip sample separation; and finally (4) executing the contact model fit (Hertz-Sneddon – green curve) to the extend curve and determine the resulting Young's elastic modulus for the sample indentation.

3.11 Statistical analysis of AFM and cell morphology data sets

To effectively analyse and compare mammalian cell AFM outputs as well as morphology measurements across each mammalian cell monolayer length scale, certain statistical tests were used. Variation within each data set (AFM and morphology measurements) was assessed using standard error of the mean (s.e.m) as well as standard deviation of the mean. The standard error of the mean was used to demonstrate the variation from the mean within the population(s) measured. If the s.e.m is large (relative to the mean), this indicates that the output values are spread across a large range. Conversely, if the s.e.m is small, this indicates that all values within the population lay close to the population mean. The s.e.m was calculated as follows;

$$SE_{\mu_\chi} = \frac{S}{\sqrt{n}} \qquad (3\text{-}4)$$

Where, $[\mu_\chi]$ denotes the sample mean, [S] the standard deviation of the mean and [n] the number of samples being assessed.

To assess the variance for normality (normal versus non-normal data distribution), the Shaprio-Wilk test was applied [170]. Following the establishment of data distribution, it was found that AFM [E] data outputs presented with primarily non-normal data distribution, however cell morphology outputs presented with both normal and non-normal data distributions. As a result, to effectively assess the significance in variation between mammalian cell Young's moduli [E] and morphology measurements across alternate cell and monolayer developmental length scales, the Mann-Whitney U test was used. The Mann-Whitney U test is non-parametric test that allows for two (or more) populations to be compared without making the assumption that the values within the populations are normally distributed [171]. The Mann-Whitney U test asserts the null

hypothesis that the medians of two samples are identical. Since the data outputs in Chapters 4, 5, 7 and 8 of this thesis comprised both normal and non-normal data distributions, the Mann-Whitney U test was selected. Each test was carried out at 0.01 significance and two-tailed comparison carried out for all data set comparisons.

CHAPTER 4

Application of current AFM protocols for mammalian cell Young's elastic moduli analysis: Adapting the experimental approach.

4.1 Introduction

When investigating how the mechanical properties of live mammalian cells, such as Young's elastic modulus, during the process of monolayer formation, great detail and attention are required when attempting to establish a reproducible protocol for analysing derived AFM Young's elastic moduli outputs. Notably, although there is a vast amount of AFM studies describing different aspects of cell mechanical analysis, difficulty arises when attempting to refer to and compare AFM experimental outcomes due to the lack of synergy among both the physical properties measured between each AFM assay, as well as differences in experimental approaches and protocols. The primary variation in AFM experimental parameters among mechanical measurement of mammalian cells largely revolves around variation in;

(1) The selected tissue or cell line investigated (immortal or primary)
(2) Cell sample preparation (fixed or live cell samples for AFM indentation)
(3) Cantilever geometry
(4) Selection of loading force (nN)
(5) Sample indentation depths
(6) Cell region of indentation (cell nuclear region or periphery cytoplasm)
(7) Measurement environment (air or liquid media)
(8) Contact model selection for cell elastic [E] output derivation

As a result, referral to previous AFM studies for experimental protocols and/or outcomes of AFM cell Young's elastic moduli analysis is often fairly complex. To effectively measure and compare cellular Young's moduli outputs, reproducible AFM data outputs are needed [100]. To put into a measurable context, evidence has shown that in measuring fluctuations in elasticity outputs for soft mammalian cell samples, among the aforementioned AFM assay parameters, three primary AFM testing parameters can greatly affect the comparison of Young's moduli elasticity outputs for measurements on similar soft polymer/biological samples; Firstly, live cell Young's elastic moduli outputs strongly fluctuate at shallow indentation depths approaching the point of contact with a cells surface. By increasing the indentation depth, cell [E] reaches a plateau, before once again increasing when the maximal depth results in affects felt from the underlying substrate stiffness [100]. As a result, shallow specified depths are often only analysed to avoid underlying substrate effects [164], [172]. Secondly, and often not absolutely considered, is the resulting final indentation depth achieved, which is greatly dependent on the selected cantilever loading force used. The selection of cantilever loading force is greatly varied among AFM studies on mammalian cell lines. Finally, variations in the selected contact model chosen for deriving sample Young's elastic moduli [E] outputs from AFM indentation curves can also result in considerably varied experimental outcomes among AFM cell elasticity studies. The contact model chosen is most often dependent on the selected indenting cantilever geometry [164], [173], [174]. Thus, AFM studies carrying out similar cell mechanical analysis objectives, can produce different outcomes by not having used similar cantilever geometries. Differences in the geometry of AFM cantilever probe selected i.e. spherical [110]–[112] versus pyramidal [113] and/or loading force i.e. 0.4nN [113], 0.2 -1.0nN [111] or 2.5nN [112], could result in the variation in AFM cell [E] trends derived for cells at alternate stages of cell development.

Therefore, the purpose of this chapter was to investigate and analyse selected AFM parameters and protocols on a chosen mammalian cell line. The overarching objective was to assess current AFM methodologies, and the applicability of certain AFM test parameters as an initial assessment of using AFM for the mammalian cell monolayer developmental stage analyses in this thesis.

This will allow for improved reproducibility of the results presented in each chapter, and was achieved by carrying out the following assays;

(1) Selection of an appropriate mammalian cell line.
(2) Selection and assessment of an appropriate cantilever probe on the mammalian cell line.
(3) Assessment and application of the JPK data analysis platform for AFM Young's moduli elasticity analysis, and application of the Hertz-Sneddon contact model at cell deformation depths within the limits of the Hertz-Sneddon contact model.
(4) Troubleshooting precise and repeated region of AFM indentation/deformation of nuclear region on the mammalian cell line to make data comparison accurate.
(5) AFM surface topography imaging of selected cell line at specified developmental stages. Stages of cell development selected are single cell; semi-confluent and maximal density monolayer cells.

4.2 Materials and methods

The specific materials and methods used to carry out all AFM experimental troubleshooting assays on the live cell line in this chapter are detailed as follows;

4.2.1 Cell culture

To test and analyse various AFM protocol parameters, the Madin-Darby canine kidney (MDCK) cell line was selected for all live cell AFM measurements. MDCK cells were cultured, maintained and prepared for AFM experimentation as described previously (Ch3. Section 3.4 – 3.6).

4.2.2 Cantilevers

For all MDCK cell AFM [E] analyses in this chapter, PNP-TR silicon nitride Cr/Au coated cantilevers were used. The cantilevers were borosilicate glass with a 5µm diameter, and a nominal spring constant of 0.08 Nm^{-1}. Cantilever probes were mounted and calibrated as described previously (Ch3. Section 3.7.3- 3.7.5). To compare and address the appropriate selection of a colloidal geometry cantilever probe for live MDCK cell measurements, silicon coated diving board QRC8-10 pyramidal tipped cantilever with a spring constant of 0.50 Nm^{-1} (Bruker, Germany), was used to carry out the cantilever geometry comparison assay.

4.2.3 AFM

For all live cell MDCK mechanical analysis tests, both single point as well as force mapping force spectroscopy mode were used as detailed (Ch3. Section 3.7.6 and 3.7.7). For fixed cell topography imaging, AFM imaging mode was used (Ch3. Section 3.9.2).

4.2.4 Fluorescent cell imaging - AFM

In order to assess intracellular regional selection under the AFM microscope, MDCK cells were transduced to express an actin protein bound conjugated green fluorescent protein (GFP) marker [166]. MDCK cells were transduced to express GFP as described previously (Ch3. Section 3.8.1), with confirmation of reagent uptake confirmed as described previously (Ch3. Section 3.8.2).

4.2.5 Data processing

Unless otherwise stated, all resulting force curve [E] (Young's elastic modulus) values detailed were obtained by fitting the Hertz-Sneddon contact model(s) for a colloidal probe (and pyramidal probe - where presented) (Ch3. Section 3.10). As previously stated, all force indentation parameters were kept uniform for each consecutive experiment as to allow for the correct application and reproducibility of the contact model. The Hertz-Sneddon contact model was applied to the approach (extend) portion for all acquired force-displacement curves, for both single point force spectroscopy and force mapping AFM data. Pre-processing JPK data processing functions (Ch3. Section 3.10.1) were used to process the raw curve files prior to application of the Hertz-Sneddon contact model.

4.3 Results

4.*3.1 Selection of a live mammalian cell line for AFM indentation*

The MDCK cell line was selected as the cell line for investigating and troubleshooting the selected AFM indentation parameters and experimental protocols. The clone type was kindly donated and is referenced previously [175]. The MDCK cell line is a model mammalian cell line utilised for a variety of biological *in- vitro* cell culture studies including cell-adhesion, motility, and polarity assays. The MDCK cell line is known to form well established viable monolayers when maintained under optimal culture conditions, and with controlled seeding densities, it is possible to culture the MDCK cells at alternate selected length scales. The MDCK cell line has also been shown to be well suited for three dimensional culture assays and multicellular rearrangements such as branching morphogenesis [176].

Under optimal culture conditions, the MDCK monolayer can spontaneously form three-dimensional dome structures (Figure 4-1). Furthermore, the MDCK cell line was selected due to the number of evidenced resources detailing the internal cytoskeletal characteristics of MDCK cells [177], [178], as well as Young's elastic modulus outputs of MDCK [110], [151], [179]. Referral to previous mechanical analysis assays on MDCK cells, allowed for a benchmark of cell culture and Young's elastic moduli characteristics from which to begin the AFM protocol establishment for live cell indentation at alternate cell monolayer length scales.

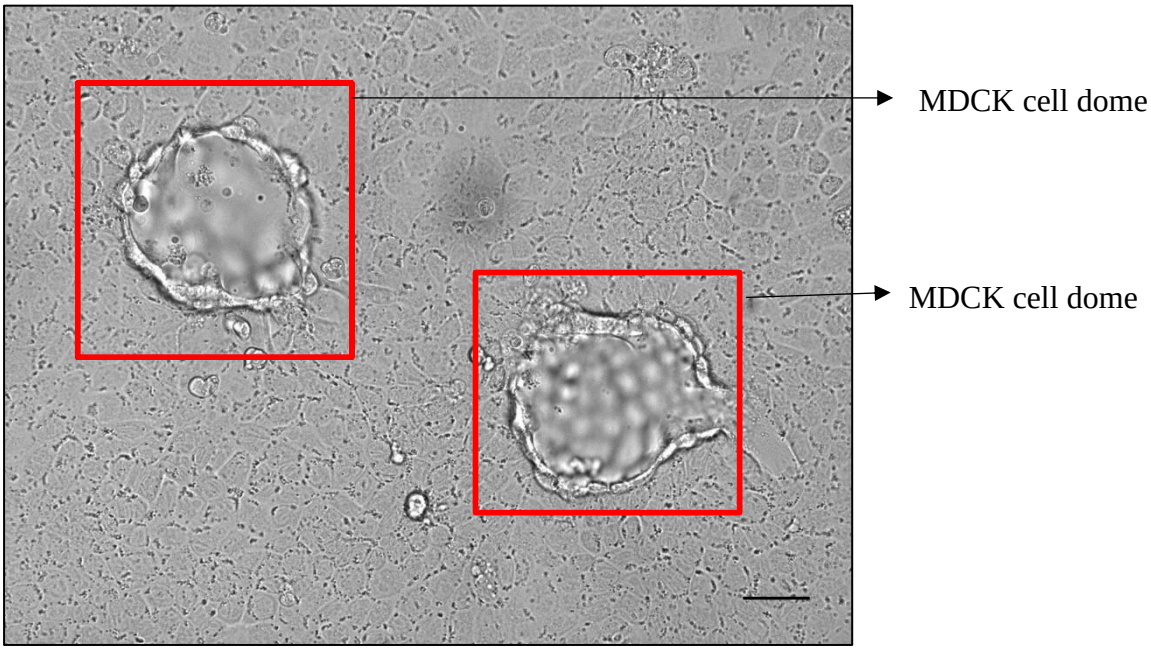

Figure 4-1. Floid EVOS micrograph image of MDCK cells. MDCK cells at maximal density monolayer length scale. Red boxes show MDCK dome formation within an established maximal density fully confluent MDCK monolayer [Scale bar 20µm].

4.3.2 AFM cantilever selection for live cell [E] measurement – comparison of probes

As previously discussed, the cantilever geometry selected for live MDCK cell AFM parameter tests were the PNP-TR silicon nitride, Cr/Au coated cantilevers that had a

borosilicate glass 5µm diameter spherical probes. Spherical geometry cantilevers were selected based on previous studies suggesting that spherical shaped cantilevers produce less membrane tethering and more evenly distributed force indentations/deformations compared to sharp conical/pyramidal shaped probes [159], [161], [163], [172]. Further to this, spherical cantilever geometries with large curve radii (around 5µm) have been shown to allow for improved application of the Hertz-Sneddon contact model whereby less effects of the underlying substrate are present for shallow indentation ranges [132].

To compare and assess cantilever geometry for live cell MDCK AFM Young's elastic moduli measurements, a cantilever probe geometry comparison was carried out to compare a spherical geometry cantilever with a pyramidal geometry cantilever. The cantilevers were calibrated in the exact same manner as described previously (Ch3. Section 3.7.4) and pre-warmed in liquid serum free media for the same amount of time (1 hour). Figure 4-2 illustrates the force indentation results produced by indenting a fully confluent monolayer MDCK cell, over the cell nuclear region, using the two different geometry cantilever probe geometries. Notably, for the cantilever comparison, a specified loading rate (8µm/s) and loading force (2.5nN) was used. The loading rate was selected as not to obtain any direct effects arising from hydrodynamic drag; The degree of hydrodynamic drag is often dependent on the inherent viscosity of the liquid media that the cells are indented in. It is suggested that loading rates over and above a recommended approach rate of ~10µm/s, can induce hydrodynamic drag of the cantilever and thus inhibit the approach and retract portions of the force-displacement curve from returning to the baseline 'zero' force point [180]. Furthermore, it is also recommended to keep cantilever loading velocities within optimal ranges as to reduce the effect of irreversible cell deformations. Therefore, lower loading rates below the 10µm/s threshold, but not significantly low should be more suitable when acquiring single force indentations as well as larger force map indexes for a given MDCK cell

region. As a result, a selected 8μm/s was used. As an initial test, a 2.5nN loading force was selected to compare the two cantilever probes.

Referring to Figure 4-2A, it is evident that the pyramidal shaped probe produced a greater amount of membrane tethering ,or double membrane effects and curve shoulder effects, whereby the cantilever pierces through the cell membrane at the selected loading force [123]. This is due to the increased localised penetrative force concentrated at the tip of the pyramidal shaped cantilever probe. This can be avoided with either larger spherical cantilever geometries, or if using sharper cantilever geometries, carefully selecting and lesser forces and/or careful AFM protocol approaches.

When using a spherical cantilever probe (Figure 4-2B), the force indentation curve produced far less membrane tethering and qualitative force curves at the selected indentation parameters. It should be noted that the composition of the cantilevers probes was also considered with regards to the pre-warming of the cantilever probes. Silicon nitride coated cantilevers tend to have comparatively lower force constants (spring constant) in comparison to gold coated cantilevers, which can make them far more suitable for soft biological samples such as mammalian cells. However, given that gold is chemically inert, gold coated cantilevers can produce far more stable reflectively of the laser beam to the AFM receiving photodiode. This can be seen as a more optimal outcome in liquid testing environments such as serum free cell culture media.

Using the JPK SPM data analysis software, and applying the same pre-processing functions to the acquired force curves, the Hertz-Sneddon contact model fit for the spherical cantilever, and the Hertz-Sneddon contact model fit for the pyramidal cantilever were applied to the associated acquired force-displacement curves. Based on the contact model fit, the resulting Young's elastic moduli [E] outputs for a single indentation on a live MDCK cell (confluent monolayer length scale) were 6.17 kPa for a

pyramidal probe and 2.15 kPa for the spherical probe (for a single indentation over the central cell body region of an MDCK cell). Resulting MDCK Young's moduli [E] values for pyramidal shaped cantilevers were in the region of AFM cell Young's elastic moduli [E] values for MDCK cell undergoing AFM indentation using conical shaped cantilever probes – 5.7 ± 0.1 kPa (monolayer MDCK cells) [151].

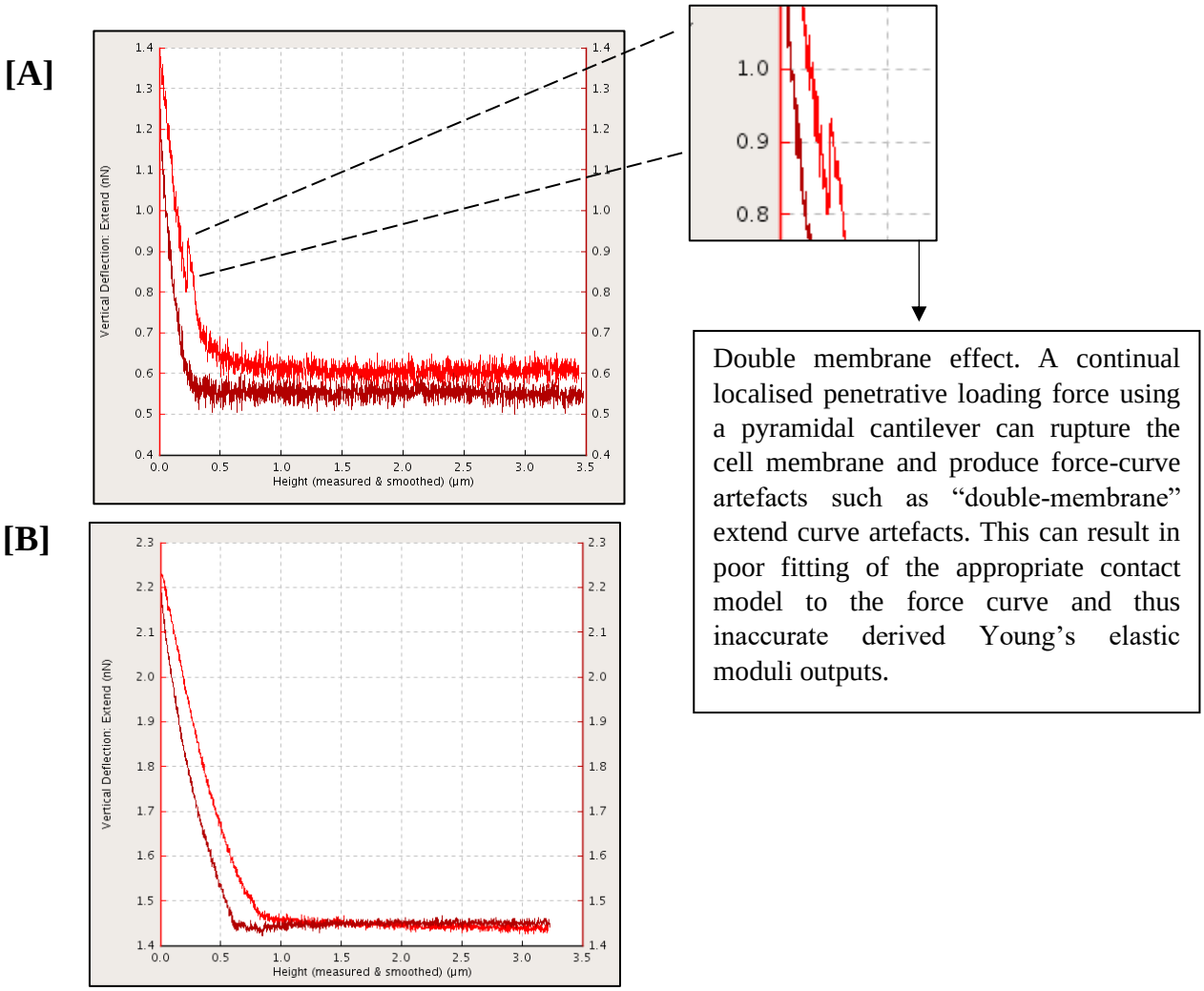

Figure 4-2. Cantilever geometry comparison. 3nN force indentation of an MDCK cell at the monolayer stage length scale using **[A]** pyramidal and **[B]** spherical shaped cantilevers. Under the same calibration conditions, the pyramidal cantilever exhibited extend curve artefacts such as double membrane effects, compared to the force-displacement curve of the spherical geometry cantilever probe.

4.3.3 JPK data processing software – Contact point determination and Hertz-Sneddon model fitting

Following application of the JPK pre-processing functions to a force indentation curve (Ch 3. Section 3.10.1), an attempt was made to assess how variation in the apparent automatic "contact point" section of the force curve i.e. the part of the curve where the JPK software assumes the cantilever probe has contacted the sample surface and begins sample indentation/deformation, is assigned. The contact point of the curve is where the deflection of the cantilever first begins to gain positive force or cantilever deflection along the y-axis and the gradient of the extend portion of the force-displacement curve begins to increase. The initial automatic contact point appointed by the JPK data processing software was not always accurate based on visual observation of the force-displacement curve approach portion and incline point. The JPK software does allow for manual control and the selection of contact point for the force-displacement curve. The main purpose of addressing how the contact point affects the derived Young's elastic moduli for live cell indentations (using the JPK processing software) was to assess the fitting of the Hertz-Sneddon contact model. An inaccurately appointed contact point can result in poor fitting of the Hertz-Sneddon contact model and thus inaccurate derived Young's elastic moduli for the sample indentation. The JPK software thus allows for the manual movement (through the DP toolbox) to appoint a more accurate contact point. This can be force controlled, whereby the user can assign the contact point as the region where $F > 0$, or the user can fit the Hertz-contact model to a different point (indentation/deformation or displacement controlled) of the force indentation curve to derive the Young's elastic modulus for a specified indentation depth range, within the limits of the Hertz elastic regime. In the example presented (Figure 4-3), by manually controlling and selected an appropriate contact point, the Hertz-Sneddon contact model is then accurately fit to the selected force-displacement curve. The fitting of the model

demonstrates that there is a limit as the application of the Hertz-Sneddon model past certain depths of sample deformation. In the example shown, the Hertz-Sneddon contact model accurately fits for the sample deformation to a limit of around 1µm deformation, past this point, the accuracy of the contact model fit it less valid. This would require the user to then manually select alternate regions of the curve to analyse and assess the fit of the contact model, and/or the elastic modulus output for higher sample deformations. In doing this however, the user would need to consider the total thickness of the sample, as well as address at what limit of deformation the underlying substrate will begin to affect the derive elastic modulus output.

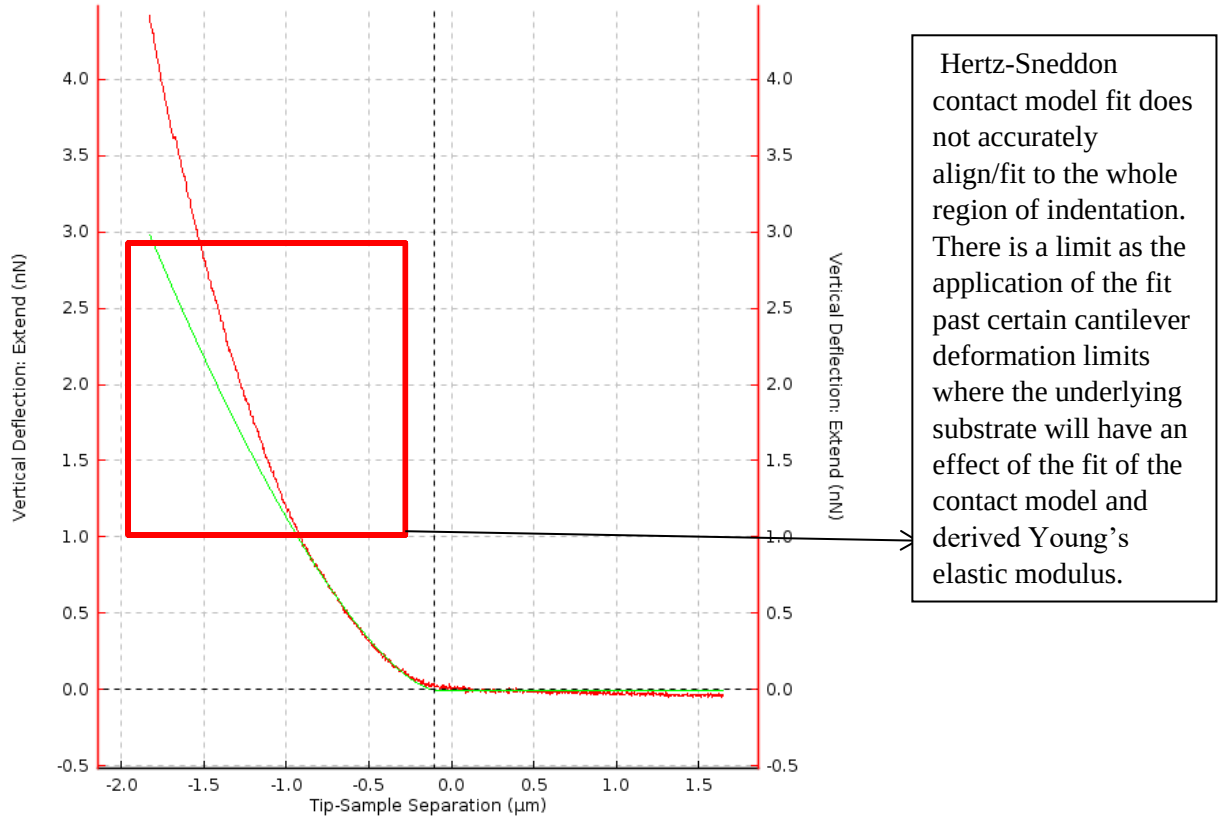

Figure 4-3. Force curve contact point determination and Hertz-Sneddon contact model fit. By appointing a specific contact point in the force-displacement curve, the Hertz-Sneddon contact model (green plot) can be accurately fit to the extend portion (red plot) of the force curve. In the example shown, the Hertz-Sneddon model fits to a limit of cell deformation at around 1µm).

As a result of the aforementioned matter with the JPK automated contact point selection, careful consideration and manual selection of the accurate contact point was carried out for all acquired AFM force-displacement indentations. This was carried out such that the contact model accurately fit the portion of each force-indentation curve that was required for data output analysis i.e. specific cell deformations depths. This was carried out for all AFM outputs in this thesis.

4.3.4 MDCK cell force map analysis – Cell region discrimination and application of the Hertz-Sneddon contact model

Since live mammalian cells are constantly undergoing a multitude of dynamic physical and developmental processes, being consistent in selecting an internal cell region for live cell AFM analysis that can be readily identified for AFM cantilever indentation, as well as be present in every cell undergoing cantilever indentation is paramount for accurate live cell Young's elastic moduli analysis. It is often the case that the majority of AFM indentation studies on mammalian cells refer to the cell body or nuclear region of a cell for cantilever indentation. The nuclear of a mammalian cell is assumed where the largest cell organelle – the nucleus – is situated. Since all mammalian cells have a nuclear organelle, the cell body region represents a global regional parameter by which to control the location of AFM indentation for multiple cell sample indentation assays. Due to the great deal of heterogeneity and variation in cell height along the cytoplasmic region of a mammalian cell, which can result in erroneous AFM force-curve data, selection of the central cell body region is also preferred for AFM indentation experiments. Furthermore, the cell body/nuclear region is also assumed the highest point of a cell due to the size and structure of the nuclear organelle. Further to this, and as previously discussed (Chapter 2, section 2.13), when deriving a mammalian cell force map, appropriate application of the Hertz-Sneddon contact model is paramount for

deriving true Young's elastic moduli properties from the chosen cell line. An appreciation for cell sample height (thickness) and the appropriate cell deformation/indentation limit for the Hertz-Sneddon contact model is required. To investigate the application of the Hertz-Sneddon contact model on the selected cell line, a MDCK force map (32 × 32 map index) (at the single cell stage) was acquired. The MDCK force map (height channel) (Figure 4-4A) was analysed alongside the Young' moduli stiffness map (Figure 4-4B). The height map for the force map index represents the height of the single MDCK cell sample following cantilever indention. The Young's moduli force map (sometimes referred to as the stiffness map) represents the values of each force map pixel within the force map index (height map) Young's moduli value. The Young's moduli are derived by application of the Hertz-Sneddon contact model function to each map index pixel (using the JPK force-curve analysis toolbox) (Chapter 3, section 3.10.1).

Referring to the height and Young's moduli maps presented (Figure 4), it is evident that the substrate surrounding the MDCK cell region influences the derived force map analysis (Young's moduli map) in such a way that it is not easy to discriminate any differences in the fitting of the contact model and derived Young's moduli within the different MDCK intracellular regions.

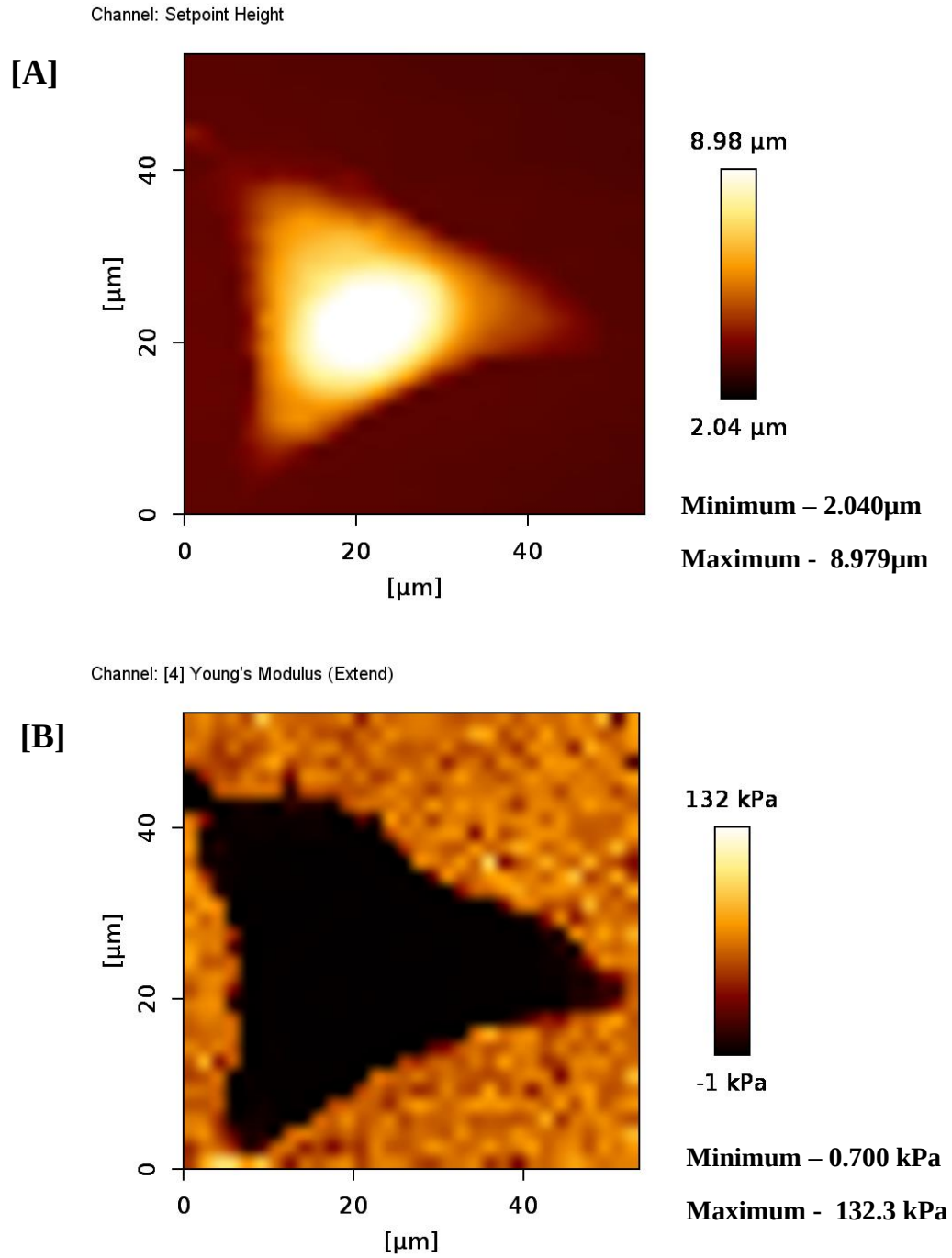

Figure 4-4. MDCK single cell force map [A] height channel and [B] Young's elastic modulus stiffness map. MDCK force-map analysis using the Hertz-Sneddon contact model results in a significant contribution (visually) of the surrounding substrate. With this initial analysis, little direct conclusion about the elastic material properties of the MDCK can be derived, not the appropriate fitting of the Hertz-Sneddon contact model.

In an attempt to better asess the Young's moduli trends of the internal regions of the MDCK cell - and avoid the effects of the substrate on the MDCK force map index, the Young's moduli stiffness map can be manually adjusted across different threshold limits (Figure 4-5). Map index Young's moduli range limits illustrated are 50 kPa, 10 kPa and 2 kPa. Notably, while this can allow for improved visualisation and interpretation of the elastic properties of internal regions of the MDCK cell, this method does not allow for direct data analysis i.e. precise range of Young's moduli values within each cell MDCK region, nor does it correlate the height and thickness of the cell region to the derived Young's moduli outputs. Therefore, a map of values is presented, but whether or not these values represent realistic Young's moduli values at each cell region, is not clear. The surface and thickness of the MDCK can affect the true value of the Young's elastic modulus values derived as a result of the underlying substrate. As a result, more precise analysis needs to be carried out.

This can be achieved (still using a rudimentary approach) but selecting specific regions of the height map (cell body/nuclear region) – the highest region of the height map, and then selecting the same region on the Young's moduli stiffness map. By carrying out the following steps (Figure 4-6AB), histogram plots can be obtained for the selected height and Young' moduli regions (Figure 4-6C and D respectively). The results demonstrated that a range of values can be derived for the selected internal cell regions. This analysis derived average MDCK cell body height (following cantilever indentation) of 8.780 kPa, and Young's moduli average of 316.5 kPa. This can begin to give a more in-depth analysis of the MDCK cell across selected cell body internal regions. However, this does not allow for proper consideration of the application of the Hertz-Sneddon contact model and the assumptions made about the limits of sample thickness.

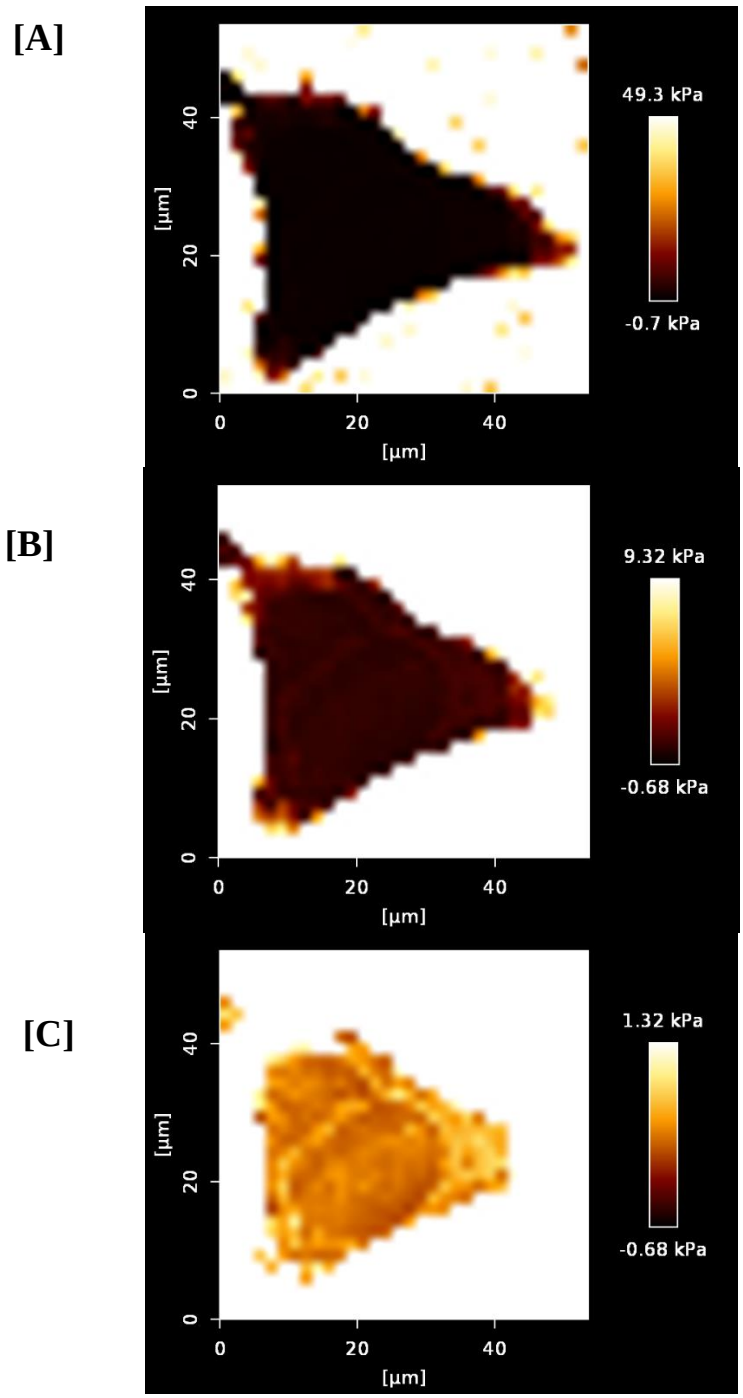

Figure 4-5. MDCK Young's moduli stiffness maps manually adjusted across different threshold limits to visualise the internal elastic property trends of the MDCK cells. Map index Young's moduli range limits illustrated are **[A]** 50 kPa, **[B]** 10 kPa and **[C]**2 kPa.

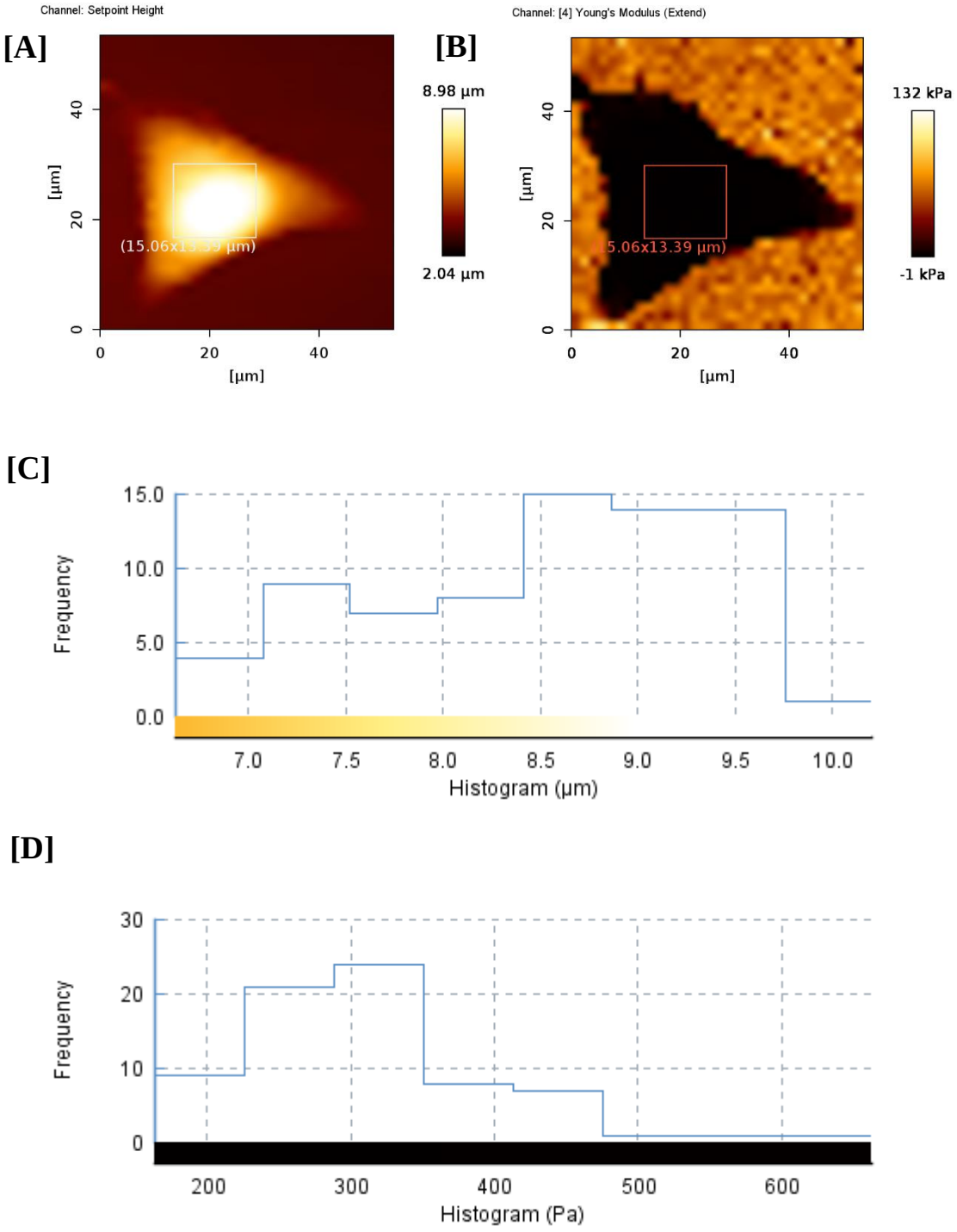

Figure 4-6. MDCK single cell force map region selected. [A] height channel and **[B]** Young's elastic modulus stiffness maps with associated histogram plots for selected box regions **[C]** height trends for selected region and **[D]** Young's elastic modulus trends for selected box region.

The aforementioned method of selected specific regions of the MDCK height and Young's moduli stiffness maps can provide useful information about the range of elastic properties and heights of the cell sample, to be more precise when analysing MDCK force indentation and force maps, a more in-depth approach is still required. The specific range of cell height in relation to which regions can be appropriately fit to the Hertz-Sneddon contact model is required. To achieve this analysis, the follow steps were taken; By analysing the metadata of the force maps, force map indexes for the surrounding cell substrate correlated to a cantilever height of ~ 2.040µm – 3.050µm. The derived Young's moduli values for data points in this range was 55,972.6 ± 19,217.83 kPa. This region can therefore in essence be set to a zero-height channel value as the 0µm region (substrate region). Following the metadata values to reach a values that produced drastically lower Young's moduli values in comparison to the neighbouring metadata for the force map index pixels, demonstrated that cantilever set-point height values of ~3.076µm upwards, demonstrated significant reductions in Young's elastic moduli outputs within the range of soft biological samples < 10 kPa (the metadata range was compared to force-indentation curve images to ensure full qualitative curves were being analysed for the metadata values obtained – no irregular curve artefacts were observed). Scatter plots depicting the height values and corresponding Young's elastic moduli values for the MDCK force map - for the whole scan range (Figure 4-7) and above the 3.076µm height threshold (Figure 4-8) , allowed for a better representation of the range of values obtained from the MDCK cell force map. Reducing the range of force map height analysis to a threshold above the apparent substrate region allows for the analysis of apparently MDCK cell-only indentation points.

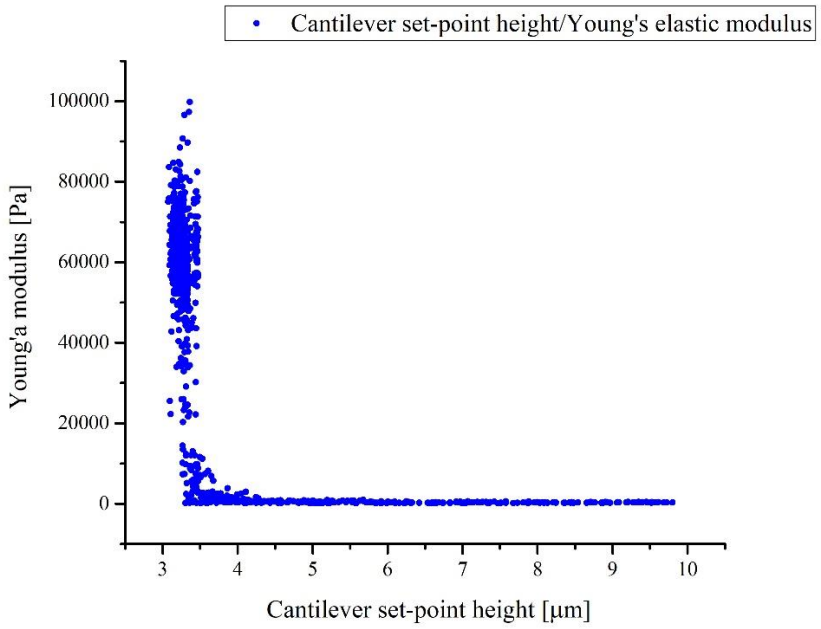

Figure 4-7. Scatter plot for cantilever height to Young's elastic moduli values for MDCK single cell force map region (data points for whole map) (n= 1024).

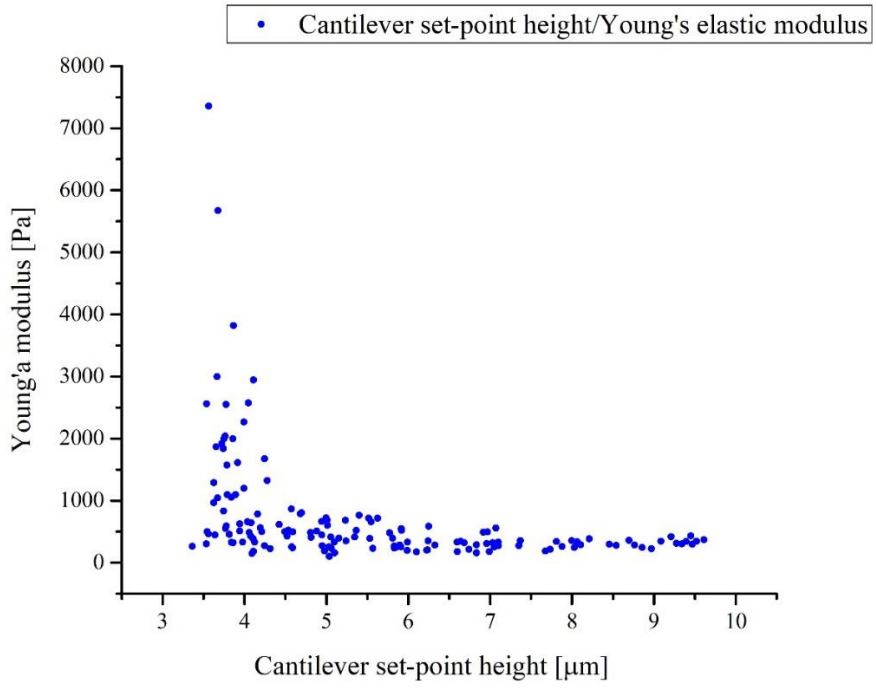

Figure 4-8. Scatter plot for cantilever height to Young's elastic moduli values for MDCK single cell force map region. Data points above 3.076µm cantilever height threshold (n = 149).

However, referring to the data analysed and presented in Figures 4-7 and 4-8, a problem is still posed when deriving any conclusions about the values obtained for the apparent cell only MDCK cell region. This the application on the Hertz-Sneddon contact model to thinner cell edge regions. Along the cell boundary edge, and indeed along cell body and cytoplasmic regions, the thickness of the cell does not fit within the limits for application of the Hertz-Sneddon contact model. It is likely that the range presented (Figure 4-8) of Young's elastic moduli values for the MDCK cell is still greatly subjective towards the material properties of the underlying substrate. As discussed in the introduction of this thesis. The hertz-Sneddon contact model has a limit to which the Young's elastic modulus can be derived from a sample; this is around a maximum limit of 10% of sample thickness.

To address the most accurate region for deriving more true cell elastic properties, the height of the MDCK cell was analysed using a height offset cross-section from the MDCK height map channel (Figure 4-9). The height cross-section offset demonstrated that the single MDCK has a maximal height along the cell body region of 9.8µm. In the height offset, the minimum z-range of 2.04µm is assigned as the base of the cell on the underlying substrate (relative value illustrated as 0µm in the height map). Therefore, the apparent maximal height of the MDCK cell following cantilever indentation is approximately ~ 7.76µm.

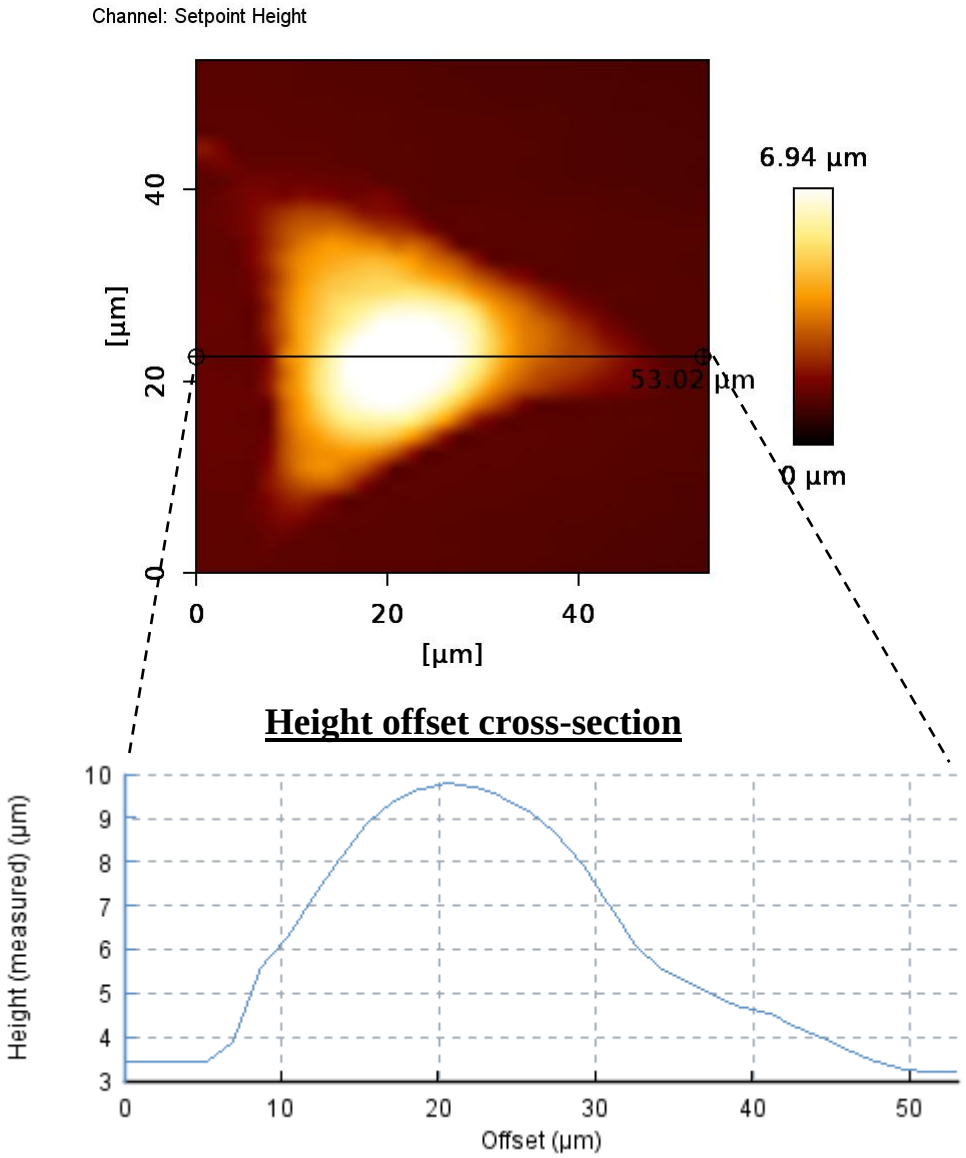

Figure 4-9. MDCK cell height offset cross-section for force map setpoint height channel. MDCK single height was found to approximately 6.94um (relative value for height map image where a zero value is substituted for the underlying substrate. Absolute values found the apparent height of the MDCK following cantilever indentation at approximately 7.76µm.

Based on the height offset cross section for the MDCK height map, a thickness of the MDCK cell can be approximated – this can then be utilised for the most appropriate and accurate region of the cell to derive true Young's moduli values using the Hertz-Sneddon contact model. It also demonstrates how the height of the MDCK cell along the cytoplasmic regions can vary considerably across the cell, surface gradients down from the cell body nuclear region could affect proper contact with the cantilever at certain uneven cell surface topographies could also result in poor analysis and application of the Hertz-Sneddon model. Based on the MDCK force map height offset, a 10% maximal limit thickness for fitting the Hertz-Sneddon contact model would be 10% of 7.76µm (approximately). This would mean fitting the Hertz-Sneddon contact model to indentation points within the cell body/nuclear organelle region to a maximum of a 776nm indentation depth. These values are relative as to the consideration that the substrate in the data is set at 0µm. In the force map raw data, this equates to fitting the Hertz-Sneddon contact model to cantilever height offset values of 9.085µm upwards. These values fall within the 10% sample thickness limit (fitting to a maximum of 776µm) for the accurate fitting of the Hertz-Sneddon contact model and deriving the apparent Young's elastic modulus of the MDCK cell at those indentation points.

Analysis of the values in this region (Figure 4-10) demonstrated a variable Young's moduli output trend. Young's elastic moduli values for the single MDCK cell body nuclear region was found to be 330.89 ± 64.07 Pa. Interestingly, the cantilever height at indentation was also found to be variable across the nuclear region at 9.28 ± 0.23µm.

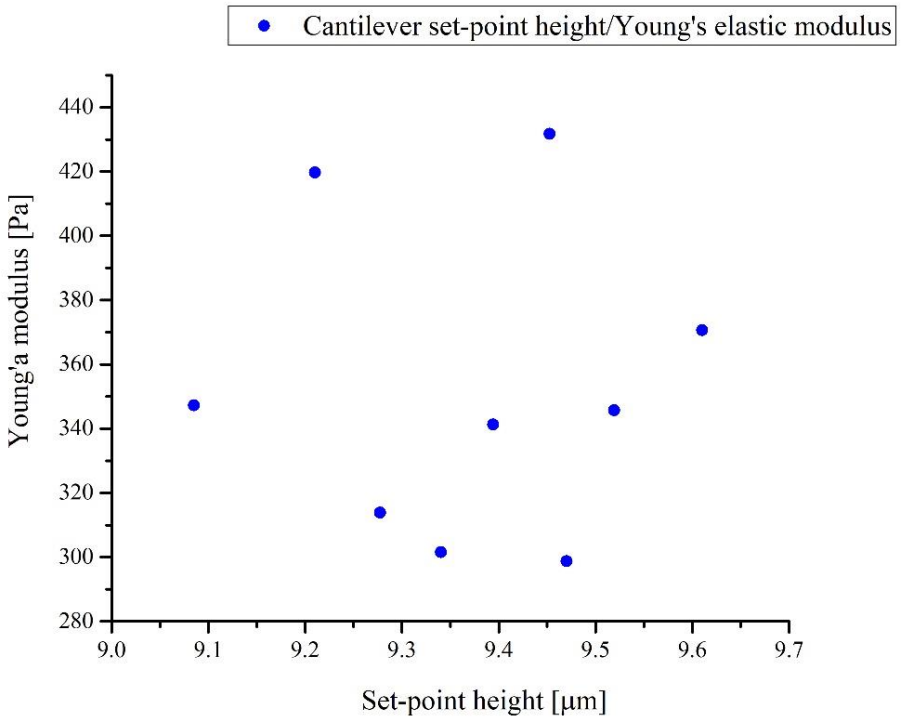

Figure 4-10. Scatter plot for cantilever height to Young's elastic moduli values for MDCK single cell force map region. Data points above 9.085µm cantilever height threshold (n = 9).

Referring to figure 4-10, it is evident that even at more appropriate indentation depths for Hertz-Sneddon derivation of the Young's elastic modulus, the nuclear region a single MDCK cell presents with an interesting trend for surface mechanical properties. Using this approach of assessing MDCK cell height (thickness) and appropriate region of analysis (cell body nuclear region) for deriving the Young's elastic modulus trends of the MDCK cells is this thesis was carried out. For all subsequent MDCK AFM analysis, the nuclear region of the cells was identified using GFP fluorescence and AFM calibration set-up and optical overlay. The JPK AFM at the ESRIC facility has a single microscope filter fitted for the addition of cell fluorescent imaging under the AFM DIC microscope. This filter allowed for the addition of GFP fluorescent imaging. Therefore, prior to AFM indentation, the MDCK cell samples were transfected to express GFP for

the actin protein network (as described previously (Ch.3, Section 3.8.1). GFP was selected for the actin protein network as it clearly highlighted the region of the cell were the cell nuclear organelle is located (as illustrated Ch3. Section 3.8.1), and being a major cytoskeletal network protein, also allowed for cell boundary discrimination in higher cell length scale densities such as confluent MDCK cell monolayers.

4.3.5 MDCK fixed AFM imaging – Surface topography and fixed cell imaging at alternate developmental cell stages

Having selected an appropriate cantilever geometry for live MDCK cell AFM indentation Young's elastic moduli measurements, the selected spherical cantilever was assessed for the quality of AFM imaging on the selected MDCK cells at varying stages of cell monolayer development. It is suggested that spherical shaped cantilevers are not the most appropriate probe type for fixed mammalian cell topographical AFM imaging due their larger tip surface area. It is often recommended that conical or pyramidal cantilevers with higher spring constants be selected for fixed cell AFM imaging. Therefore, to address the suitability of the selected cantilever probe for fixed cell AFM imaging, MDCK cells were fixed - as described previously (Ch3. Section 3.9.2), and imaged using the AFM imaging mode (contact mode). The MDCK cells were fixed and imaged at selected stages of MDCK monolayer length scales; single cells, semi-confluent cluster and confluent cell monolayer. For fixed MDCK cell AFM imaging, the imaging parameters were kept uniform for each image acquisition with loading rate and set-point force manually adjusted for each cell sample as to improve the resolution and image quality of each fixed cell sample. Image loading rates were set at $8\mu m/s^{-1}$, and set-point force up to 3nN. Figures 4-11 and 4-12 illustrate the MDCK fixed cell images acquired using the AFM contact imaging mode and a spherical geometry cantilever.

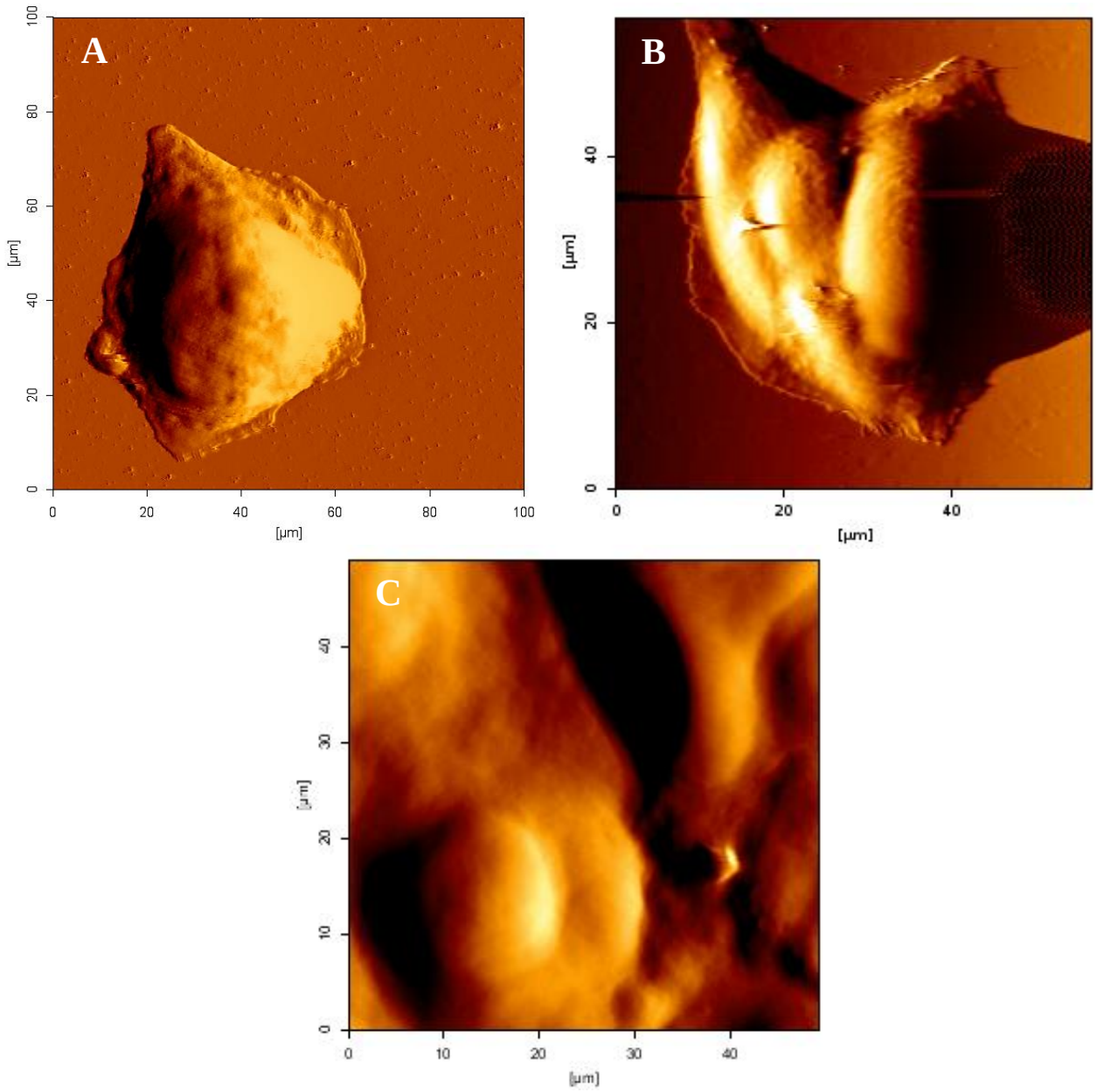

Figure 4-11. Fixed MDCK cell AFM imaging using spherical cantilever probes (in contact mode). At a nominal selected imaging force of 3nN for fixed MDCK cells, colloidal cantilever probe AFM images on a **[A]** single **[B]** semi-confluent cluster **[C]** and monolayer MDCK cells produced clear non-tethering AFM images. Fixed MDCK cell images were analysed and are presented in the error signal channel (this is the vertical deflection of the cantilever in contact mode). This can be used to create three-dimensional depiction of the cell surface for each fixed cell imaging.

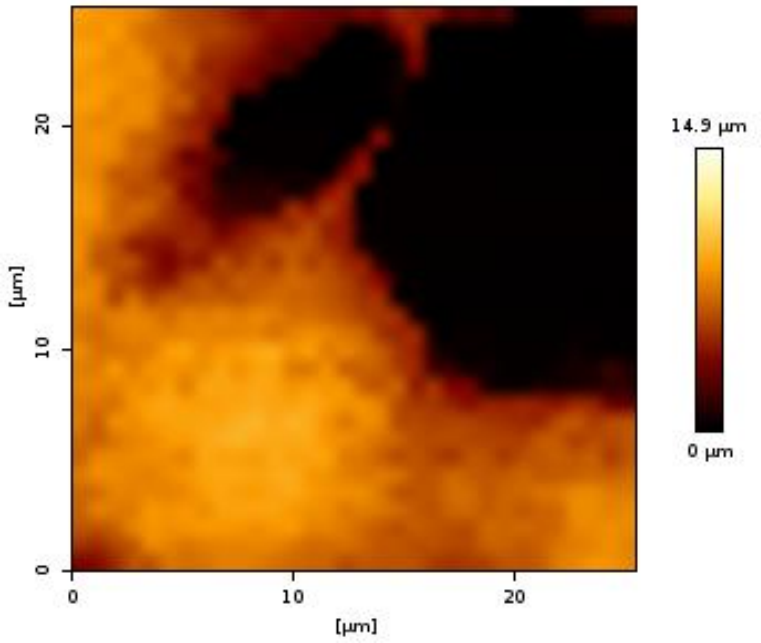

Figure 4-12. Fixed MDCK cell AFM imaging using the spherical cantilever. At a nominal selected imaging force of 3nN for fixed MDCK cells (edge of fixed MDCK cell semi-confluent monolayer), spherical cantilever AFM images produced clear non-tethering AFM images. Fixed MDCK cell images were analysed and are presented in the height signal channel. This channel demonstrates the height of the MDCK cell following indentation – height channel is set at relative values (which assigns the base of the substrate at 0µm).

Therefore, based on the results presented for fixed cell AFM imaging, the spherical cantilever can in fact (at the correct image scanning parameters) be used for MDCK cell imaging. Having selected a single cantilever loading velocity (8µm/s^{-1}), changing the selected loading velocity could influence the time scale for image acquisition. This is more appropriate when working with live MDCK cells that are more susceptible to culture environment changes over long periods. However, too great of a velocity (< 10um/s^{-1}) could greatly affect the mechanical response of the surface of the cell, even using a less penetrating spherical probe.

4.4 Conclusion and summary of findings

The primary goal of the analyses carried out in this chapter, was to investigate how current AFM protocol parameters such as cantilever geometry, region of cell indentation, application of the Hertz-Sneddon contact model to appropriate regions of the MDCK cell and loading forces can be applied to a specified selected mammalian cell line. As previously noted, attempting to define a set of reproducible and reliable AFM parameters and data analysis models is paramount when attempting to make objective conclusions about the data outputs derived following live mammalian cell indentation. The results presented for the mechanical response and AFM approach of MDCK cell indentation using a spherical cantilever, demonstrated the most suitable approach for the preliminary investigation of MDCK cell Young's elastic moduli outputs. The accurate selection, indentation depth and assessment of MDCK central nuclear region can be manually controlled. Evaluating the thickness of the MDCK cells using cross-section height offsets can be used to selected data points within the cell sample thickness threshold limit for application of the Hertz-Sneddon contact model. Surface topography is approachable using AFM imaging, and the spherical geometry cantilever preferably utilised.

The key AFM experimental protocol parameters defined following each troubleshooting assay in this chapter are;

4.4.1 Selection of an appropriate AFM cantilever geometry

Based on the results presented in section 4.3.2, localised pyramidal geometry cantilevers are less suitable for live MDCK cell AFM indentation. This was the case for the selected MDCK cell line. Spherical cantilever geometry produced more qualitative force-curves with less double membrane effects. Utilising spherical shaped cantilevers appears more suitable for the live cell AFM indentation analysis for the MDCK cell line selected. Ensuring both qualitive and quantitate data acquisition and cell Young's elastic moduli elasticity outputs for cell monolayer analysis is paramount when investigating cell development and monolayer proliferation.

4.4.2 MDCK cell force map analysis – Cell region discrimination and application of the Hertz-Sneddon contact model

An accurate method for precisely selecting the cell body/nuclear organelle region of the MDCK cells was defined using live cell fluorescence microscopy with AFM indentation analysis. Based on the force map analysis presented (height and corresponding Young's elastic moduli stiffness map), the apparent nuclear region (based on height of the cell) was analysed for data points corresponding to the limit of sample thickness for application of the Hertz-Sneddon contact model.

4.4.3 Application of an appropriate reproducible method of AFM elastic modulus output analysis

For live MDCK AFM force-displacement curves, the JPK software was utilised for all force curve pre-processing functions. This was followed by application of the suitable

indentation depth fitting of the Hertz-Sneddon contact model. Accuracy of each fit was assessed for each indentation force displacement curve. Manual application and adjustment of the Hertz-Sneddon fitting model (rather than automatic fitting) was seen as most suitable for deriving accurate MDCK elastic moduli outputs.

4.4.4 AFM surface topography cell imaging

Fixed cell AFM imaging applications are suitable using the selected colloidal cantilever probe. MDCK cell surface topography and surface stiffness mapping can be accurately obtained using each mode under defined AFM parameter conditions. A spherical cantilever is not often recommended for fixed cell surface imaging. However, the surface topography imaging presented (section 4.3.5) demonstrated that under suitable AFM parameters, a clear surface can be obtained for the selected MDCK cell line.

Application and amendments to the listed AFM protocol parameters are detailed in the chapters to follow.

CHAPTER 5

Effect of stage of cell monolayer development on atomic force spectroscopy Young's elastic modulus measurements

5.1 Introduction

When attempting to derive the Young's elastic modulus trends of different cell lines by AFM, little consideration is given regarding how the stage of cell development and monolayer confluence affects derived AFM output trends. Current AFM studies investigating multiscale trends in mammalian cell elastic moduli outputs have evidenced differences in single, groups of cells and monolayer outputs for similar cell-line origins and/or cantilever geometries [109]–[113]. The variation in derived elastic modulus outputs for mammalian cell lines at alternate stages of monolayer developmental scales, ascends the question if such variations are due to differences in (1) cell line (species and/or tissue type), or (2) if the derived elastic moduli trends may result from variation in AFM methodology approaches. It may well be the case that selected cell lines have differences in the internal characteristics that affect the degree to which a selected cantilever at a given loading force deforms the cell; Mammalian cells transition through multiple structural morphologies with progressive monolayer development [109], [181], [182]. Variation in cell volume [179], cell height with monolayer confluence [183], activity of the cortical cell membrane [89], [184] as well as change in the intrinsic position of the nuclear organelle [185], all comprise some of the morphological modifications that occur as cell proliferation and monolayer formation ensues. However, it may also be the case that variation in derived cell Young's elastic moduli trends may not be due to biological variation, but arise due to

the alternate indentation and deformation depths associated with greater and/or loading forces and more localised penetrative cantilever geometries. As stated, the Young's elastic moduli outputs from AFM indentation has been reported to be sensitive to the indentation depth analysed [100], [111], [186], [187]. Furthermore, differences in the geometry of the AFM cantilever selected i.e. spherical [110]–[112] versus pyramidal [113] and/or loading force i.e. 0.4nN [113], 0.2 -1.0nN [111] or 2.5nN [112], could result in the variation in Young's elastic moduli trends derived for cells at alternate cell proliferation length scales. As demonstrated in Chapter 4 of this thesis, the contact model selected to derive the Young's elastic moduli [E] trends for mammalian cells lines has to be carefully applied to specified sample regions (to account for thickness of the sample and the limits of the contact model). While many AFM studies do indent the nuclear body region of the cells, utilising different cantilever loading forces could render derived Young's elastic moduli [E] trends as somewhat inaccurate as a result of the depth of cell indentation investigated and the contact model selected.

Few AFM studies investigating mammalian cell elastic moduli, directly account for the depth of indentation at selected loading forces, nor do they consider how the developmental stage of the cell may affect the maximal indentation depth achieved, therefore, as a result of the discussed cell developmental events, more attention must be given when selecting and implementing specific AFM parameters for live mammalian cell Young's elastic moduli analysis.

Therefore, the purpose of this chapter was to investigate, apply and analyse selected AFM parameters on the selected MDCK mammalian cell line at selected stages of progressive monolayer development. Utilising the assessed framework of AFM parameters from Chapter 4, This was achieved by the following experiments;

(1) Investigating cell indentation/deformation depths and resulting Young's elastic moduli AFM outputs at alternate stages of cell monolayer development using an AFM loading force range (nN). The loading force range being (0.5nN – 3nN). Stages of cell development selected are single cell; semi-confluent and maximal density monolayer cells. This range of selected cantilever loading forces was selected to coincide with the range of forces selected from AFM studies in the literature i.e. AFM studies specifically investigating Young's moduli trends at increasing stages of cell proliferation and monolayer development.

(2) Assessment of potential cytoskeletal protein contribution (actin) to derived cell AFM Young's elastic moduli trends at each stage of cell monolayer development investigated.

These assays were carried out as an initial primary investigation to demonstrate that at different stages of mammalian cell monolayer development and confluence, alternate AFM loading forces and resulting derived Young's moduli outputs are greatly affected by the developmental state (cell confluence) of the MDCK cells. The loading force range used was selected to encompass some of the AFM loading forces used for mammalian cell indentation in the current AFM literature.

5.2 Materials and methods

The specific materials and methods used to carry out the MDCK developmental stage AFM assay in this chapter is detailed as follows;

5.2.1 Cell culture

The MDCK cell line was selected for the AFM analysis in this chapter based on the culture characteristics and phenotypes described previously (Ch4. Section 4.3.1).

MDCK cells were cultured, maintained and prepared for AFM experimentation as described previously (Ch3. Section 3.4 – 3.6). Prepared sample dishes were monitored closely for each required group, namely single cell, semi-confluent and maximal denisty confluence monolayers, estbalished at ~ 24h, 72h and 288h respectively. Samples were always prepared at least 24 hours prior to analysis (to allow for adequate cellular attachment for AFM analysis).

5.2.2 Cantilevers

Spherical geometry cantilevers, as detailed (Ch3. Section 3.7.3- 3.7.5) were used for the live MDCK cell AFM indentation in this chapter.

5.2.3 AFM

All AFM MDCK measurements (force-displacement curves) were obtained in contact mode. For MDCK cell Young's elastic moduli analysis, force-displacement curves were obtained over a period of no more than 1 hour per MDCK cell sample. Indentation approach rate (8μm s^{-1}), z-depth (4µm) and sampling rate (4096 Hz) were kept constant to allow for data reproducibility and implementation of the Hertz-Sneddon contact model. The approach rate (8µm s^{-1}) was within the accepted limit as to not encounter effects resulting from hydrodynamic drag [132],[140]. For assessment of AFM loading force (0.5nN-3nN) on alternate MDCK monolayer development cell stages, a total of 10 MDCK cells was analysed across each cell MDCK developmental length scale group. For each MDCK cell, within a monolayer stage developmental group, the nuclear organelle cell body region was subjected to each loading force within the 0.5nN - 3.0nN loading force range. A total of 10 indentations for each loading force were acquired for each individual cell within each cell developmental group. For all nuclear region indentations, only qualitative non-tethering force-displacement curves exhibiting defined extend-retract portions of the curves were used for subsequent data analysis.

5.2.4 Live MDCK AFM cell imaging – AFM optical overlay

In order to accurately discriminate the nuclear and cytoplasmic intracellular regions of the MDCK cells during AFM experimentation, MDCK cells were transduced to express an actin protein bound conjugated green fluorescent protein (GFP) marker, as described (Ch3. Section 3.8.1). All force indentation curves obtained from each cell sample were gathered within the approximated nuclear region for all cells (Figure 5-1). In order to investigate the effects of alternate AFM loading forces (0.5nN-3.0nN) on live MDCK cells the nuclear region overlay protocol was used.

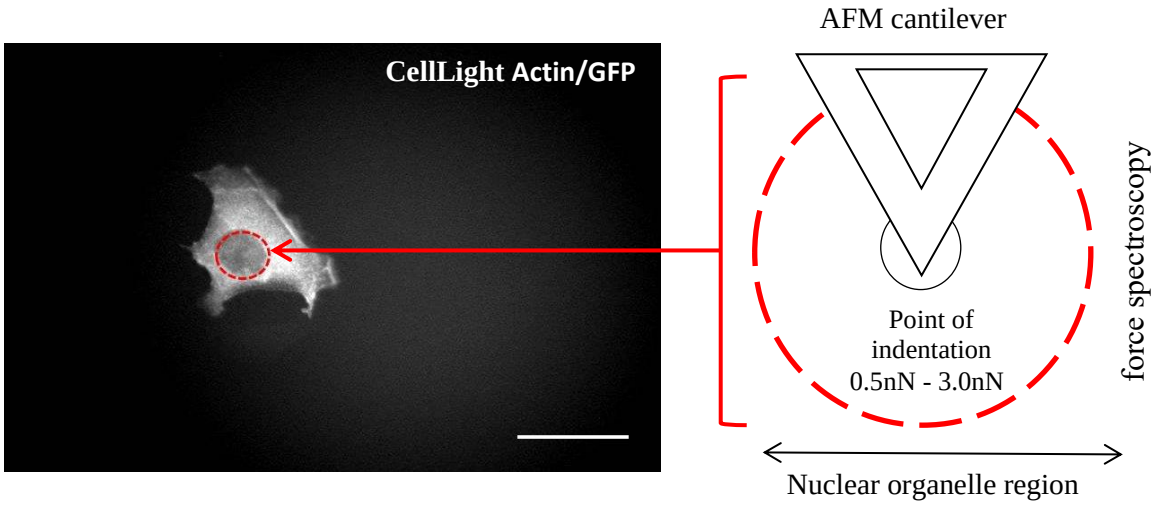

Figure 5-1. Single MDCK cell AFM fluorescent micrograph in greyscale. The MDCK nuclear region was identified and selected as the cell region lacking any prominent actin GFP fluorescence marker signal. Incremental loading force indentations were carried out across the selected 0.5nN – 3nN force set-point range, with each indentation point kept within the apparent measured nuclear region boundary [Scale bar 20µm].

5.2.5 Data processing – MDCK Young's moduli analysis

All obtained force-displacement curves were analysed by fitting the Hertz-Sneddon contact model for a spherical cantilever over the 0.5nN-3nN indentation force set-point range. The Hertz-Sneddon contact model was applied to the approach (extend) portion for all acquired force-displacement curves. Pre-processing JPK data processing functions (Chapter 3, Section 3.10.1) were used to process the raw curve files prior to application of the Hertz-Sneddon contact model at the selected force-curve indentation depths. All acquired AFM force curve outputs for live MDCK nuclear region indentation analysis was then graphed and Young's moduli trends analysed.

5.2.6 MDCK actin GFP fluorescence intensity analysis

MDCK actin GFP fluorescence intensity across each developmental stage through monolayer development was evaluated by 2D fluoresence microscopy. For actin intenstiy analyses, MDCK cells were fixed and incubated with an ActinGreen ™ ReadyProbe Reagent (ThermoFisher) as previosly described (Chapter 3, Section 3.9.1). Uptake of the ActinGreen ™ ReadyProbe was confirmed using an EVOS FLoid microscope imaging station. Actin-GFP intensity was calculated and analysed as described previously (Chapter 3, Section 3.8.2). Actin/GFP channel intensity was analysed for variations across each developmental length scale using the integrated density (IntDen) measurement function within the ImageJ measurements toolbox, as described (Chapter 3, Section 3.8.2). The ratio for total actin intensity to cell area for each developmental length scale was also calculated and analysed across each stage of MDCK development.

5.2.7 Statistical analysis of outcomes

To effectively analyse and compare mammalian cell Young's moduli AFM output measurements across each MDCK monolayer developmental length scale, certain statistical tests were used as described (Chapter 3, Section 3.11). Variation within each data set was assessed using standard error of the mean. To effectively analyse and compare MDCK AFM and actin GFP intensity measurements across each developmental length scale, the Mann-Whitney U test was used to calculate the degree of significance between the derived MDCK GFP intensity outputs.

5.3 Results

5.3.1 Stage of MDCK cell monolayer development and resulting AFM Youngs elastic moduli outputs

As stated in the introduction of this chapter, few AFM studies directly account for the depth of cell indentation at alternate selected cantilever loading forces, nor do they consider how the developmental state, in terms of cell monolayer confluence of a mammalian cell, may affect the maximal indentation depth achieved. In the AFM assay carried out in this chapter, a number of AFM indentations in the identified nuclear region of an MDCK cell from three monolayer developmental groups, i.e. MDCK single cells, MDCK cells within a semi-confluent monolayer and MDCK cells within a highly confluent monolayer was carried out. A number of cantilever loading force set-points, ranging from 0.5nN to 3nN was chosen for MDCK cell indentation. As a result, at each loading force set-point, a corresponding MDCK cell indentation depth was achieved for all three sample groups. The results demonstrated that the maximal achieved indentation depth of a MDCK cell achieved at each loading force was observed to be subject to the stage of MDCK cell monolayer development. The results are shown in Figure 5-2 and Table 5-1.

Referring to the results presented for final achieved cell indentation depths at each loading force, one can clearly observe that the indentation depth achieved using the same force set-point is dependent on the status of the MDCK cells, i.e. the degree of developmental confluence. A few interesting observations were made for the indentation depth outputs at each cantilever loading force. Firstly, at the lower range of force 0.5nN to 0.8nN, the slope of the curve between the three stages of MDCK development was relatively uniform. This suggests that within this region, the cantilever may be deforming the same material within the cells. The indentation region or depth for the forces described (around 500nm to 1000nm) are within the region of the actin cortex [90]–[93] (Chapter 2, section 2.8.3). It may be the case that the morphology of the cells i.e. cell height or surface topography produces an apparent difference in deformation depth for the three MDCK groups, however, the mechanical properties in this region results in a similar slope for the forces deforming this region. Therefore, this region of the graph may provide information about the actin cortex dynamics for this depth of cell deformation. Based on the slopes in the graph (between 0.5nN and 0.8nN), it may be the case that the actin cortex is what is being detected, yet for different MDCK cell stages, requires higher forces to deform at different cell monolayer stages. Perhaps the organisation of the actin cytoskeleton in this region is different between the three cell stages. Interestingly, within this loading force range, the depth of cell indentation has already reached the limits for the application of the Hertz-Sneddon contact model. It is suggested that cell deformations of around 500nm are most suitable for application of the contact model [123]. The AFM studies carried out investigating cell confluence in relation to the derived Young's elastic modulus use cantilever loading forces considerably greater (~ 2.5nN for example) than the 0.5nN to 0.8nN forces presented here. Therefore, at what limit of deformation the contact model in these studies used to derive the mechanical properties of proliferating cells is important, as

the results presented here suggest forces greater than 0.8nN are substantially deforming adherent cells beyond the limit of an accurate Hertz-Sneddon contact model fit. Another interesting finding presented for the three curves, is that they all follow a similar trend. There is an initial increase in the slope of the curves, followed by a plateau, followed then by additional deformation and then a further plateau (in the case of the single and semi-confluent MDCK cells). What is interesting for these trends is that beyond certain depths of cell deformation, the force remains relatively constant in this region. Where there are higher indentation depths, one would expect the force to increase. This suggests that at these indentation forces, a decline in force may arise due to a separation of two regions i.e. a higher force resulted in the cantilever sensing the modulus two different materials, perhaps of the more viscous internal cytosol region of the cell.

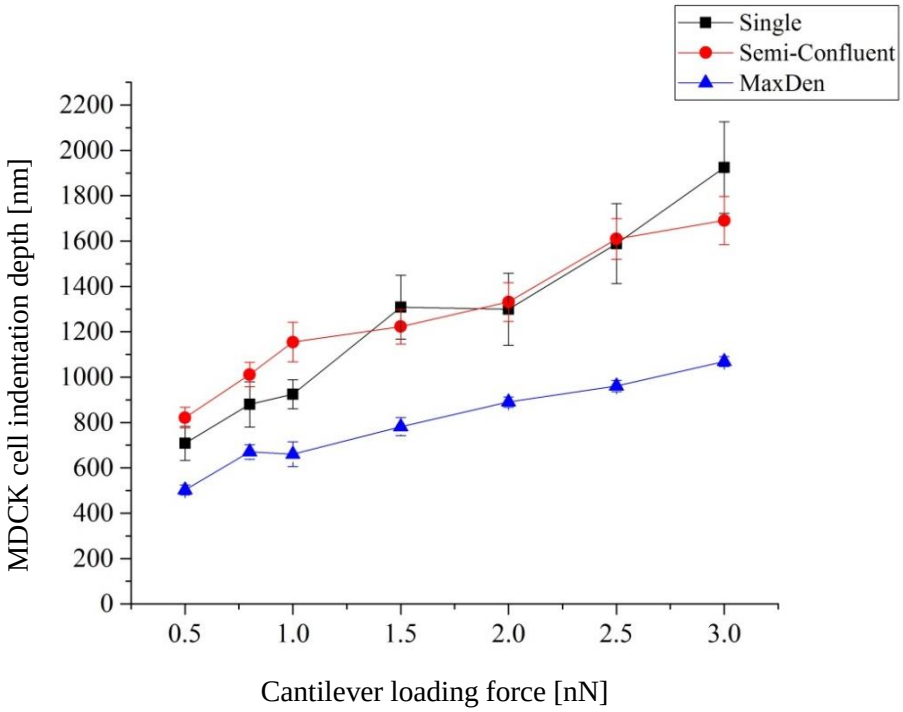

Figure 5-2. AFM cantilever indentation outputs across a (0.5nN to 3.0nN) loading force range for MDCK cells at alternate stages of cell monolayer development. Error bars indicate standard error of the mean for averaged measurements acquired from depth outputs for all sample groups.

Table 5-1. Maximal measured indentation depth [I. Depth] for loading force indentation range (0.5nN-3.0nN) on single, semi-confluent and maximal density MDCK monolayer confluence. Values presented are averages of each cell group with (+/- standard error of the arithmetical mean).

Parameter	**Single cell confluence (n=10)**	**Semi-confluent monolayer (n=10)**	**Maximal confluent monolayer (n=10)**
Set-point [nN] (n=10)	**I. Depth [nm]**	**I. Depth [nm]**	**I. Depth [nm]**
0.5	708.1 (± 74.5)	821.6 (± 45.2)	503.1 (± 21.8)
0.8	880.1(± 99.6)	1011.6 (± 53.2)	670.1 (± 32.1)
1.0	924.8 (± 64)	1154.3 (± 87.1)	659.7 (± 54.7)
1.5	1308.5 (± 140.7)	1222.7 (± 77.2)	781.9 (± 39.8)
2.0	1299.8 (± 158.9)	1331.6 (± 85)	890.1 (± 22.8)
2.5	1588.9 (± 176)	1609.6 (± 89.8)	960.5 (± 24.8)
3.0	1924.1 (± 201.6)	1691.1 (± 106)	1069.2 (± 22.1)

Next, the derived Young's elastic modulus as a result of MDCK cell confluence and cell indentation depths was then analysed. The results are presented in Figure 5-3 and Table 5-2. In the case of the results presented here, the JPK data processing software for force-curve analysis was used. As demonstrated in Chapter 4 (section 4.3.3), application of the Hertz-Sneddon contact model fit is only applicable for the initial indentation region of the MDCK cells. The Young's modulus trends presented here demonstrate that there is a significant difference in the derived [E] outputs at different cantilever loading set-points for MDCK cells at different stages of monolayer development. However, only low range force set-points are applicable when attempting to properly interpret the data as beyond certain deformation limits (the values of which are presented in Figure 5-2), the data is no longer compatible with the Hertz-Sneddon contact model. This is due to fitting the model to cell indentation depths that would present with artificial [E] outputs as a result of effects stemming from the underlying substrate. Therefore, AFM studies

utilising these loading force ranges would have to consider how the stage of adherent cell deformation by a cantilever could result in deformation depths beyond the limit of certain contact models to derive the mechanical properties of the cell following indentation. Stage of dell development must be considered, and appropriate corrections, with either lesser indentation forces or contact model corrections (Chapter 2, section 2.13) applied. To compare the differences in the MDCK cell mechanical properties at low indentation forces (0.5nN to 0.8nN); a similar trend was observed in the slope for the [E] curves of single and semi-confluent MDCK cells, however the gradient of the slop for the [E] curve of maximal density MDCK cells was greater. The data presented suggest that high cell density results in a greater derived Young's elastic moduli output. This agrees with previous findings for epithelial cell as high cell densities [110]. What is interesting is the shape of the slope of the curves between the three different length scales. At low loading forces, single and semi-confluent cells present with a similar slope, which suggests (as did the indentation depth results) that the same material or cellular component is being measured. This cellular component may be the actin cortex based on the indentation depths achieved. However, since the maximal density cells presented with a greater derived Young's moduli trend compared to single and semi-confluent MDCK cells, this may further corroborate the suggestion the dynamics of the actin cortex in this region for higher cell developmental length scales, behaves differently compared to earlier stages of cell monolayer development. Therefore, even at low force indentation ranges, the stage of adherent cell monolayer development can produce different elastic moduli outputs.

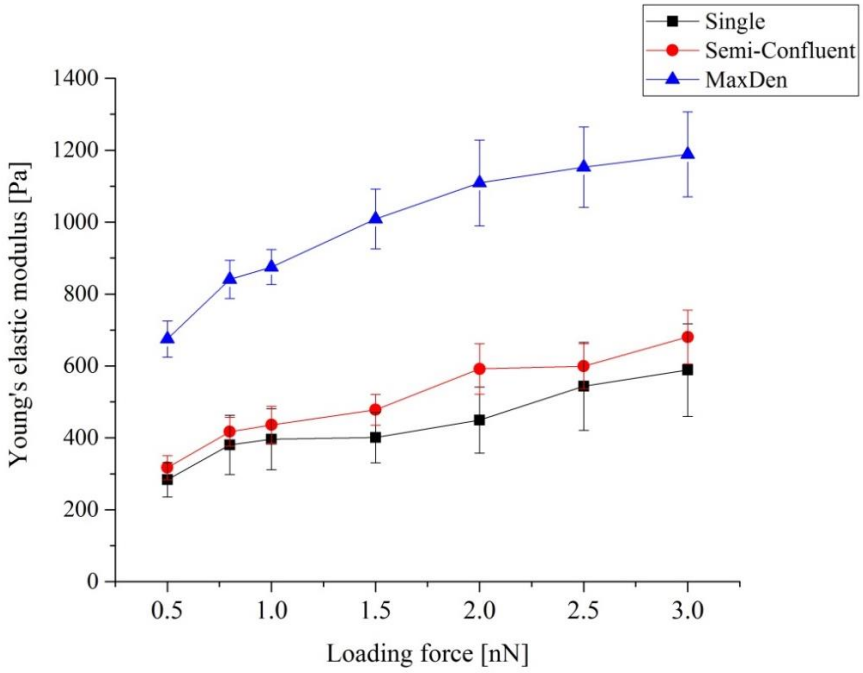

Figure 5-3. Young's elastic moduli outputs derived for a (0.5nN to 3.0nN) loading force range for MDCK cells at alternate stages of cell monolayer development. Error bars indicate standard error of the mean for averaged measurements acquired from depth outputs for all sample groups.

Table 5-2. Hertz-Sneddon derived Young's elastic moduli for loading force indentation range (0.5nN-3.0nN) on single, semi-confluent and maximal density MDCK monolayer confluence. Values presented are averages of each cell group with (+/- standard error of the arithmetical mean).

Parameter	**Single cell confluence (n =10)**	**Semi-confluent monolayer (n=10)**	**Maximal confluent monolayer (n=10)**
Set-point [nN] (n=10)	**E [Pa]**	**E [Pa]**	**E [Pa]**
0.5	283.5 (± 47.6)	317.4 (± 33.2)	675.1 (± 50.5)
0.8	380.3 (± 82.2)	417.1 (± 40)	840.7 (± 52.9)
1.0	396.4 (± 84.5)	436.1 (± 51.8)	875.2 (± 48.9)
1.5	400.9 (± 69.9)	478.2 (± 42.6)	1008.8 (± 82.9)
2.0	449.4 (± 91.9)	591.8 (± 70.1)	1109.2 (± 119.4)
2.5	543.6 (± 122.5)	599.3 (± 62.7)	1153.2 (± 111.6)
3.0	588.6 (± 128.7)	680.4 (± 75.1)	1188.7 (± 118.1)

5.3.2 Cortical actin distribution in MDCK cells at different monolayer developmental stages

Previous reports have demonstrated a variation in the distribution of cortical F-actin for epithelial cells at alternate cell developmental length scales; Vero cells have been shown to exhibit variation in F-actin intensity at non-confluent (higher F-actin intensity) and monolayer (lower F-actin intensity) developmental length scales [111]. Therefore, using a similar method for cortical actin analysis, the F-actin intensity and distribution (in terms of cell area) of MDCK cells across the three MDCK developmental stages was analysed (Figure 5-5). This was carried out to investigate if the Young's elastic moduli trends observed (particularly at higher cell density length scales) arise due to a difference in actin cortex protein expression or activity.

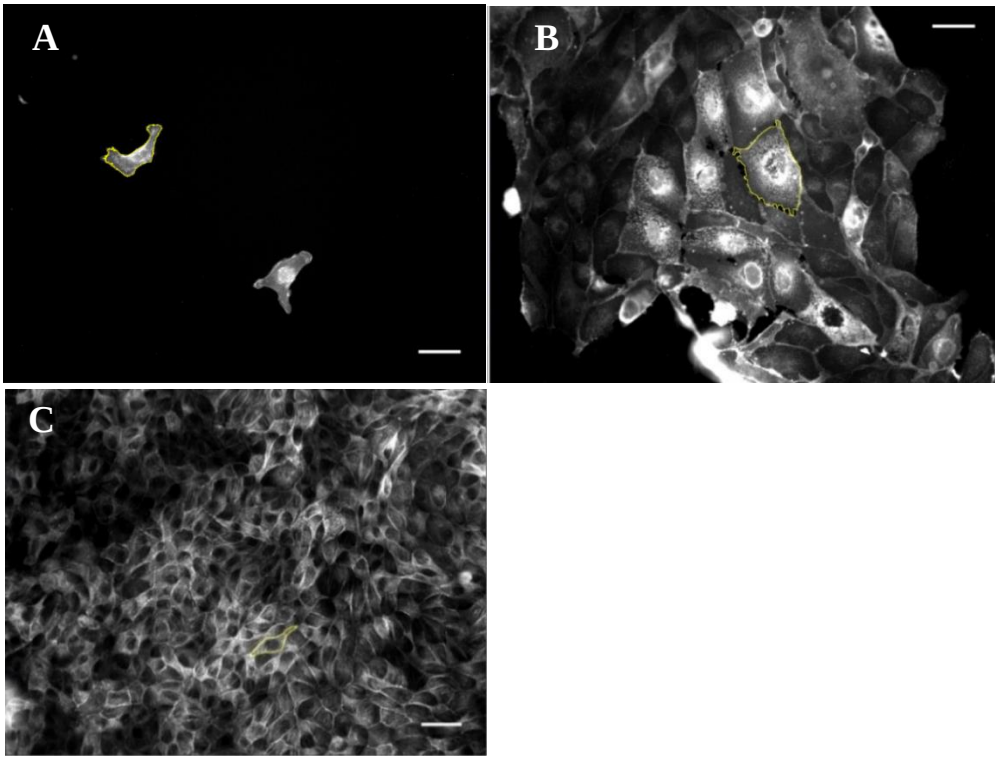

Figure 5-4. MDCK actin GFP fluorescence analysis using ImageJ ROI selection and background thresholding. MDCK cell body area and actin GFP signal intensity measurements were obtained for each developmental length scale; **[A]** single cell **[B]** semi-confluent monolayer and **[C]** maximal density monolayer confluence [Scale bars 20μm].

MDCK actin GFP fluorescent images acquired and analysed for variation in cortical actin intensity, demonstrated a significant difference ($p < 0.00001$) in the corrected total cell fluorescence for (CTCF) cortical actin between single (non-confluent) and maximal density confluence MDCK cells, as well as semi-confluent and maximal density confluence MDCK cells ($p < 0.00001$), and no significant difference between single and semi-confluent MDCK cells ($p = 0.177$) (Figure 5-6). As with previous reports, the total amount of cortical actin is reduced at higher monolayer cell length scales. In the results presented here, maximal density highly dense confluent MDCK cells demonstrated the lowest cortical actin intensity, in comparison to single and semi-confluent monolayer MDCK cells. The ratio between MDCK F-actin intensity and cell area (CTCF/cell area) (Figure 5-7) demonstrated that single cells presented with the greatest actin intensity per cell, followed by maximal density and semi-confluent MDCK monolayer cells.

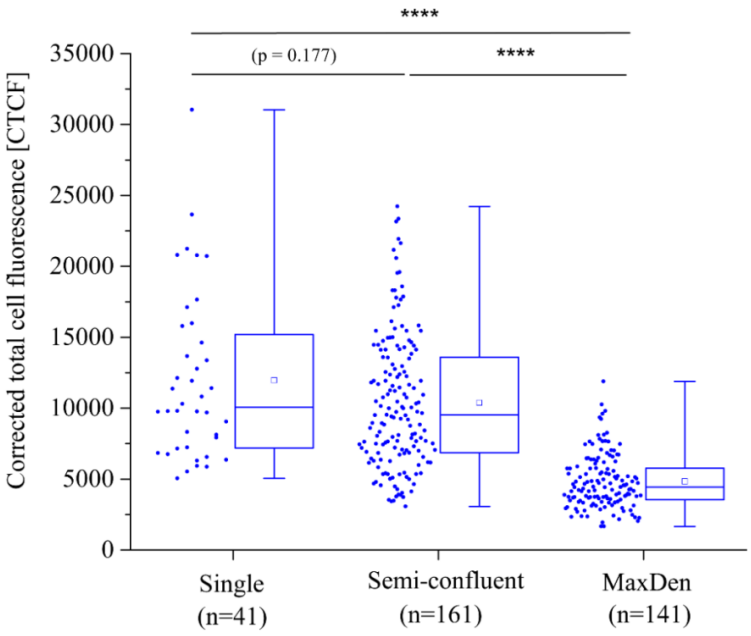

Figure 5-5. Box plots denoting corrected total cell fluorescence (CTCF) for cortical actin GFP MDCK cell fluorescence. Lines within each box represent the median, the box itself presents the lower (25%) and upper (75%) quartiles, while the whiskers present the lowest and highest extreme values. Box points represent the average means of each cell cohort. (p-values) were calculated using the Mann-Whitney U test at .01 significance. (**** $p < 0.00001$). (n) = (41) single cells (161) semi-confluent cells and (141) maximal density confluence cells.

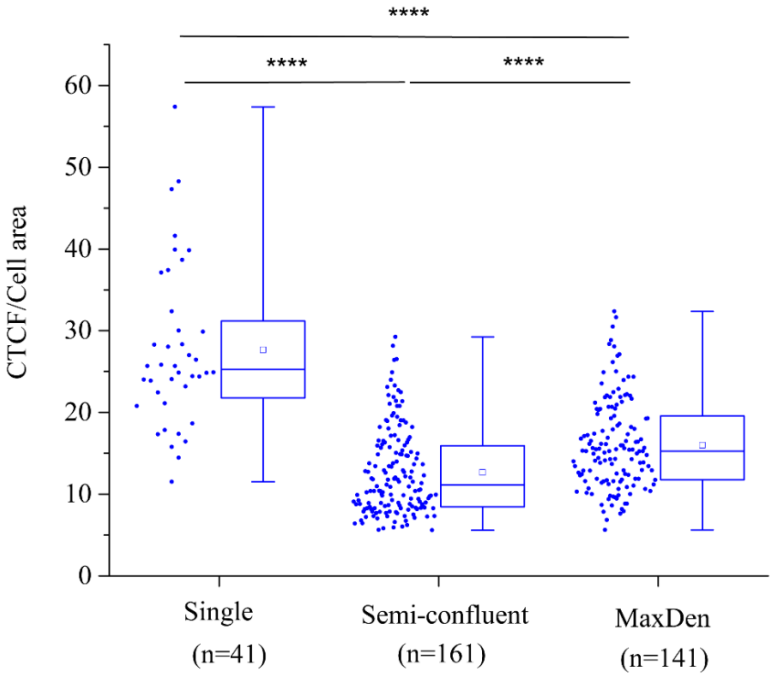

Figure 5- 6. Box plots denoting the ratio between corrected total cell fluorescence (CTCF) to total cell area for each developmental length scale. Lines within each box represent the median, the box itself presents the lower (25%) and upper (75%) quartiles, while the whiskers present the lowest and highest extreme values. Box points represent the average means of each cell cohort. (P-values) were calculated using the Mann-Whitney U test at .01 significance. (**** $p < 0.00001$). (n) = (41) single cells (161) semi-confluent cells and (141) maximal density confluence cells.

5.4 Discussion

Following the investigation into how current AFM protocol parameters such as cantilever geometry, region of cell indentation and cantilever loading force can be applied to a specified selected mammalian cell line (Chapter 4), the primary aim of this chapter was to explore how progression of cell monolayer development can affect the outcome and derived Young's elastic moduli trends during AFM indentation experiments. How a mammalian cell responds and adapts their elastic properties during cell proliferation and an increasing number of cell-cell contacts is the overarching aim of this thesis. Current AFM studies utilise a number of alternate cantilever loading forces when indenting and deforming mammalian cells. A progressive increase in

cantilever loading force (0.5nN to 3nN) on MDCK cells at three different stages of cell monolayer development, demonstrated an alternate membrane response (depth of indentation and resulting Young's modulus elasticity output). The stage of cell monolayer development and cell density i.e. single cells, semi-confluent monolayer cells and fully confluent maximal density cells had a significant effect on derived AFM Young's elastic moduli outputs for indentation ranges within the limits of the application of the Hertz-Sneddon contact model. Interestingly, the Young's elastic moduli trends derived are comparable to previous reported AFM findings investigating MDCK elastic moduli trends for alternate cell densities (cells/mm^2). In those studies, MDCK cells presented with lower elastic moduli trends at lower isolated cell densities (5-10 cells/mm^2), compared to higher cell densities (500 cells/mm^2), at a 500nm cell indentation depth [110]. However, such investigations did not account for variation in Young's moduli trends at highly confluent MDCK cell densities, nor do they account for variation in cell indentation depths for different cell density length scales and varied cantilever loading force set-points. Such investigations did attribute the variation in derived cell elastic moduli trends for MDCK cells, to the formation of mature cell-cell junction complexes and cell-cell junctional actin assembly. At greater cell densities and confluence, MDCK cells showed an increase in the presence of short microvilli in the apical domain, along with incrassate apical actin [110].

An appreciation for stage of cell monolayer development and cell confluency is necessary when selecting an appropriate AFM protocol for mammalian cell analysis. A number of mammalian cell lines have exhibited a variation in their derived cell elastic moduli outputs at alternate stages of monolayer developmental length scales; Vero epithelial cells presented with greater Young's moduli outputs at the single cell length cell compared to monolayer cells [111]. MDCK epithelial cells (canine) presented with lower elastic moduli at low isolated cell densities (5-10 cells/mm^2), compared to higher

cell densities (500 cells/mm^2) (as noted) [110], while NIH3T3 murine embryo fibroblast cells exhibited no significant different in cell elasticity trends with variation in cell density/development [110]. Human umbilical vein endothelial cells (HUVEC) cells exhibited greater cell elasticity outputs for grouped (3-5 cell clusters), followed by single cells, with HUVEC monolayer cells having the lowest elastic moduli [E] outputs [109]. Human mammary epithelial cells (HUMEC) exhibited greater elastic moduli trends at the monolayer length scale, compared to cells at the single cell developmental stage [113]. A similar trend was presented for HUMEC cells whereby the derived elasticity of the cells was found to gradually decrease towards the periphery of a monolayer compared to single isolated cells [114]. The underlying mechanism described for the observed increase in cortical membrane elasticity and tension at higher cell densities has been attributed to the formation of dense apical microvilli and incrassate actin fibres at higher cell densities [110]. In the final results section of this chapter (section 5.3.2), a variation in cortical actin intensity was investigated and presented. Highly confluent maximal density MDCK cells exhibited a lower GFP actin intensity compared to non-confluent (single) and semi-confluent MDCK cells. A similar reduction in actin GFP intensity outputs has been demonstrated for epithelial cells at alternate mammalian cell length scales [111]. However, the GFP analysis and results presented here are not wholly comparable with the presence of incrassate cortical actin and microvilli in the apical cell domain. Further investigation into which morphological attributes are most responsible for the alternate cell membrane response during AFM indentation is required. In summary, by analysing variations in the derived AFM elastic moduli [E] trends for MDCK cells at increasing stages of monolayer development at alternate loading forces, it was possible to identify an inherent variation in MDCK cell membrane resistance towards an external deformation load. While it was shown that MDCK cells at alternate stages of monolayer development present with varied GFP

actin intensity trends, additional investigation into how and why MDCK cells respond/deform differently to an increase in deformation load through monolayer development is required. A complete appreciation as to how an MDCK cell responds during AFM mechanical investigations is necessary when attempting to interpret and define a pathway of mammalian monolayer development.

5.5 Conclusion and summary of findings

Using a precise incremental loading force range (0.5nN-3nN), the results of this chapter demonstrated the varied depth of deformation and resulting elasticity AFM Young's moduli [E] outputs for MDCK cells probed at specific single cell, semi-confluent and maximal density monolayer developmental stages. The future focus and development for the work and results presented in this chapter will encompass further investigation into which morphological attributes are most responsible for the different membrane response of MDCK cells undergoing AFM indentation. The significance of the results obtained will demonstrate the requirement for future AFM studies to include an appreciation for specific stage of cell development in their protocols, but also highlight which potential mechanisms are responsible for how a single cell transforms and alters its mechanical properties during monolayer development.

CHAPTER 6

Stage of MDCK cell development and associated AFM Young's elastic moduli trends: A review of potential underlying mechanisms for observed outcomes

6.1 Introduction

The AFM indentation results presented (Chapter 5), demonstrated an interesting outcome for MDCK cells undergoing AFM indentation at alternate stages of proliferation and monolayer development. The results showed that a low range 0.5nN to 0.8nN cantilever indentation forces, MDCK cells present with considerable variation in both their degree of deformation by the cantilever, as well as derived Young's elastic moduli outputs. To assess what potential cell morphological attributes may be contributing to the results observed, a rudimentary analysis for actin-GFP intensity for the three MDCK cell monolayer developmental groups was then analysed. Interestingly, the results did not follow the Young's elastic moduli trends observed in the literature; Given that highly confluent maximal density MDCK cells presented with the greatest elastic moduli trends, they did not exhibit the greatest actin-GFP intensity, in terms of total GFP fluorescence. Single and semi-confluent MDCK cells exhibited a similar degree of actin-GFP intensity of fluorescence. However, upon calculation of the total amount of actin-GFP fluorescence per MDCK cell (CTCF/cell), the reasoning for the results was further distorted; While single and semi-confluent MDCK cells presented with similar indentation and actin-GFP, they exhibited significantly different CTCF/cell. After single MDCK cells, maximal density cells exhibited a greater amount of CTCF/cell, followed by semi-confluent MDCK cells.

The variation in Young's elastic moduli trends for MDCK cells across a range of AFM cantilever loading forces, affirmed the notion that much more consideration needs to be taken into account when defining an AFM protocol for live mammalian cell indentation. A slight variation in cantilever loading force, or little consideration of timing of stage of cell monolayer development, could render any conclusion about derived cell elastic properties somewhat inaccurate. Thus, attempting to interpret how a particular cell line transforms its mechanical properties would not be wholly precise.

Based on the results presented in Chapter 5, the purpose of this chapter is to outline and hypothesize which cellular mechanisms and intracellular components may give rise the interesting AFM and actin-GFP fluorescence results presented. The structural components of mammalian cells which are most associated with derived Young's elastic moduli properties, such as the actin cell cortex, cell junctional complexes and cell nucleus is discussed. This is followed by two hypotheses, each of which suggest what may give rise the AFM results obtained, namely (1) variation and changes in cell morphology with progressive cell monolayer development, and (2) development of increased stress along the cell interface boundary with progressive monolayer development and increasing number of cell-cell bonds. These hypotheses are discussed, and then validated in the results chapters to follow.

6.2 The structural model of mammalian cell(s) undergoing AFM indentation

An appreciation for the inherent structural changes that occur through mammalian monolayer formation is paramount when attempting to analyse derived AFM Young's elastic moduli outputs. As described and illustrated in Chapter 2, mammalian cells are linked together by specific types of intercellular adhesion junctions (Figure 6-1); adherens junctions, gap junctions, tight junctions and desmosomal or hemidesmosomal

junctions. Specifically, two adhesion complexes, adherens and desmosomal cell junctions, serve to join and integrate the internal cell cytoskeleton network with the outer extracellular matrix environment [46], with tight junctions serving to bind cells (epithelia cells specifically) tightly to one another. Cell junctional complexes are linked via cadherin transmembrane complexes to a cells internal cytoskeletal network.

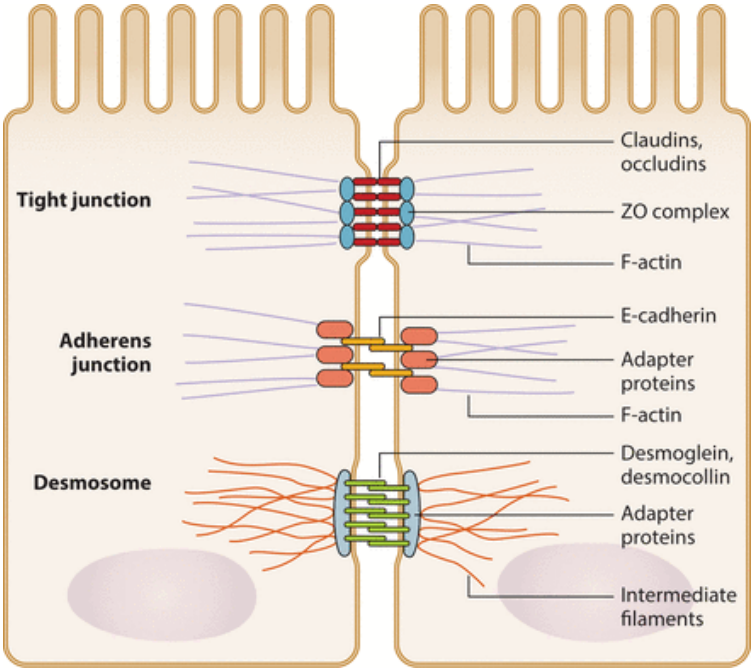

Figure 6- 1. Mammalian cell-cell junctional complexes. Mammalian cells are linked to one another and the ECM via specific cell and ECM complexes (Figure taken from Harras, et al, 2014) [46].

A cells cytoskeleton is composed of three types of filaments; microfilaments, intermediate filaments and microtubules as illustrated in Chapter 2 (section 2.8.2). These primary three filaments (Figure 6-2) each conform to their own structural conformation in solution at 37°C due to the thermal fluctuations acting on a 10-micron long filament [189]. Therefore, within mammalian cells undergoing AFM indentation in liquid media (37°C), the mechanical function of each filament is subject to the

conformation and activity of the cell cytoskeleton for a particular cell undergoing monolayer development.

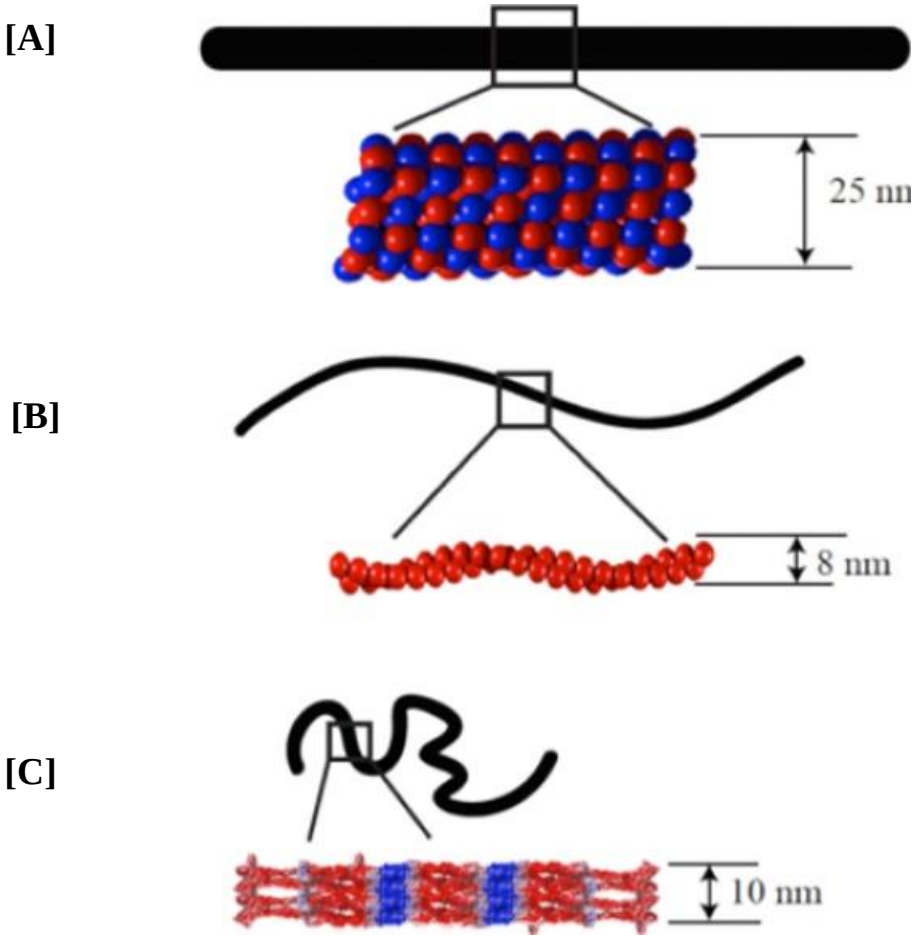

Figure 6- 2. Schematic diagram of estimated diameter, subunit packing and filament configuration in solution at 37°C of each of the three cytoskeletal polymer types [A] microtubules, **[B]** F-actin, and **[C]** intermediate filaments [189].

As previously discussed, (Chapter 2. Section 2.8.3), the majority of cellular mechanobiology studies implicate actin microfilaments and stress fibres as the most significant principle modulator of external load force, cellular elastic properties and tension [22], [76]. The cortical region of many cell lines is comprised of a dense actin meshwork. Notably, although actin is present throughout the cytoplasm of a cell, the most concentrated region is found at the cell membrane boundary, creating a peripheral network of loosely cross-linked F-actin meshwork beneath the plasma membrane [190],

[191]. This is commonly referred to as the actin cortex. The thickness of the actin cortex has been estimated to range from 130nm to 1μm [90]–[93], with cortical actin mesh densities estimated at ~ 100nm [77]. The architecture and mechanics of the actin cortex has been evidenced to be subject to state of cell pluripotency [89], with further evidence demonstrating the increase in the number of cell-cell adhesion complexes as well as cytoskeletal activity with progressive cell development [109], [164], [181], [184], [192]. The AFM results presented for the MDCK cell line at alternate stages of cell monolayer development, previous studies investigating MDCK Young's elastic moduli trends at higher cell densities (such as maximal confluent monolayer cells) did attribute the variation in derived cell Young's elastic moduli trends for MDCK cells to the formation of mature cell-cell junctions and junctional actin assembly; At greater cell densities and confluence, MDCK cells showed an increase in in dense and short microvilli in the apical domain, along with incrassate apical actin [110].

Therefore, the results obtained in Chapter 5 could be principally be described using a rudimentary AFM indentation depth/cell deformation dependent model for live cell AFM analysis, whereby the parameters required for consideration in live cell AFM analysis are;

1. Final calculated Young's elastic modulus output is dependent on *f* (Indentation depth)
2. *f* (Indentation depth) is dependent on *f* (F-actin cell cortex dynamics/maturity)
3. Actin cell cortex dynamics is dependent on *f* (cell monolayer length scale)

If we assign variables to each experimental parameter;

- Young's elastic modulus [E] = x
- Indentation depth = y
- Actin cortex maturity = Z
- Stage of cell development (single, semi-confluent, maximal density cell) = d

It is then possible to formulate an initial simplified equation for how the developmental stages of cell development affect live cell AFM measurement and Young's elastic modulus outputs;

$$X \prod Y|(Z|d) \tag{6-1}$$

whereby variable x (final derived live cell Young's elastic moduli outputs) is dependent on variables Y (indentation depth) that in turn are conditioned by variable Z cell cortical maturity) which in turn is wholly dependent on variable d (the monolayer developmental stage of the live cell undergoing AFM indentation.

Referring to the aforementioned model, it is evident that certain cellular characteristics need to be further investigated in order to complete the model. As stated in the introduction of this chapter, two possible hypotheses surrounding which cellular mechanisms within this model could be most responsible for the results obtained is to be investigated in the results chapters to follow.

6.3 Hypothesis 1: Morphological variation of MDCK cells across three stages of cell monolayer development

One possible reason for the alternate AFM Young's elastic moduli trends observed in MDCK cells, is the variation and adaptation in cell morphology with progressive cell development and monolayer formation. During cell development, morphological changes such as variations in cell volume, height, shape, thickness of the cell cortex, as well as location of the nuclear organelle, all comprise some of the morphological modifications that occur as cell proliferation ensues (Figure 6-3). The biological process whereby cells adapt their morphology during cell division and proliferation has repeatedly been attributed to the actomyosin cortex, microtubules as well as additional

associated cytoskeletal elements such as membrane transport proteins, which in turn regulate internal cell hydrostatic pressure and cell functions [193], [194]. Incremental increases in AFM cantilever loading force and resulting derived Young's elastic moduli, are therefore subject to the presence of the aforementioned biological changes that arise through mammalian cell monolayer development. Therefore, investigation of various MDCK structural characteristics across each monolayer developmental length scale, by means of fluorescence cell morphological imaging, could clarify if the progressive change in cell structure and size are most accountable for the AFM results observed. The investigation of this hypothesis is carried out in the results chapter to follow – Chapter 7.

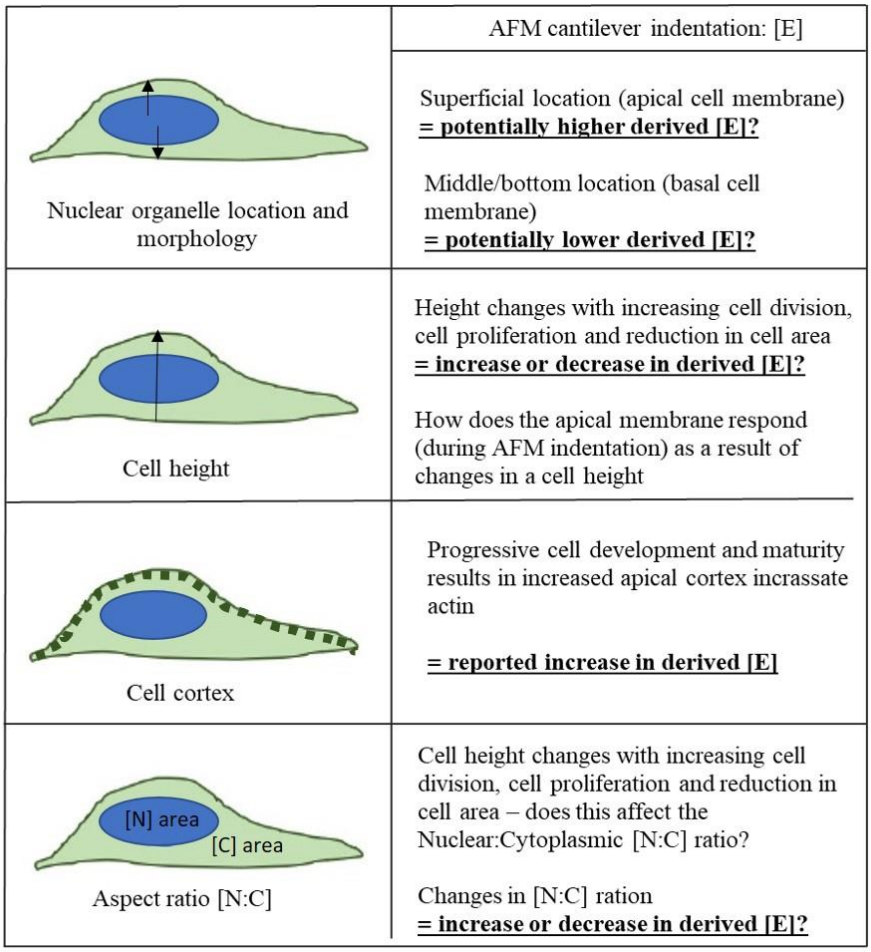

Figure 6-3. Mammalian cell morphology transitions with monolayer development. Example mammalian cell morphology transitions that occur during cell monolayer development and proliferation. How particular morphology variations affect derived AFM Young's elastic moduli measurements are not fully accounted for.

6.4 Hypothesis 2: Progressive cell development of MDCK cells results in the alteration of MDCK cortical region Young's elastic moduli properties as well as variation in physical stress at the cell-cell membrane boundary

As previously noted, mammalian cells readily adapt their morphological structure during progressive cell and monolayer proliferation. Such morphological adaptions have been attributed to multiple internal cytoskeletal and membrane signalling pathways. At both single cell and confluent cell monolayer length scales, the interplay between these mechanisms has been evidenced to generate greater cell cortical elasticity trends in mitotic cells as they progress through each stage of cellular mitosis and monolayer development [79], [195]. Gradients in cortical elasticity trends within the cortical actin layer has been associated with multiple cell developmental events such as cell migration, formation of cell-cell junction complexes and cell division (mitosis) [13], [79], [80], [81], with a down-regulation of cortical actin density along the cell-cell junction interface evidenced in multiple mammalian cell lines; MDCK [84], cancerous cells [85], zebrafish [83], and xenopus gastrula cells [86]. Furthermore, as well as cytoskeletal processes affecting derived AFM Young's elastic modulus outputs at alternate cell developmental stages, there is suggestion that spatial and lateral confinement of epithelial monolayers results in greater intracellular pressure; Micro-pillar arrays designed to create spatial confinement mimicking that of proliferating epithelial monolayers demonstrated that without sufficient micro-pillar flexibility, compacted epithelial cells lack adequate space for optimal cell rounding and cell division. As a result, driven by an increase in actomyosin contraction and hydrostatic pressure with mitotic cell rounding, epithelial cells migrate up micro-pillars to reduce cell confinement and undergo unperturbed cell mitosis [80]. Cell migration with surface area restriction *in vitro*, often results in a process whereby cell "domes" form with

extended proliferation and a reduction in substrate surface area for proliferation [196], [197].The presence of apical microvilli, with incrassate cortical actin, increased cortical elasticity outputs hydrostatic pressure with spatial restriction (Figure 6-4), suggests an additional plausible underlying mechanism for the greater derived Young's elastic moduli trend outputs with increase in MDCK monolayer development observed in Chapter 5. Further to this, the reported variation in the mechanical properties along cell-cell junctional boundaries suggests a possible cell mechanical mechanism, whereby cells adapt (through their respective cell junction complexes) to increasing cell numbers and stress along the cell interface boundaries (Figure 6-5).

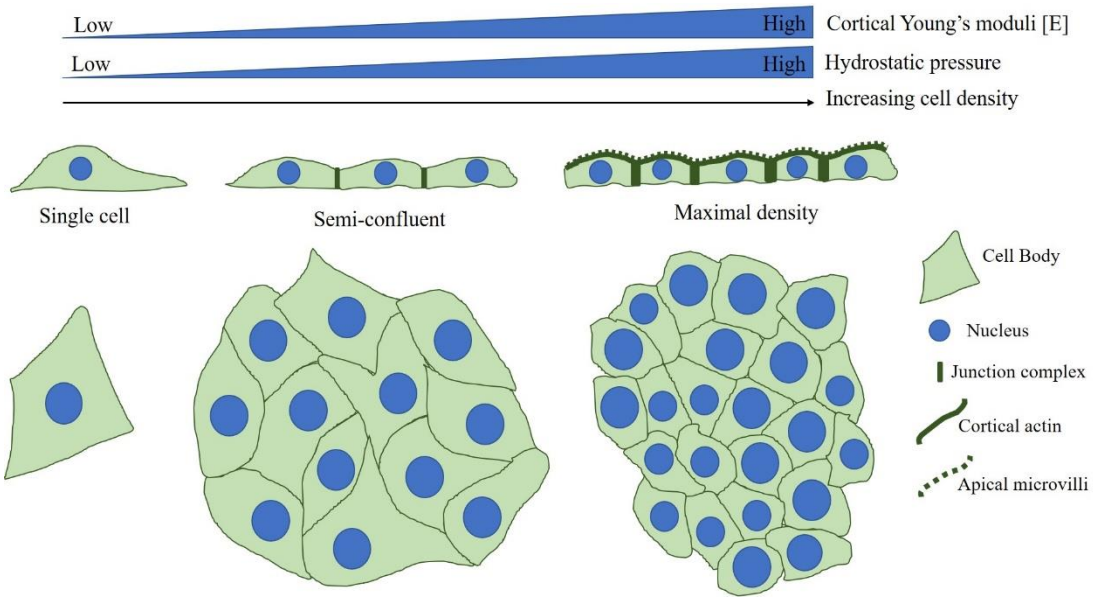

Figure 6-4. Progressive development of MDCK cells and resulting formation of specific structural cytoskeletal components. The presence of apical microvilli, incrassate cortical actin, increased MDCK cortical elasticity, hydrostatic pressure and spatial restriction with MDCK monolayer development could all encompass the physical mechanisms that give rise to increased cortical tension and resulting AFM Young's moduli [E] outputs.

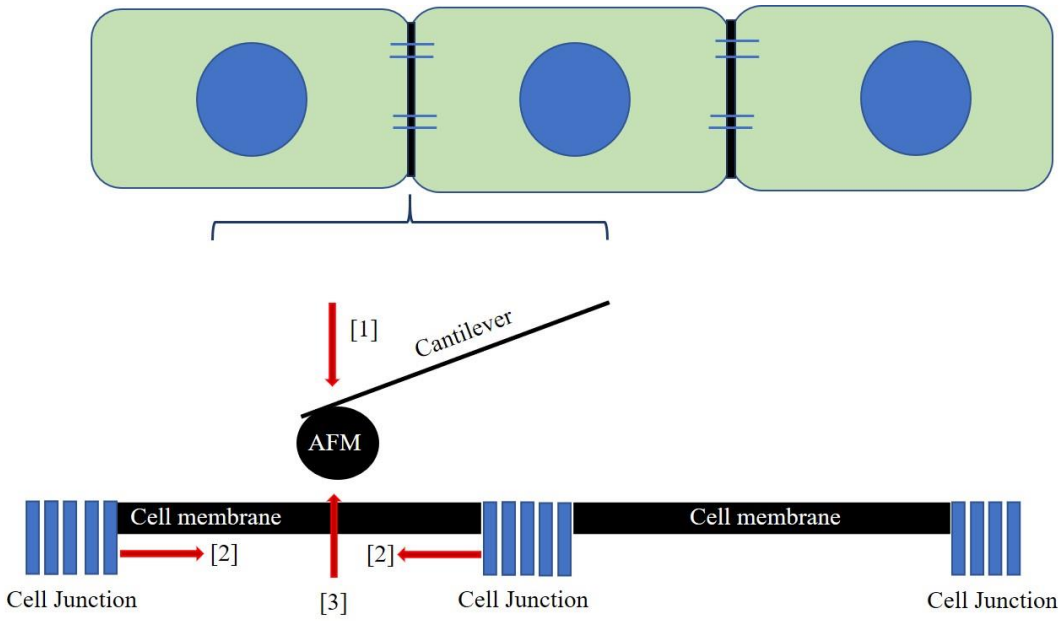

Figure 6-5. [A] Schematic for proposed of cell cortical elasticity trends with progressive cell monolayer proliferation and cell-cell bond formation. As a result of the development and maturation of cell-cell junction complexes, upon AFM cantilever deformation **[1],** cell-cell junctions react to membrane load compression **[2].** As a result of the stability of the cell-cell bonds, an increase in stress arises within the cell-cell junctional region, which could result in the alternate deformation response resisting the downward load of cantilever deformation on the apical surface of the cell and cell junction regions. Depending on the stage and maturity of cell-cell bond integrity and stability, this may directly affect the resulting resistance **[3]** and derived Young's elastic moduli of the apical membrane towards an external deformation force.

Therefore, force mapping analysis of MDCK cells undergoing incremental stages of monolayer development (single, divided doublet pairs, cell cluster to maximal density monolayer) could clarify if the development of the varied elasticity trends in the cell cortical and cell-cell boundary region is most responsible for the AFM results obtained in Chapter 5. Does the progression of cell development with increasing cell bonds and maturation of cell bonds at higher cell densities directly account for the different membrane response for MDCK cells existing at different stages of monolayer development? Referring to the mechanical properties of the mammalian cell cortex, the effect that the formation and maturation of the cell-cell junction region has on the

mechanical properties of the actin cell cortex at higher cell monolayer length scales will be investigated by analysing the cell cortical region at increasing stages of MDCK cell monolayer development. This will be achieved by using a cantilever deformation force that will deform the MDCK cells at a depth associated with the thickness of the cell actin cortex region. However, care and consideration will be carried out for the application of the Hertz-Sneddon contact model. The Young's elastic modulus is to be derived for indentation depths at a maximum of 10% sample thickness. This will be achieved by carrying out cross section height-offset analyses of the MDCK cell monolayer scales using the method investigated in Chapter 4 (section 4.3.4). For the MDCK cell-cell junction region, a similar method will be carried out as to ensure only appropriate MDCK cell sample thickness was analysed and any effects of the underlying substrate does not affect the derived Young's elastic moduli trends. The Young's elastic moduli outputs derived along the cell MDCK cell cortical region, and cell-cell junction regions will elucidate if a progressive increase in MDCK proliferation (cell density), and formation and maturation of cell-cell bonds with monolayer formation, can result in a variation in stress within the cell cortical region and along cell-cell junctions. Notably, although the Young's elastic modulus is used in the case of this research thesis to investigate mammalian cell mechanics, many assumptions are made by the Hertz-Sneddon model about the cells. Mammalian cells are biological materials, and are not in essence linearly elastic materials (as the Hertz contact model assumes). As a non-linear material, if the mammalian cell is compressed or stretched along its boundary, the apparent Young's elastic modulus of the mammalian cell, as non-linear material, will increase. Therefore, if this is the case, where the maturation and material properties of the MDCK cell junction region and interaction of the junctional complexes with the cortical region cytoskeleton progresses, this could result in an apparent increases stress along the cell-cell junction region as well as an increase

in the Young's moduli trends along the cell cortical region. The investigation of this hypothesis is carried out and the results are presented in Chapter 8.

6.5 Summary and Conclusion

In summary, based on the results presented in Chapter 5, it is possible that two different cell mechanical frameworks are most responsible for the variation in MDCK cell AFM Young's elastic moduli trends with progressive cell monolayer development. (1) Changes in cell morphology with progressive cell division and/or (2) the development of increasing actin cortex elasticity (Young's elastic modulus) with increase in cell density and stress along cell-cell junctional regions are the two primary hypotheses proposed to account for the results observed in Chapter 5. Investigating each of these hypotheses by means of cell morphological analysis (Chapter 7), and further AFM indentation, using force mapping (Chapter 8), will highlight which of the two theories is most applicable when investigating MDCK AFM Young's elastic moduli trends, and formulation of an appropriate AFM protocol for mammalian cell mechanical analysis with progressive cell development.

CHAPTER 7

Hypothesis 1: Morphological variation of MDCK cells across three stages of cell monolayer development

7.1 Introduction

The purpose of this chapter was to investigate potential variations in MDCK cell morphology through monolayer development as a means to determine if it could affect the derived AFM Young's elastic moduli outputs of MDCK cells between different stages of cell monolayer formation, as demonstrated in Chapter 5; single MDCK cells in comparison to semi-confluent and maximal density monolayer cells. Fluorescent microscopy methods (FLoid EVOS imaging and 3D confocal imaging) were used to analyse and measure variations in MDCK cell (1) height, (2) cortical layer thickness and (3) size, as well as (4) shape and volume of the internal nuclear organelle at each stage of MDCK monolayer development.

The biological process whereby a mammalian cell adapts its shape and height for cell division and proliferation has repeatedly been attributed to the actin cortex, microtubules as well as additional associated cytoskeletal elements and membrane transport proteins regulating internal cell hydrostatic pressure and cell mechanical function during mitosis [193], [194]. At both single cell and confluent cell monolayer length scales, the interplay between these mechanisms has been evidenced to generate greater cortical tension in mitotic cells as they progress through each stage of cellular mitosis and monolayer development [79], [195]. Variation in cell volume [179], cell height [183], and activity of the cortical cell membrane [89], [184] as well as change in the intrinsic position of the nuclear organelle [185], all comprise some of the

morphological modifications that occur as cell proliferation ensues. Further to this, and as noted in Chapter 6, as the number of cell bonds increases with cell division and monolayer confluence, cell motility declines with a reduced surface area for cell division. This results in cell compaction and shrinkage, and a transformation in the cytoplasmic-nuclear surface area ratio. Continued cell division slows as a result of the aforementioned physical constraints – collectively referred to as contact inhibition of cell proliferation [198]. It has been evidenced that contact inhibition in MDCK cell development is more influenced by mechanical constraint as opposed to an increase in the number of cell-cell contacts [198]. It should be noted that how cell size and growth are co-ordinated is only partially understood. When a cell divides to produce daughter cells and are mitotically active, they must double and segregate their genetic contents (DNA) as well as internal cellular organelles. The commencement of intracellular proliferative events have been evidenced to affect cell growth, with adaptation and uniformity in cell size being a consistent characteristic of healthy tissue cells [199].

As a result of the aforementioned morphology transitions that mammalian cells progress through, differences in the selection of an appropriate AFM protocol steps i.e. cantilever loading force, and cell indentation/deformation depths with respect to cell monolayer development can have a great effect on derived AFM Young's moduli [E] output trends. Any morphological heterogeneity (at both the macro whole cell and micro intracellular scale) may greatly affect the Young's elastic moduli outcomes of AFM indentation assays investigating mammalian cell proliferation and monolayer development.

7.2 Materials and methods

The specific materials and methods used to carry out the MDCK developmental morphology assay are detailed as follows;

7.2.1 Cell culture

MDCK cells were cultured, maintained and prepared for AFM experimentation as described previously (Chapter 3. Section 3.4 – 3.6). MDCK cell samples for morphological analysis were monitored closely for each required group, namely single cell, semi-confluent and maximal denisty confluence monolayers, established at ~ 24h, 72h and 288h respectively.

7.2.2 Fixing of MDCK cell samples for fixed cell imaging and morphology analysis

For experiments where the cell samples were required to be fixed for 3D confocal fluorescent imaging, cell samples were fixed prior to imaging and image analysis. Fixing of MDCK cells and preparation of samples was carried out to assess the selected cell line for 3D morphological variations across a cell developmental length scale using 3D confocal microscopy. MDCK cells were fixed as previously described (Chapter 3, Section 3.9.1).

7.2.3 Confocal microscopy

MDCK cell morphology from single cell through monolayer development was evaluated by confocal fluoresence microscopy. MDCK cells were prepared for confocal microscopy image acquisition and subsequent image analysis as described previously (Chapter 3, Section 3.9.3). To analyse and assess 3D MDCK morphological variations for the selected cell line, cell height, nuclear organelle z-diameter (height) and cortical membrane thickness was analysed from the aquired confocal stackes using the Imaris software XYZ stack section viewer toolbox. z-projections for each cell developmental length scale were analysed for morphology variations across each developmental length scale. To analyse variation in MDCK cell body as well as nuclear organelle area,

MDCK nuclear/Hoescht and actin/GFP fluorescent images were converted from RGB colour to 32-bit greyscale images. MDCK cell body (GFP channel) integrated intensity were detected and analysed by individually outlining and selecting each MDCK cell body using the ImageJ ROI measurement toolbox. MDCK cell body and nuclear area measurements were obtained for each MDCK developmental length scale; single cell, semi-confluent monolayer and maximal density monolayer confluence.

7.2.4 Statistical analysis of outcomes

To effectively analyse and compare MDCK morphology measurement outputs across each developmental length scale, certain statistical tests were used as described (Chapter 3. Section 3.11). Variation within each data set was assessed using standard error of the mean. To effectively analyse and compare MDCK morphology outputs across each developmental length scale, the Mann-Whitney U test was used to calculate the degree of significance between the derived MDCK morphology outputs.

7.3 Results

7.3.1 MDCK confocal and fluorescence imaging

MDCK cell morphology through monolayer development was evaluated by 2D and 3D fluoresence microscopy. For nuclear organelle and cell boundary morphology analysis, MDCK cells were bathed in Hoechst 33342 nucleic acid cell-perment nulcear counterstain (ThermoFisher), followed by fixation in 4% paraformaldeyde, and incubation with an ActinGreen ^{TM} ReadyProbe Reagent (ThermoFisher). Uptake of cell fluroesnce for each MDCK cell length scale was confirmed via a sample image test using an EVOS FLoid microscope imaging station (Figure 7-1). 3D confocal

fluorescent image stacks were aquired and analysed across each MDCK developmental length scale (Figure 7-2).

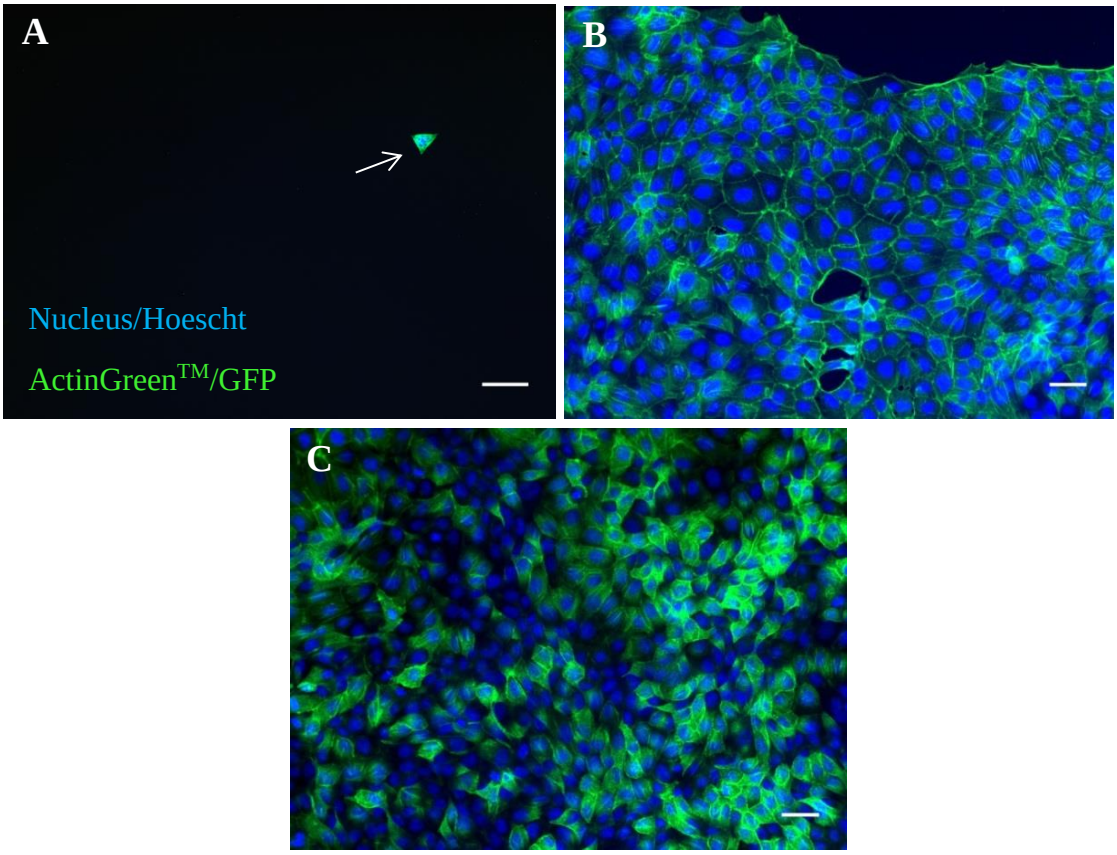

Figure 7-1. **MDCK cell fluorescent EVOS Floid imaging station micrographs**. Live MDCK cell labelling was carried out using an ActinGreen™ GFP ReadyProbe Reagent probe and Hoescht 33342 nucleic acid stain. Live MDCK cell staining was carried out for all three MDCK developmental groups **[A]** single cell (arrow detonating single MDCK cell), **[B]** semi-confluent monolayer and **[C]** maximal density monolayer confluence [Scale bars 20µm].

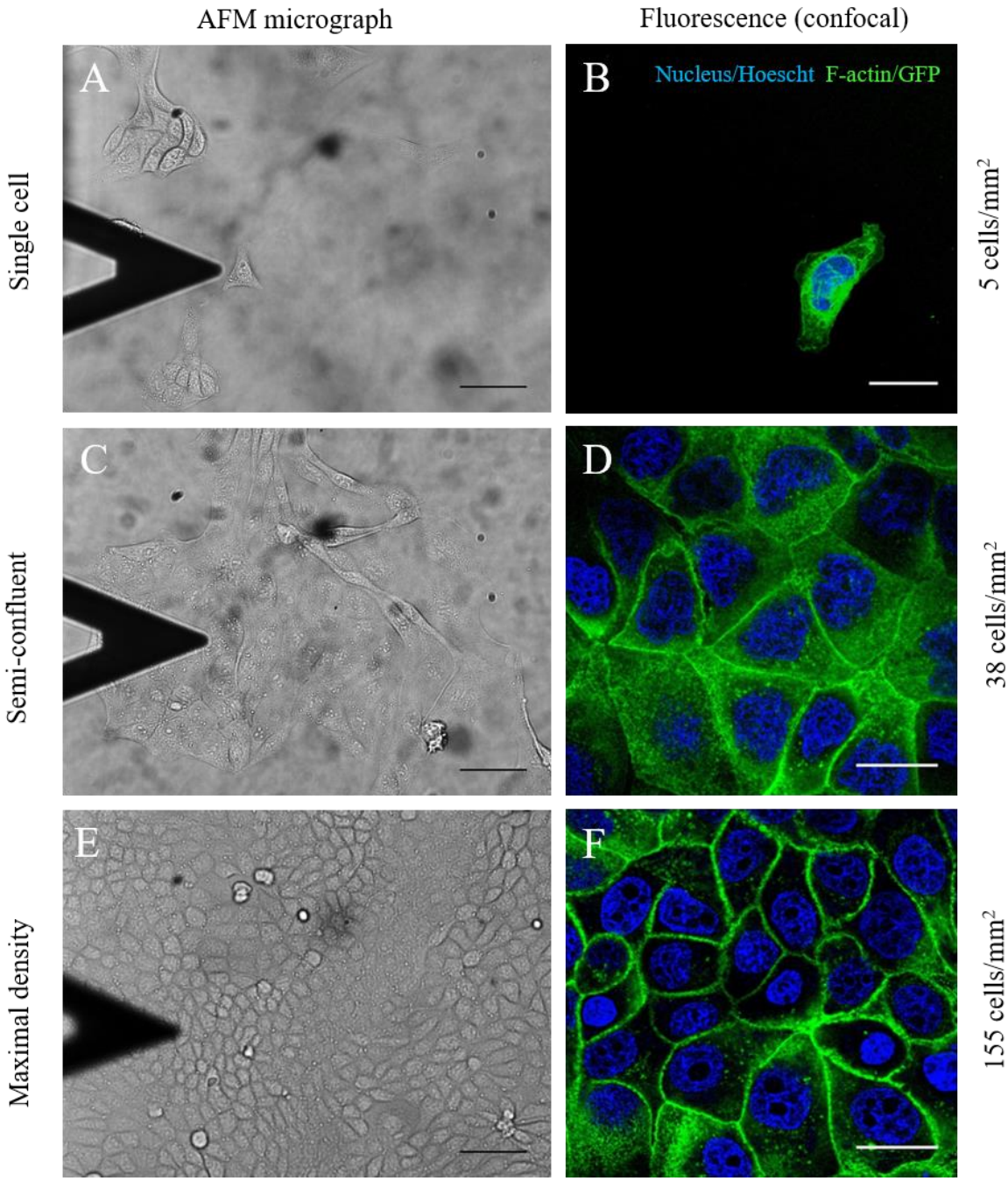

Figure 7-2. MDCK plating density for AFM elasticity and morphological analysis. AFM brightfield micrographs [A, C, and E] and confocal fluorescence [B, D and F] for single, semi-confluent and maximal density monolayer MDCK cells respectively. The AFM cantilever (colloidal probe) can be seen in the brightfield images. MDCK cell length scales were plated to develop cell densities of ~ 5, 38 and 155 cells/mm^2. Scale bars represent 50µm on the brightfield images and 20µm on the confocal images.

To analyse and assess morphological variations in MDCK cell height, nuclear organelle z-diameter and cortical membrane thickness (Figure 7-3), MDCK stacks at each length scale were projected using the Imaris XYZ stack section viewer toolbox (Figure 7-4A). MDCK z-projections for each MDCK cell developmental length scale (Figure 7-4B) were then analysed for morphology variations across each MDCK developmental length scale.

MDCK cell morphology was analysed and measurments aquired using the Imaris imaging analysis software. Following the generation of isosurface bodies for the nuclear organelle (Hoescht 33342) channel using the Imaris Surpass toolbox (Figure 7-5), nuclear organelle volume, surface area, and sphercity values were obtained for nuclei across each MDCK developmental length scale. 2D MDCK cell area (cell body) as well as nuclear organelle area were analysed using Image J (Figure 7-6).

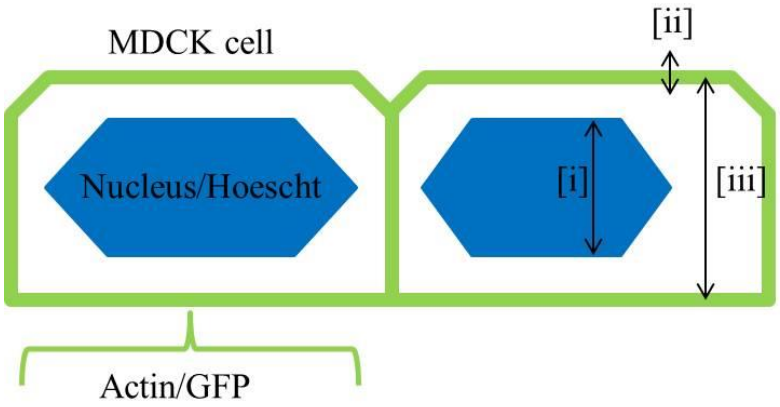

Figure 7-3. MDCK morphology measurement schematic. MDCK confocal stacks were analyzed across the Nuclear/Hoescht and Actin/GFP channels for each developmental length scale. MDCK morphological measurements (i) nuclear z-diameter (ii) actin cortical thickness and (iii) cell height were acquired from Imaris XYZ section slices.

[A] Imaris XYZ section toolbox (MDCK maximal confluence monolayer stack**)**

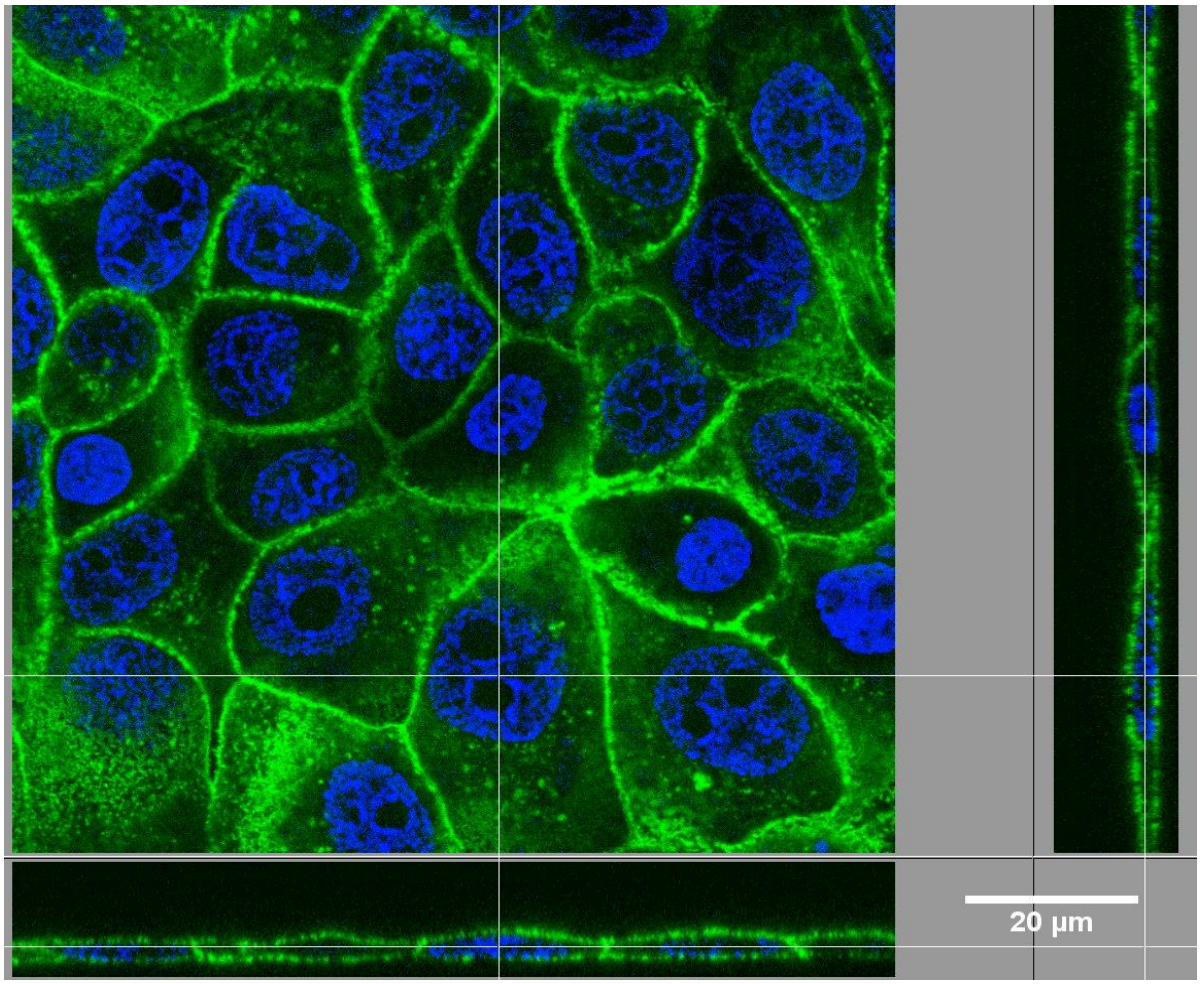

[B] MDCK z-projection slices

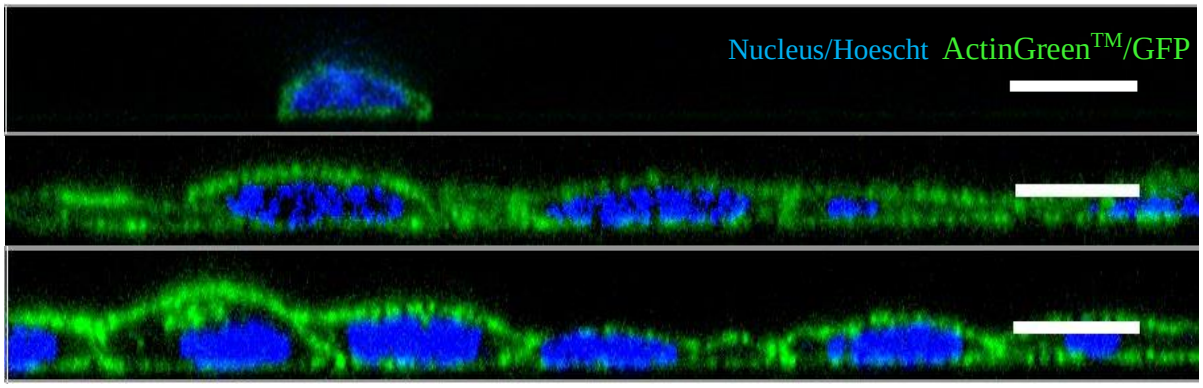

Figure 7-4. MDCK cell morphology measurements across each developmental length scale were acquired from [A] XYZ slices in the Imaris sectional toolbox **[B]** z-projection slices were used to measure and analyze variations in nuclear z-diameter, actin cortical thickness and cell height for each MDCK developmental length scale; single (top panel) semi-confluent monolayer confluence (middle panel) and maximal density monolayer confluence (bottom panel). [Scale bars 20µm].

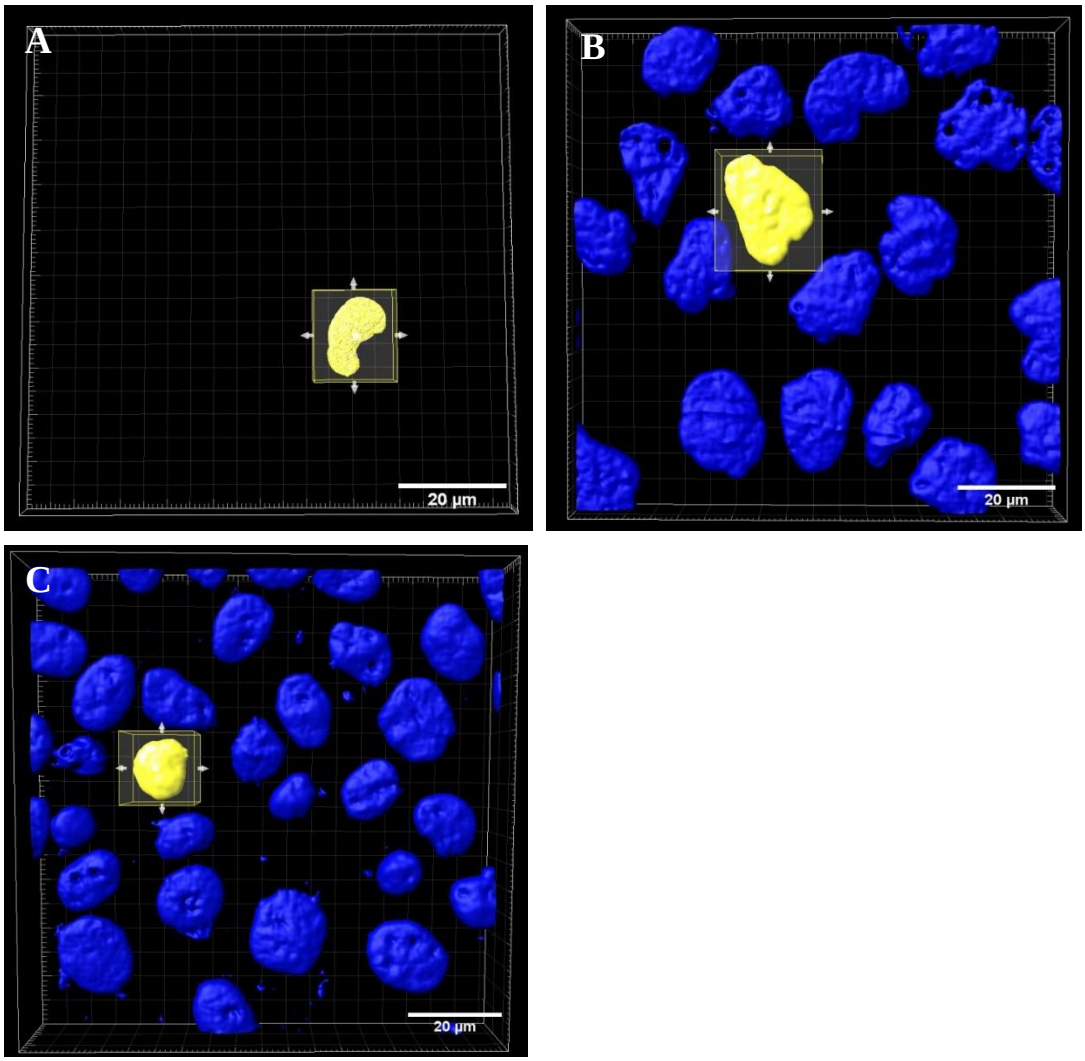

Figure 7-5. Nuclear organelle IsoSurface rendering [A] single, **[B]** semi-confluent monolayer and **[C]** maximal density monolayer confluence. MDCK cell 3D confocal stacks. Nuclear organelle surfaces were genertaed from the nuclear/Hoescht confocal stack channel. Nuclear organelle volume, surface area, and sphercity measurments were aquired for each cell developmental length scale [Scale bars 20µm].

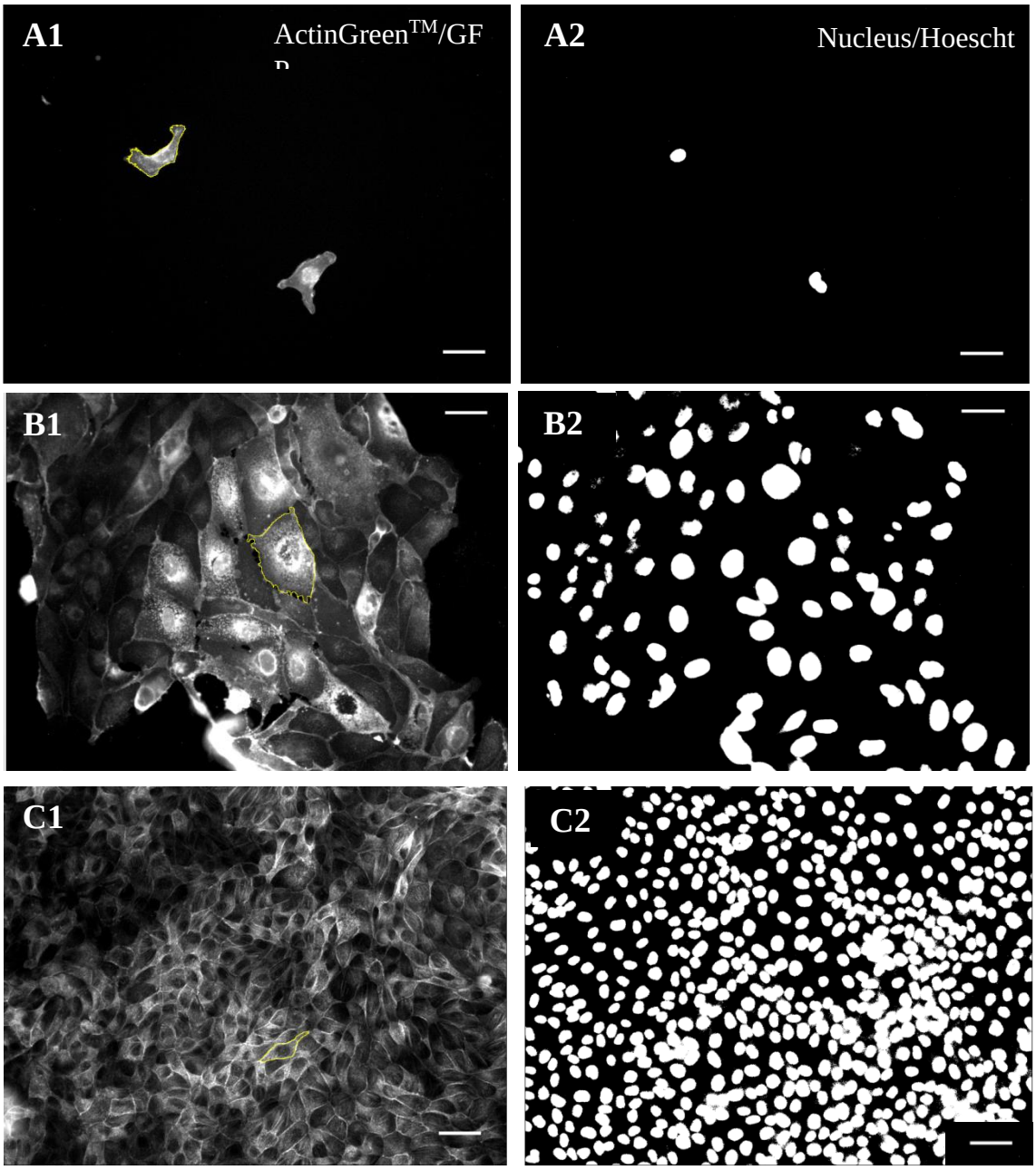

Figure 7-6. MDCK 2D morphology analysis using ImageJ ROI selection and background thresholding. 32-bit greyscale images**.** MDCK cell body selection **[A1]** Single cell **[B1]** semi-confluent monolayer and **[C1]** maximal density monolayer confluence. MDCK nuclear organelle selection **[A2]** Single cell **[B2]** semi-confluent monolayer and **[C2]** maximal density monolayer. [Scale bars 20µm].

7.3.2 MDCK cell morphology variation with progressive cell and monolayer development

MDCK cells were subjected to confocal and FLoid EVOS fluorescent imaging and morphology analysis in order to investigate how the morphology and state of cell development across an increasing developmental length scale may contribute to variation in MDCK cell indentation depth(s) and associated Young's moduli [E] trend outputs. MDCK cell area, and height, as well as nuclear organelle area and height were acquired and analysed for variation in MDCK morphology across each developmental scale. The results presented (Figure 7-7) demonstrated a significant difference ($p < 0.00001$) in MDCK cell height between all three development length scales, with single MDCK cells presenting with the greatest height (8.3 ± 2.4µm) followed by maximal density (4.3 ± 1.1µm) and semi-confluent MDCK cells (3.2 ± 0.72µm). The increase in cell height between the semi-confluent and maximal density MDCK cells is in accordance with previous findings [198]. A significant difference ($p < 0.00001$) in MDCK cell area between single and semi-confluent as well as semi-confluent and maximal density MDCK cells, with no significant difference ($p = 0.284$) between single and maximal density confluent MDCK cells was observed. Semi-confluent MDCK cells presented with greatest over-all cell area (526.3 ± 151.9µm) followed by single (217.9 ± 68.1µm) and maximal density (205.1 ± 68.8µm) MDCK cells.

Nuclear organelle height and area morphology measurements demonstrated a significant difference ($p < 0.00001$) in nuclear organelle height across all three monolayer developmental length scales, with single MDCK cells presenting with the greatest nuclear organelle height (5.6 ± 1.9µm) followed by maximal density (3.0 ± 0.93µm) and semi-confluent cells (2.1 ± 0.70µm). A significant difference ($p < 0.00001$) in nuclear organelle area between single and semi-confluent, as well as semi-confluent and maximal density MDCK cells, with no significant difference ($p = 0.190$) between single

and maximal density confluent MDCK cells. Semi-confluent MDCK cells presented with greatest over-all nuclear organelle area (161.3 ± 34.2µm) followed by maximal density (72.7 ± 18.1µm) and single (71.3 ±18.7µm) MDCK cells.

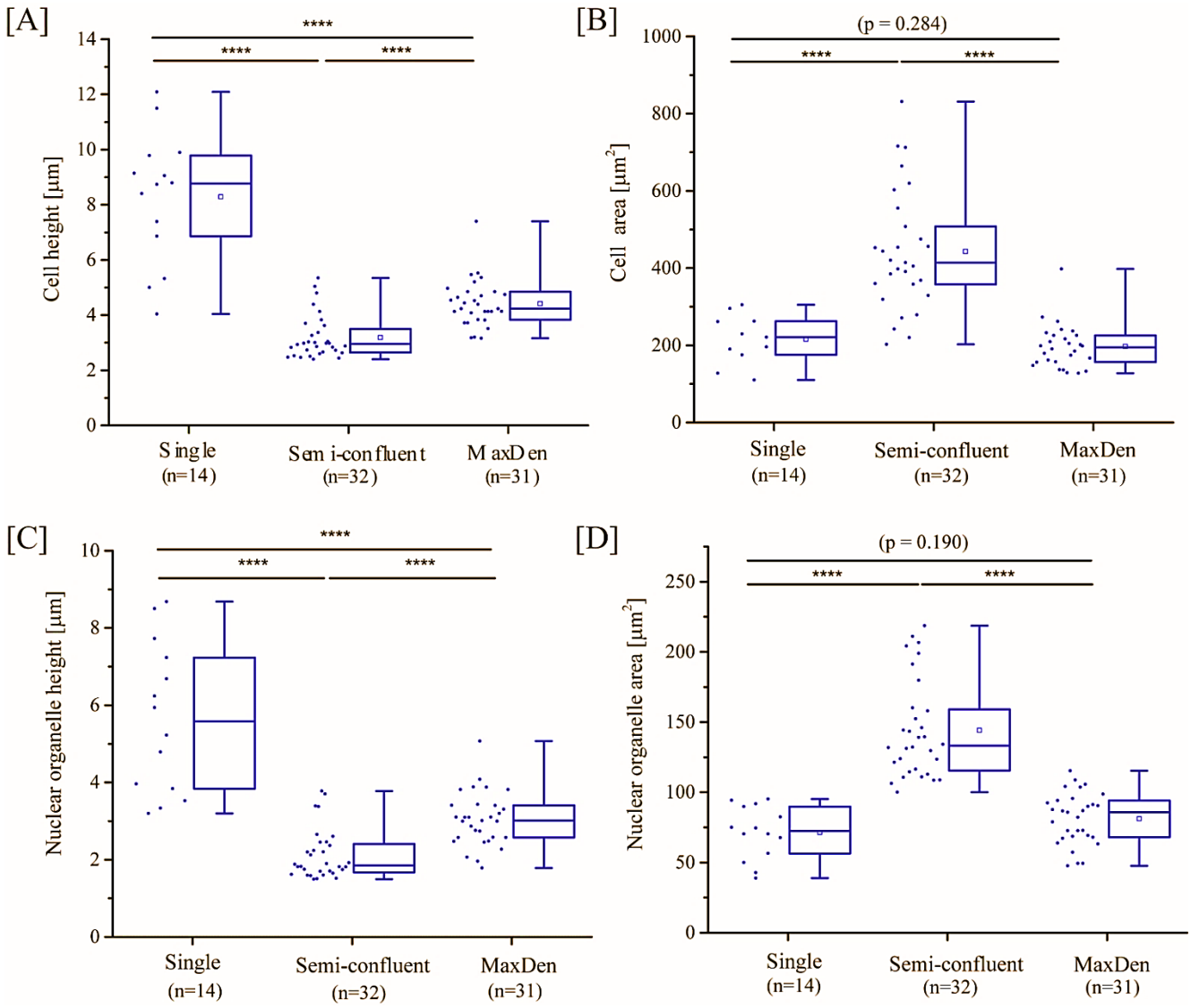

Figure 7-7. Box plots of MDCK morphology measurements for cell body height and area [A and B] and nuclear organelle height and area [C and D]. Lines within each box represent the median, the box itself presents the lower (25%) and upper (75%) quartiles, while the whiskers present the lowest and highest extreme values. Box plots display MDCK morphology output measurements for single, semi-confluent and maximal density confluence MDCK cell developmental length scales. (n) = number of MDCK cells per length scale analysed. (p-values) were calculated using the Mann-Whitney U test at .01 significance. (**** $p < 0.00001$).

The ratio between MDCK nuclear organelle area and cell body area or the – Nuclear to Cytoplasmic ratio (N: C) is shown in Figure 7-8A. The (N:C) ratio of a mammalian cell has typically been used as an indicator of cell maturity and/or nuclear mutation (in the case of cancer cell development). Typically, as a cell matures, the size of the nuclear organelle decreases, as is seen with multiple blood type mammalian cells; erythroblasts, leukocytes and megakaryocytes [200]. The results presented here demonstrate a reversal in the (N:C) ratio with cell length scale. However, development in terms of cell-cell number is not to be confused with cell-cycle maturity. The results here demonstrated that the nuclear organelle to cell body ratio remains relatively constant across each developmental length scale, and therefore, is not likely to have a direct significant contribution to the indentation and Young's elastic moduli results presented in Chapter 5. The ratio between nuclear organelle height and MDCK cell height was also analysed (Figure 7-8B), with semi-confluent monolayer MDCK cells presenting with the lowest nuclear to cell height ratio, followed by maximal density monolayer and then single MDCK cells.

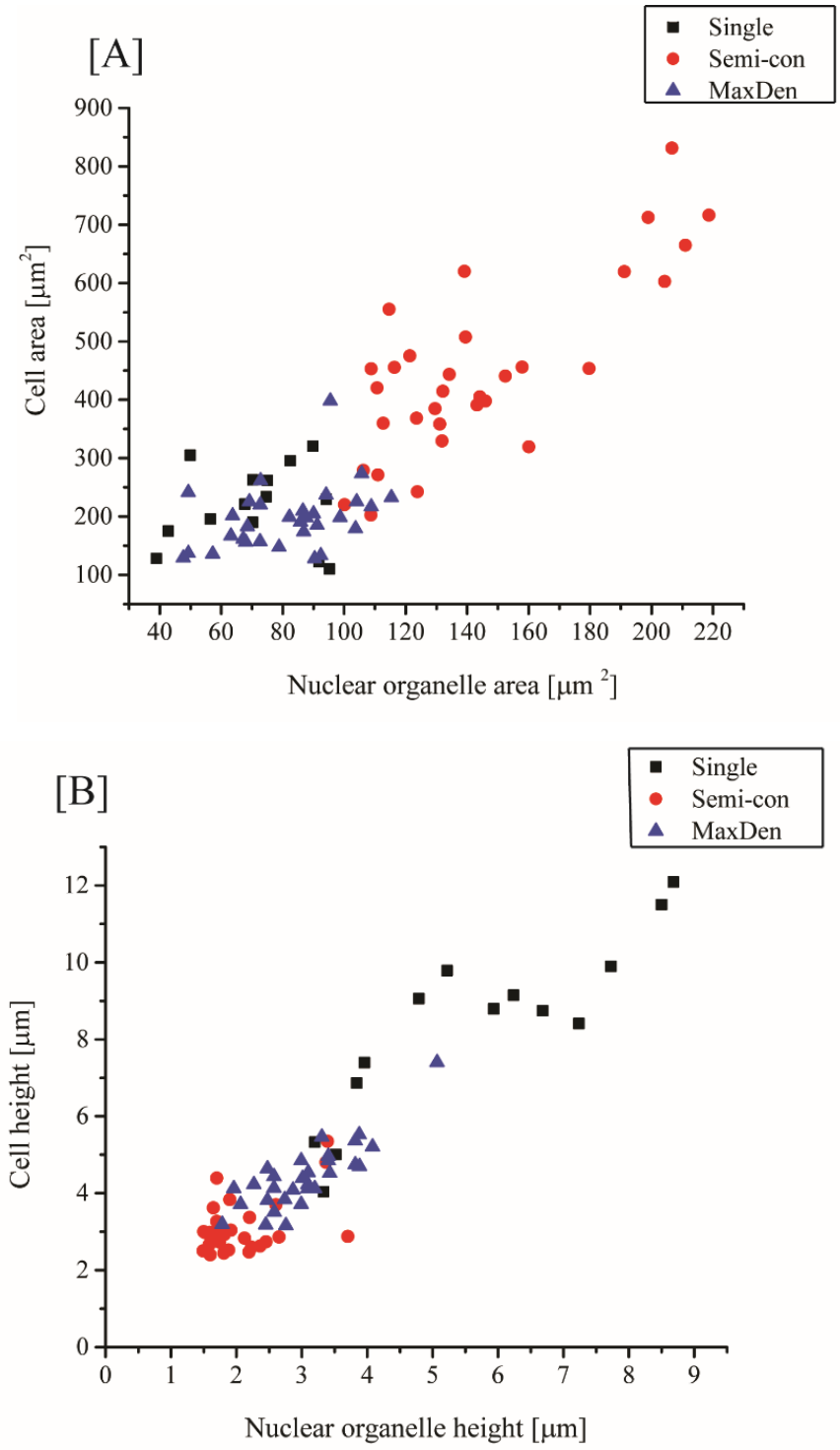

Figure 7-8. Scatter plots depicting the ratios between MDCK cell height and nuclear organelle morphology. Comparison between MDCK nuclear organelle area and cell body area [A] as well as the ratio between nuclear organelle height and cell height [B] for MDCK cells at single, semi-confluent and maximal MDCK monolayer confluence development length scales.

The MDCK cell area results presented here correlate with the compressive model narrative describing a reduction in cell area with increase in cell density [198]. Therefore, it is plausible to assume that a compressive state is evoked upon MDCK cells as they progress through monolayer development. Intermediate monolayer length scales (semi-confluent cells) present with varied cell morphological outputs compared to higher density monolayer length scales. As such, differences in the activity and architecture of the apical actin cell cortex is likely to be varied and affect the derived AFM outputs.

MDCK nuclear organelle sphericity, both (2D) and (3D), was analysed from EVOS FLoid and confocal fluorescence images (and stacks). The sphericity of an object is defined as the measure of object elipticity or platiness [201], and is derived by quantifying the ratio between the largest inscribed sphere (3D) or circle (2D) placed over an object and smallest inscribed sphere (3D) or circle (2D) within the object (Figure 7-9). A sphericity ratio tending to 1.0 describes an object of near complete sphericity (spherical). Nuclear organelle sphericity values demonstrated no significant difference for (2D) (Figure 7-10A) sphericity at each MDCK developmental length scale. Mean sphericity values for each MDCK length scale were acquired as 0.64 ± 0.14 (single cells) 0.69 ± 0.08 (semi-confluent) and 0.69 ± 0.11 (maximal density cells) Therefore, in (2D) the shape of the nucleus remains fairly uniform across the developmental length scale.

However, (3D) sphericity analyses demonstrated a significant difference in the sphericity of single (0.73 ± 0.10) and semi-confluent (0.64 ± 0.10) MDCK monolayer cells ($p < 0.001$), as well as between semi-confluent and maximal density (0.77 ± 0.09) confluence MDCK monolayer cells ($p < 0.001$) (Figure 7-10B), with no significant difference in the (3D) sphericity of single and maximal density MDCK nuclear

organelles. Since AFM indentation of the nuclear region of MDCK cells is a 3D process, 3D nuclear sphericity is of more relevance. The sphericity of MDCK nuclear organelles is fairly regular with sphericity ratios predominately above 0.5. This suggests a biological process whereby changes and the establishment of increasing cell-cell bonds may affect the inherent shape of the internal cell nuclear organelle.

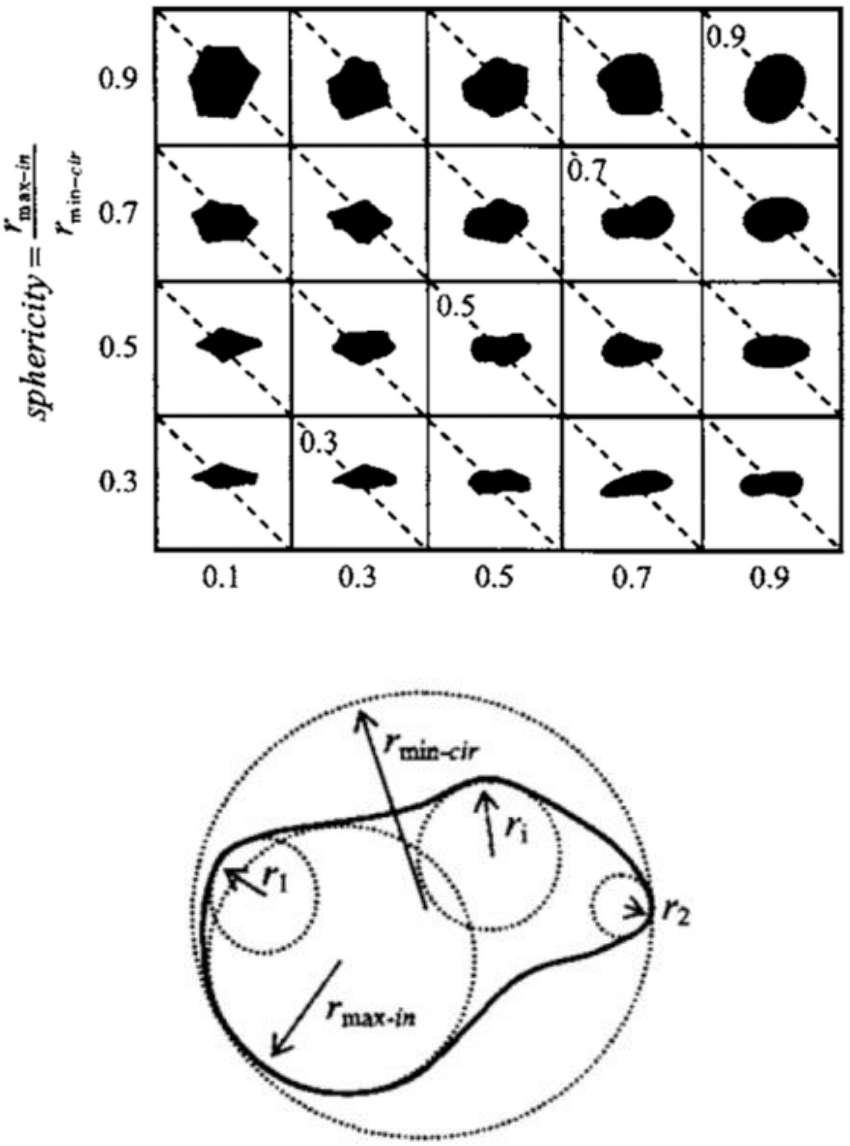

Figure 7-9. Particle shape determination (sphericity chart) (Figure, Rodriguez et al 2008) [201].

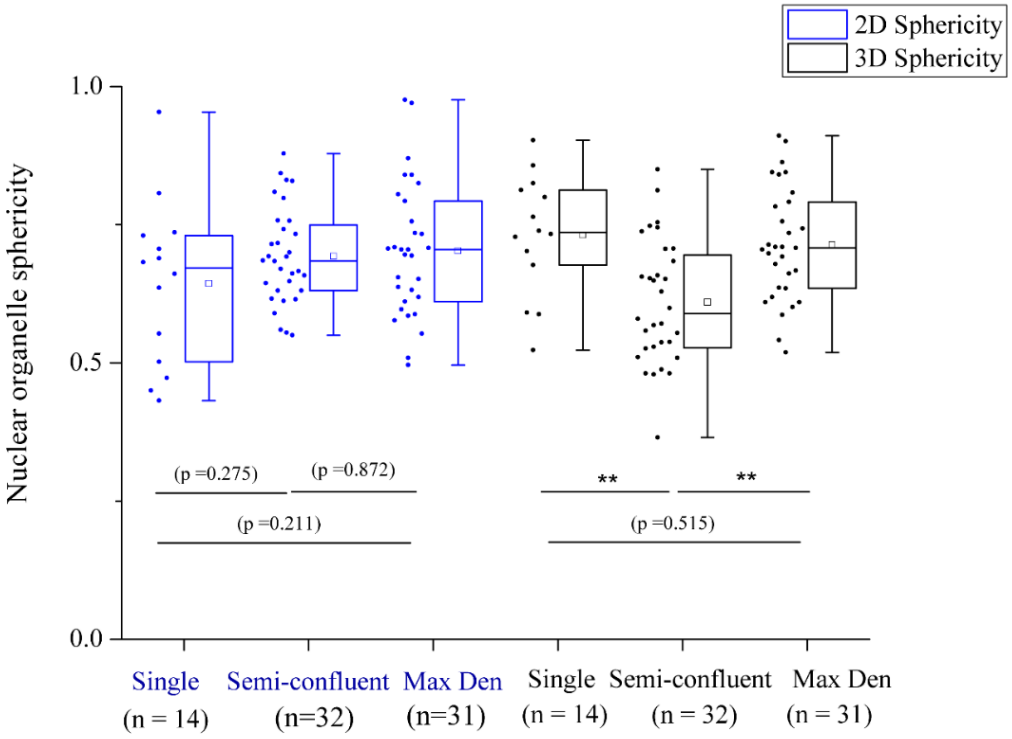

Figure 7-10. Box plots denoting (2D) and (3D) MDCK nuclear organelle sphericity. Lines within each box represent the median, the box itself presents the lower (25%) and upper (75%) quartiles, while the whiskers present the lowest and highest extreme values. Box plots display MDCK morphology output measurements for (2D) and (3D) single, semi-confluent and maximal density confluence. MDCK cell developmental length scales. (P-values) were calculated using the Mann-Whitney U test at .01 significance. (**p < 0.001). (n) = (14) single cells (32) semi-confluent cells and (31) maximal density confluence cells.

The thickness of the actin cell cortex has been estimated to range from 130nm to 1µm [90]–[93], with cortical actin mesh densities estimated at ~ 100nm [77]. As a result, it is highly probably that actin cortical thickness values for MDCK cells at different stages of monolayer development could affect the MDCK cell cortical membrane response and resistance to an external loading force such as AFM cantilever deformation. Therefore, the actin cortical thickness of MDCK cells across each monolayer developmental length scale was derived. Cortical membrane thickness measurements for MDCK cells are presented in Figure 7-11. The results here demonstrated no significant difference (p =

0.022) between the actin cortical thickness of single (1.15 ± 0.55µm) and maximal density (0.90 ± 0.44µm) MDCK cells, with significant variation ($p < 0.0001$) between single and semi-confluent (0.644 ± 0.13µm), and between semi-confluent and maximal density MDCK cells ($p < 0.001$). Across the MDCK cell developmental length scale, cortical membrane thickness decreased most significantly between the single cell and semi-confluent monolayer cells (~ 1µm to 0.6 µm), followed by a slight increase (~ 0.6µm to 0.9µm) between semi-confluent and maximal density MDCK cells.

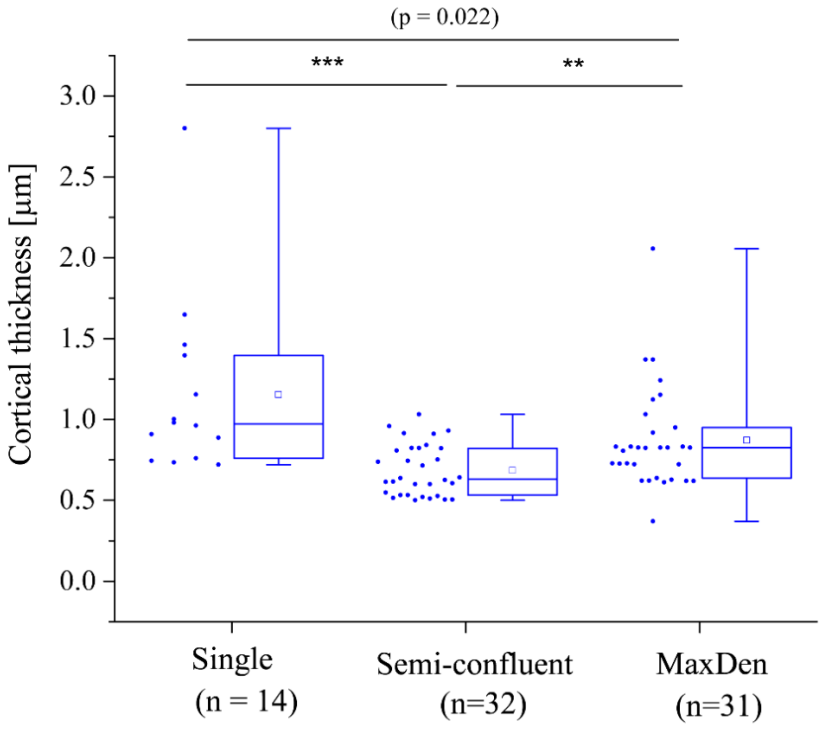

Figure 7- 11. Box plots denoting MDCK cortical membrane thickness. Lines within each box represent the median, the box itself presents the lower (25%) and upper (75%) quartiles, while the whiskers present the lowest and highest extreme values. Box plots display MDCK cortical membrane thickness for single, semi-confluent and maximal density confluence. MDCK cell developmental length scales. (P-values) were calculated using the Mann-Whitney U test at .01 significance. (**$p < 0.001$). (n) = (14) single cells (32) semi-confluent cells and (31) maximal density confluence cells.

7.4 Discussion

Differences in AFM loading force with respect to cell developmental and confluence has a significant effect on derived AFM Young's modulus elasticity output trends (Chapter 5). Given the morphological transformations that arise as a mammalian cell transitions through monolayer formation [181], [183], as well as the evidenced transition in cell morphology and proliferation with increasing cell constraint [198], differences in cantilever loading force with respect to cell monolayer developmental state and confluence can have a great effect on derived AFM Young's elastic moduli output trends, and create a potentially great deal of disparity among AFM assays investigating mammalian cell elastic properties. Notably, referring to the derived MDCK live cell morphology measurements, it is evident that cells undergo considerable morphological transitions as the degree of cell proliferation and monolayer confluency increases. The affect that such morphological variations may have on acquired AFM measurements could be accounted for by referring to the maximal indention/deformation depth and resulting elastic moduli outputs for each cell monolayer developmental scale. At similar cantilever loading set points, marginal increases in indentation depth between single, semi-confluent and maximal density cells resulted in considerable variation in calculated elastic moduli outputs with increasing cell monolayer length scale. For example, referring to an approximated cortical membrane depth of deformation (~1μm), a loading force set-point of 1.5nN (for single cells) 0.8nN (for semi-confluent) and 3.0nN (for maximal density) was required to deform the MDCK cells to the specified deformation depth. This suggests an inherent physical difference in cell membrane resistance to deformation forces, given the differences observed for cortical membrane thickness, cell height and nuclear organelle morphology. This is confirmed when referring to the calculated elasticity values for each increasing stage of cell development. i.e. cells presenting with a greater resistance

to deformation (maximal density MDCK cells) displayed stiffer elastic moduli trends across the range of loading forces, and cells presenting with less membrane resistance to deformation – single and semi-confluent cells, produced the greater indentation depth profiles, with softer elastic moduli trends.

Total MDCK cell height measurements were in accordance with previously published MDCK cell height measurements for confluent MDCK cells [179], [202]. Less evidence for cell height measurements is accounted for at the single cell length scale. Evidence for MDCK cells at ~ 15 days post seeding demonstrated columnar morphology with ~ 10-18μm heights [203]. Therefore, given the reported morphological variations that occur as a cell develops from a single cell into a maximal density fully confluent cell monolayer, changes in cell structure – particularly in cell height - could affect the response of the cortical nuclear region following AFM cantilever indentation at selected loading set-points. Furthermore, by investigating MDCK fluctuations in cell area at single and multi-cell developmental scales, it was observed that in order for cells to maintain a fixed volume as they oscillate in size (with mitosis and proliferation), they would need to enlarge in height by 20% [179]. As well as fluid exchange between increasing numbers of neighbouring cells, the role of the cytoskeletal protein myosin-2 was confirmed as a key regulator of MDCK cell volume control, with a 50% reduction in cell volume fluctuations following a myosin-2 blebbistatin inhibition assay [179]. Given the fact that myosin-2 is a key actin binding protein, and therefore major contributor to cell cortical stress and function, cytoskeletal control and morphology induced variations across MDCK cell developmental stages will likely have a substantial contribution to the varied [E] trends at alternate developmental length scales.

Fluctuations in cell volume in response to cell proliferation and collective cell movement with monolayer development may in fact result in incremental variations in

the structure and morphology of the internal nuclear organelle, as cell division and monolayer development progresses. As a result, the elasticity output generated from a deformation load over the nuclear region of a developing cell will be dependent on the height, volume and stage of cell mitosis in which the cell is undergoing. The results presented in this chapter, demonstrate a considerable variation in nuclear organelle morphology for the three MDCK cell development stages, with single MDCK cells presenting with the greatest nuclear organelle height compared to both monolayer length scales. The nuclear organelle trends here are in agreement and correlate with previous evidence demonstrating the variation in nuclear organelle height for adherent cells; single (isolated) cells have nuclear organelle heights (4-10μm) greater than those of monolayer cells (1-6μm) [204]. However, the results presented here demonstrated less variation in MDCK nuclear organelle sphericity. Therefore, is it possible to assume that the shape of the nuclear organelle remains fairly regular across the developing cell stages.

As well as MDCK cell height, area and nuclear organelle morphology dynamics, the thickness and presence of the actin cortical layer could also greatly contribute to the variation in indentation and resulting [E] trends for each MDCK developmental stage. The thickness and density of the actin cell cortex is a major controlling factor towards overall cortical mechanical function with thickness estimates ranging from 130nm to 1μm [90]–[93], and cortical actin mesh densities estimated at ~ 100nm [77]. A recent dual-colour resolution STED microscopy assay identified a mean 230 (+105/-125) nm distribution in the width between the peripheral actin cortex and cell membrane [93], with recently derived evidence revealing two different actin density populations (weak and robust)[205]. This suggests that actin polymerization varies within the defined superficial cortical shell beneath the cell membrane. Furthermore the presence and density of actin filaments within the cell cortical region has been shown to greatly affect

the elasticity profiles of cells undergoing AFM measurements, with elasticity outputs at shallow indentation depths (100-500nm) largely controlled by the macro-scale properties of the cell cortex [186], [206]. The resulting variance in AFM Young's elastic moduli outputs across different cell lines (and through monolayer development) could therefore possibly arise due to changes in the membrane cortex thickness and dynamics or density of the two defined sub-membrane actin populations. Given that cortical actin is one of the primary elements controlling cell-cell adhesion as well as cell shape, an increase in cell number with monolayer development i.e. cell migration, mitosis and volume fluctuations, will greatly affect cortical actin function and thus outward resistance to a deformation force.

Referring the results presented for the cortical thickness of the three alternate MDCK developmental stages, the apparent cortical membrane thickness reduction between single and semi-confluent MDCK cells may arise as a result of internal morphological events that arise with increase in cell area, and/or cell height. The partial increase in cortical thickness between semi-confluent and maximal density MDCK cells may however arise due to developmental of dense and short microvilli in the apical domain [178], along with incrassate apical actin [110].

While shallow AFM cantilever deformations (< 500nm) are less likely affected by any repulsive response from the nuclear organelle at deeper indentations (> 2000nm) [114], variation in actin cortical thickness, cell heights as well as nuclear organelle morphology at alternate developmental length scales may affect and complicate any derived conclusions from mammalian cell AFM Young's elastic moduli investigations. Few AFM studies directly account for the depth of indentation at selected loading forces, nor do they consider how the morphological state of the cell may affect the maximal indentation depth and/or internal size and location of the cell nucleus.

Furthermore, evidence has suggested that variations in AFM elasticity outputs are greatly affected by whether the loading depth (as a function of cantilever probe) is within the cortical superficial membrane cell surface, or greater cytoplasmic region [164]. Both regions are subject to a great amount of morphological variation through cell monolayer development.

7.5 Conclusion and summary of findings

In this chapter, the first hypothesis proposed in Chapter 6 - changes and transitions in MDCK morphology with monolayer development - may account for differences in AFM Young's elastic moduli outputs at alternate stages of monolayer development was investigated. MDCK cell morphology through progressive proliferation and monolayer development was analysed using fluorescent image analysis. The results demonstrated that at the alternative monolayer development stages investigated under cantilever indentation/deformation at a specific loading force, MDCK cell height, area, cortical thickness as well nuclear morphology can vary significantly with progressive cell monolayer proliferation. It should be noted that some structural indices were not significantly varied with cell monolayer proliferation, and remained somewhat constant. Therefore, certain MDCK cell morphological elements may not present as a valid contribution to the AFM Young's moduli trends obtained in Chapter 5. The hypothesis presented in Chapter 6, suggested that morphological attributes such as cell volume, height, shape, thickness of the cell cortex, as well as location of the morphology of the nuclear organelle may contribute to apparent varied membrane response of MDCK cells following cantilever indentation/deformation at different monolayer developmental stages. The results in this chapter showed that the most significant variation in MDCK morphology between the three developmental length scales (where statistical significance was observed between all three groups) was; cell height and nuclear

organelle height. It is plausible to assume that changes in cell height and nuclear organelle height can affect the process of cell membrane indentation. As a result, it is imperative that such events are to be considered when planning and/or attempting to interpret and compare live cell AFM mechanical property measurements for mammalian tissue analysis. A change in cell height and internal morphology of the nuclear organelle both encompass physical biological processes that would involve reorganisation and activity of the internal cell environment and cytoskeletal components. Therefore, one could assume that these two morphological changes are indirectly responsible for the AFM Young's elastic moduli MDCK cell indentation trends observed in Chapter 5.

Following on from this hypothesis, and expanding on the internal mechanisms at play during morphological alternations in MDCK development (such as cortical cell tension) will add further validation of the alternate indentation and resulting Young's elastic moduli trends observed in Chapter 5.

CHAPTER 8

Hypothesis 2: Progressive cell development of MDCK cells results in the alteration of MDCK cortical region Young's elastic moduli properties as well as variation in physical stress at the cell-cell membrane boundary

8.1 Introduction

The purpose of this chapter was to investigate if the variations observed in MDCK cell Young's elastic moduli trends through monolayer development (Chapter 5), arise due the second cellular mechanism hypothesized in Chapter 6: The progressive division and development of MDCK cells as a cell monolayer forms results in increased cellular stress and variation in the Young's elastic modulus along the cell cortical region and cell-cell membrane boundary. In Chapter 7, the most notable morphological transformations of MDCK cells at three different stages of monolayer development was presented. It was observed that while certain MDCK morphological attributes did in fact change between different MDCK monolayer length scales, only some were significantly different through different stages of cell monolayer development. Whether or not MDCK cell morphology is solely responsible for the varied indentation results produced in Chapter 5 is still unclear. However, it should be noted that whole cell structural changes are inherently governed by internal cytoskeletal components such as the actin filament meshwork in the cell cortex. Therefore, investigation, by means of further AFM indentation; force mapping analysis of MDCK cells undergoing incremental stages of monolayer development was carried out in this chapter. This was carried out to clarify if the Young's moduli trends observed in Chapter 5 arise as a result of the variation and increased stress in the MDCK actin cortical layer and MDCK cell-cell

boundary region as a result of the formation and maturation of increasing cell-cell junction complexes. The thickness and density of the actin cell cortex is a major contributing factor towards Young's elastic moduli outputs trends, with actin cortex thickness estimates ranging from 130nm to 1µm [90]–[93], and cortical actin mesh densities estimated at ~ 100nm [77].Furthermore, given the evidence demonstrating the downregulation of cortical actin density along the cell-cell junction interface for multiple cell lines [82]–[86], the aim of this chapter was to analyse the theory of actin cortex gradient transitions and downregulation at cell-cell interface junctions by analysing AFM Young's moduli elasticity outputs pertaining to the inner cell cortical layer across a more precise incremental MDCK cell developmental length scale. To do this, 8 × 8 force map indexes were acquired for the nuclear cortical region of MDCK cells at incremental stages of cell division and monolayer development, as well as along the cell-cell boundary interface (at 32 × 32 map indexes). The MDCK developmental stages specifically analysed using AFM indentation were (1) single, (2) cell doublet pair, (3) internal cell cluster cell, (4) periphery cell cluster cell and (5) semi-confluent and (6) maximal density monolayer confluence cells.

To ensure that Young's elastic moduli trends pertaining to the inner actin filament cortex was examined, force map indexes at a loading force of 0.8nN were acquired for each MDCK cell sample stage. Based on the indentation depths achieved for each developmental length scale at 0.8nN (Ch5. Section 5.3.1), a 0.8nN loading force was selected such that it would encompass a suitable range of deformation depth for the actin cortical region thickness (130nm – 1µm) previously evidenced [90]–[93]. By using a relatively low loading force, any mechanical affects pertaining to the presence of the inner nuclear organelle at deformation depths of ~2-4µm could then be avoided [114].

Derived AFM Young's elastic moduli results for each MDCK cell developmental parameter were then analysed for trends across the MDCK cell developmental stages using two approaches; (1) Young's elastic moduli trends for MDCK cortical regions at developmental stages using appropriate indentation depths for the nuclear region of the MDCK cells at the limits discussed for the Hertz-Sneddon contact model, and (2) AFM Young's moduli [E] trends for MDCK cell (whole cell force mapping) at incremental stages of cell monolayer development to analyse the cell junctional regions (at appropriate cantilever deformation depths for correct application of the Hertz-Sneddon contact model.

8.2 Materials and methods

The materials and methods used to carry out the force mapping AFM assays in this chapter are detailed as follows;

8.2.1 Cell culture

MDCK cells were cultured, maintained and prepared for AFM experimentation as described previously (Chapter 3. Section 3.3 – 3.6). As with previous MDCK AFM indentation assays, only properly attached MDCK cells were selected for AFM indentation. To prepare the MDCK cell AFM samples at the selected incremental cell length scales, MDCK cells were suspended and plated at low seeding densities (~2 x 10^3) to ensure the presence of single attached cell phenotypes. Prepared AFM sample dishes were monitored closely for each required cell length scale phenotype. Single, cell doublet pair, cell cluster and cell monolayer (semi-confluent and maximal density) cells were indentified (on average) at around 24h, 24-48h, 48h ,72h and 288h respectively.

8.2.2 Cantilever probes

Colloidal geometry cantilevers, as detailed (Chapter 3. Section 3.7.3- 3.7.5) were used for the live MDCK cell AFM indentation in this chapter.

8.2.3 AFM

All AFM elasticity measurements (force-displacement curves) were obtained in force mapping contact mode (described previously Chapter 3. Sections 3.7.7). For nuclear region force mapping, force map indexes of 8 × 8 pixels (64 force-displacement curves) were acquired with a 0.8nN loading force. For nuclear region force mapping at 0.8nN, a total of 10 MDCK cells per developmental stage (6 groups) was acquired. For MDCK cell boundary and cell-cell junction force mapping, force map indexes of 32 × 32 pixels were acquired with a 0.8nN loading force. All MDCK force maps were gathered over an experimental period of no more than 1 hour per sample dish. As previous, indentation extend speed (8 μm/s^{-1}), Z-length (4 µm) and sampling rate (4096 Hz) parameters were kept uniform for each consecutive experiment to allow for data output reproducibility and accurate application of the Hertz-Sneddon contact model. For force mapping of MDCK cell-cell interface boundary regions, the amount of 32 × 32 force map indexes for each developmental length scale are; (4) single cell maps, (3) doublet pair maps, (2) cluster of cells maps, (3) semi-confluent monolayer maps and (4) maximal density monolayer maps.

8.2.4 Live MDCK cell fluorescent imaging – AFM optical overlay

MDCK cell nuclear regions were identified using a live cell transfection protocol for GFP targeting the actin protein network (Chapter 3. Section 3.8.1). AFM direct optical overlay (Figure 8-1) was carried out to locate nuclear organelle regions.

8.2.5 MDCK actin GFP fluorescence intensity analysis

MDCK actin GFP fluorescence intensity through monolayer development was evaluated by 2D fluoresence microscopy. For actin intensity analyses MDCK cells were fixed and incubated with an ActinGreen ™ ReadyProbe Reagent (ThermoFisher) as previously described (Chapter 3.Section 3.9.1). Uptake of the ActinGreen ™ ReadyProbe was confirmed as descibed previously (Chapter 3. Section 3.8.2). Actin/GFP channel intensity was analysed for variations across each developmental length scale using the integrated density (IntDen) measurement function within the ImageJ measurements toolbox, as described (Chapter 3. Section 3.8.2).

8.2.6 Data processing – MDCK Young's elastic moduli analysis

All obtained force-displacement curves were analysed by fitting the Hertz-Sneddon contact model for a spherical cantilever to the force curves obtained for all 0.8nN loading force maps. The contact model was applied to indentation ranges within the limits described for the appropriate application of the Hertz-Sneddon contact model.

8.2.7 Statistical analysis of outcomes

To effectively analyse and compare MDCK Young's elastic moduli measurement outputs across each MDCK monolayer developmental length scale, certain statistical tests were used as described (Chapter 3. Section 3.11). Variation within each data set was assessed using standard error of the mean. To effectively analyse and compare MDCK Young's elastic moduli outputs across each developmental length scale, the Mann-Whitney U test was used to calculate the degree of significance between the derived MDCK Young's elastic moduli outputs.

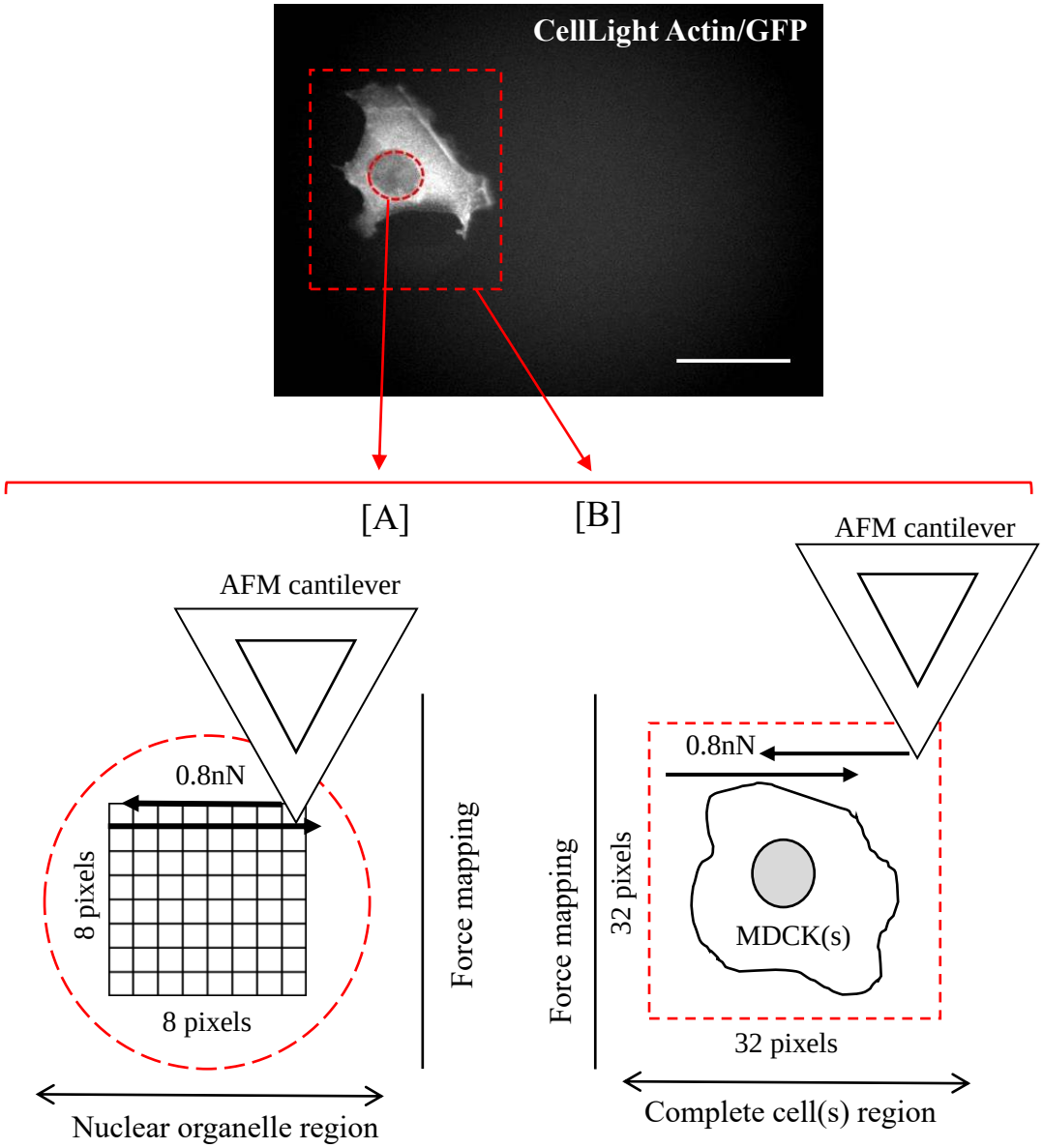

Figure 8-1. Single MDCK cell AFM fluorescent micrograph in greyscale. The MDCK nuclear region was identified as the cell region lacking any prominent actin GFP fluorescence marker signal. **[A]** Nuclear region 8 × 8 Force map scan indexes (64 indentations in total) were selected for the chosen 0.8nN loading force of the MDCK cells. Each MDCK force map index was kept within the apparent measured nuclear region boundary. **[B]** MDCK cell boundary and cell-cell junction interface regions were analysed by acquiring whole cell 32 × 32 force map indexes for MDCK cells at each development length scale [Scale bar 20µm].

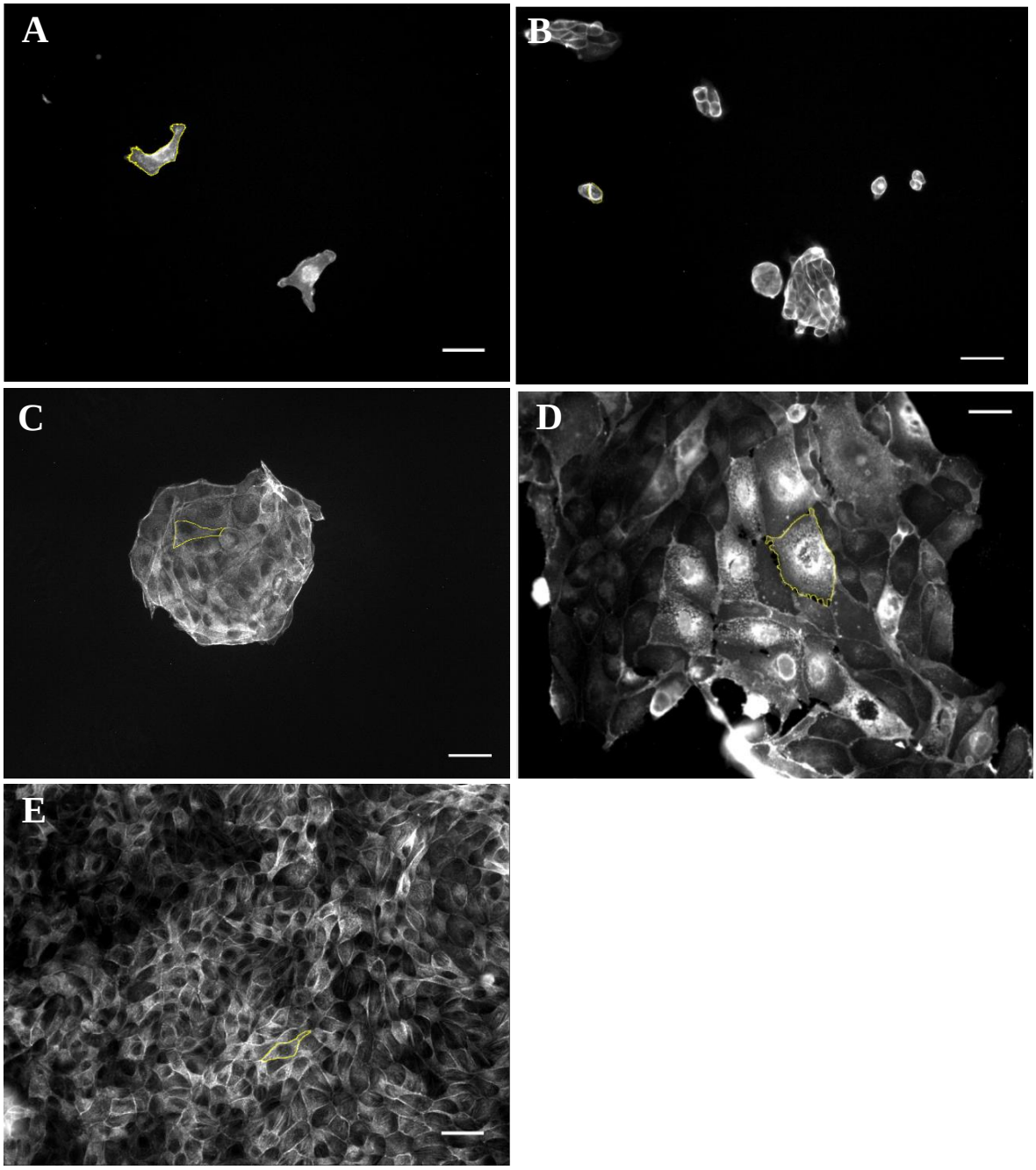

Figure 8-2. **MDCK actin GFP fluorescence analysis using ImageJ ROI selection and background thresholding**. MDCK EVOS FLoid Actin/GFP fluorescent images were converted from RGB colour to 32-bit greyscale images. MDCK cell body (GFP channel) edges and integrated intensity were detected and analysed by individually outlining and selecting each MDCK cell body using the ImageJ ROI measurement toolbox. MDCK cell body area and actin GFP signal intensity measurements were obtained for each developmental length scale; **[A]** single cells **[B]** doublet pair cells **[C]** cells forming a cell cluster (internal and periphery), and **[D]** semi-confluent monolayer and **[E]** maximal density confluence MDCK cells [Scale bars 20μm].

8.3 Results

8.3.1 Live MDCK cell AFM optical overlay for defined increasing cell developmental length scale

Optical overlay micrographs for MDCK cells at each stage of cell monolayer development length scale (Figure 8-3) were acquired using the AFM image overlay tool to position the cells within the 100µm/100µm AFM force map scanning range limits (Ch3. Section 3.7.5). The nuclear region of the cells was identified as the non-labelled (central) portions of the cells.

8.3.2 MDCK cell cortex Young's elastic moduli trends with increase in stage of cell monolayer development and confluence

To ensure that the derived MDCK Young's elastic moduli trends were those pertaining the inner actin filament cortex, force map indexes were acquired at a loading force of 0.8nN. This loading force was selected to achieve suitable deformation depths that would encompass a suitable range of deformation depth for the actin cortical region thickness (130nm – 1µm) previously evidenced [90]–[93]. By using a low loading force, it was also possible to attempt to avoid any mechanical contribution of the inner cell nuclear organelle at greater deformation depths of ~2-4µm [114]. MDCK cortical region Young's elastic moduli trends across incremental stages of cell monolayer development was analysed by AFM force mapping. To do this, force map indexes for the nuclear region of the MDCK cells at each stage of confluence and monolayer development was acquired. As demonstrated in Chapter 4 (section 4.3.4), the nuclear cell body region is most appropriate for deriving and analysing Young's moduli trends for live mammalian cells due to the thickness and height of the cell body region falling within the limits of sample thickness for an appropriate Hertz-Sneddon model fit. The cell body region of the MDCK cells was found to encompass cell heights (thickness)

limits that could allow for application of the Hertz-Sneddon contact model. For the force mapping Young's elastic moduli data acquired in this chapter, the same consideration regarding the height and thickness of the MDCK cell samples was taken into account when deriving the Young's elastic moduli outputs using the Hertz-Sneddon contact model. The height of the sample was acquired from the height set-point channel of each acquired force map. This then allowed for the calculation of what the most suitable indentation depth would be to apply the Hertz-Sneddon model fit i.e. A maximum of 10% total MDCK cell sample thickness (the nuclear cell body region being the indentation point of reference). In the case of the nuclear body region force maps acquired the heights of the MDCK cell samples were found to be as follows; for single MDCK cells, 5.6µm- 9.1µm. For doublet pair MDCK cells, 6.6µm – 8.6µm. For MDCK cluster cells (internal of the cluster), 5.4µm – 8.2µm. for MDCK cluster cells (periphery external cluster cells) 5.6µm – 7.6µm. For semi-confluent MDCK monolayer cells, 5.9µm – 7.5µm. For fully confluent maximal density MDCK monolayer cells, 5.8µm – 6.7µm.

In each MDCK cell sample, for each instance (depending on the precise maximal height of each MDCK cell within a sample group) consideration was given such that only a maximum of 10% of the thickness of the cell sample was analysed using the Hertz-Sneddon contact model. In the case of the MDCK cell groups, this resulted in the fitting of the Hertz-Sneddon contact model to MDCK cell indentation/deformation depths (at the cell nucleus/body region) as follows; For single MDCK cells, 562nm-901nm, for doublet pair MDCK cells, 663nm-860nm. For MDCK cluster cells (internal cluster cells), 546nm – 824nm. For MDCK cluster cells (periphery external cluster cells), 575nm – 761nm. For semi-confluent MDCK monolayer cells, 598nm -704nm. For fully confluent maximal density MDCK monolayer cells, 588nm – 672nm. The MDCK

deformation limits analysed with the Hertz-Sneddon contact model were within the region and range of the inner actin cortex layer referenced in the literature.

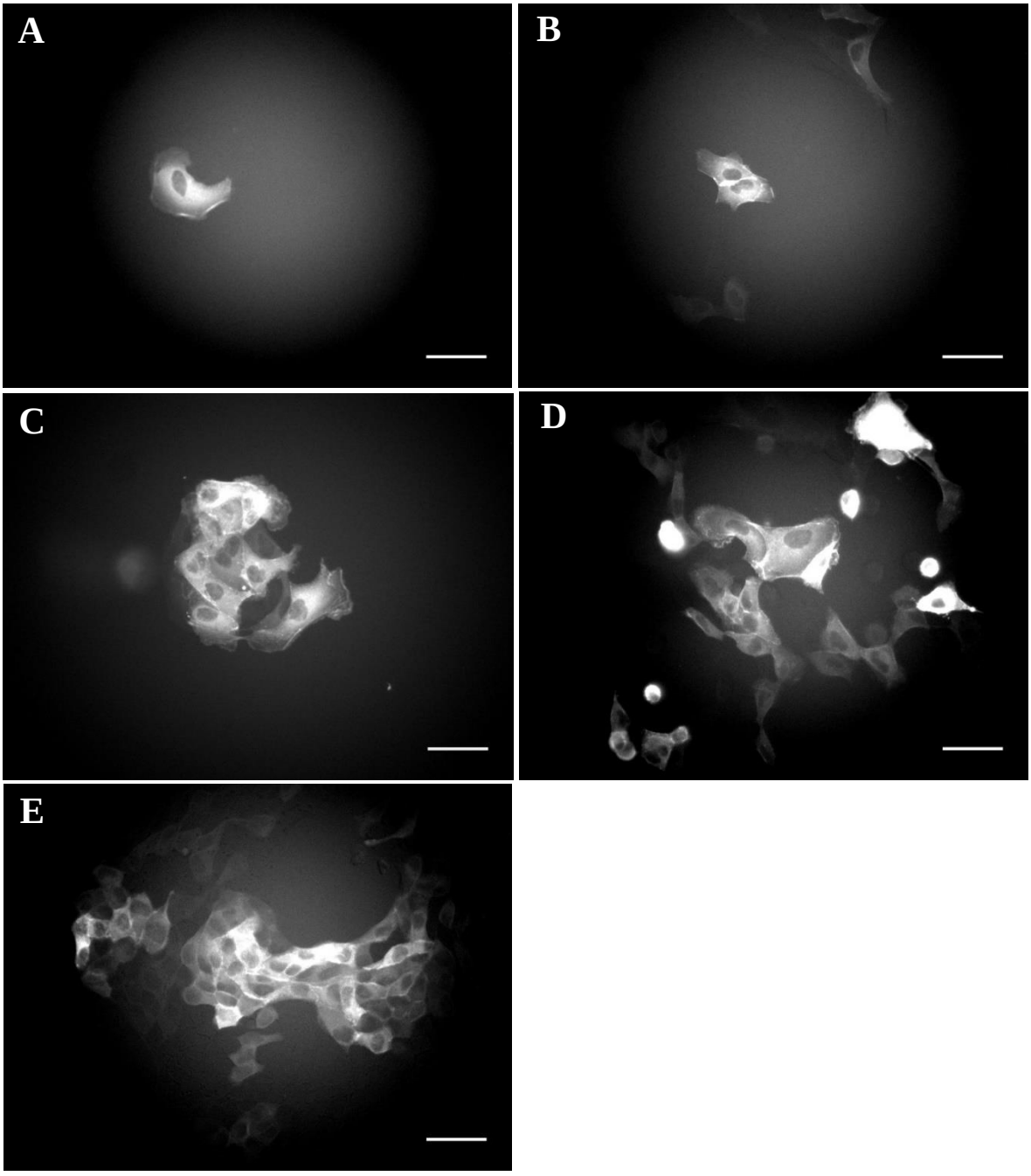

Figure 8-3. Example AFM optical overlay micrographs for actin GFP labelled live MDCK cell samples. Optical overlay images were acquired prior to all AFM indentation experiments for each cell length scale parameter **[A]** single cells **[B]** doublet pair cells **[C]** cells forming a cell cluster (internal and periphery), and **[D]** semi-confluent monolayer and **[E]** maximal density confluence MDCK cells [Scale bars 20μm].

Figure 8-4 illustrates an example Young's moduli stiffness map and corresponding height map for the nuclear region of a single MDCK cell. The example shown demonstrates the colour scale of data (Young's elastic moduli) for a Hertz-Sneddon model fit to 10% of the sample indentation range.

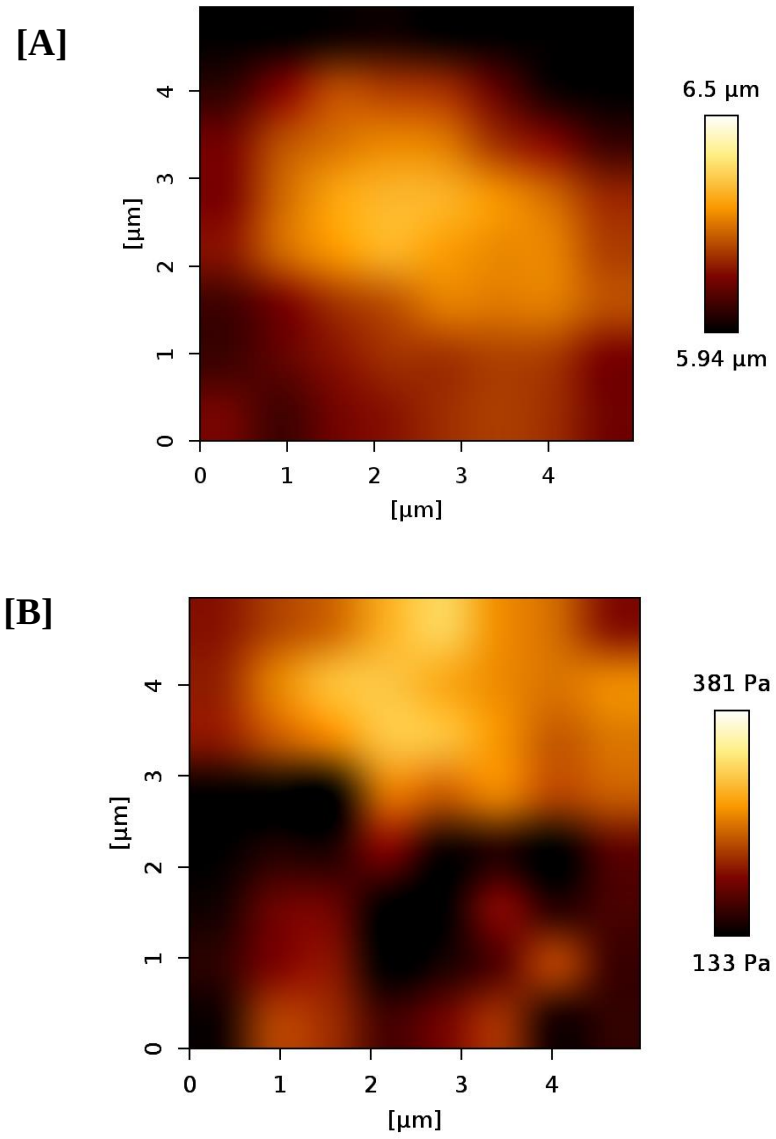

Figure 8-4. Example JPK Young's elastic modulus stiffness map **[A]** and corresponding height map **[B]** for a single MDCK cell (nuclear region) analysed to derive the Young's elastic modulus at 10% of the maximal indentation height (thickness of the MDCK sample).

A MATLAB re-plot for the nuclear region of the MDCK cell height and Young's moduli stiffness map was carried out for a more precise presentation and visualisation of the values derived (Figure 8-5). Each point of the height and stiffness map represents a single indentation within the MDCK force map index.

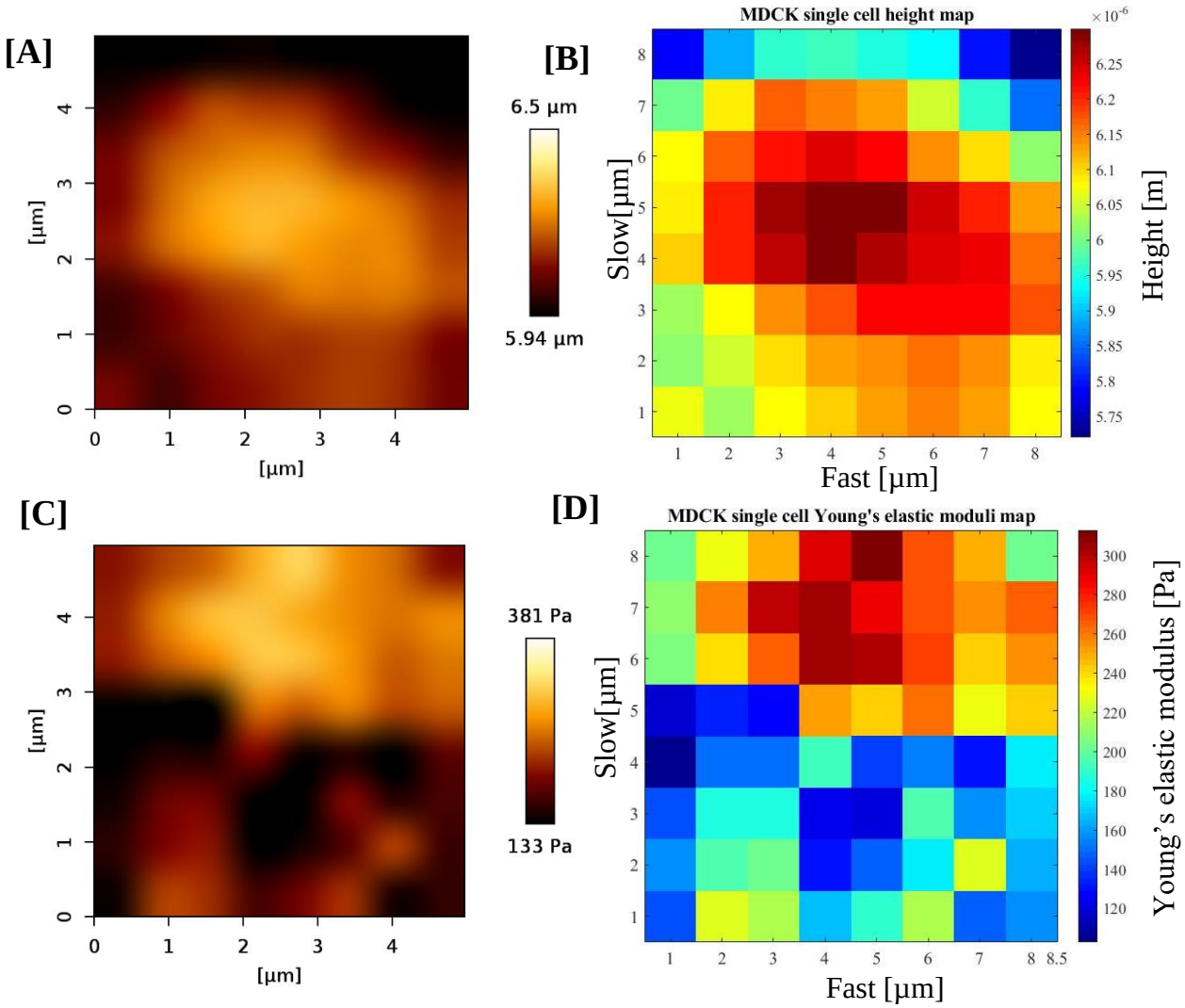

Figure 8-5. MDCK JPK force map index **[A]** height map and **[B]** Matlab re-plot with resulting JPK **[C]** Young's elastic modulus stiffness map and **[D]** Matlab replot. The representative derived Young's elastic modulus value of each force map pixel of the MDCK nuclear region is shown by the Youngs elastic modulus channel. Derived Young's elastic modulus points across nuclear region force maps demonstrated the mechanical properties are nonhomogeneous across the nuclear region of an MDCK cell.

The MDCK height and Young's elastic moduli force maps presented, demonstrated that while the height of an MDCK cell appears to peak in an approximate central region of the map, the resulting derived Young's elastic modulus values are not uniform across the nuclear region of the MDCK cell. Peaks in Young's elastic moduli values can be seen across multiple locations of the MDCK force map. This suggests an inherent heterogeneity in the mechanical function of the MDCK cell cortical region.

In order to assess and compare MDCK nuclear region force map indexes acquired here to the results obtained for the nuclear region indentation results presented in Chapter 5, single, semiconfluent and maximal density MDCK cells were first analysed for Young's elastic moduli trends (Figure 8-6A and B). Young's moduli trend the for the actin cortex region (deformation depth analysed) for the MDCK cells demonstrated a significant ($p < 0.00001$) variation in the derived Young's moduli trends across the three MDCK monolayer confluence developmental lengths scales. The resulting derived Young's moduli trends demonstrated an increase in MDCK cortical stiffness (Young' elastic modulus) between single (231.2 ± 114.6 Pa) and semi-confluent (346.5 ± 139.1 Pa) length scales, followed by a decrease between semiconfluent and maximal density confluence MDCK cells (245.9 ± 63.8 Pa). The results here do not agree with the indentation trends results demonstrated in Chapter 5. Here, higher MDCK cell length scales do not result in increased derived Young' elastic modulus trends as demonstrated in Chapter 5. This was the case for the data presented in Chapter 5 at the 0.8nN loading force. The difference in the trends presented here, may arise due to the method of analysis of the force indentation curves. Here, the data points for each MDCK developmental group were assessed for sample height (thickness) such only an appropriate region of the indentation curve was used to apply the Hertz-Sneddon contact model (a maximum of 10% sample thickness).

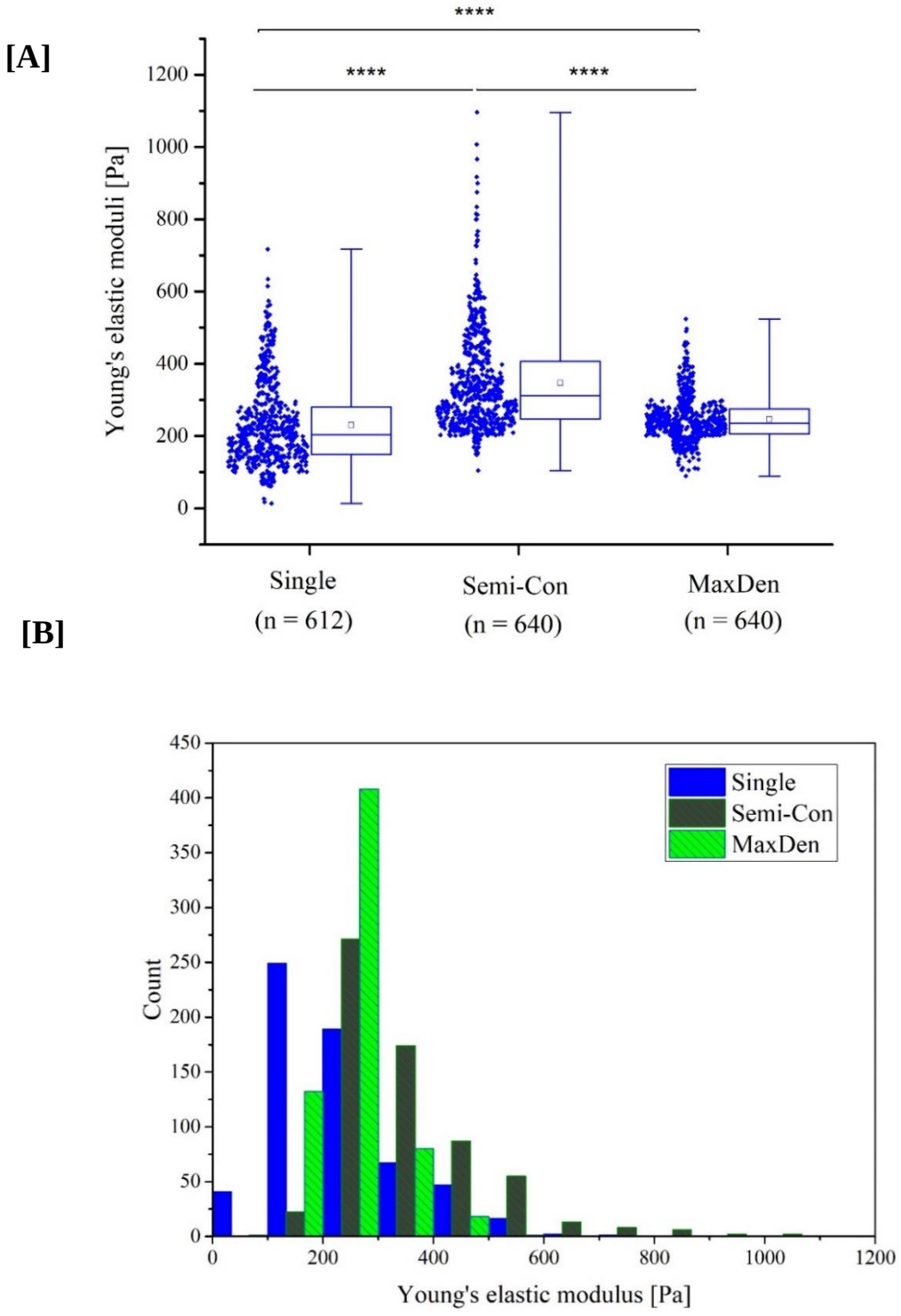

Figure 8-6. [A] Box plots and [B] histogram distributions denoting the 0.8nN force map Young's elastic moduli distributions for MDCK monolayer length scales. Lines within each box represent the median, the box itself presents the lower (25%) and upper (75%) quartiles, while the whiskers present the lowest and highest extreme values. Box points represent the means of each cell data cohort. (p-values) were calculated using the Mann-Whitney U test at .01 significance. (**** $p < 0.00001$). (n) = number of data points gathered for each MDCK developmental condition.

The results here demonstrate that the material properties of the MDCK cells do vary at specified indentation/deformation depths. Previous literature has shown that at higher cell densities and confluence, MDCK cells show an increase in dense and short microvilli in the apical domain, along with incrassate apical actin [110]. The presence of such biological components was thought to contribute to the increased Young's moduli trends presented in Chapter 5. However, in this chapter, the whole indentation range at alternate cantilever loading forces was not addresses, but rather, the material properties of the MDCK cells at a specified cantilever loading force to investigate the actin cell cortical region. The results presented here further demonstrate (and coincide) with the narrative presented in chapter 5, that care must be given when utilising different cantilever loading force ranges in mammalian cell AFM studies. What cell property and parameter are being investigated can be different depending on the deformation depth as well as contact model (correct application of the contact model) chosen. Apical region transformations through MDCK monolayer development could contribute to the variation in MDCK cell membrane resistance and AFM derived Young's elastic moduli outputs for each MDCK cell monolayer developmental stage.

To further investigate and address how MDCK cortical Young' elastic moduli trends are affected by the initial formation and development of cell-cell bonds, force map indexes for the nuclear region of MDCK cells at an incremental cell developmental length scale were then analysed (Figure 8-7A and B). The same consideration was taken in terms of application of the Hertz-Sneddon contact model to derive Young's elastic moduli trends within the limit of MDCK cell sample thickness. This was carried out for MDCK doublet pairs, as well as peripheral cluster and cells within a cell cluster, and were included in the length scale analysis.

[A]

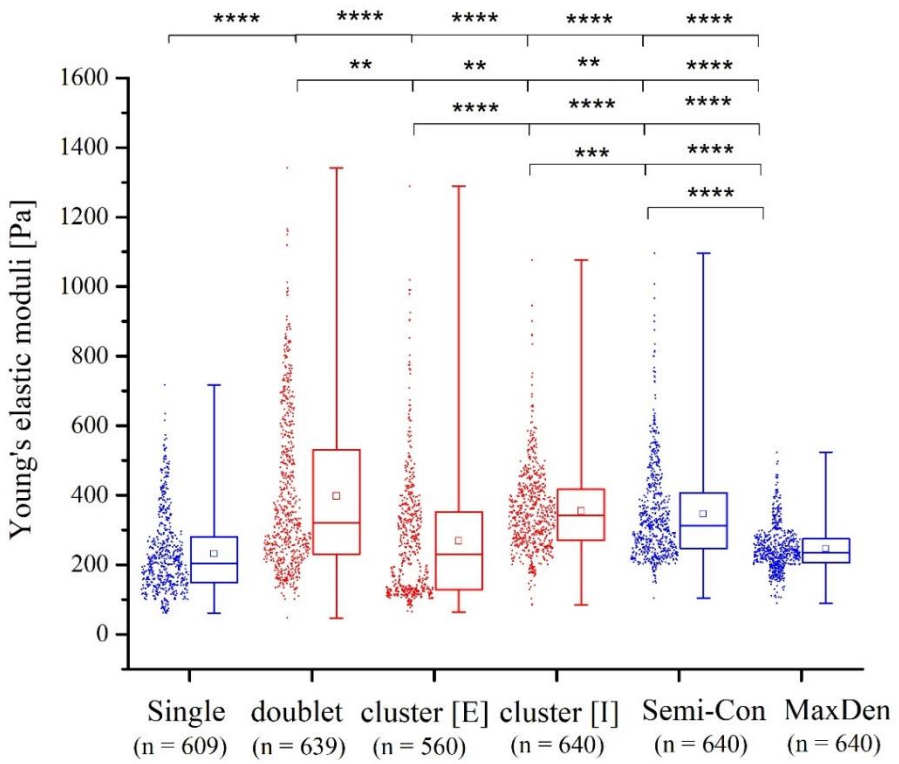

[B]

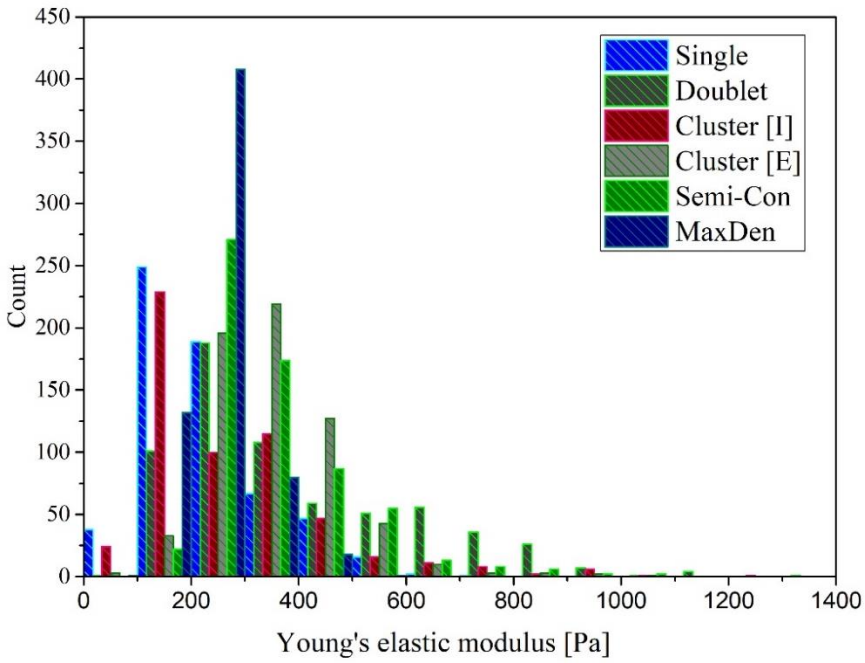

Figure 8-7. [A] Box plots and [B] histogram distributions denoting the 0.8nN force map Young's elastic moduli distributions for intermediate MDCK monolayer length scales. Lines within each box represent the median, the box itself presents the lower (25%) and upper (75%) quartiles, while the whiskers present the lowest and highest extreme values. Box points represent the means of each cell data cohort. (p-values) were calculated using the Mann-Whitney U test at .01 significance. (**** $p < 0.00001$, *** $p < 0.0001$, **$p < 0.001$). (n) = number of data points gathered for each MDCK developmental condition.

Young's elastic moduli trends derived the MDCK nuclear cortical region for incremental stages of monolayer development (doublet pair, and cluster cells) demonstrated a significant ($p < 0.00001$, and $p < 0.001$) variation in the Young's moduli elastic properties across the incremental developmental stages of cell proliferation.

Referring to figure 8-7A, it was found that an increase in cell number (division of one cell to a doublet pair cell(s), resulted in an increase in the cortical region elastic output properties for the cell (within the actin cortex layer). As the MDCK cells continue to proliferate and divide, forming cell clusters, MDCK cells lying on the outer region of the cluster exhibited a reduction in the actin cortical region Young's elastic moduli outputs. Conversely, cells within the internal central region of the clusters presented with higher Young's elastic moduli trends compared to single, doublet pair and periphery cluster cells. Further cell proliferation and monolayer formation through to the semiconfluent monolayer length scale, resulted in a moderate reduction in Young's elastic moduli values for the MDCK actin cortex region, and a further decrease at high density confluence MDCK monolayer cells. In order of greatest Young's moduli outputs (for the MDCK cell actin cortical layer region), doublet pair cells presented with greatest Young's moduli trends (397.1 ± 219.3 Pa) followed by cells within the centre of a cluster (354.7 ± 120.6), then cells within a semi-confluent monolayer (346.5 ± 139.1), cells on the periphery of a cluster (268.6 ± 174.8 Pa) followed by maximal density monolayer cells (245.9 ± 63.8 Pa) and single MDCK cells (231.2 ± 114.6 Pa).

Based on the results presented for the intermediate MDCK developmental stages (doublet pair, and cluster cells), it is evident that the state of cell development and division has a great effect on the overall derived Young's elastic moduli values for the cortical actin region of MDCK cells. The results presented here, further demonstrate (as with the results presented in Chapter 5), that stage of cell development needs to fully

considered when implanting an AFM experiment to investigate the Young's moduli trends of mammalian cells. The establishment of cell-cell bonds (from the single to cell doublet pair) resulted in a significant increase in MDCK cell cortical Young's elastic moduli outputs and cell membrane stiffness. Further cell division and development (cell cluster density) resulted in a further increase in MDCK cell cortical region Young's elastic moduli trends for cells within the centre of the developing cluster. Interestingly, MDCK cells within the two different cell monolayer densities (semi-confluent and maximal density) exhibited greater Young's moduli trends than cells along the periphery of a cluster as well as single cells.

8.3.3 MDCK cell-cell junctional region Young's elastic moduli trends with increase in monolayer developmental length scale and confluence

Given the evidence demonstrating the down regulation of cortical actin density along the cell-cell junction interface for multiple cell lines [82]–[86], the theory of actin cortex gradient transitions and down regulation at cell-cell interface junctions was next investigated. The results presented for the force mapping of the cell body nuclear regions – at force deformation depths pertaining to the inner actin cortical region – demonstrated and interesting outcome. Firstly, as with the results presented in chapter 5, the stage of cell development is as important as the current AFM protocol considerations when designing an experiment to investigate Young's elastic moduli trends for mammalian cells. Secondly, based on the second hypothesis presented in Chapter 6, the derived Young's moduli trends at incremental stages of MDCK cell proliferation demonstrated that cell division and increase in number of cell-cell bonds can result in a variation in Young's elastic moduli trends. Therefore, the cell-cell junctional regions were investigated across each stage of MDCK cell proliferation and monolayer development.

This analysis was carried out to assess if the apparent down regulation in cortical actin along cell-cell interface zones is associated with the variation in derived MDCK cortical Young's moduli measurements along the MDCK cell cortical region. An important consideration – in terms of data analysis – has to be noted for the data analyses in this chapter. As with the force indentations carried out previously, consideration as the thickness of the MDCK cell sample along cell-cell junction regions was investigated, as to ensure only appropriate maximal deformation depths were analysed by application of the Hertz-Sneddon contact model. This was achieved by carrying out height offset cross sections for all MDCK force maps for each developmental length scale (Figures 8-8 to 8-11). From these offset cross-sections, the reduction in MDCK cell sample height (thickness) along the cell-cell junction regions was analysed, and the Hertz-Sneddon contact model only applied to the maximal limits for fitting of the contact model to these regions. This was carried out for all force map pixel data points within the cell-cell junction regions. Cell junction regions were analysed for MDCK cell doublet pairs, cell cluster cells and cells within semi-confluent and maximal density monolayer cells. Height offsets for MDCK cells analysed found cell-cell junction region heights at an estimated 3.54μm for maximal density MDCK monolayers, 3.40μm for semi-confluent MDCK monolayer cells, 9.91μm for MDCK doublet pairs, and 12.5-14μm for MDCK cluster cells. As with the analysis of the MDCK nuclear cell body region, in each MDCK cell sample, for **each** instance (depending on the precise maximal height of each MDCK cell within a sample group) consideration was given such that only a maximum of 10% of the thickness of the cell sample was analysed. In the case of the MDCK cell groups, this resulted in the fitting of the Hertz-Sneddon contact model to MDCK cell indentation/deformation depths (at the cell-cell junction regions) as follows; For doublet pair MDCK cells, 591nm. For MDCK cluster cells 350nm. For semi-confluent MDCK monolayer cells, 340nm. For fully confluent maximal density MDCK monolayer cells,

350nm. Data points along the minimum height offset channel points (along the cell-cell junction regions) were analysed from MATLAB replots of the setpoint height channel [C] and Young's moduli elastic moduli force maps.

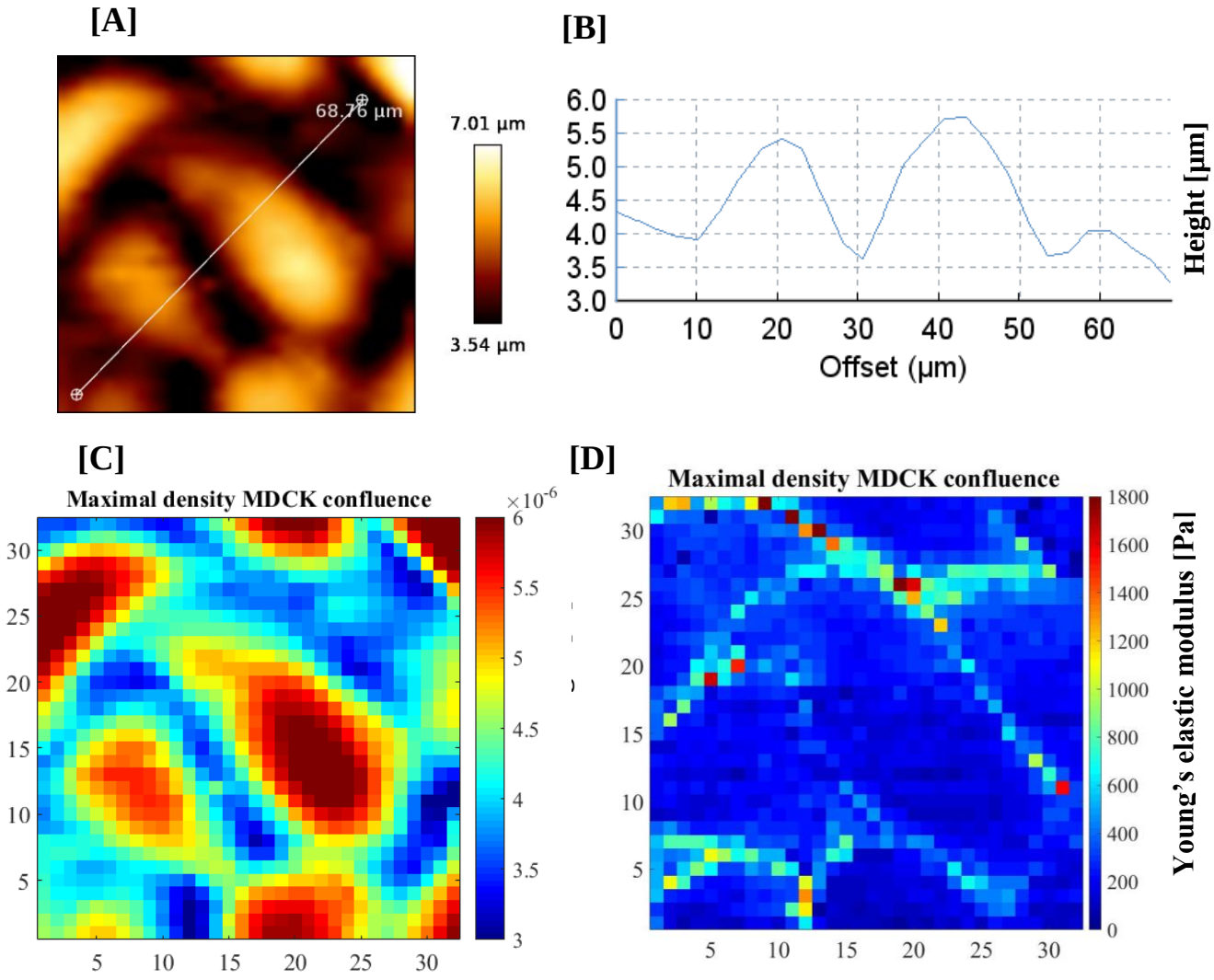

Figure 8-8. MDCK cell-cell junction region Young's elastic moduli [E] analysis for maximal density monolayer cells. MDCK setpoint height channel and height offset cross section **[A and B]** were used to assess sample thickness at the cell-cell junction regions. MATLAB replots of the setpoint height channel **[C]** and Young's moduli elastic moduli force map **[D].** Referring to minimum of height offset (3.54µm), maximal 350nm cell deformation was analysed by the Hertz-Sneddon contact model.

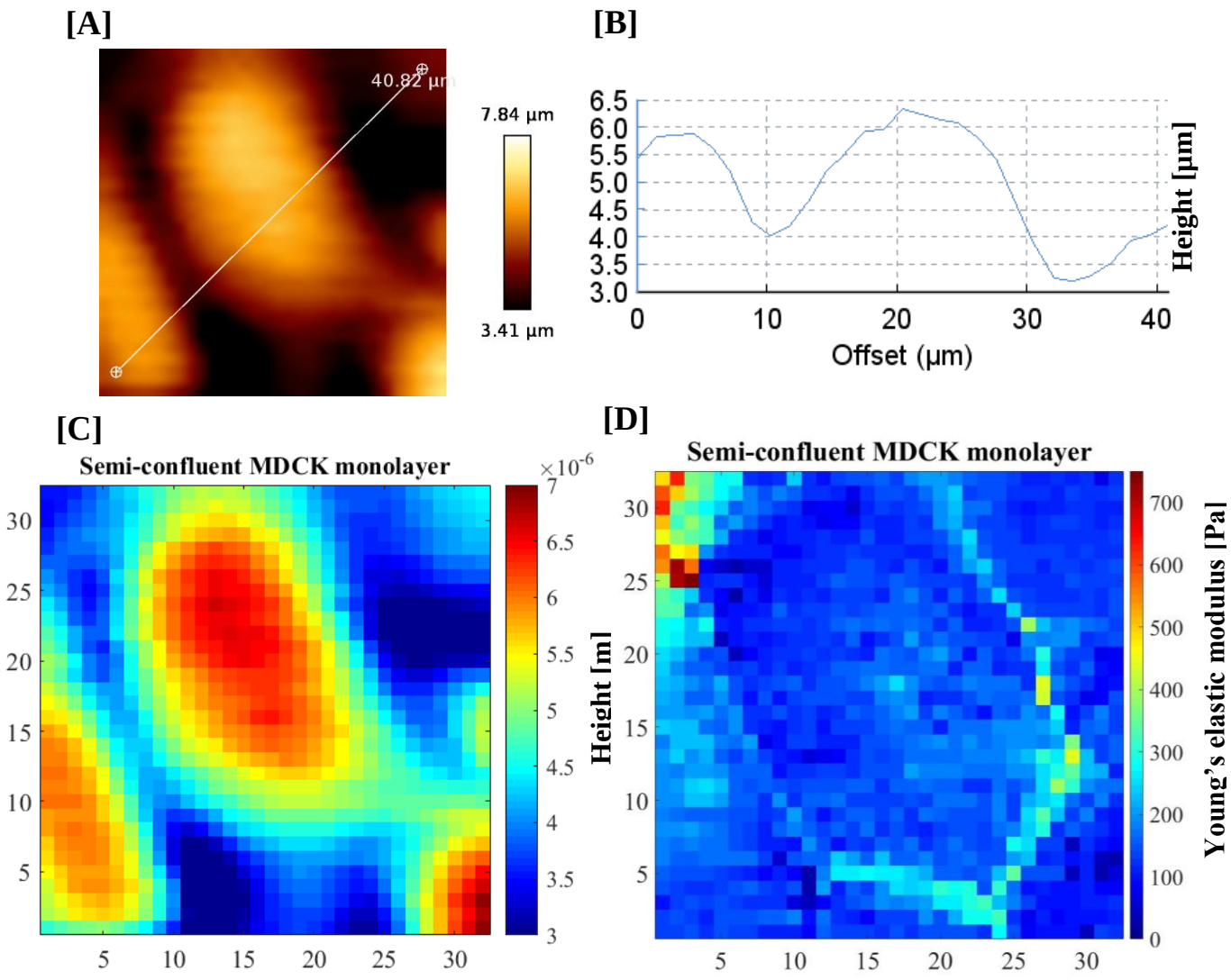

Figure 8-9. MDCK cell-cell junction region Young's elastic moduli [E] analysis for semi-confluent monolayer cells. MDCK setpoint height channel and height offset cross section **[A and B]** were used to assess sample thickness at the cell-cell junction regions. MATLAB replots of the setpoint height channel **[C]** and Young's moduli elastic moduli force map **[D].** Referring to minimum of height offset (3.40µm), maximal 340nm cell deformation was analysed by the Hertz-Sneddon contact model.

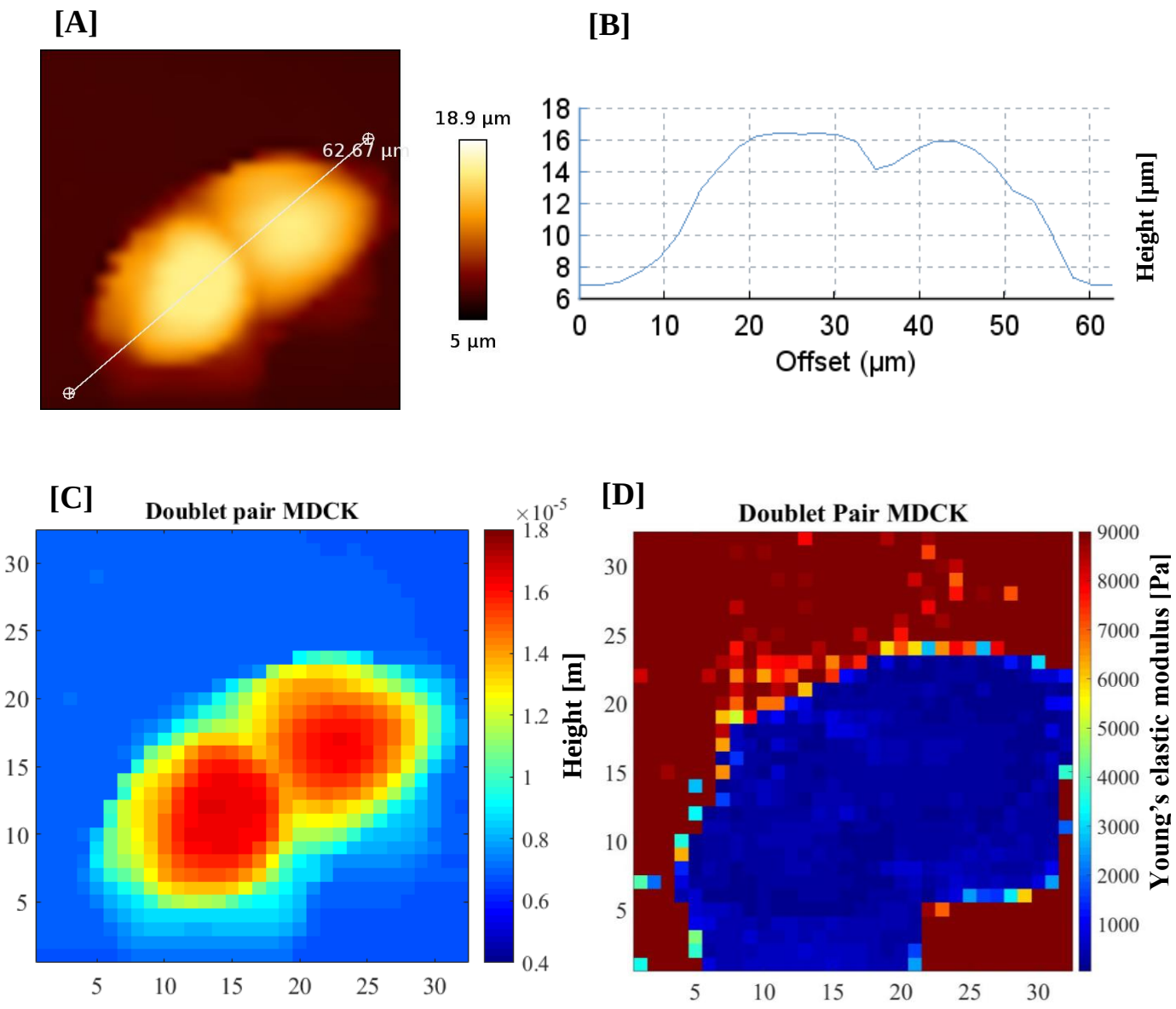

Figure 8-10. MDCK cell-cell junction region Young's elastic moduli [E] analysis for doublet pair cells. MDCK setpoint height channel and height offset cross section **[A and B]** were used to assess sample thickness at the cell-cell junction regions. MATLAB replots of the setpoint height channel **[C]** and Young's moduli elastic moduli force map **[D].** Analysing height setpoint channel data points, for the doublet pair force map, all data points at 6.64µm was found to be underlying substrate. Cell cytoplasm regions (cell edges) were found at 7.5µm. Analysing cell junction regions in height offset cross sections found region to be approximately 12.5µm to 13.5µm. Subtracting baseline at minimum of height of cell junction region 12.5µm – 6.64µm results in 5.91µm. Therefore, a maximum of 591nm cell deformation was analysed by the Hertz-Sneddon contact model.

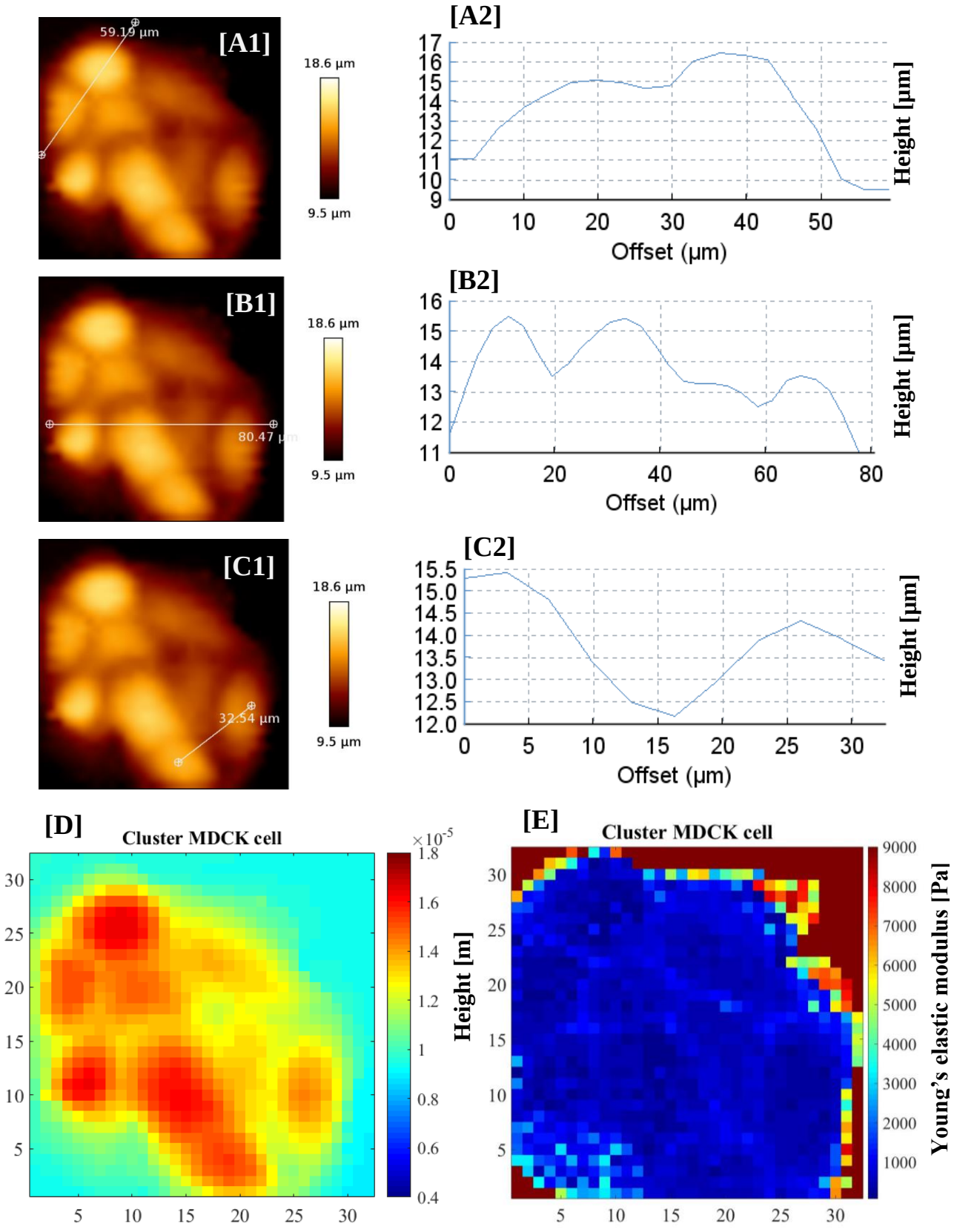

Figure legend on following page

Figure 8-11. MDCK cell-cell junction region Young's elastic moduli [E] analysis for cluster cells. MDCK setpoint height channel and height offset cross section **[A and B]** were used to assess sample thickness at the cell-cell junction regions. MATLAB replots of the setpoint height channel **[C]** and Young's moduli elastic moduli force map **[D].** Analysing height setpoint channel data points, for the doublet pair force map, all data points at 8.93µm was found to be underlying substrate. Cell cytoplasm regions (cell edges) were found at 10.53µm. Analysing cell junction regions in height offset cross sections found region to be approximately 12.5µm to 14.0µm. Subtracting baseline at minimum of height of cell junction region 12.5µm – 8.93µm results in 3.50µm. Therefore, a maximum of 350nm cell deformation was analysed by the Hertz-Sneddon contact model.

Having shown the Young's elastic moduli trends for MDCK cell body nuclear regions with increase in stage of cell confluence and monolayer development (section 8.3.2), next, the Young's elastic moduli trends for the MDCK cell-cell junction regions was analysed. The Young's elastic moduli outputs for the cell junction regions are presented in Figure 8-12A and B.

Young's elastic moduli trends for the cell junctions demonstrated a significant ($p < 0.00001$, $p < 0.001$) difference between the [E] trends for MDCK cell junction regions for intermediate stages of MDCK monolayer development. The results were as follows, in order of greatest averaged Young's elastic moduli outputs for cell junction regions of; external cells of a MDCK cluster (794.5 ± 218.4 Pa), followed by internal cells within a MDCK cell cluster (682.2 ± 197.3 Pa), followed by maximal density MDCK monolayer cell junction regions (489.5 ± 244.6 Pa), followed by doublet pair MDCK cell junction regions (364.9 ± 126.9 Pa), and lastly cell junction regions of semi-confluent MDCK monolayer cells (290.9 ± 108.2 Pa).

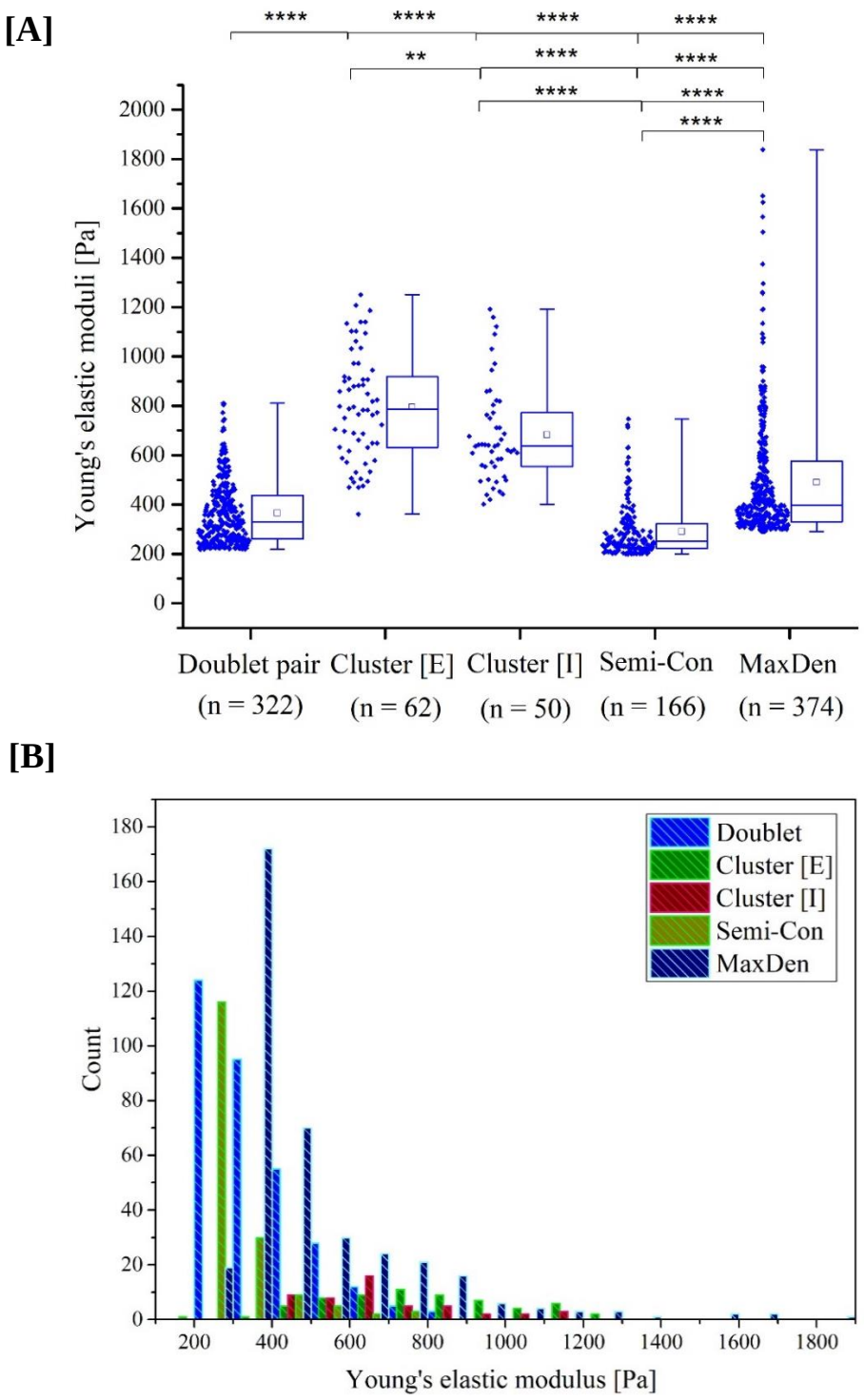

Figure 8-12. **Box plots denoting the Young's elastic moduli outputs for MDCK cell cell-cell junctional regions.** Lines within each box represent the median, the box itself presents the lower (25%) and upper (75%) quartiles, while the whiskers present the lowest and highest extreme values. Box points represent the means of each cell data cohort. (p-values) were calculated using the Mann-Whitney U test at .01 significance. (**** $p < 0.00001$, ** $p < 0.001$). (n) = number of data points gathered for each MDCK developmental condition.

The Young's elastic moduli results presented for the cell junctional regions of MDCK cells at alternate stages of monolayer development, demonstrated that the stage of cell proliferation can greatly affect the derived Young's elastic moduli trends for the cell junction regions. The organisation of the cell junction regions, with respect to cytoskeletal organisation and the physical characteristics of the cell junction ECM components may change and adapt at different stages of MDCK monolayer development.

8.3.4 Cortical actin distribution in MDCK cells at different stages of monolayer development.

The variation in cortical F-actin density was previously demonstrated for MDCK stages of development; single cell, semi-confluent and maximal density monolayer cells (Chapter 5, Section 5.3.2). The analysis was carried out based on previous reports demonstrating the variation in the distribution of cortical F-actin for epithelial cells at alternate cell developmental length scales; Vero cells have been shown to exhibit variation in F-Actin intensity at non-confluent (higher F-actin intensity) and monolayer (lower F-actin intensity) developmental length scales [111]. Furthermore, at greater cell densities and monolayer confluence, MDCK cells showed an increase in dense and short microvilli in the apical domain, along with incrassate apical actin [110]. Therefore, to address how the expression of F-actin varies at intermediate stages of MDCK monolayer development, the actin-GFP intensity of MDCK cell doublet pairs and cell clusters, alongside MDCK single and monolayer length scales was analysed (Figure 8-13). MDCK F-actin (GFP) fluorescent images acquired and analysed for variation in cortical actin intensity, demonstrated a variable significant difference (as well as little significant difference), in the corrected total cell fluorescence for (CTCF) cortical F-actin across the full MDCK monolayer developmental groups.

Therefore, it appears that intermediate stages of MDCK monolayer development do not follow the same trends presented as previous i.e. higher cell densities such as MDCK cell cluster cells do not present with a reduction in F-actin intensity in comparison to single and cell doublet pair MDCK cells. Therefore, MDCK stages of intermediate cell development events (in terms of F-actin intensity) are not as obvious in comparison to Young's elastic moduli trends presented across the same stages of MDCK monolayer development.

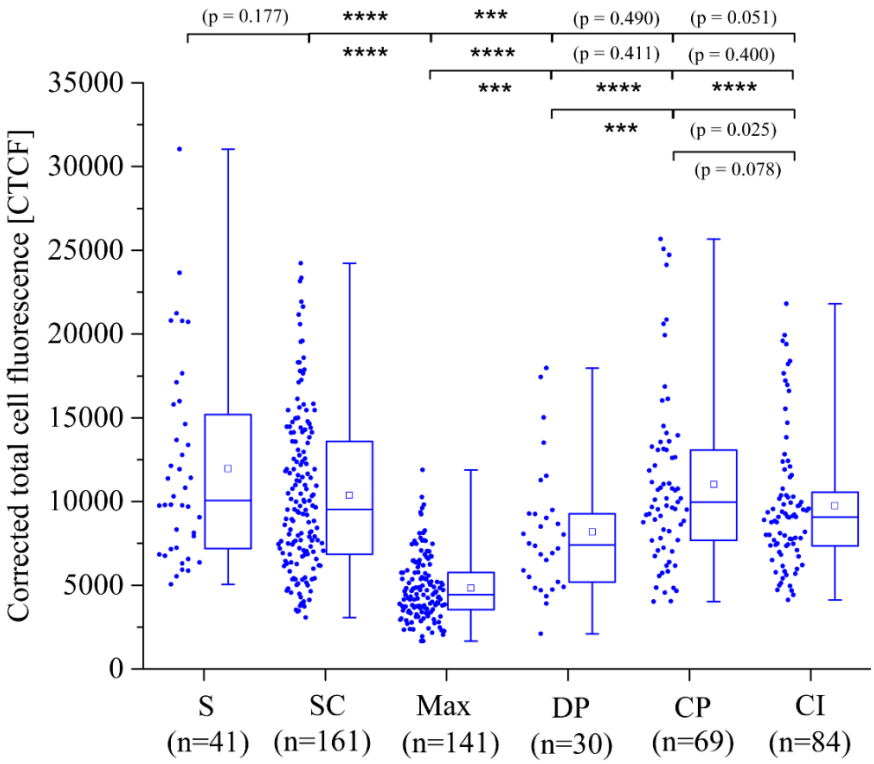

Figure 8-13. **Box plots denoting corrected total cell fluorescence (CTCF) for cortical actin GFP MDCK cell fluorescence**. Lines within each box represent the median, the box itself presents the lower (25%) and upper (75%) quartiles, while the whiskers present the lowest and highest extreme values. Box points represent the average means of each cell cohort. Box plots display MDCK actin GFP fluorescence output measurements for single, semi-confluent and maximal density confluence MDCK cell developmental length scales. (p-values) were calculated using the Mann-Whitney U test at .01 significance. (**** $p < 0.00001$) (*** $p < 0.0001$). (n) = (41) single cells (161) semi-confluent cells and (141) maximal density confluence cells, (30) doublet pair cells, (69) cluster periphery cells and (84) internal cluster MDCK cells.

8.4 Discussion

The purpose of this chapter was to investigate if the variations observed in MDCK cell Young's elastic moduli trends through monolayer development (Chapter 5), arise due the second cell mechanism hypothesized in Chapter 6: The progressive division and development MDCK cells as a monolayer forms, results in increased cellular stress and derived Young's elastic moduli properties along the cell cortical region and cell-cell membrane boundary. MDCK cell force mapping analysis of MDCK cells undergoing incremental stages of monolayer development was carried out to clarify if the development of increased stress in the cell cortical and cell-cell boundary region is most responsible for the AFM results obtained in Chapter 5, and if this proposed mechanism is more probable than that of the cellular scale morphological variations presented in Chapter 7. To derive MDCK force maps, a single selected loading force of 0.8nN was selected in order to analyse MDCK [E] trends of the upper actin cell cortical layer. The majority of cellular mechano-biology studies implicate the inner actin microfilament cortical layer as the most significant and principle modulator of external cellular stiffness and tension [22], [68], [76], [181], [207]–[209]. The actin cortex is described as the thin network of crosslinked actin protein filaments bound to the inner surface of the plasma membrane, and is present in almost all mammalian cells [77]. Gradients within the cortical actin layer have been associated with multiple cell developmental events such as cell migration and cell division [13], [79], [80], as well as with associated cell shape transformations during cell development [81]. Interestingly, towards the end of cell division in mitosis, the gradient of cortical cell tension becomes localised towards the cell centre, which is thought to drive cell furrow ingression and cleavage of the cell [82]. A similar process has been evidenced during the formation of cell-cell adhesion contacts; a gradient decrease in cortical tension is observed towards the cell-cell interface zones in developing zebrafish progenitor cells [83]. The down

regulation of cortical actin density along the cell-cell junction interface has been evidenced in multiple mammalian cell lines; MDCK [84], cancerous cells [85], zebrafish [83], and xenopus gastrula cells [86]. Therefore, the progressive establishment of cell-cell contact and adhesion complexes with tissue development encompasses a transition in cell tension with an increase in stage of cell development. Further to this, evidence has demonstrated that an increase in cell density (cell-cell contacts) with monolayer proliferation, results in a bi-phasic transitional process whereby physical constraint or compression of cells leads to a reduction in cell area, increase in cell height, which, along with interfacial cell-cell contact formations, leads to a reduction in cell division and proliferation [198]. This biphasic response of proliferating cells within a cell monolayer, challenges the conventional notion and theory of cell contact inhibition being the sole inducer responsible for the cessation of cell division and monolayer proliferation. Thus, the process of contact inhibition as a result of mechanical interaction and constraint within a monolayer is bi-phasic, and does not arise simply from intercellular contact(s) formation alone. The concept of spatial and lateral confinement of epithelial monolayers resulting in greater intracellular pressure has also been investigated; Micro-pillar arrays designed to create spatial confinement mimicking that of proliferating epithelial monolayers demonstrated that without sufficient micro-pillar flexibility, compacted epithelial cells lack adequate space for optimal cell rounding and cell division. As a result, driven by an increase in actomyosin contraction and hydrostatic pressure with mitotic cell rounding, epithelial cells migrate up micro-pillars to reduce cell confinement and undergo unperturbed cell mitosis [80].

Addressing the results for the cell body actin cortex region for MDCK cells undergoing monolayer proliferation, if one attempts to interpret the results based on proliferative activity of the MDCK cells; divided doublet pair cells presented with the greatest Young's moduli trends along their actin cortical region, however they exhibited lesser Young's moduli outputs along their cell junction regions compared to higher cell densities. The maturation of cell junctions at this stage of development has not yet ensued, and the cell-cell junction region following the division of a single cell will be relativity newly established. Therefore, the actin cortical region, following cell division - which involves multiple cell cytoskeletal re-organisation events such as actin cortex furrow formation, and the actin ring that forms to divide cytoplasmic contents during cytokinesis will present with greater derived Young's moduli values compared to single cells. Following cell proliferative activity, cells lining the external region of a cell cluster, which, similar to doublet pair cells are readily dividing more actively than cells on the internal region of cluster (this may arise due effects stemming from contact inhibition of cells within the internal region of cell cluster), external cluster cells, presented with lower actin cortex Young's moduli trends, compared to internal cluster cells, but greater cell junction Young's moduli trends compared to internal cell cluster junction regions. Interestingly, cell junction regions of MDCK cells at the cluster (periphery and external regions) presented with the greatest Young's elastic moduli outputs along their cell-cell junction regions compared to all other developmental length scales. Again, if one imagines how the proliferative activity of the mammalian cells ensues between the cell cluster and monolayer length scales, between the cell cluster and higher density semi-confluent monolayer length scale, cell division activity declines as a result of contact inhibition pathways. At this length scale however, there is still capacity for further cell division (as is the case with internal cell cluster cells). As demonstrated in previous reports, contact inhibition does result in the complete

cessation of cell division [198]. This may result in the similar actin cortex trends presented for MDCK cell cluster and semi-confluent cell length scales. However, along their cell-cell bond regions, cluster cells presented with greater derived Young's moduli trends. This may arise as result of differing activity and transmission of mechanical stress across these regions for more mature cells bonds (semi-confluent cells) as opposed to cluster cells (more actively dividing and less mature cell-junctions).

Moving onto to higher cell length scales, maximal density MDCK monolayer cells present with higher Young's moduli trends compared to lesser semi-confluent densities along the cell junction region. At this stage of cell development, cell-cell bonds have been firmly established, and cell division activity declines. The activity of the actin cytoskeletal network for events that dominate at lower cell length scales, such as cell membrane furrow formation and cytokinesis, and establishment of new cell contact junctions, will decline. This may explain the reduced Young's elastic moduli trends presented for the cell body actin cortical region of maximal density MDCK monolayer cells. Interestingly, the results presented here for AFM indentation of adherent cells at high cell densities do not agree with previous reports demonstrating an increase in derived Young's elastic moduli trends with increase in cell density [111]. This may be due to a variation in AFM protocol approaches (the primary topic discussed in Chapter 4 of this thesis). Differences in the chosen cantilever indentation force, as well as proper application of the selected contact model to derive elasticity outputs could produce a difference in results between AFM studies. It may be the case that different cell properties as a result of differing indentation depths are being investigated and presented. For example, the material properties of the actin cortex versus the material properties of the internal cell cytoplasmic region.

To attempt to understand or propose a mechanical mechanism through which cell development can be described (through interpretation of the derived Young's elastic modulus in these AFM experiments), referral and discussion into the activity of the intracellular microfilament actin network is required. Notably, at both single cell and semi-confluent cell monolayer densities, the interplay between cytoskeletal mechanisms has been evidenced to generate greater cortical tension in mitotic cells as they progress through each stage of cellular mitosis and development [79], [195]. As the number of cell bonds increases with cell division, cell motility declines with a reduced surface area for cell division. This results in cell compaction or shrinkage, and the cytoplasmic-nuclear surface area ratio declines. Continued cell division slows, but does not stop, as a result of the aforementioned physical constraints, collectively referred to as contact inhibition of cell growth [198]. It has been evidenced that contact inhibition in MDCK cell development is more greatly influenced by mechanical constraint as opposed to an increase in the number of cell-cell contacts and junction formation [198], therefore, derived Young's moduli trends presented for cells with reduced mechanical constraint (single cells, doublet cells and periphery cells of a cell cluster) may arise as a result of inherent biological variances pertaining to the inner activity of the dense actin cortex, with cells at higher orders of mechanical constraint (internal cluster cells, semi-confluent monolayer cells and maximal density compacted cells) producing mechanical properties that are influenced by actin cortical cytoskeletal activity as well as increased mechanical constraint. Furthermore, when investigating the mechanical properties of cells using external mechanical perturbations on the surface of the cells, many of the established models used by researchers characterise the response of cells to the actin microfilament network that resides beneath the plasma cell membrane. Much of the discussion in the mechanical properties of mammalian cells, and indeed this research thesis, has attributed the actin cortical layer as the primary force bearing element of a

mammalian cells. Notably, many of these models predict that external applied loads to the cell surface are transmitted across and through the cell body equally at all points, and arise solely from the actin cell cortex. However, there are opposing models that counter these predictions; A tensegrity model predicts that external mechanical stresses are transmitted across the cell surface and through the cytoplasm by distinct internal molecular networks that are physically coupled to the external anchors of the cell i.e. the ECM and cell junction adhesion complexes [210]**.** More specifically, this model states that a mammalian cell is pre-stressed tensegrity structure, and local mechanical stresses will result in large scale cytoskeletal structural rearrangements, even across relatively large distances. According to this model, as a result of the discrete molecular elements within the cells, the internal load-bearing cytoskeletal network will change orientation following an external load until a new equilibrium is attained. These orientation changes differ from the conventional "actin cortex only" models of cell mechanics in that the application of an external load stress will result in both local and deep structural rearrangements of the cell, from the surface membrane to the internal cytosol region [210]. Therefore, based on the results presented in this chapter, if we consider the cell tensegrity model, the derived Young's moduli trends at different stages of monolayer development will be subject to the degree of cell-cell adhesion and cell-ECM adhesion. Where the maturation and formation of cell bonds has been well established at higher monolayer developmental length scales, the transferal of stress or tension across these domains into the actin cortex may be relativity less as a result of the reduced activity of these discrete molecular components linked to the internal microfilament network. This may result in reduced stiffness (in the case here, the Young's elastic modulus) along the actin cell cortical region compared to cells undergoing more active proliferation and formation of cell-cell bonds. The degree of structural rearrangement is dependent of the presence and activity of the discrete internal molecular proteins within a cell. For

example, the dynamic deformation of the actin cell cortex has been linked to particular actin binding proteins (ABPs). One such ABP, namely myosin-2, has been described as the most significant ABP linked to the generation of contractile tension in the actin cytoskeletal network [77]. As described in Chapter 2 of this thesis (section 2.8.3),Myosin proteins are described as motor proteins whose function is to move along actin microfilaments through the coupling hydrolysis of ATP, thus driving the movement and contraction of actin microfilaments [58]. The family of myosin proteins has been evidenced to play a critical role in the function of many cell membrane related functions. For example, myosin-1 and myosin-5 have been shown to bind the internal region of the plasma membrane as well as membranes of the intracellular organelles such as the nucleus and mitochondria, with myosin-1 serving as linker protein between the plasma membrane and the actin microfilament bundles of the cell microvilli brush border [58]. Therefore, as the tensegrity model implies, it is plausible to assume that proteins such as myosin's, which are bound to both the actin cortex and other internal cell structures are important in the transmission of external mechanical loads and conferral of cell-cell and cell-ECM associated stresses. Notably, evidence has shown that myosin-2 activity is the predominant factor affecting overall actin cortical tension [92], with the induced inhibition of myosin-2 activity resulting in a near 80% decrease in cell cortical tension [77]. Therefore, it is possible that multiple internal cytoskeletal mechanisms within the cell cortex (actin as well as mysosin-2 activity and dynamics) are involved in the formation and transition of cortical and intercellular tension and stress through cell monolayer development.

8.5 Conclusion and summary of findings

In this chapter, the Young's elastic moduli trends for the actin cortical nuclear region and cell-cell junction regions of live MDCK cells across incremental stages of cell division and monolayer development was investigated. The results in this chapter demonstrated that cell activity (in terms of cell division with less contact inhibition) and the formation of cell-cell bonds at the cell junction regions can have a considerable effect of the derived Young's moduli measurements at different stages of cell monolayer development. The discussion of the results presented in this chapter draw on previous reported evidence and models of cell mechanical analysis to state that conventional actin cortex only models describing differences in derived cell mechanical outputs may be incomplete. Based on the differences of the derived Young's elastic moduli for the cell junction regions at different stages of monolayer development (with consideration to the actin cell cortex region), suggests that the cell tensegrity model [210], may better describe the differences observed between the different monolayer length scales. The transmission of cell mechanical cues and differences in cell Young's moduli properties as a result of the formation and maturation of cell bonds, with respect to cell division and proliferative ability (governed to a limit by contact inhibition) can be explained with referral to the cell tensegrity model.

The results of this chapter further demonstrate that it is imperative to consider stage of cell monolayer development when planning and/ attempting to interpret and compare live cell mechanical measurements for mammalian cell AFM analysis. Referring to the literature that has investigated differences in cell density and monolayer development, little consideration is given for potential variations in the mechanical properties of intermediate (cell doublet and clusters) as well as monolayer subgroups (semi-confluent and maximal density confluence) when investigating mammalian cell mechanical properties.

CHAPTER 9

Looking back, and working forward

9.1 Introduction

As discussed in the onset of this thesis, the human body comprises a multitude of different types of heterogeneous tissue structures, each of which are formed by millions of layers of cells. However, less evidence exists to explain how single cells contribute to the mechanical integrity and behaviour of tissue or organ in a collective way, despite efforts made in an attempt to investigate how the mechanical properties of tissue components at each hierarchical scale (e.g. subcellular, cellular and tissue scales). Among all the mechanical properties that one can measure from biological tissue samples, the Young's elastic modulus [E] has become a hallmark parameter, which has been demonstrated to be a key factor in a multitude of cell developmental and pathological events such as mitosis, apoptosis, senescence and mutations (cancer cell development). As discussed, and presented in this thesis, there are multiple methods available for investigating cell mechanical outputs. In this thesis, AFM was chosen as the primary tool for mammalian cell mechanical characterisation. Due to its capability of producing high resolution three-dimensional images, which combined with force spectroscopy, an AFM is able to define and assign surface properties, such as surface topography and elastic modulus to specific cellular regions in an in vitro culture environment [16]. However, given its capabilities, much of the AFM studies focussing on mammalian cell [E] analysis do not account for certain protocol considerations such as state of cell development in terms of how intracellular physical changes can affect conventional AFM protocol set-ups and experimental outcomes. The mechanical

properties (Young's elastic modulus in particular), of mammalian cells is often investigated at the single or monolayer length scale, thus making the measurement values and conclusion drawn from different cell length scales in certain published studies impossible to compare.

This thesis had two major goals; the first was to establish and test an appropriate AFM protocol for investigating mammalian cell Young's elastic moduli trends for a selected mammalian cell line (MDCK) (Chapter 4). This was followed by an investigation into how the defined AFM parameters are affected by the stage of cell monolayer development. Three specified MDCK monolayer developmental stages (single, semi-confluent and maximal density monolayer) were investigated (Chapter 5). In Chapter 5, the stage of cell development was shown to affect the final derived indentation depth and derived Young's moduli trends for the MDCK cells. In order to interpret the results observed in Chapter 5, the second goal of this thesis was to then discuss and propose which biomolecular components of the MDCK cells was giving rise to the results obtained. In this approach, two hypotheses were suggested (Chapter 6); morphological variation in cell development (investigated in Chapter 7), and the development of increased stiffness along the cell cortex or cell-junction regions (investigated in Chapter 8). In Chapter 8 of this thesis, a more precise appreciation for the derived Young's elastic moduli [E] outputs trends of the MDCK mammalian cell line across defined incremental stages of cell development was carried out.

9.2 Chapter conclusions

The specific conclusions that were made from each chapter of this thesis are summarised as follows;

Chapter 4: Application of current AFM protocols for mammalian cell Young's elastic moduli analysis: Adapting the experimental approach

In this chapter, a suitable AFM protocol for live MDCK cell AFM indentation measurements were investigated. The key AFM experimental protocol parameters defined following each troubleshooting assay in this chapter are;

(1) Selection of a suitable cantilever geometry – Spherical cantilever
(2) Accurate method for precise selection the cell body/nuclear organelle region using live cell fluorescence microscopy with AFM indentation analysis.
(3) Application of an appropriate method of deriving the Young's elastic modulus [E] for live MDCK AFM force-displacement curves. The JPK software was used to analyse all obtained force-displacement curves. Application of a suitable indentation depth fitting of the Hertz-Sneddon contact model was achievable, with accuracy of fit assessed for each indentation force displacement curve.
(4) Force mapping as well as fixed cell imaging applications is suitable using the selected spherical cantilever.

Chapter 5: Effect of stage of cell monolayer development on atomic force spectroscopy Young's elastic modulus [E] measurements

The results presented in this chapter demonstrated that stage of MDCK cell development i.e. single, semi-confluent and maximal density monolayer cells, has a significant effect on the resulting indentation depth and derived Young's elastic moduli [E] outputs for MDCK cells deformed at specified cantilever loading force ranges. The key experimental outcomes presented in this chapter are;

(1) Maximal density monolayer MDCK cells presented with the lowest indentation depth and greatest derived Young's moduli [E] trends following AFM indentation over the nuclear region of the MDCK cells, followed by semi-confluent and the single MDCK cells. This was observed at multiple indentation loading forces (nN). However, results derived at low range forces (0.5nN to 0.8nN) resulted in deformations within the limits for application of the Hertz-Sneddon contact model. Indentations depths beyond 0.8nN were not within the linear-elastic regime and therefore are not accurate for the application of the Hertz-Sneddon contact model to derived true Young's elastic moduli measurements.

(2) The total amount of actin GFP fluorescence is reduced at higher stages of MDCK cell development (maximal density monolayer); maximal density MDCK cells demonstrated the lowest cortical F-actin amounts, in comparison to single and semi-confluent monolayer MDCK cells. The ratio between MDCK F-actin intensity and cell area (CTCF/cell area), demonstrated that single cells presented with the greatest F-actin intensity per cell, followed by maximal density and semi-confluent monolayer MDCK cells.

Chapter 6: Stage of MDCK cell development and associated AFM Young's elastic moduli trends: A review of potential underlying mechanisms for observed outcomes

The purpose of Chapter 6 was to highlight and discuss the possible mechanisms most responsible for the AFM indentation results derived in Chapter 5. Topics such as mammalian cell internal structure, evidenced cytoskeletal mechanical functions and contribution to cell mechanics was emphasised. Based on the derived Young's elastic modulus trends from Chapter 5, and literature evidence, two hypotheses, namely (1) cell morphological variation and (2) actin cortical properties, was proposed as potential explanations for the interesting results presented for MDCK cells at different stages of

monolayer development. The two hypotheses were then addressed and investigated the results chapters that followed.

Chapter 7: Hypothesis 1: Morphological variation of MDCK cells across three stages of cell monolayer development

The results presented in this chapter demonstrated the morphological transitions of MDCK cells as they develop through progressive proliferation and monolayer formation (single, to semi-confluent and maximal density monolayer cells). This was achieved using fluorescent image analysis. The results of this chapter demonstrated that MDCK cell height, cell body area, cortical thickness as well nuclear morphology can vary significantly with progressive cell monolayer proliferation. However, only certain aspects were shown to be statistically significantly different across the three monolayer developmental stages. Therefore, at this stage of the thesis, it still remained somewhat unclear as to what mechanisms were most responsible for the results presented for the MDCK indentation results presented in Chapter 5. None-the-less, the key experimental outcomes presented in this chapter were;

(1) Single isolated MDCK cells have the greatest **cell height**, followed by maximal density and semi-confluent monolayer MDCK cells.
(2) Semi-confluent MDCK cells presented with greatest over-all **cell area** followed by single and maximal density monolater MDCK cells.
(3) Single MDCK cells presented with the greatest **nuclear organelle height** followed by maximal density and semi-confluent monolayer cells
(4) Semi-confluent MDCK cells presented with greatest **nuclear organelle area** followed by maximal density and single MDCK cells.
(5) Single MDCK cell nuclear organelle has the greatest volume followed by semi-confluent and maximal density cells **nuclear organelle volume.**

(6) MDCK **nuclear organelle surface area** was greatest for maximal density MDCK cells, followed by single and then semi-confluent MDCK cells.

(7) No significant variation was observed in **2D nuclear organelle sphericity** for single, semi-confluent and maximal density monolayer MDCK cells, with a sphericity range of 0.64-0.69.

(8) **3D nuclear organelle sphericity** demonstrated a notable variation for single, semi-confluent and maximal density monolayer MDCK cells, with a sphericity range of 0.64-0.77.

(9) **Cortical membrane thickness** was found to vary across the MDCK developmental length scale with single MDCK cells presenting with the thickness cortical membrane, followed by maximal density and semi-confluent MDCK cells. The cortical membrane thickness range for MDCK cells was found to be ~0.6μm-1μm. Variation in cortical membrane thickness as well the presence of apical microvilli, and incrassate actin filaments are the morphological entities suggested to contribute most the AFM [E] trends presented in this chapter.

Chapter 8: Hypothesis 2: Progressive cell development of MDCK cells results in the alteration of MDCK cortical region Young's elastic moduli properties as well as variation in physical stress at the cell-cell membrane boundary

In this chapter, the Young's elastic modulus profiles for the actin cell cortical region (over the cell body/nuclear region) and cell-cell junction regions of live MDCK cells across the three initially investigated developmental stages (single, semi-confluent and maximal density) as well as intermediate developmental stages (doublet pairs and cell clusters) was analysed. This was carried out in supplement to the morphological results and indentation results presented in Chapter(s) 5 and 7, in an effort to determine if the activity and stiffness of the actin cortex is more accountable for the derived Young's

moduli trends presented in Chapter 5. The key experimental outcomes presented in this chapter are;

(1) Intermediate stages of cell monolayer development (cell doublets and internal cell within a cell cluster) exhibited the greatest average actin cortex Young's moduli trends, followed by semi-confluent monolayer cells, external cluster cells and then single MDCK cells.

(2) AFM Young's moduli stiffness map(s) for MDCK cells along the cell junction regions at different stages of monolayer development demonstrated higher Young's elastic moduli trends compared to the cell body region.

(3) MDCK cluster cells and doublet pair cells presented with greater Young's elastic moduli trends compared to semi-confluent (lowest derived values) and maximal density monolayer cells.

(4) The outcomes presented for both the MDCK cells at higher cell densities (maximal cell density) did not agree with previous literature findings that demonstrates higher density cells as having greater elastic moduli outputs compared to low density monolayers. This may be there result of different AFM experimental approaches or the method to derive the Young's elastic moduli outputs (contact model application to different regions of cell indentation/deformation).

(5) Analysis of F-actin intensity for MDCK cells at different stages of development was analysed to address how the expression of F-actin varies at intermediate MDCK developmental stages. MDCK cell doublet and cell cluster developmental stages, alongside single and monolayer length scales was analysed. MDCK F-actin (GFP) fluorescent images acquired and analysed for variation in cortical actin intensity, demonstrated a variable significant

difference in the corrected total cell fluorescence for (CTCF) cortical F-actin across the incremental cell developmental length scales.

Referring to literature and evidence previously discussed, it has been suggested in the reported findings that mammalian cell Young's moduli outputs are predominantly due to the density and alignment of the sub-cortical F-actin meshwork, which was confirmed by the chemical inhibition of fibre activity and resulted in reduced Young's moduli outputs [109]**.** Additional studies investigating intracellular regional [E] trends through cell division (cytokinesis) have also implicated variations in cytoskeletal activity and cell stiffness in the division 'furrow' of actively dividing cells, with the greatest Young's moduli values observed immediately following cell division [13]. Furthermore, supporting evidence has demonstrated the greatest concentration of focal and traction forces at the periphery of cell clusters [211]. Such outcomes are in some way consistent with the results derived in Chapter 8, whereby the greatest derived Young's moduli trends across the developmental length scale was derived for cells within MDCK cell clusters. Therefore, great consideration regarding the developmental state, number of cell-cell bonds, has to be considered when carrying out an AFM cell indentation assay. Even at relatively low loading forces, cell geometry and stage of cell monolayer development can greatly affect the derived Young's elastic moduli values through alterations in actin cortex dynamics and cell junction assembly and force transmission.

9.3 Limitations

There are certain limitations to consider for the scope of this research. The mechanical modelling of living biological samples is subjective as to the stage of cell monolayer development (as presented and discussed in this research thesis), but further to this,

accounting for the precise internal developmental process (cytoskeletal arrangement and movement of additional large organelles (such as the mitochondria) could also contribute to variation in derived mechanical outputs for mammalian cells. Furthermore, although highly useful, the AFM and selected contact models used to analyse mammalian cell elasticity consider the cells as linear elastic bodies. However, in reality mammalian cells have viscoelastic behaviour, although this may have been mitigated by using a low indentation rate. Another limitation in the results acquired and scope of this research lies with the contact model utilised to derive the Young's elastic modulus from the AFM force-displacement curves; The contact model used to fit and derive the elastic properties from the force-displacement curves (Hertz-Sneddon model) does not wholly fit the physical parameters of the derived AFM indentation measurements, which is not uncommon for most AFM studies. It should be noted here that the scope of this thesis was not to investigate or develop new contact models for AFM analysis, nor was it to investigate the limitations presented with the Hertz contact model for mammalian cell mechanical analysis, and therefore, the Hertz-Sneddon contact model was accepted as a suitable model for mammalian cell (MDCK) cell AFM analysis. The Hertz contact model (and remodelled Hertz-Sneddon model) does have its limitations. However, the advantage of using the Hertz-Sneddon theorem is that the limitations are well reported and understood. As such, it is possible to refer to the limitations and varying experimental approaches i.e. maintain forces and set-points and indentation depths within the limits of the contact theorem to combat any affects that it may have on the data outputs and ensure accurate and appropriate fitting of the model to the derived indentation curves.

9.4 Working forward

Aspects of the results presented in this thesis presented promise and scope for future work and investigations. Specifically, the results presented could help improve the method(s) and approaches of AFM mammalian cell elasticity investigations and techniques currently used for mechanical studies on soft biological samples and cell mammalian lines. Further investigation into the contribution of the key inter and intracellular cytoskeletal components to the derived Young's elastic moduli outputs for MDCK cells, could further elucidate which cellular components contribute most to the results presented across defined stages of cell monolayer developmental.

The following future investigations are proposed, that would advance this thesis into greater depth for biological mechanical measurements;

Further investigation into the development of an appropriate AFM model for live mammalian cell AFM analysis:

Based on the work presented in Chapter 5; defining an AFM indentation depth dependent model for live cell AFM analysis. Such a model (as presented in Chapter 6, Section 6.2), could include and consider factors such as; final calculated [E] outputs in relation to cantilever indentation depth for particular mammalian cell lines. Indentation depth (for different cell lines) in relation to F-actin cortex dynamics and maturity. The overarching question being; do different cell lines respond differently towards similar AFM indentation deformations?

Further investigation into the morphological adaptations of MDCK cells through monolayer proliferation and development:

Based on the work presented in Chapter(s) 7 and 8; The morphological adaptations and transitions of MDCK cells through cell proliferation could be further investigated. Additional imaging analysis to investigate added MDCK cell morphological attributes

across MDCK development, such as cell volume (using an efficient cell mask fluorescent probe), cortical actin stress fibre density and alignment analysis, apical actin microvilli intensity and fluorescent analysis could be investigated. In addition to this, added appreciation as to the morphological components that most affect MDCK AFM Young's moduli outputs, the cell cortical region and cell junction regions could be further investigated using chemical perturbation. By directly destabilizing the actin cytoskeleton using chemical reagents such as cytochalasin D (prevents actin polymerization) and phallodin(s) (stabilizes actin polymerization) or preventing the binding of myosin-2 to actin using blebbistatin, could elucidate which cytoskeletal mechanism is most responsible for the derived Young's moduli output trends across incremental cell monolayer developmental stages. This would involve incubation of the MDCK cells with the different molecular reagents followed by repeat of the AFM as well as morphological investigation assays.

Further investigation into the Young's moduli trends of MDCK cells through monolayer proliferation and development: Cancer cell AFM analysis through proliferation

Based on the work presented in Chapter(s) 7 and 8, as well as any promising results that may be obtained through chemical perturbation of various cytoskeletal components (see above), a follow on from the MDCK cell AFM analysis could be adapted to investigate how the AFM protocol and developmental analysis (cell cortical Young's moduli trends and cell junction region mechanical properties) presents in cancerous cell lines. Moreover, how pathological changes in a cell(s) function, for example tumour growth, produce highly variable mechanical outputs when investigated across different stages of cell development.

References

[1] C. M. Ramsden, M. B. Powner, J. F. Carr, M. J. K. Smart, L. da Cruz, and P. J. Coffey, “Stem cells in retinal regeneration: past, present and future,” *Development*, vol. 140, no. 12, pp. 2576–2585, 2013.

[2] D.-H. Park, C. V Borlongan, D. J. Eve, and P. R. Sanberg, “The emerging field of cell and tissue engineering,” *Med. Sci. Monit.*, vol. 14, no. 11, pp. 206-220, 2008.

[3] L. Labusca, D. D. Herea, and K. Mashayekhi, “Stem cells as delivery vehicles for regenerative medicine-challenges and perspectives.,” *World J. Stem Cells*, vol. 10, no. 5, pp. 43–56, 2018.

[4] F. Wei *et al.*, “Mesenchymal stem cells neither fully acquire the electrophysiological properties of mature cardiomyocytes nor promote ventricular arrhythmias in infarcted rats,” *Basic Res. Cardiol.*, vol. 107, no. 4, 2012.

[5] P. Thored *et al.*, “Persistent production of neurons from adult brain stem cells during recovery after stroke.,” *Stem Cells*, vol. 24, no. 3, pp. 739–747, 2006.

[6] T. Mammoto and D. E. Ingber, “Mechanical control of tissue and organ development,” *Development*, vol. 137, no. 9, pp. 1407–1420, 2010.

[7] S. E. Cross, Y.-S. Jin, J. Rao, and J. K. Gimzewski, “Nanomechanical analysis of cells from cancer patients.,” *Nat. Nanotechnol.*, vol. 2, no. 12, pp. 780–783, 2007.

[8] T. G. Kuznetsova, M. N. Starodubtseva, N. I. Yegorenkov, S. A. Chizhik, and R. I. Zhdanov, “Atomic force microscopy probing of cell elasticity,” vol. 38, pp. 824–833, 2007.

[9] N. I. Nikolaev, T. Muller, D. J. Williams, and Y. Liu, “Changes in the stiffness of human mesenchymal stem cells with the progress of cell death as measured by atomic force microscopy,” *J. Biomech.*, vol. 47, no. 3, pp. 625–630, 2014.

[10] M. J. Wozniak, N. Kawazoe, T. Tateishi, and G. Chen, “Monitoring of mechanical properties of serially passaged bovine articular chondrocytes by atomic force microscopy,” *Micron*, vol. 40, no. 8, pp. 870–875, 2009.

[11] K. S. Kim, H. K. Park, J. W. Lee, Y. I Kim, and M. K. Shin, “Investigate correlation between mechanical property and aging biomarker in passaged human dermal fibroblasts,” *Microsc. Res. Tech.*, vol. 78, no. 4, pp. 277–282, 2015.

[12] T. K. Berdyyeva, C. D. Woodworth, and I. Sokolov, “Human epithelial cells increase their rigidity with ageing in vitro: direct measurements,” *Phys. Med. Biol*, vol. 50, pp. 81–92, 2005.

[13] R. Matzke, K. Jacobson, and M. Radmacher, “Direct, high-resolution measurement of furrow stiffening during division of adherent cells,” *Nat. Cell Biol.*, vol. 3, pp. 607–610, 2001.

[14] A. Pillarisetti, J. P. Desai, H. Ladjal, A. Schiffmacher, A. Ferreira, and C. L. Keefer, “Mechanical phenotyping of mouse embryonic stem cells: increase in stiffness with differentiation.,” *Cell. Reprogram.*, vol. 13, no. 4, pp. 371–380, 2011.

[15] G. Ofek, V. P. Willard, E. J. Koay, J. C. Hu, P. Lin, and K. Athanasiou, “Mechanical characterization of differentiated human embryonic stem cells.,” *J. Biomech. Eng.*, vol. 131, no. 6, p. 061011, 2009.

[16] R. Kiss *et al.*, “Elasticity of human embryonic stem cells as determined by atomic force microscopy.,” *J. Biomech. Eng.*, vol. 133, no. 10, p. 101009, 2011.

[17] M. Targosz-Korecka, G. D. Brzezinka, K. E. Malek, E. Stepień, and M. Szymonski, “Stiffness memory of EA.hy926 endothelial cells in response to chronic hyperglycemia.,” *Cardiovasc. Diabetol.*, vol. 12, p. 96, 2013.

[18] F. Castiglione, F. Pappalardo, C. Bianca, G. Russo, and S. Motta, “Modeling biology spanning different scales: An open challenge,” *Biomed Res. Int.*, vol. 2014, 2014.

[19] Stephen C. Cowen and S. B. Doty, *Tissue mechanics*, 2nd ed. 2007.

[20] K. Haase, A. E. Pelling, and K. Haase, “Investigating cell mechanics with atomic force microscopy,” *J. R. Soc. Interface*, vol. 12, no. figure 1, p. 20140970, 2015.

[21] J. D. Humphrey, “Mechanisms of arterial remodeling in hypertension coupled roles of wall shear and intramural stress,” *Hypertension*, vol. 52, no. 2, pp. 195–200, 2008.

[22] R. Akhtar, M. J. Sherratt, J. K. Cruickshank, and B. Derby, “Characterizing the elastic properties of tissues,” *Mater. Today*, vol. 14, no. 3, pp. 96–105, 2011.

[23] A. R. Bausch and K. Kroy, “A bottom-up approach to cell mechanics,” *Nat. Phys.*, vol. 2, no. 4, pp. 231–238, 2006.

[24] W. Julius, *The law of bone remodelling*. 1986.

[25] L. J. Raggatt and N. C. Partridge, “Cellular and molecular mechanisms of bone remodeling,” *J. Biol. Chem.*, vol. 285, no. 33, pp. 25103–25108, 2010.

[26] S. Y. Tee, J. Fu, C. S. Chen, and P. A. Janmey, “Cell shape and substrate rigidity both regulate cell stiffness,” *Biophys. J.*, vol. 100, no. 5, pp. L25–L27, 2011.

[27] P. Tsimbouri, “Adult Stem Cell Responses to Nanostimuli,” *J. Funct. Biomater.*, vol. 6, no. 3, pp. 598–622, 2015.

[28] B. D. Gerard J. Tortora, *Principles of Anatomy and Physiology*, 13, illust ed. Wiley, 2011.

[29] E. Lawerence, *Hendersons dictionary of biology*, 15th editi. Pearson Education Limited.

[30] E. E. Konofagou, T. P. Harrigan, J. Ophir, and T. A. Krouskop, “Poroelastography: Imaging the poroelastic properties of tissues,” *Ultrasound Med. Biol.*, vol. 27, no. 10, pp. 1387–1397, 2001.

[31] D. Remache, M. Caliez, M. Gratton, and S. Dos Santos, “The effects of cyclic tensile and stress-relaxation tests on porcine skin,” *J. Mech. Behav. Biomed. Mater.*, vol. 77, no. March 2017, pp. 242–249, 2018.

[32] J. Li, S. Yim, A. Pacheck, B. Sanchez, and S. B. Rutkove, “Electrical Impedance Myography to Detect the Effects of Electrical Muscle Stimulation in Wild Type and Mdx Mice,” *PLoS One*, vol. 11, no. 3, p. e0151415, 2016.

[33] T. Pereira, C. Correia, and J. Cardoso, “Novel methods for pulse wave velocity measurement,” *J. Med. Biol. Eng.*, vol. 35, no. 5, pp. 555–565, 2015.

[34] J. Y. Hwang *et al.*, “Non-contact acoustic radiation force impulse microscopy via photoacoustic detection for probing breast cancer cell mechanics,” *Biomed. Opt. Express*, vol. 6, no. 1, p. 11, 2015.

[35] D. A. Fedosov, H. Lei, B. Caswell, S. Suresh, and G. E. Karniadakis, “Multiscale modeling of red blood cell mechanics and blood flow in malaria,” *PLoS Comput. Biol.*, vol. 7, no. 12, 2011.

[36] P. Katira, R. T. Bonnecaze, and M. H. Zaman, “Modeling the Mechanics of Cancer: Effect of Changes in Cellular and Extra-Cellular Mechanical Properties,” *Front. Oncol.*, vol. 3, no. June, pp. 1–7, 2013.

[37] C. Frantz, K. M. Stewart, and V. M. Weaver, “The extracellular matrix at a glance,” *J. Cell Sci.*, vol. 123, no. 24, pp. 4195–4200, 2010.

[38] M. Abedin and N. King, “Diverse evolutionary paths to cell adhesion,” *Trends Cell Biol.*, vol. 20, no. 12, pp. 734–742, 2010.

[39] J. W. M. Beenakker, B. A. Ashcroft, J. H. N. Lindeman, and T. H. Oosterkamp, “Mechanical properties of the extracellular matrix of the aorta studied by enzymatic treatments,” *Biophys. J.*, vol. 102, no. 8, pp. 1731–1737, 2012.

[40] J. Peloquin, J. Huynh, R. M. Williams, and C. A. Reinhart-King, “Indentation measurements of the subendothelial matrix in bovine carotid arteries,” *J. Biomech.*, vol. 44, no. 5, pp. 815–821, Mar. 2011.

[41] M. P. E. Wenger, L. Bozec, M. A. Horton, and P. Mesquidaz, “Mechanical properties of collagen fibrils,” *Biophys. J.*, vol. 93, no. 4, pp. 1255–1263, 2007.

[42] P. Dutov, O. Antipova, S. Varma, J. P. R. O. Orgel, and J. D. Schieber, “Measurement of elastic modulus of collagen type i single fiber,” *PLoS One*, vol. 11, no. 1, pp. 1–13, 2016.

[43] J.-P. Collet, H. Shuman, R. E. Ledger, S. Lee, and J. W. Weisel, “The elasticity of an individual fibrin fiber in a clot,” *Proc. Natl. Acad. Sci.*, vol. 102, no. 26, pp. 9133–9137, 2005.

[44] B. B. Aaron and J. M. Gosline, “Optical properties of single elastin fibres indicate random protein conformation,” *Nature*, 1980.

[45] Q. Wei and H. Huang, “Insights into the Role of Cell–Cell Junctions in Physiology and Disease,” *Int. Rev. Cell Mol. Biol.*, vol. 306, pp. 187–221, Jan. 2013.

[46] A. R. Harris, A. Daeden, and G. T. Charras, “Formation of adherens junctions leads to the emergence of a tissue-level tension in epithelial monolayers,” *J. Cell Sci.*, vol. 127, no. 11, pp. 2507–2517, 2014.

[47] T. Rozario and D. W. DeSimone, “The extracellular matrix in development and morphogenesis: A dynamic view,” *Dev. Biol.*, vol. 341, no. 1, pp. 126–140, 2010.

[48] L. Feller, Y. Jadwat, R. A. G. Khammissa, R. Meyerov, I. Schechter, and J. Lemmer, “Cellular responses evoked by different surface characteristics of intraosseous titanium implants,” *Biomed Res. Int.*, vol. 2015, 2015.

[49] A. E. Ekpenyong *et al.*, “Viscoelastic Properties of Differentiating Blood Cells Are Fate- and Function-Dependent,” *PLoS One*, vol. 7, no. 9, 2012.

[50] “Stiffness — an unknown world of mechanical science?,” *Injury*, vol. 31, pp. 14–84, May 2000.

[51] M. Radmacher, “Measuring the elastic properties of living cells by the atomic force microscope in Atomic Force Microscopy in Cell Biology.,” *Methods Cell Biol*, vol. 68, pp. 67–90, 2002.

[52] Z. Wang, M. J. Golob, and N. C. Chesler, “Viscoelastic Properties of Cardiovascular Tissues,” in *Viscoelastic and Viscoplastic Materials*, 2016.

[53] M. N. Starodubtseva, “Mechanical properties of cells and ageing,” *Ageing Res. Rev.*, vol. 10, no. 1, pp. 16–25, Jan. 2011.

[54] K. S. Fancey, “A mechanical model for creep, recovery and stress relaxation in polymeric materials,” *J. Mater. Sci.*, 2005.

[55] J. J. Gilman and J. J. Gilman, “Shear modulus,” *Electron. Basis Strength Mater.*, pp. 142–173, 2009.

[56] D. Halliday, R. Resnick, and J. Walker, *Fundamentals of Physics Extended 9th Edition*. 2010.

[57] W. STOECKENIUS, “Structure of the Plasma Membrane,” *Circulation*, vol. 26, no. 5, pp. 1066–1069, Jun. 2012.

[58] L. Harvey, B. Arnold, Z. S Lawrence, l M. Pau, B. David, and D. James, *Molecular Cell Biology. 4th edition*. 2000.

[59] M. Ruiz, “Cell_membrane_detailed_diagram.” [Online]. Available: https://en.wikipedia.org/wiki/Cell_membrane#/media/File:Cell_membrane_detailed_diagram_4.svg. [Accessed: 31-Jul-2019].

[60] P. A. Janmey and C. A. McCulloch, “Cell Mechanics: Integrating Cell Responses to Mechanical Stimuli,” *Annu. Rev. Biomed. Eng.*, 2007.

[61] G. Van Meer, D. R. Voelker, and G. W. Feigenson, “Membrane lipids: where they are,” *Nat. Rev. Mol. Cell Biol.*, vol. 101, no. 1, pp. 1–4, 2009.

[62] G. E. Crawford and J. C. Earnshaw, “Viscoelastic relaxation of bilayer lipid membranes. Frequency-dependent tension and membrane viscosity,” *Biophys. J.*, vol. 52, no. 1, pp. 87–94, 1987.

[63] W. J. Tyler, “The mechanobiology of brain function,” *Nat. Rev. Neurosci.*, vol. 13, no. 12, pp. 867–878, 2012.

[64] B. Pontes *et al.*, “Membrane Elastic Properties and Cell Function,” *PLoS One*, 2013.

[65] T. Jadidi, H. Seyyed-Allaei, M. R. R. Tabar, and A. Mashaghi, “Poisson's Ratio and Young's Modulus of Lipid Bilayers in Different Phases,” *Front. Bioeng. Biotechnol.*, vol. 2, no. April, pp. 1–6, 2014.

[66] G. Espinosa, I. Lopez-Montero, F. Monroy, and D. Langevin, “Shear rheology of lipid monolayers and insights on membrane fluidity,” *Proc. Natl. Acad. Sci.*, vol. 108, no. 15, pp. 6008–6013, 2011.

[67] Z. Al-Rekabi and S. Contera, “Multifrequency AFM reveals lipid membrane mechanical properties and the effect of cholesterol in modulating viscoelasticity,” *Proc. Natl. Acad. Sci.*, vol. 115, no. 11, pp. 2658–2663, 2018.

[68] J. Pourati *et al.*, “Is cytoskeletal tension a major determinant of cell deformability in adherent endothelial cells?,” *Am. J. Physiol.*, vol. 274, no. 5 Pt 1, pp. C1283–C1289, 1998.

[69] P. F. Davies and S. C. Tripathi, “Mechanical stress mechanisms and the cell. An endothelial paradigm.,” *Circ. Res.*, vol. 72, no. 2, pp. 239–245, 1993.

[70] R. U. OpenStax College, “The Cytoplasm and Cellular Organelles,” *Anatomy & Physiology*. [Online]. Available: http://cnx.org/contents/14fb4ad7-39a1-4eee-ab6e-3ef2482e3e22@9.1. [Accessed 22 July 2019].

[71] T. Hawkins, M. Mirigian, M. Selcuk Yasar, and J. L. Ross, “Mechanics of microtubules,” *J. Biomech.*, vol. 43, no. 1, pp. 23–30, 2010.

[72] H. Kojima, A. Ishijima, and T. Yanagida, “Direct measurement of stiffness of single actin filaments with and without tropomyosin by in vitro nanomanipulation.,” *Proc. Natl. Acad. Sci. U. S. A.*, vol. 91, no. 26, pp. 12962–6, 1994.

[73] F. Gittes, B. Mickey, J. Nettleton, and J. Howard, “Flexural rigidity of microtubules and actin filaments measured from thermal fluctuations in shape,” *J. Cell Biol.*, 1993.

[74] X. Liu and G. H. Pollack, “Mechanics of F-actin characterized with microfabricated cantilevers,” *Biophys. J.*, 2002.

[75] C. Guzmán *et al.*, “Exploring the Mechanical Properties of Single Vimentin Intermediate Filaments by Atomic Force Microscopy,” *J. Mol. Biol.*, vol. 360, no. 3, pp. 623–630, 2006.

[76] N. Gavara and R. S. Chadwick, “Relationship between cell stiffness and stress fiber amount, assessed by simultaneous atomic force microscopy and live-cell fluorescence imaging,” *Biomech. Model. Mechanobiol.*, vol. 15, no. 3, pp. 511–523, 2016.

[77] P. Chugh *et al.*, “Actin cortex architecture regulates cell surface tension,” *Nat. Cell Biol.*, vol. 19, no. 6, pp. 689–697, 2017.

[78] F. Eghiaian, A. Rigato, and S. Scheuring, “Structural, mechanical, and dynamical variability of the actin cortex in living cells,” *Biophys. J.*, vol. 108, no. 6, pp. 1330–1340, 2015.

[79] M. P. Stewart, J. Helenius, Y. Toyoda, S. P. Ramanathan, D. J. Muller, and A. a Hyman, “Hydrostatic pressure and the actomyosin cortex drive mitotic cell rounding.,” *Nature*, vol. 469, no. 7329, pp. 226–230, 2011.

[80] B. Sorce *et al.*, “Mitotic cells contract actomyosin cortex and generate pressure to round against or escape epithelial confinement,” *Nat. Commun.*, vol. 6, no. 8872, pp. 1–12, 2015.

[81] N. Ramkumar and B. Baum, “Coupling changes in cell shape,” *Nat. Publ. Gr.*, pp. 1–28, 2016.

[82] C. Schwayer, M. Sikora, J. Slováková, R. Kardos, and C. P. Heisenberg, “Actin Rings of Power,” *Dev. Cell*, vol. 37, no. 6, pp. 493–506, 2016.

[83] M. L. Manning, R. A. Foty, M. S. Steinberg, and E.-M. Schoetz, “Coaction of intercellular adhesion and cortical tension specifies tissue surface tension,” *Proc. Natl. Acad. Sci.*, vol. 107, no. 28, pp. 12517–12522, 2010.

[84] S. Yamada and W. J. Nelson, “Localized zones of Rho and Rac activities drive initiation and expansion of epithelial cell-cell adhesion,” *J. Cell Biol.*, vol. 178, no. 3, pp. 517–527, 2007.

[85] C. Hidalgo-Carcedo *et al.*, “Collective cell migration requires suppression of actomyosin at cell-cell contacts mediated by DDR1 and the cell polarity regulators Par3 and Par6,” *Nat. Cell Biol.*, vol. 13, no. 1, pp. 49–58, 2011.

[86] R. David, O. Luu, E. W. Damm, J. W. H. Wen, M. Nagel, and R. Winklbauer, “Tissue cohesion and the mechanics of cell rearrangement,” *Development*, vol. 141, no. 19, pp. 3672–3682, 2014.

[87] R. Winklbauer, “Cell adhesion strength from cortical tension - an integration of concepts,” *J. Cell Sci.*, vol. 128, no. 20, pp. 3687–3693, 2015.

[88] J. L. Maître and C. P. Heisenberg, “Three functions of cadherins in cell adhesion,” *Curr. Biol.*, vol. 23, no. 14, pp. 626–633, 2013.

[89] K. J. Chalut and E. K. Paluch, “The Actin Cortex: A Bridge between Cell Shape and Function,” *Dev. Cell*, vol. 38, no. 6, pp. 571–573, 2016.

[90] E. Fischer-Friedrich, Y. Toyoda, C. J. Cattin, D. J. Müller, A. A. Hyman, and F. Jülicher, “Rheology of the Active Cell Cortex in Mitosis,” *Biophys. J.*, vol. 111, no. 3, pp. 589–600, 2016.

[91] A. G. Clark, K. Dierkes, and E. K. Paluch, “Monitoring actin cortex thickness in live cells,” *Biophys. J.*, vol. 105, no. 3, pp. 570–580, 2013.

[92] A. G. Clark, O. Wartlick, G. Salbreux, and E. K. Paluch, “Stresses at the cell surface during animal cell morphogenesis,” *Curr. Biol.*, vol. 24, no. 10, pp. R484–R494, 2014.

[93] M. P. Clausen, H. Colin-York, F. Schneider, C. Eggeling, and M. Fritzsche, “Dissecting the actin cortex density and membrane-cortex distance in living cells by super-resolution microscopy,” *J. Phys. D. Appl. Phys.*, vol. 50, no. 6, p. 064002, 2017.

[94] M. Unal *et al.*, “Micro and Nano-scale Technologies for Cell Mechanics,” *Nanobiomedicine*, p. 1, 2014.

[95] O. Campàs *et al.*, “Quantifying cell-generated mechanical forces within living embryonic tissues.,” *Nat. Methods*, vol. 11, no. 2, pp. 183–9, 2014.

[96] G. Y. H. Lee and C. T. Lim, “Biomechanics approaches to studying human diseases,” *Trends in Biotechnology*, vol. 25, no. 3. pp. 111–118, 2007.

[97] O. Otto *et al.*, “Real-time deformability cytometry: on-the-fly cell mechanical phenotyping.,” *Nat. Methods*, vol. 12, no. 3, p. 199–202, 4 p following 202, 2015.

[98] E. Guzniczak *et al.*, “High-throughput assessment of mechanical properties of stem cell derived red blood cells, toward cellular downstream processing,” *Sci. Rep.*, vol. 7, no. 1, pp. 1–11, 2017.

[99] J. Guck and E. R. Chilvers, “Mechanics meets medicine.,” *Sci. Transl. Med.*, vol. 5, no. p212, 2013.

[100] A. Demichelis, C. Divieto, L. Mortati, S. Pavarelli, G. Sassi, and M. P. Sassi, “Toward the realization of reproducible atomic force microscopy measurements of elastic modulus in biological samples,” *J. Biomech.*, vol. 48, no. 6, pp. 1099–1104, 2015.

[101] J. T. Zahn *et al.*, “Age-dependent changes in microscale stiffness and mechanoresponses of cells,” *Small*, vol. 7, no. 10, pp. 1480–1487, 2011.

[102] I. Sokolov, “Atomic force microscopy in cancer cell research,” *Cancer Nanotechnol.*, vol. 1, pp. 1–17, 2007.

[103] M. Fraldi, A. Cugno, L. Deseri, K. Dayal, and N. M. Pugno, “A frequency-based hypothesis for mechanically targeting and selectively attacking cancer cells,” *J. R. Soc. Interface*, vol. 12, no. 111, p. 20150656, 2015.

[104] M. Lekka, P. Laidler, D. Gil, J. Lekki, Z. Stachura, and a Z. Hrynkiewicz, “Elasticity of normal and cancerous human bladder cells studied by scanning force microscopy.,” *Eur. Biophys. J.*, vol. 28, no. 4, pp. 312–316, 1999.

[105] V. Swaminathan, K. Mythreye, E. Tim O’Brien, A. Berchuck, G. C. Blobe, and R. Superfine, “Mechanical Stiffness grades metastatic potential in patient tumor cells and in cancer cell lines,” *Cancer Res.*, vol. 71, no. 15, pp. 5075–5080, 2011.

[106] W. Xu, R. Mezencev, B. Kim, L. Wang, J. McDonald, and T. Sulchek, “Cell Stiffness Is a Biomarker of the Metastatic Potential of Ovarian Cancer Cells,” *PLoS One*, vol. 7, no. 10, 2012.

[107] E. Jonieztz, “The forces of cancer,” *Science (80-.).*, vol. 491, pp. S56–S57, 2012.

[108] T. Sugitate, T. Kihara, X. Y. Liu, and J. Miyake, “Mechanical role of the nucleus in a cell in terms of elastic modulus,” *Curr. Appl. Phys.*, vol. 9, no. 4 SUPPL., 2009.

[109] K. M. Stroka and H. Aranda-Espinoza, “Effects of morphology vs. cell-cell interactions on endothelial cell stiffness,” *Cell. Mol. Bioeng.*, vol. 4, no. 1, pp. 9–27, 2011.

[110] Y. W. Chiou, H. K. Lin, M. J. Tang, H. H. Lin, and M. L. Yeh, “The Influence of Physical and Physiological Cues on Atomic Force Microscopy-Based Cell Stiffness Assessment,” *PLoS One*, 2013.

[111] Y. M. Efremov, A. A. Dokrunova, D. V. Bagrov, K. S. Kudryashova, O. S. Sokolova, and K. V. Shaitan, “The effects of confluency on cell mechanical properties,” *J. Biomech.*, 2013.

[112] X. Guo, K. Bonin, K. Scarpinato, and M. Guthold, “The effect of neighboring cells on the stiffness of cancerous and non-cancerous human mammary epithelial cells,” *New J. Phys.*, vol. 16, 2014.

[113] N. Schierbaum, J. Rheinlaender, and T. E. Schäffer, “Viscoelastic properties of normal and cancerous human breast cells are affected differently by contact to adjacent cells,” *Acta Biomater.*, vol. 55, pp. 239–248, 2017.

[114] X. Guo, K. Bonin, K. Scarpinato, and M. Guthold, “The effect of neighboring cells on the stiffness of cancerous and non-cancerous human mammary epithelial cells,” *New J. Phys.*, vol. 16, 2014.

[115] G. Binnig and C. F. Quate, “Atomic Force Microscope,” *Phys. Rev. Lett.*, vol. 56, no. 9, pp. 930–933, 1986.

[116] Y. Seo and W. Jhe, “Atomic force microscopy and spectroscopy,” *Reports Prog. Phys.*, vol. 71, no. 1, 2008.

[117] M. Krieg *et al.*, “Atomic force microscopy-based mechanobiology,” *Nat. Rev. Phys.*, 2019.

[118] P. K. Viji Babu and M. Radmacher, “Mechanics of Brain Tissues Studied by Atomic Force Microscopy: A Perspective,” *Front. Neurosci.*, vol. 13, no. June, pp. 1–9, 2019.

[119] J. Chen, “Nanobiomechanics of living cells: A review,” *Interface Focus*, vol. 4, no. 2, 2014.

[120] B. Cappella and G. Dietler, “Force-distance curves by atomic force microscopy,” *Surf. Sci. Rep.*, 1999.

[121] T. Submitted, A.P Kao., “Spatial Mechanical Behaviour of Skin,” pp. 1–251, 2016.

[122] B. . Derjaguin, V. . Muller, and Y. . Toporov, “Effect of contact deformations on the adhesion of particles,” *J. Colloid Interface Sci.*, vol. 53, no. 2, pp. 314–326, Nov. 1975.

[123] T. Neumann, “Determining the elastic modulus of biological samples using atomic force microscopy,” *JPK Instruments Appl. Rep.*, pp. 1–9, 2008.

[124] Helen GreenWood Hansma, “No Title,” *research on bioloigcal atomic force microscopy*. [Online]. Available: http://web.physics.ucsb.edu/~hhansma/biomolecules.htm. [Accessed: 27-Jun-2019].

[125] N. Hilal, W. R. Bowen, L. Alkhatib, and O. Ogunbiyi, “A Review of Atomic Force Microscopy Applied to Cell Interactions with Membranes,” *Chem. Eng. Res. Des.*, vol. 84, no. 4, pp. 282–292, Apr. 2006.

[126] JPK Instruments, “Data processing software manual.” 2012.

[127] L. Deng *et al.*, “Fast and slow dynamics of the cytoskeleton,” *Nat. Mater.*, 2006.

[128] K. Robi, N. Jakob, K. Matevz, and V. Matjaz, “The Physiology of Sports Injuries and Repair Processes,” *Curr. Issues Sport. Exerc. Med.*, no. June, 2013.

[129] H. Hertz, “über die berührung fester elastischer körper,” *J. fur die Reine und Angew. Math.*, vol. 1882, no. 92, pp. 156–171, 1882.

[130] I. N. Sneddon, “The relation between load and penetration in the axisymmetric boussinesq problem for a punch of arbitrary profile,” *Int. J. Eng. Sci.*, vol. 3, no. 1, pp. 47–57, 1965.

[131] M. Rahmat, H. Ghiasi, and P. Hubert, “An interaction stress analysis of nanoscale elastic asperity contacts,” *Nanoscale*, vol. 4, no. 1, pp. 157–166, 2012.

[132] E. K. Dimitriadis, F. Horkay, J. Maresca, B. Kachar, and R. S. Chadwick, “Determination of elastic moduli of thin layers of soft material using the atomic force microscope,” *Biophys. J.*, vol. 82, no. 5, pp. 2798–2810, 2002.

[133] K. L. J. K. L. Johnson, *Contact Mechanics*. Cambridge University Press, 28.08.1987.

[134] “The Engineering ToolBox,” 2019. [Online]. Available: https://www.engineeringtoolbox.com/poissons-ratio-d_1224.html. [Accessed: 18-Jul-2019].

[135] N. Nijenhuis, X. Zhao, A. Carisey, C. Ballestrem, and B. Derby, “Combining AFM and acoustic probes to reveal changes in the elastic stiffness tensor of living cells,” *Biophys. J.*, vol. 107, no. 7, pp. 1502–1512, 2014.

[136] D. Shin and K. Athanasiou, “Cytoindentation for obtaining cell biomechanical properties,” *J. Orthop. Res.*, vol. 17, no. 6, pp. 880–890, 1999.

[137] R. Hooke, *De Potentia Restitutiva, or of Spring. Explaining the Power of Springing Bodies*. London, 1703.

[138] Y. Ding, G. K. Xu, and G. F. Wang, “On the determination of elastic moduli of cells by AFM based indentation,” *Sci. Rep.*, vol. 7, pp. 1–8, 2017.

[139] R. Mahaffy, S. Park, E. Gerde, J. Kas, and C. Shih, “Quantitative Analysis of the Viscoelastic Properties of Thin Regions of Fibroblasts Using Atomic Force Microscopy,” *Biophys. J.*, vol. 86, no. March, pp. 1777–1793, 2004.

[140] D. C. Lin, E. K. Dimitriadis, and F. Horkay, “Robust Strategies for Automated AFM Force Curve Analysis—II: Adhesion-Influenced Indentation of Soft, Elastic Materials,” *J. Biomech. Eng.*, vol. 129, no. 6, p. 904, 2007.

[141] V.M. Muller, B.V. Derjaguin Yu, P.Toporov, “On two methods of calculation of the force of sticking of an elastic sphere to a rigid plane,” *Colloids and Surfaces*, vol. 7, no. 3, pp. 251–259, 1983.

[142] K. L. Johnson, K. Kendall, and A. D. Roberts, “Surface energy and the contact of elastic solids,” *Proc. R. Soc. Lond. A. Math. Phys. Sci.*, vol. 324, no. 1558, pp. 301–313, 2012.

[143] C. P. Broedersz and F. C. Mackintosh, “Modeling semiflexible polymer networks,” *Rev. Mod. Phys.*, 2014.

[144] F. Rico, P. Roca-Cusachs, N. Gavara, R. Farré, M. Rotger, and D. Navajas, “Probing mechanical properties of living cells by atomic force microscopy with blunted pyramidal cantilever tips,” *Phys. Rev. E - Stat. Nonlinear, Soft Matter Phys.*, 2005.

[145] A. Rigato, A. Miyagi, S. Scheuring, and F. Rico, “High-frequency microrheology reveals cytoskeleton dynamics in living cells,” *Nat. Phys.*, 2017.

[146] N. Gavara and R. S. Chadwick, “Determination of the elastic moduli of thin samples and adherent cells using conical atomic force microscope tips,” *Nat. Nanotechnol.*, 2012.

[147] V. Managuli and S. Roy, “Asymptotical Correction to Bottom Substrate Effect Arising in AFM Indentation of Thin Samples and Adherent Cells Using Conical Tips,” *Exp. Mech.*, vol. 58, no. 5, pp. 733–741, Jun. 2018.

[148] C. Storm, J. J. Pastore, F. C. MacKintosh, T. C. Lubensky, and P. A. Janmey, “Nonlinear elasticity in biological gels,” *Nature*, 2005.

[149] J. Friedrichs *et al.*, “A practical guide to quantify cell adhesion using single-cell force spectroscopy,” *Methods*, 2013.

[150] A. B. Mathur, A. M. Collinsworth, W. M. Reichert, W. E. Kraus, and G. A. Truskey, “Endothelial, cardiac muscle and skeletal muscle exhibit different viscous and elastic properties as determined by atomic force microscopy,” *J. Biomech.*, vol. 34, no. 12, pp. 1545–1553, 2001.

[151] A. Pietuch *et al.*, “Mechanical properties of MDCK II cells exposed to gold nanorods,” *Beilstein J. Nanotechnol.*, vol. 6, no. 1, pp. 223–231, 2015.

[152] A. Nagelkerke, J. Bussink, A. E. Rowan, and P. N. Span, “The mechanical microenvironment in cancer: How physics affects tumours,” *Semin. Cancer Biol.*, vol. 35, pp. 62–70, 2015.

[153] E. C. Faria *et al.*, “Measurement of elastic properties of prostate cancer cells using AFM,” *Analyst*, vol. 133, no. 11, p. 1498, 2008.

[154] J. R. Ramos, J. Pabijan, R. Garcia, and M. Lekka, “The softening of human bladder cancer cells happens at an early stage of the malignancy process,” *Beilstein J. Nanotechnol.*, vol. 5, no. 1, pp. 447–457, 2014.

[155] J. P. Marquez, G. M. Genin, G. I. Zahalak, and E. L. Elson, “The relationship between cell and tissue strain in three-dimensional bio-artificial tissues.,” *Biophys. J.*, vol. 88, no. 2, pp. 778–89, 2005.

[156] V. H. Barocas and R. T. Tranquillo, “An anisotropic biphasic theory of tissue-equivalent mechanics: the interplay among cell traction, fibrillar network deformation, fibril alignment, and cell contact guidance.,” *J. Biomech. Eng.*, vol. 119, no. 2, pp. 137–145, 1997.

[157] T. J. Langan and R. C. Chou, “Cell Cycle Synchronization,” vol. 761, pp. 75–83, 2011.

[158] M. E. Dokukin, N. V Guz, and I. Sokolov, “Quantitative Study of the Elastic Modulus of Loosely Attached Cells in AFM Indentation Experiments,” *Biophysj*, vol. 104, no. 10, pp. 2123–2131, 2013.

[159] M. Chyasnavichyus, S. L. Young, R. Geryak, and V. V Tsukruk, “Probing elastic properties of soft materials with AFM : Data analysis for different tip geometries,” *Polymer (Guildf).*, pp. 1–9, 2016.

[160] M. R. Angle, A. Wang, A. Thomas, A. T. Schaefer, and N. A. Melosh, “Article Penetration of Cell Membranes and Synthetic Lipid Bilayers by Nanoprobes,” *Biophysj*, vol. 107, no. 9, pp. 2091–2100, 2014.

[161] N. Guz, M. Dokukin, V. Kalaparthi, and I. Sokolov, “If Cell Mechanics Can Be Described by Elastic Modulus: Study of Different Models and Probes Used in Indentation Experiments,” *Biophys. J.*, vol. 107, no. 3, 2014.

[162] G. Thomas, N. a Burnham, T. A. Camesano, and Q. Wen, “Measuring the mechanical properties of living cells using atomic force microscopy.,” *J. Vis. Exp.*, no. 76, pp. 1–8, 2013.

[163] Y. Zhang, G. Forgacs, and M. Grandbois, “Multiple Membrane Tethers Probed by Atomic Force Microscopy,” vol. 89, no. December, pp. 4320–4329, 2005.

[164] R. Vargas-Pinto, H. Gong, A. Vahabikashi, and M. Johnson, “The effect of the endothelial cell cortex on atomic force microscopy measurements,” *Biophys. J.*, vol. 105, no. 2, pp. 300–309, 2013.

[165] J. te Riet *et al.*, “Interlaboratory round robin on cantilever calibration for AFM force spectroscopy,” *Ultramicroscopy*, vol. 111, no. 12, pp. 1659–1669, 2011.

[166] F. M. Boyce and N. L. R. Buchert, “Baculovirus-mediated transfer into mammalian cells,” vol. 93, no. March, pp. 2348–2352, 1996.

[167] A. Burgess, S. Vigneron, E. Brioudes, J.-C. Labbé, T. Lorca, and A. Castro, “Loss of human Greatwall results in G2 arrest and multiple mitotic defects due to deregulation of the cyclin B-Cdc2/PP2A balance,” *Proc. Natl. Acad. Sci.*, vol. 107, no. 28, pp. 12564–12569, 2010.

[168] O. Gavet and J. Pines, “Europe PMC Funders Group Progressive activation of CyclinB1-Cdk1 coordinates entry to mitosis,” vol. 18, no. 4, pp. 533–543, 2012.

[169] T. A. Potapova, S. Sivakumar, J. N. Flynn, R. Li, and G. J. Gorbsky, “Mitotic progression becomes irreversible in prometaphase and collapses when Wee1 and Cdc25 are inhibited,” *Mol. Biol. Cell*, vol. 22, no. 8, pp. 1191–1206, 2011.

[170] A. S. S. Shapiro and M. B. Wilk, “Biometrika Trust An Analysis of Variance Test for Normality (Complete Samples) Published by : Oxford University Press on behalf of Biometrika Trust Stable URL : http://www.jstor.org/stable/2333709 Accessed : 25-04-2018 16 : 06 UTC An analysis of varianc,” vol. 52, no. 3, pp. 591–611, 2016.

[171] H. B. Mann and D. R. Whitney, “On a Test of Whether one of Two Random Variables is Stochastically Larger than the Other,” *Ann. Math. Stat.*, vol. 18, no. 1, pp. 50–60, 1947.

[172] A. R. Harris and G. T. Charras, “Experimental validation of atomic force microscopy-based cell elasticity measurements.,” *Nanotechnology*, vol. 22, no. 34, p. 345102, 2011.

[173] A. Demichelis, C. Divieto, L. Mortati, S. Pavarelli, G. Sassi, and M. P. Sassi, “Toward the realization of reproducible atomic force microscopy measurements of elastic modulus in biological samples,” *J. Biomech.*, 2015.

[174] N. Guz, M. Dokukin, V. Kalaparthi, and I. Sokolov, “If Cell Mechanics Can Be Described by Elastic Modulus: Study of Different Models and Probes Used in Indentation Experiments,” *Biophys. J.*, vol. 107, no. 3, pp. 564–575, 2014.

[175] F. M. Berglund, N. R. Weerasinghe, L. Davidson, J. C. Lim, B. J. Eickholt, and N. R. Leslie, “Disruption of epithelial architecture caused by loss of PTEN or by oncogenic mutant p110α/PIK3CA but not by HER2 or mutant AKT1,” *Oncogene*, vol. 32, no. 37, pp. 4417–4426, 2013.

[176] N. Elia and J. Lippincott-schwartz, “Culturing Three Dimensional MDCK cells for Analyzing Intracellular Dynamics,” *Curr. Protoc. cell Biol.*, 2009.

[177] J. H. Hoh and C. a Schoenenberger, “Surface morphology and mechanical properties of MDCK monolayers by atomic force microscopy.,” *J. Cell Sci.*, vol. 107 (Pt 5, pp. 1105–1114, 1994.

[178] R. Bacallao, C. Antony, C. Dotti, E. Karsenti, E. H. K. Stelzer, and K. Simons, “The SubceUular Organization of Madin-Darby Canine Kidney Cells during the Formation of a Polarized Epithelium,” vol. 109, no. 6, pp. 2817–2832, 1989.

[179] S. M. Zehnder, M. Suaris, M. M. Bellaire, and T. E. Angelini, “Cell volume fluctuations in MDCK monolayers,” *Biophys. J.*, vol. 108, no. 2, pp. 247–250, 2015.

[180] J. V. Méndez-Méndez, M. T. Alonso-Rasgado, E. Correia Faria, E. A. Flores-Johnson, and R. D. Snook, “Numerical study of the hydrodynamic drag force in atomic force microscopy measurements undertaken in fluids,” *Micron*, vol. 66, pp. 37–46, 2014.

[181] E. Paluch and C.-P. Heisenberg, “Biology and physics of cell shape changes in development.,” *Curr. Biol.*, vol. 19, no. 17, pp. R790-9, 2009.

[182] C. S. Chen, M. Mrksich, S. Huang, G. M. Whitesides, and D. E. Ingber, “Geometric Control of Cell Life and Death,” *Science (80-.).*, vol. 1425, no. 1997, 2009.

[183] T. Kondo and S. Hayashi, “Mechanisms of cell height changes that mediate epithelial invagination,” *Dev. Growth Differ.*, vol. 57, no. 4, pp. 313–323, 2015.

[184] T. Lecuit and P.-F. Lenne, “Cell surface mechanics and the control of cell shape, tissue patterns and morphogenesis.,” *Nat. Rev. Mol. Cell Biol.*, vol. 8, no. 8, pp. 633–644, 2007.

[185] M. Almonacid *et al.*, “Active diffusion positions the nucleus in mouse oocytes,” *Nat. Cell Biol.*, vol. 17, no. 4, pp. 470–479, 2015.

[186] R. Vargas-Pinto, H. Gong, A. Vahabikashi, and M. Johnson, “The effect of the endothelial cell cortex on atomic force microscopy measurements,” *Biophys. J.*, vol. 105, no. 2, 2013.

[187] K. Bodensiek, S. Li, M. Simons, I. A. T. Schaap, S. Nawaz, and P. Sa, “Cell Visco-Elasticity Measured with AFM and Optical Trapping at Sub-Micrometer Deformations,” vol. 7, no. 9, 2012.

[188] J. Alcaraz, L. Buscemi, M. Puig-De-Morales, J. Colchero, A. Baró, and D. Navajas, “Correction of microrheological measurements of soft samples with atomic force microscopy for the hydrodynamic drag on the cantilever,” *Langmuir*, vol. 18, no. 3, pp. 716–721, 2002.

[189] E. E. Charrier and P. A. Janmey, “Mechanical Properties of Intermediate Filament Proteins,” *Methods Enzymol.*, vol. 568, pp. 35–57, 2016.

[190] D. Bray, “Cell Movements: From Molecules To Motility, 2nd Edition,” *Shock*, vol. 15. p. 327, 2001.

[191] S. Tojkander, G. Gateva, and P. Lappalainen, “Actin stress fibers - assembly, dynamics and biological roles.,” *J. Cell Sci.*, vol. 125, no. Pt 8, pp. 1855–1864, 2012.

[192] R. Farhadifar, J. C. Röper, B. Aigouy, S. Eaton, and F. Jülicher, “The Influence of Cell Mechanics, Cell-Cell Interactions, and Proliferation on Epithelial Packing,” *Curr. Biol.*, vol. 17, no. 24, pp. 2095–2104, 2007.

[193] O. M. Lancaster and B. Baum, “Shaping up to divide: Coordinating actin and microtubule cytoskeletal remodelling during mitosis,” *Semin. Cell Dev. Biol.*, vol. 34, pp. 109–115, 2014.

[194] C. Cadart, E. Zlotek-Zlotkiewicz, M. Le Berre, M. Piel, and H. K. Matthews, “Exploring the function of cell shape and size during mitosis,” *Dev. Cell*, vol. 29, no. 2, pp. 159–169, 2014.

[195] E. Fischer-Friedrich, A. a Hyman, F. Jülicher, D. J. Müller, and J. Helenius, “Quantification of surface tension and internal pressure generated by single mitotic cells.,” *Sci. Rep.*, vol. 4, p. 6213, 2014.

[196] J. E. Lever, “Regulation of Dome Formation in Kidney Epithelial Cell Cultures,” *Ann. N. Y. Acad. Sci.*, vol. 372, no. 1, pp. 371–383, 1981.

[197] C. Birek, J. E. Aubin, U. Bhargava, D. M. Brunette, and A. H. Melcher, “Dome formation by oral epithelia in vitro,” *In Vitro*, vol. 18, no. 4, pp. 382–392, 1982.

[198] A. Atala, “Collective and single cell behavior in epithelial contact inhibition,” *J. Urol.*, vol. 188, no. 4, pp. 1396–1397, 2012.

[199] M. B. Ginzberg, N. Chang, R. Kafri, and M. W. Kirschner, “Cell size sensing in animal cells coordinates growth rates and cell cycle progression to maintain cell size uniformity,” *bioRxiv*, p. 123851, 2017.

[200] M. L. Turgeon, *Clinical hematology: theory and procedures*. Lippincott Williams & Wilkins, 2005.

[201] T. Rodriguez, J.M., Johansson, J.M.A., Edeskär, “Particle Shape Determination by Two-Dimensional Image Analysis in Geotechnical Engineering,” *Site Investig. Lab. Test.*, no. Eurocode 7, pp. 1–12, 2008.

[202] F. Tria, E. Caglioti, V. Loreto, and A. Pagnani, “Supplementary material,” *Mol. Biol. Evol.*, no. April, 2010.

[203] R. Bacallao, C. Antony, C. Dotti, E. Karsenti, E. H. K. Stelzer, and K. Simons, “The subcellular organization of Madin-Darby canine kidney cells during the formation of a polarized epithelium,” *J. Cell Biol.*, vol. 109, no. 6 I, pp. 2817–2832, 1989.

[204] S. Neelam, P. R. Hayes, Q. Zhang, R. B. Dickinson, and T. P. Lele, “Vertical uniformity of cells and nuclei in epithelial monolayers,” *Sci. Rep.*, vol. 6, no. January, pp. 1–10, 2016.

[205] J. F. Joanny, K. Kruse, J. Prost, and S. Ramaswamy, “The actin cortex as an active wetting layer Active Matter. Guest editors: Ramin Golestarian, Sriram Ramaswamy,” *Eur. Phys. J. E*, vol. 36, no. 5, 2013.

[206] M. Fritzsche, C. Erlenkamper, E. Moeendarbary, G. T. Charras, and K. Kruse, “Actin kinetics shapes cortical network structure and mechanics,” *Cell*, vol. 112, no. 4, pp. 453–65, 2003.

[207] R. M. Mège, J. Gavard, and M. Lambert, “Regulation of cell-cell junctions by the cytoskeleton,” *Curr. Opin. Cell Biol.*, vol. 18, no. 5, pp. 541–548, 2006.

[208] G. Salbreux, G. Charras, and E. Paluch, “Actin cortex mechanics and cellular morphogenesis,” *Trends Cell Biol.*, vol. 22, no. 10, pp. 536–545, 2012.

[209] C. Guillot and T. Lecuit, “Mechanics of epithelial tissue homeostasis and morphogenesis,” *Science (80)*, vol. 340, no. 6137, pp. 1185–1189, 2013.

[210] D. E. Ingber, “Tensegrity I. Cell structure and hierarchical systems biology,” *J. Cell Sci.*, 2003.

[211] A. F. Mertz, Y. Che, S. Banerjee, J. M. Goldstein, K. a Rosowski, and S. F. Revilla, “Epithelial Cell – Matrix Traction Forces,” *Proc. Natl. Acad. Sci.*, vol. 110, no. 3, pp. 842–847, 2013.